Exploring the formation of planets with microwave measurements of protoplanetary dust analogs

Vanesa Tobon Valencia

Aix*Marseille université
Initiative d'excellence

NNT/NL : 2020AIXM0001/001ED000

THÈSE DE DOCTORAT

Soutenue à Aix-Marseille Université
le 28 Octobre 2022 par

Vanesa TOBON VALENCIA

Exploring the formation of planets with microwave measurements of protoplanetary dust analogs

Discipline
Physique et Sciences de la Matière

Spécialité
Optique, Photonique et Traitement d'Image

École doctorale
ED 352 PHYSIQUE ET SCIENCES DE LA MATIERE

Laboratoire/Partenaires de recherche
Institut Fresnel
Institut de Planétologie et d'Astrophysique de Grenoble (IPAG)

Composition du jury

Rodolphe VAILLON CNRS - Institut d'Électronique et des Systèmes	Président du jury
Anaelle MAURY CEA-IRFU/DAP/AIM	Rapporteuse
Elodie CHOQUET Conseil National des Astronomes et Physiciens CNAP	Examinatrice
Azar MAALOUF Lab-STICC	Invité
Amélie LITMAN Aix-Marseille Université Institut Fresnel	Directrice de thèse
Jean-Michel GEFFRIN CNRS - Institut Fresnel	Co-directeur de thèse
François MENARD CNRS - IPAG	Co-encadrant de thèse et examinateur

INSTITUT FRESNEL

IPAG

I, undersigned, Vanesa Tobon Valencia, hereby declare that the work presented in this manuscript is my own work, carried out under the scientific direction of Amélie Litman and Jean-Michel Geffrin in accordance with the principles of honesty, integrity and responsibility inherent to the research mission. The research work and the writing of this manuscript have been carried out in compliance with both the french national charter for Research Integrity and the Aix-Marseille University charter on the fight against plagiarism.

This work has not been submitted previously either in this country or in another country in the same or in a similar version to any other examination body.

Marseille [15-07-2022]

Résumé

La formation planétaire débute par l'agglomération de poussières circumstellaires pour former des corps plus gros. Cependant, cette croissance n'est pas entièrement comprise et le modèle standard du scénario d'accrétion fait face à différentes barrières. Plusieurs scénarios ont été proposés pour surmonter ces barrières avec, par exemple, des poussières irrégulières comme des agrégats fractals de grains, au lieu des poussières sphériques compactes qui avaient été étudiés les premières vues la simplicité des modèles. Les télescopes actuels permettent d'observer les disques protoplanétaires en lumière diffusée et d'obtenir ainsi des informations indirectes, mais comment interpréter ces informations pour remonter à la morphologie de ces poussières et comment ces barrières peuvent-elles être dépassées ? Comment faire sans informations directes sur la poussière ? Pour faire avancer ces connaissances, nous proposons des mesures en laboratoire, donc dans des conditions expérimentales contrôlées, afin de réaliser des interprétations à partir des caractéristiques de diffusion d'objets connus.

Au travers de cette thèse, on cherche à fournir des outils réalistes pour interpréter les observations de disques protoplanétaires en mettant à profit des expériences de diffusion en micro-ondes. Des analogues de poussière contrôlés géométriquement et utilisant un indice de réfraction similaire au silicate astronomique, grâce à la fabrication additive, ont été mis à profit. Les dimensions de ces analogues ont été choisies pour conserver le rapport dimension sur longueur d'onde, ce qui permet de reproduire des phénomènes de diffusion similaires au observations, grâce à l'invariance par changement d'échelles des équations de Maxwell.

Au cours de ma thèse, j'ai étudié différents paramètres caractéristiques (dans le domaine de diffusion de Mie) tels que la fonction de phase, le degré de polarisation linéaire et d'autres éléments de la matrice de Mueller avec trois morphologies de poussières : des agrégats fractals, et deux familles de grains ayant différents types de rugosité. L'objectif était de comprendre ces différents paramètres et de donner des idées ou des outils qui permettent de mieux appréhender les informations indirectes contenues dans les signaux diffusés.

Les mesures des analogues de poussières ont été effectuées dans la chambre anéchoïque du CCRM et validées avec des simulations numériques. Grâce aux orientations et aux longueurs d'ondes multiples que notre installation permet, deux types d'analyses ont été réalisées avec les trois morphologies : premièrement, celle des paramètres de diffusion moyennés sur plusieurs orientations d'analogues à différentes longueurs d'onde, et deuxièmement, celle des paramètres de diffusion incluant une distribution de taille, de type loi de puissance. Sur la base de ces deux analyses, j'ai pu

identifier les propriétés de diffusion qui caractérisent chaque morphologie à l'aide de leurs paramètres de diffusion. J'ai identifié les changements des paramètres de diffusion entre différents objets d'une morphologie donnée et aussi entre les différentes morphologies. Je les ai aussi comparées aux paramètres de diffusion de morphologies similaires trouvés dans la littérature, vérifiant ainsi la cohérence de nos résultats.

Nos résultats ont prouvé que le contrôle de la géométrie, de l'indice de réfraction et de l'orientation de nos analogues est essentiel pour interpréter leurs propriétés de diffusion, fournissant des mesures de diffusion uniques grâce à notre expérience micro-ondes au CCRM et à la fabrication additive. De plus, ces résultats suggèrent que les porosités de nos agrégats et la rugosité de nos grains compacts affectent clairement et de manière spécifique leurs propriétés de diffusion. Par ailleurs, j'ai montré l'intérêt de poursuivre le développement instrumental des télescopes pour obtenir plus que l'intensité totale diffusée (fonction de phase) et le degré de polarisation linéaire. En effet, les autres paramètres de diffusion peuvent donner plus d'indices sur la morphologie des poussières des disques protoplanétaires. Enfin, je propose d'augmenter la taille des analogues et de tester d'autres indices de réfraction qui existent dans les disques, afin d'obtenir des paramètres de diffusion plus proches des observations. Il serait également intéressant d'effectuer des mesures plus proches de la rétrodiffusion.

Mots clés: Poussière protoplanétaire, diffusion, analogie micro-onde, analogues, agrégats fractals, grains, chondres, inclusion réfractaire, fonction de phase, degré de polarisation linéaire, éléments de la matrice de Mueller.

Abstract

The first stages of planetary formation begin with the agglomeration of protoplanetary dust to form bigger bodies. However, this dust growth is not fully understood and the standard accretion scenario model still contains different barriers inhibiting the growth of this dust. Several scenarios have been proposed to overcome these barriers, for example irregular dust, e.g., fractal aggregates and grains, contrary to compact spherical dust that was accepted to simplify models. Scattered light observations of protoplanetary disks can be done with nowadays telescopes, obtaining indirect information on this dust. But how can we interpret these scattering information to know if this dust has different morphologies and therefore help to improve the understanding of these barriers? how can we do this when we do not have direct information about dust? One solution is to study the scattering of dust analogs with laboratory experiments where the control of the experimental conditions is possible and therefore the interpretation of scattering information is also possible.

This thesis is dedicated to provide more realistic tools to interpret protoplanetary disk observations with microwave scattering experiments, where our dust analogs are geometrically controlled thanks to additive manufacturing, using a refractive index similar to astronomical silicate. The size of these analogs is chosen to be proportional to real dust compared to the used wavelengths to do the observations, in order to respect the electromagnetic scale invariance rule and thus reproduce similar scattering behaviors as real dust.

During my PhD I studied the scattering parameters (in the Mie scattering regime) such as the phase function, degree of linear polarization and other Mueller matrix elements of three dust morphologies, e.g. fractal aggregates, and two families of grains with different types of roughness. The goal was to understand their scattering properties and thus give insights or tools to understand the indirect information that is gathered with scattered light observations.

Measurements of dust analog were performed in the anechoic chamber of CCRM and cross-validated with numerical simulations. Thanks to the multi-orientation and multi-wavelength that our setup provides, two types of analyses were performed with the three types of morphologies: first, scattering parameters averaged over several orientations of analogs at different wavelengths, and second, scattering parameters including a power-law size distribution. Based on these two analyses, I was able to identify characteristic scattering properties of each morphology, showed with their scattering parameters. I identified the differences of their scattering parameters within a given morphology and between the different morphologies, and I compared them with scattering parameters of similar morphologies found in literature, verifying the

coherence of our results.

Based on our results, I proved that the control of geometry, refractive index and orientation of our analogs are key to interpret their scattering properties, providing unique scattering measurements thanks to our microwave experiment in CCRM and to the additive manufacturing. Furthermore, these results suggest that porosities of our aggregates and roughness of our compact grains clearly affect in specific ways their scattering properties. Moreover, I showed the interest to continue the instrumental development of telescopes to obtain more than the total scattered intensity (phase function) and degree of linear polarization. Indeed, the other scattering parameters (which are related to the non-sphericity, the degree of circular polarization and the polarization at 45°) can give more clues about the morphology of dust in protoplanetary disks. Finally, I suggested to increase the size of our analogs and test other refractive indices to obtain closer scattering parameters to observations of forming disks, as well as to perform measurements at backscattering angles.

Keywords: protoplanetary dust, scattering, microwave analogy, analogs, fractal aggregates, grains, chondrules, refractive inclusion, phase function, degree of linear polarization, Mueller matrix elements.

Acknowledgements

El dolor ha sido reto
y el porvenir esperanza,
construimos como escribiendo un poema
creando, borrando y volviendo a escribir.
-Vidaluz Meneses

During my PhD I found incredible people that pushed me to do my best, breaking difficult mental barriers each day to rebuilt my thoughts. I would like to first thanks my three advisers, Jean-Michel Geffrin, Amélie Litman and François Ménard for their enormous patient to teach me in each of their expertise. The long discussions I had with Jean-Michel to understand how to use the microwave analogy, and all the knowledge behind for measuring our analogs in the anechoic chamber. The short but fruitful explanations of Amélie, in which she tried to fulfill the knowledge gaps that I had due to the multidisciplinary of my PhD. And finally, François which in fact this project was his whole idea, showing me all his passion for the subject.

I had the opportunity to collaborate with an amazing group: Julien Milli, Jean-Baptiste Renard, Pascal Rannou and Azar Maalouf. All of them explained me their different domains and helped me during my PhD. I would also like to thank the Institut Fresnel and the Hipe group where I belonged this three years; Hervé Tortel, for the discussions in simulations and models; Christelle Eyraud, for her help with my time to time questions; both of them were always smiling and asking for how I was doing. Thanks to Pierre Sabouroux and Clement Baruteau for their emotional support. Thanks to Astrid Dufaure, who helped me and stayed next to me these two last years in the same office making my days happier.

I am profoundly grateful with my family: my late father, mother and sister. They all incredibly helped me to arrive where I am right now. Their love and support have been essential for this process. Thanks to Boris for being there all time, motivating me with his enormous love and for the long intellectual discussions we had. I am also thankful for finding an amazing group of friends that made my life easier in Marseille and helped me to remember that I needed to have breaks and laughters. Thanks to Miguel, Luis, Carla, Isael, Chang, Eric, Tilman, Sisira, Maëlle, Clement, Samuel, Camille, etc.

Finally, I would like to thank the jury members for accepting to read this thesis and give me very valuable feedbacks, suggestions and questions that clearly enhanced the quality of this manuscript.

Contents

Résumé 4

Abstract 6

Acknowledgements 7

Contents 8

List of Figures 11

List of Tables 22

Abbreviations 24

Introduction 25

Résumé version longue 28

1 State of the art 40
- 1.1 Introduction . . . 41
- 1.2 Stellar and planetary formation . . . 41
  - 1.2.1 Formation . . . 42
  - 1.2.2 Empirical evolutionary sequence . . . 43
  - 1.2.3 Protoplanetary disk . . . 45
- 1.3 Electromagnetic scattering theory . . . 58
  - 1.3.1 Electromagnetic wave . . . 61
  - 1.3.2 Stokes parameters . . . 62
  - 1.3.3 Amplitude scattering matrix or Jones matrix . . . 66
  - 1.3.4 Scattering matrix or Mueller matrix . . . 68
  - 1.3.5 Scattering parameters to be studied . . . 70
  - 1.3.6 Conclusions . . . 71
- 1.4 Laboratory techniques for measuring scattering parameters . . . 71
  - 1.4.1 Microwave scattering technique . . . 72
  - 1.4.2 Light scattering technique . . . 75
  - 1.4.3 Summary . . . 83
- 1.5 Microwave scattering experiment at CCRM . . . 85
  - 1.5.1 Anechoic chamber facility . . . 85
  - 1.5.2 Experimental setup . . . 86

1.5.3 Measurements . . . 89
1.6 Numerical simulations . . . 90
1.7 Microwave analogy of protoplanetary dust . . . 91
1.7.1 Size analogy . . . 92
1.7.2 Material analogy . . . 93
1.7.3 Microwave analogy assumptions . . . 97
1.8 Conclusions . . . 99

2 Fractal aggregates **101**
2.1 Introduction . . . 102
2.2 Fractal definition . . . 105
2.3 Analogs of dust aggregates . . . 106
2.3.1 Virtual generation . . . 106
2.3.2 3D-printing by stereolithography . . . 108
2.3.3 Aggregate size analogy . . . 109
2.4 Scattering properties of fractal-like aggregates . . . 110
2.4.1 Setup parameters . . . 111
2.4.2 Aggregates with average orientation . . . 116
2.4.3 Aggregates with average orientation and size distribution effect 136
2.4.4 Direct comparison of scattering parameters found in the literature 146
2.5 Estimation of fractal dimension . . . 153
2.5.1 D_f estimation methods . . . 153
2.5.2 Estimated fractal dimension with our aggregates phase functions 158
2.6 Conclusions . . . 170

3 Irregular compact grains **172**
3.1 Introduction . . . 173
3.2 Analogs of grains . . . 176
3.2.1 Virtual generation . . . 177
3.2.2 3D printing by stereolithography . . . 178
3.2.3 Grain size analogy . . . 179
3.3 Scattering properties of grains . . . 179
3.3.1 Setup parameters . . . 180
3.3.2 Grains with average orientation . . . 183
3.3.3 Grains with average orientation and size distribution effect . . . 201
3.3.4 Direct comparison of scattering parameters found in literature . 214
3.4 Analogs of chondrules and CAI . . . 219
3.4.1 Virtual generation . . . 219
3.4.2 3D printing by fused filament fabrication . . . 220
3.4.3 Chondrules and CAI size analogy . . . 222
3.5 Scattering properties of chondrules and CAI . . . 223
3.5.1 Setup parameters . . . 223
3.5.2 Chondrules and CAI with average orientation . . . 224

3.5.3 Chondrules and CAI with average orientation and size distribution effect 243
3.5.4 Direct comparison of scattering parameters found in literature . 261
3.6 Conclusions 264

General conclusions and perspectives **267**

Our papers **272**

Bibliography **276**

List of Figures

0.1 Schéma des mesures protoplanétaires avec deux types de sources qui rencontrent des poussières et produisent de la lumière diffusée. Cette diffusion est détectée par les télescopes à différents angles de réception (θ_{rec}). 29
0.2 Installation expérimentale dans deux types de configurations. 30
0.3 Mesures (lignes continues) et simulations numériques (lignes discontinues) des paramètres de diffusion de l'agrégat Ag_DLA_Df2.0_N74_1 (dimension fractale 2) à différents paramètres de taille X_{mon}. 34
0.4 Mesures (lignes continues) et simulations numériques (lignes discontinues) des paramètres de diffusion des agrégats avec une distribution de taille en loi de puissance $n_s = 3.5$. 35
0.5 Mesures (lignes continues) des paramètres de diffusion de la chondre C0_PLA_orange_r5.04 à différents paramètres de taille X. 38
0.6 Mesures (lignes continues) des paramètres de diffusion des chondres et CAI avec une distribution de taille en loi de puissance $n_s = 3.5$. 39

1.1 Empirical evolutionary sequence based on the shape of SED, the bolometric temperature and the disk mass [taken and modified from 35]. . 44
1.2 Vertical structure of protoplanetary disk considering a vertical hydrostatic equilibrium (taken from [42]). 46
1.3 Collisional outcomes for silica colliding particles at a distance of 1 AU [taken from 63]. 51
1.4 Representation of a protoplanetary disk with its transport and growth processes (on the right) as well as dust sizes (on the left) [taken from 59]. 53
1.5 Scheme to represent the two types of sources that encounter dust in protoplanetary disks, producing scattered light that is detected by telescopes at different angles of reception (θ_{rec}). 54
1.6 Images of protoplanetary disks seen in scattered light with HST (color images) at NIR wavelengths for all sources, except for IRAS 04200, Oph 163131, ESO-Hα 574 and HK Tau B which are at optical wavelengths; and with ALMA (continuum images in white contours) at band 7 for all sources, except for Oph 163131 which is at band 6 [taken from 73]. . . . 55

1.7 Images of disk LkCa15 presented in polarized intensity (left image) , total intensity (middle image) and the computed degree of linear polarization (right image). Note that the color map of the total intensity is 10 times larger than for the polarized intensity and the gray circle in the middle is the coronographic mask [taken from 41]. 56
1.8 Scheme for passing from (a) the scattering parameters of dust to (b) the same parameters of protoplanetary disk. Images (a) and (b) were taken from [41]. 57
1.9 Phase function of disk HR4796A based on observations in scattered light taken from [78]. The phase function is represented over the scattering angles from 13.6° to 166.6°. 58
1.10 Electromagnetic scattering for a single particle. 59
1.11 Scattering regimes depending on the particle radius and the wavelength [taken and modified from 81]. 60
1.12 a) Vibration ellipse viewed from the plane xy with its amplitudes A and B (see Equation 1.13), semimajor axis a, semiminor axis b, angles γ and η (see Equation 1.16); b) Vibration ellipse viewed in the z direction. . . 61
1.13 Basic states of polarization represented by the Stokes vector. Note that the horizontal and vertical polarizations have inverse signs in the standard astronomical convention (see Figure 1 in [83]). 64
1.14 Incident and scattered electric fields described by their perpendicular and parallel components to the scattering plane [based on 84]. 67
1.15 Microwave scattering setup at SUNYA laboratory [taken from 86]. . . . 73
1.16 Microwave scattering setup at Bochum University [taken from 88]. . . . 74
1.17 Microwave scattering setup at the University of Florida [taken from 92]. 75
1.18 Multicolor light scattering setup at Bochum University [taken from 87]. 76
1.19 Photopolarimeter setup at Bochum University [taken from 87]. 77
1.20 Scatterometer setup at the University of Helsinki [taken and modified from 97]. 78
1.21 Light scattering setup at the Astronomical Institute of the University of Amsterdam [taken from 102]. 79
1.22 Granada light scattering setup at the Instituto de Astrofísica de Andalucía [taken from 104]. 80
1.23 PROGRA2 setup at visible wavelengths [taken from 11]. 82
1.24 PROGRA2 vials [taken and modified from PROGRA2 database]. 82
1.25 PROGRA2-surf setup [taken from 109]. 83
1.26 Photo of anechoic chamber CCRM. 86
1.27 Setup of microwaves devices at CCRM [taken from 115]. 87
1.28 Forward experimental setup where the emitting antenna is fixed at the vertical arrangement while the receiving antenna moves on the horizontal arrangement [taken from 117]. 88

1.29 Backward experimental setup where the emitting antenna is also fixed while the receiving antenna moves on the vertical arrangement [taken from 117]. 89
1.30 Scale invariance rule [taken and modified from 85]. 92
1.31 Bibliographical study of refractive index of protoplanetary dust (these specific references are at the end of this section with a prefix M for material properties). 94
1.32 Bibliographical study of permittivity of protoplanetary dust (these specific references are at the end of this section with a prefix M for material properties). 94
1.33 Refractive index of the astronomical silicate. 95

2.1 Example of one of our fractal-like aggregates created with DLA algorithm [17] with a fractal dimension of 1.7, number of monomers 74 and radius of gyration of 23.93mm. 105
2.2 3D printed aggregates, using the SLA technique, with their corresponding technical name (second column of Table 2.1). 108
2.3 Example of necessary number of orientations and positions of aggregate Ag_DLA_Df1.7_N74 to obtain mean scattering parameters. A total of 108 orientations were necessary for this aggregate. 112
2.4 Example of necessary number of measurements of aggregate Ag_DLA_Df2.0_N74_1 at $\lambda = 23\,\text{mm}$, $X_{agg} = 7.14$ and $X_{mon} = 0.75$ [taken from 126]. 112
2.5 Comparison between FEM (dashed lines) and MoM (dotted lines) numerical simulations at six different wavelengths (100 mm, 50 mm, 33.3mm, 25 mm, 20 mm and 16.7mm) indicated in terms of monomers size parameter, from $X_{mon} = 0.17$ to $X_{mon} = 1.04$ for Ag_DLA_Df2.0_N74_1. . 113
2.6 FEM numerical simulations of Ag_DLA_Df2.0_N74_1, considering co-polarized Jones matrix elements (dashed lines) and co-polarized plus cross-polarized elements (dashed-dotted lines), from $X_{mon} = 0.17$ to $X_{mon} = 1.04$. 114
2.7 Measurements in the forward and backward zone (solid lines) and numerical simulations (dashed lines) of Ag_DLA_Df2.0_N74_1, from $X_{mon} = 0.17$ to $X_{mon} = 1.04$. 116
2.8 Phase function of aggregates with different fractal dimensions, measurements (solid lines) and numerical simulations (dashed lines), from $X_{mon} = 0.17$ to $X_{mon} = 1.04$. 118
2.9 Normalized root mean square deviations on the log of the phase function plotted for all the measured aggregates, taking their FEM numerical simulation as reference. The gray line is a comparison of the Mie simulation versus FEM numerical simulation with a sphere of 32.5mm in diameter. 119

2.10 FEM numerical simulations of normalized phase function of aggregates with different fractal dimensions at $X_{mon} = 0.17$ and $X_{mon} = 1.04$. The gray line is the Mie simulation for a sphere with the same radius as that of a monomer. 120
2.11 Phase function of aggregates having the same fractal dimension $D_f = 2.0$, measurements (solid lines) and numerical simulations (dashed lines), from $X_{mon} = 0.17$ to $X_{mon} = 1.04$. 121
2.12 Measurements (solid lines) and numerical simulations (dashed lines) of the scattering phase function of three aggregates having the same fractal dimension $D_f = 2$, at different X_{mon}. 121
2.13 Example of measured (solid lines) and numerical (dashed lines) HWHM of the phase function of Ag_DLA_Df2.5_N74. 122
2.14 Numerical HWHM of the phase function for all aggregates with their corresponding inverse X_{agg}, from $\lambda = 50$ to 16.7 mm. 123
2.15 DLP of aggregates with different fractal dimensions, measurements (solid lines) and numerical simulations (dashed lines), from $X_{mon} = 0.17$ to $X_{mon} = 1.04$ (see the legend of Figure 2.8). Gray line in (a) is the Mie simulation for a sphere with the same size as that of a monomer. 125
2.16 Normalized root mean square deviations on the DLP plotted for all the measured aggregates, taking their FEM numerical simulation as reference. The gray line is a comparison of the Mie simulation versus FEM numerical simulation with a sphere of 32.5mm in diameter. . . . 126
2.17 FEM numerical simulations of normalized DLP of aggregates with different fractal dimensions at $X_{mon} = 0.17$ and $X_{mon} = 1.04$. The gray line is a Mie simulation for a sphere with the same size as that of a monomer. 126
2.18 DLP of aggregates having the same fractal dimension $D_f = 2.0$, measurements (solid lines) and numerical simulations (dashed lines), from $X_{mon} = 0.17$ to $X_{mon} = 1.04$. 127
2.19 Measurements (solid lines) and numerical simulations (dashed lines) of DLP of three aggregates having the same fractal dimension $D_f = 2$ at different X_{mon}. 127
2.20 FEM numerical simulations of $< S_{22} > / < S_{11} >$ including co-polarized and cross-polarized elements of the Jones matrix of aggregates with different fractal dimensions, from $X_{mon} = 0.17$ to $X_{mon} = 1.04$. 131
2.21 FEM numerical simulations of $< S_{22} > / < S_{11} >$ for aggregates with different fractal dimensions at $X_{mon} = 0.35$ and $X_{mon} = 0.52$. 132
2.22 $< S_{44} > / < S_{11} >$ of aggregates with different fractal dimensions. Measurements (solid lines) and numerical simulations (dashed lines), from $X_{mon} = 0.17$ to $X_{mon} = 1.04$. 134
2.23 $< S_{34} > / < S_{11} >$ of aggregates with different fractal dimensions. Measurements (solid lines) and numerical simulations (dashed lines), from $X_{mon} = 0.17$ to $X_{mon} = 1.04$. 135

2.24 Probability distribution on the size parameter X_{mon}, from 0.29 to 1.04, with three different indices (see legend) . . . 137
2.25 Phase function of aggregates with average orientation and with power law distributions of different n_s, measurements (solid lines) and numerical simulations (dashed lines). Figure (a) also presents the phase function of the most compact aggregate at $X_{mon} = 1.04$ (in brown) and most fluffy aggregate at $X_{mon} = 0.86$ (in gray) with No Size Distribution Effect (NSDE). . . . 139
2.26 DLP of aggregates with average orientation and with power law distributions of different n_s, measurements (solid lines) and numerical simulations (dashed lines). Figure (a) also presents DLP of the most compact aggregate at $X_{mon} = 1.04$ (in brown) and most fluffy aggregate at $X_{mon} = 0.86$ (in gray) with No Size Distribution Effect (NSDE). . . . 141
2.27 $< S_{22} > / < S_{11} >$ of aggregates with average orientation and with power law distributions of different n_s based on numerical simulations (dashed lines). . . . 143
2.28 $< S_{44} > / < S_{11} >$ of aggregates with average orientation and with power law distributions of different n_s, measurements (solid lines) and numerical simulations (dashed lines). . . . 144
2.29 $< S_{34} > / < S_{11} >$ of aggregates with average orientation and with power law distributions of different n_s, measurements (solid lines) and numerical simulations (dashed lines). . . . 145
2.30 Laboratory scattering measurements comparison of the phase function. (a) Phase function of samples 3 and 4 [see Figure 7 in 106], (b) phase function of our aggregates Ag_DLA_Df1.7_N74 and Ag_DLA_Df1.5_N74 with power law distribution effect of $n_s = 2$ for measurements (solid lines) and numerical simulations (dashed lines). . . . 147
2.31 Laboratory scattering measurements comparison of the DLP. (a) DLP of samples 3 and 4 [see Figure 7 in 106], (b) DLP of our aggregates Ag_DLA_Df1.7_N74 and Ag_DLA_Df1.5_N74 with power law distribution effect of $n_s = 2$ for measurements (solid lines) and numerical simulations (dashed lines). . . . 148
2.32 Laboratory scattering measurements comparison of $< S_{22} > / < S_{11} >$. (a) $< S_{22} > / < S_{11} >$ of samples 3 and 4 [see Figure 7 in 106], (b) $< S_{22} > / < S_{11} >$ of our aggregates Ag_DLA_Df1.7_N74 and Ag_DLA_Df1.5_N74 with power law distribution effect of $n_s = 2$ for measurements (solid lines) and numerical simulations (dashed lines). . . . 148
2.33 Numerical scattering comparison of the phase function. (a) Phase function of samples $r_v = 0.2$ [see Figure 4 in 137], (b) phase function of our aggregate Ag_DLA_Df2.8_N74 with power law distribution effect of $n_s = 2$ for measurements (solid lines) and numerical simulations (dashed lines). . . . 149

2.34 Numerical scattering comparison of the DLP. (a) DLP of sample $r_v = 0.2$ [see Figure 7 in 137], (b) DLP of our aggregate Ag_DLA_Df2.8_N74 with power law distribution effect of $n_s = 2$ for measurements (solid lines) and numerical simulations (dashed lines). 150
2.35 Numerical scattering comparison of the phase function. (a) Phase function of models 1, 2 and 3 [see Figure 8 in 146], (b) phase functions of our aggregates with power law distribution effect of $n_s = 5$ for measurements (solid lines) and numerical simulations (dashed lines). 151
2.36 Numerical scattering comparison of DLP. (a) DLP of models 1, 2 and 3 [see Figure 8 in 146], (b) DLP of our aggregates with power law distribution effect of $n_s = 3.5$ for measurements (solid lines) and numerical simulations (dashed lines). 151
2.37 Observational scattering comparison of phase function normalized at 90°. (a) Phase function of disk HR4796A [see Figure 17 in 78], (b) phase function of our aggregates with power law distribution effect of $n_s = 2$ for measurements (solid lines) and numerical simulations (dashed lines). 152
2.38 Structure factor in terms of q with its three corresponding zones. . . . 154
2.39 Example of fitting between normalized phase function in q-space and Butterworth filter of Ag_DLA_Df1.7_N74 with average orientation at $\lambda = 30\,\text{mm}$, corresponding to $X_{mon} = 0.58$. 157
2.40 Polynomial function g(n) relating n found with Butterworth filter and theoretical D_f. Data points are based on simulated phase functions of aggregates with average orientation. The same procedure was made to find the relations for simulated phase functions of aggregates with average orientation including a size distribution effect ($G(n)$). 158
2.41 Estimated D_f from measurements of normalized phase functions in q-space of Ag_DLA_Df2.0_N74_1 with different methods at $X_{mon} = 0.58$. Mrockza_SSE method does not give values because as can be seen in Figure (d) after $5/R_g$ there is not a linear zone to estimate D_f. Note that the theoretical D_f is included in the name of Ag_DLA_Df2.0_N74_1, thus $D_{f\,theoretical} = 2.0$. 160
2.42 Estimated D_f from measurements (solid lines) and simulations (dashed lines) of phase functions in q-space of Ag_DLA_Df2.0_N74_1 with different methods, from $X_{mon} = 0.29$ to $X_{mon} = 1.04$. 161
2.43 Estimation of D_f from measurements of normalized mean phase functions in q-space of three aggregates with $D_{f\,theoretical} = 2$ with different methods at $X_{mon} = 0.58$. Figure (a) presents also the simulation of the normalized mean phase function and estimated D_f in dot lines. 164
2.44 Estimated D_f at different X_{mon} from measurements (solid lines) and simulations (dashed lines) of normalized mean phase functions in q-space of aggregates with $D_{f\,theoretical} = 2$. 165

2.45 Estimated D_f from measurements of normalized phase function of Ag_-DLA_Df2.0_N74_1 with average orientation and size distribution effect. Figure (a) presents also the simulation of the normalized phase function and estimated D_f in dotted lines. 167
2.46 Estimated D_f compared to theoretical D_f with different methods. Measurements (solid lines with circles) and simulations (dashed lines). . . 168

3.1 Example of a grain virtual generation, where r is the initial radius of the sphere to mesh, r_{rough} are the perturbed distances from the center of the sphere r to each triangle vertex and R_{max} is the radius of the bounding sphere named maximum radius. 177
3.2 3D printed grains with their corresponding technical name. 179
3.3 Example of necessary number of measurements for grain Gr_n2_r13.3 at $\lambda = 25\,\text{mm}$, $X = 5.03$ [taken from 126]. 181
3.4 FEM numerical simulations of Gr_n2_r13.3, considering co-polarized Jones matrix elements (dashed lines) and co-polarized plus cross-polarized elements (dashed-dotted lines), from $X = 1.26$ to $X = 7.55$. 182
3.5 Phase function of grains, measurements (solid lines) and numerical simulations (dashed lines). 184
3.6 Normalized root mean square deviations on the log of the phase function plotted for all grains, taking their FEM numerical simulation as reference. The gray line is a comparison of the Mie simulation versus FEM numerical simulation with a sphere of radius 16.25mm. 185
3.7 FEM numerical simulations of phase function of grains at $\lambda = 16.7\text{mm}$ with a size parameter of $X_{mean} = 6.94$. 186
3.8 DLP of grains, measurements (solid lines) and numerical simulations (dashed lines), see legends of Figure 3.5 187
3.9 FEM numerical simulations of DLP of grains at $\lambda = 20\,\text{mm}$ with a size parameter of $X_{mean} = 5.80$. 188
3.10 Normalized root mean square deviations on the log of the DLP plotted for all grains, taking their FEM numerical simulation as reference. The gray line is a comparison of the Mie simulation versus FEM numerical simulation with a sphere of radius 16.25mm. 189
3.11 FEM numerical simulations of $< S_{22} > / < S_{11} >$ including co and cross-polarized Jones matrix elements of grains. 191
3.12 FEM numerical simulations of $< S_{22} > / < S_{11} >$ of grains at $\lambda = 16.7\text{mm}$ with a size parameter of $X_{mean} = 6.94$ and $\lambda = 100\,\text{mm}$ with a size parameter of $X_{mean} = 1.16$. 192
3.13 $< S_{44} > / < S_{11} >$ of grains, measurements (solid lines) and numerical simulations (dashed lines). 193
3.14 $< S_{34} > / < S_{11} >$ of grains, measurements (solid lines) and numerical simulations (dashed lines). See legends of Figure 3.13. 194

3.15 Phase function of grains and aggregates, measurements (solid lines) and numerical simulations (dashed lines). Note that colors are given at six wavelengths but depending on the size of the object this creates different size parameters, see Figure (d) to have comparable size parameters. . . 196
3.16 DLP of grains and aggregates, measurements (solid lines) and numerical simulations (dashed lines). 197
3.17 $< S_{22} > / < S_{11} >$ of grains and aggregates including co and cross-polarized Jones Matrix elements. 198
3.18 $< S_{44} > / < S_{11} >$ of grains and aggregates, measurements (solid lines) and numerical simulations (dashed lines). 199
3.19 $< S_{34} > / < S_{11} >$ of grains and aggregates, measurements (solid lines) and numerical simulations (dashed lines). 200
3.20 Probability distribution with three different indices (see legend) in terms of X_{mean}, from 1.16 to 6.94. 202
3.21 Phase function of grains with average orientation and with power law distributions of different n_s, measurements (solid lines) and numerical simulations (dashed lines). Figure (a) also presents the phase function of the roughest grain at $X = 1.26$ (in brown) and at $X = 7.54$ (in orange) with No Size Distribution Effect (NSDE). 203
3.22 Normalized phase function of grains with average orientation and with power law distributions of $n_s = 3.5$, measurements (solid lines) and numerical simulations (dashed lines). 204
3.23 DLP of grains with average orientation and with power law distributions of different n_s, measurements (solid lines) and numerical simulations (dashed lines). Figure (a) also presents DLP of the roughest grain at $X = 1.26$ (in brown) and at $X = 7.54$ (in orange) with No Size Distribution Effect (NSDE). 205
3.24 $< S_{22} > / < S_{11} >$ of grains with average orientation and with power law distributions of different n_s based on numerical simulations (dashed lines). 207
3.25 $< S_{44} > / < S_{11} >$ of grains with average orientation and with power law distributions of different n_s, measurements (solid lines) and numerical simulations (dashed lines). 208
3.26 $< S_{34} > / < S_{11} >$ of grains with average orientation and with power law distributions of different n_s, measurements (solid lines) and numerical simulations (dashed lines). 209
3.27 Normalized phase function of grains and aggregates with average orientation and with power law distributions of $n_s = 3.5$, measurements (solid lines) and numerical simulations (dashed lines). 211
3.28 DLP of grains and aggregates with average orientation and with power law distributions of $n_s = 3.5$, measurements (solid lines) and numerical simulations (dashed lines). 212

3.29 $< S_{22} > / < S_{11} >$ of grains and aggregates with average orientation and with power law distributions of $n_s = 3.5$, measurements (solid lines) and numerical simulations (dashed lines). 213
3.30 $< S_{44} > / < S_{11} >$ of grains and aggregates with average orientation and with power law distributions of $n_s = 3.5$, measurements (solid lines) and numerical simulations (dashed lines). 213
3.31 $< S_{34} > / < S_{11} >$ of grains and aggregates with average orientation and with power law distributions of $n_s = 3.5$, measurements (solid lines) and numerical simulations (dashed lines). 214
3.32 Laboratory scattering measurements comparison of the phase function normalized at 30° (vertical black line). (a) Phase function of three grains (Quartz, enstatite and Etna) and Fomalhaut disk (in legend as Kalas et al. 2005) [see Figure 7 in 107], (b) phase functions of our grains with power law distribution effect of $n_s = 3.5$ for measurements (solid lines) and numerical simulations (dashed lines). 216
3.33 Numerical scattering comparison of the phase function normalized at 180°. (a) Phase function of grain with $\rho = 0.336$ [see Figure 5 in 156], (b) phase functions of our grain with power law distribution effect of $n_s = 3.5$ for numerical simulations (dashed line). 217
3.34 Numerical scattering comparison of DLP. (a) DLP of grain with $\rho = 0.336$ [see Figure 5 in 156], (b) DLP of our grain with power law distribution effect of $n_s = 3.5$ for measurements (solid line) and numerical simulations (dashed line). 217
3.35 Observational scattering comparison of phase function normalized at 90°. (a) Phase function of disk HR4796A [see Figure 17 in 78], (b) phase function of our grains with power law distribution effect of $n_s = 2$ for measurements (solid lines) and numerical simulations (dashed lines). 218
3.36 X-ray computed tomography of chondrules and CAI inside its chondrite. 220
3.37 3D printed chondrules and CAI with their corresponding technical name. 222
3.38 Phase function of chondrules and CAI, measurements (solid lines) with their corresponding size parameter. 225
3.39 Normalized phase functions of chondrules and CAI at $\lambda = 16.7$mm, corresponding to $X_{mean} = 7.65$ for chondrules and $X = 21.54$ for CAI. . 227
3.40 DLP of chondrules and CAI, measurements (solid lines) with their corresponding size parameter. 228
3.41 DLP of chondrules and CAI at $\lambda = 16.7$mm, corresponding to $X_{mean} = 7.65$ for chondrules and $X = 21.53$ for CAI. 229
3.42 $< S_{44} > / < S_{11} >$ of chondrules and CAI, measurements (solid lines) with their corresponding size parameter. 230
3.43 $< S_{44} > / < S_{11} >$ of chondrules and CAI at $\lambda = 16.7$mm, corresponding to $X_{mean} = 7.65$ for chondrules and $X = 21.53$ for CAI. 231
3.44 $< S_{34} > / < S_{11} >$ of chondrules and CAI, measurements (solid lines) with their corresponding size parameter. 232

3.45 Phase function of chondrule C0_PLA_orange_r5.04 and grain Gr_n4_-r6.7, measurements (solid lines) and numerical simulations (dashed lines). 235
3.46 Phase function of chondrule, grain and aggregates, measurements (solid lines) and numerical simulations (dashed lines). 236
3.47 DLP of chondrule C0_PLA_orange_r5.04 and grain Gr_n4_r6.7, measurements (solid lines) and numerical simulations (dashed lines). 237
3.48 DLP of chondrule, grain and aggregates, measurements (solid lines) and numerical simulations (dashed lines). 238
3.49 $< S_{44} > / < S_{11} >$ of chondrule C0_PLA_orange_r5.04 and grain Gr_n4_-r6.7, measurements (solid lines) and numerical simulations (dashed lines). 239
3.50 $< S_{44} > / < S_{11} >$ of chondrule, grain and aggregates, measurements (solid lines) and numerical simulations (dashed lines). 240
3.51 $< S_{34} > / < S_{11} >$ of chondrule C0_PLA_orange_r5.04 and grain Gr_n4_-r6.7, measurements (solid lines) and numerical simulations (dashed lines). 241
3.52 $< S_{34} > / < S_{11} >$ of chondrule, grain and aggregates, measurements (solid lines) and numerical simulations (dashed lines). 242
3.53 Probability distribution with three different indices (see legend) in terms of X_{mean} for chondrules, from 1.28 to 7.65 (Figure a), and in terms of X for CAI, from 3.59 to 21.54 (Figure b). 243
3.54 Phase function of chondrules and CAI with average orientation and with power law distributions of different n_s, measurements (solid lines). . . 244
3.55 Normalized phase function of chondrules and CAI with average orientation and with power law distributions of $n_s = 3.5$, measurements (solid lines). 245
3.56 DLP of chondrules and CAI with average orientation and with power law distributions of different n_s, measurements (solid lines). 247
3.57 $< S_{44} > / < S_{11} >$ of chondrules and CAI with average orientation and with power law distributions of different n_s, measurements (solid lines). 249
3.58 $< S_{34} > / < S_{11} >$ of chondrules and CAI with average orientation and with power law distributions of different n_s, measurements (solid lines). 250
3.59 Normalized phase function with power law distribution of $n_s = 3.5$, measurements (solid lines) and numerical simulations (dashed lines). 252
3.60 Normalized phase function comparison between grains and chondrules with power law distribution of $n_s = 3.5$, measurements of grains (solid lines), numerical simulations of grains (dashed lines) and measurements of chondrules (dotted lines). 253
3.61 Normalized phase function comparison between aggregates, chondrules and CAI with power law distribution of $n_s = 3.5$, measurements of aggregates (solid lines), numerical simulations of aggregates (dashed lines) and measurements of chondrules and CAI (dotted lines). 253

3.62 DLP with power law distribution of $n_s = 3.5$, measurements (solid lines) and numerical simulations (dashed lines). 254
3.63 DLP comparison between grains and chondrules with power law distribution of $n_s = 3.5$, measurements of grains (solid lines), numerical simulations of grains (dashed lines) and measurements of chondrules (dotted lines). 255
3.64 DLP comparison between aggregates, chondrules and CAI with power law distribution of $n_s = 3.5$, measurements of aggregates (solid lines), numerical simulations of aggregates (dashed lines) and measurements of chondrules and CAI (dotted lines). 256
3.65 $< S_{44} > / < S_{11} >$ with power law distribution of $n_s = 3.5$, measurements (solid lines) and numerical simulations (dashed lines). 257
3.66 $< S_{44} > / < S_{11} >$ comparison between grains, chondrules and CAI with power law distribution of $n_s = 3.5$, measurements of grains (solid lines), numerical simulations of grains (dashed lines) and measurements of chondrules and CAI (dotted lines). 258
3.67 $< S_{44} > / < S_{11} >$ comparison between aggregates, chondrules and CAI with power law distribution of $n_s = 3.5$, measurements of aggregates (solid lines), numerical simulations of aggregates (dashed lines) and measurements of chondrules and CAI (dotted lines). 258
3.68 $< S_{34} > / < S_{11} >$ with power law distribution of $n_s = 3.5$, measurements (solid lines) and numerical simulations (dashed lines). 259
3.69 $< S_{34} > / < S_{11} >$ comparison between grains, chondrules and CAI with power law distribution of $n_s = 3.5$, measurements of grains (solid lines), numerical simulations of grains (dashed lines) and measurements of chondrules and CAI (dotted lines). 260
3.70 $< S_{34} > / < S_{11} >$ comparison between aggregates, chondrules and CAI with power law distribution of $n_s = 3.5$, measurements of aggregates (solid lines), numerical simulations of aggregates (dashed lines) and measurements of chondrules and CAI (dotted lines). 260
3.71 Laboratory scattering measurement comparison of phase function normalized at a phase angle of 150°. (a) Phase function of chondrite and mineral samples [see Figure 4 in 108], (b) phase function of our chondrules and CAI with power law distribution effect of $n_s = 3.5$ for measurements (solid lines). 262
3.72 Laboratory scattering measurement comparison of DLP. (a) DLP of chondrite and mineral samples [see Figure 5 in 108], (b) DLP of our chondrules and CAI with power law distribution effect of $n_s = 3.5$ for measurements (solid lines). 263
3.73 Observational scattering comparison of phase function normalized at 90°. (a) Phase function of disk HR4796A [see Figure 17 in 78], (b) phase function of our chondrules and CAI with power law distribution effect of $n_s = 2$ for measurements (solid lines). 264

List of Tables

1.1 Comparison between light scattering and microwave scattering techniques. . . . 84
1.2 Parameters of protoplanetary dust. . . . 92
1.3 Parameters of protoplanetary dust analogs that can be achieved with CCRM setup. . . . 93
1.4 Parameters of protoplanetary dust analogs for this specific study. . . . 93

2.1 Analog aggregate properties with monomer size parameter from X_{mon} = 1.04 (λ = 16.7 mm) to X_{mon} = 0.17 (λ = 100 mm). . . . 109
2.2 Monomer and aggregate radius corresponding to different wavelength ranges (units are noted in the first column). . . . 110
2.3 HWHM of phase function in degrees at different X_{mon} for different fractal dimensions. Measured values (numerical values). . . . 122
2.4 Angles in degrees corresponding to the maximum DLP at different X_{mon} for different fractal dimensions. Measured values (numerical values). . 128
2.5 HWHM of phase function of aggregates with average orientation and with power law distributions of different n_s. Measured values (numerical values), both in degrees. . . . 140
2.6 Levels of maximum DLP of aggregates with average orientation and with power law distributions of different n_s. Measured values (numerical values). . . . 142
2.7 Estimation of $< D_f >$ with its corresponding bias and consistency based on phase functions in q-space of aggregates with average orientation, from X_{mon} = 0.29 to X_{mon} = 1.04. For bias see Equation 2.10 and for consistency see Equation 2.11. The name of each aggregate contains $D_{f\,theoretical}$. . . . 162
2.8 Estimation of $< D_f >$ with its corresponding bias and consistency based on mean phase functions in q-space of aggregates with $D_{f\,theoretical} = 2$. 166
2.9 Estimation of $< D_f >$ with its corresponding bias and consistency based on phase functions in q-space of aggregates with average orientation and size distribution effect of $X_{mon}^{-3.5}$. . . . 168

3.1 Refractive index and size parameter in some previous scattering studies of rough particles. . . . 175
3.2 Analog grain properties. . . . 178
3.3 Grain radius corresponding to different wavelength ranges (units are noted in the first column). . . . 179

3.4 HWHM of phase function in degrees at different X_{mean} of grains. Measured values (numerical values). 186
3.5 HWHM of phase function of grains with average orientation and with power law distributions of different n_s. Measured values (numerical values), both in degrees. 203
3.6 Backscattering levels of phase functions of grains with average orientation and with power law distributions of different n_s. Calculated with the difference of the maximum numerical value at 180° and the minimum numerical value of the phase function curve. 204
3.7 Levels of maximum DLP of grains with average orientation and with power law distributions of different n_s. Measured values (numerical values). 206
3.8 Analog chondrule and CAI properties. 222
3.9 Chondrule and CAI radius corresponding to different wavelength ranges (units are noted in the first column). 223
3.10 HWHM of phase function in degrees at different X_{mean} of chondrules and X of CAI. 226
3.11 HWHM of phase function of chondrules and CAI with average orientation and with power law distributions of different n_s. Measured values in degrees. 245
3.12 Levels of maximum DLP of chondrules and CAI with average orientation and with power law distributions of different n_s. Measured values. . . . 248

Abbreviations

AU

astronomical units. 45

CAI

Calcium-Aluminum-rich Inclusion. 176, 219, 220, 222, 223

CCRM

Centre Commun de Ressources en Micro-Ondes. 12, 22, 85–87, 90–93, 95, 110, 130, 132, 133, 139, 152, 170, 176, 204, 210, 233, 267

CTTM

Centre de Transfert de Technologie du Mans. 104, 108, 176

DLA

Diffusion Limited Aggregation. 13, 105–107, 109

DLP

degree of linear polarization. 66

FEM

Finite Element Method. 90, 91, 110, 113, 115, 176, 181, 223

FFF

Fused Filament Fabrication. 220, 221

MoM

Method of Moment. 90, 91, 110, 113

PPD

protoplanetary disk. 45, 46, 53

SIR

scale invariance rule. 72, 91, 103, 174

SLA

stereolithography. 13, 108, 109, 178, 220, 221

Introduction

The first stages of planetary formation begin with the agglomeration of sub-micron-sized dust particles forming bigger bodies, planetesimals, and then planets. However this dust growth is not fully understood and the standard accretion scenario model [1, 2] still faces some problems known as the growth barriers that are yet to be resolved [3]. As of today, 5113 exoplanets have been discovered (July 11, 2022, http://exoplanet.eu). Unfortunately the forming mechanisms of these planets are not well known. Several scenarios have been proposed to overcome these barriers, as for example instabilities, e.g., streaming and gravitational instabilities. Nevertheless, instabilities are mechanisms that happen at very specific/unique conditions, and the drift barrier prevails [4]. Alternative solutions have been proposed, considering irregular dust, e.g., fractal aggregates and grains, contrary to compact spherical dust (accepted to take profit of simplified models), avoiding two growth barriers, the fragmentation and the radial drift barrier [5]. Indeed, optical properties of this dust have been modelled using the Mie theory and the Distribution of Hollow Spheres (DHS) [6]. However, these scattering simulations of perfect spheres do not fit with protoplanetary disk observations [7], proving the necessity to consider irregular shapes of dust.

Scattered light observations of protoplanetary disks can be made with nowadays telescopes, i.e. the Atacama Large Millimeter Array (ALMA), the Very Large Telescope (VLT), the James Webb Space Telescope (JWST) and the Hubble Space Telescope (HST), obtaining indirect information on this dust. But how can we interpret these scattering information to know if this dust has irregular morphologies and therefore help to improve the understanding of these barriers? How can we do this when we do not have direct information about dust? One solution is to study the scattering of irregular dust with laboratory experiments where the control of the experimental conditions is possible and therefore the interpretation of scattering information is possible as well.

Two main types of laboratory scattering experiments can be used for this purpose, microwave scattering experiments and light scattering experiments, from which the scattering parameters (based on Mueller matrix elements) of protoplanetary dust analogs can be retrieved. The interpretation of these scattering parameters, gives insights on the material, the shape and the size of these dust analogs. Therefore, these laboratory measurements can give clues to interpret observations.

The light scattering experiments use optical sources to study particles in the (sub) millimeter size range, therefore with size parameters in the Mie/geometric scattering range. These particles can be ejected by an aerosol generator so measurements are done for a cloud of particles [8]. Particles large enough (mm sizes) can be positioned

on a holder and measured individually [9]. Other light scattering instruments use ultrasonic levitation [10], or even microgravity levitation [11] performing measurements of randomly oriented particles and in some cases in fixed positions with controlled acoustic levitation. Unfortunately, light scattering experiments face some challenges: uncontrolled geometrical shapes of analogs, which leads to scattering parameters that are difficult to interpret; small size aggregates which tends to stick together with air ejections and levitation due to Van der Waals forces, making difficult to measure a cloud of aggregates sufficiently separated or even one isolated grain without the contribution of neighboring grains.

On the other hand, microwave scattering experiments use microwaves (antennas) that can scan over a range of wavelengths to study particles in the millimeter to centimeter size range, thus size parameters in the Rayleigh/Mie scattering range. As the size of these particles is large, particles are positioned in stable-oriented systems. The advantage of this technique is that particles can have originally sizes from nanometer to kilometers and thanks to the Scale Invariance Rule (SIR) of the Maxwell equations, their analogs, in this case dust analogs, can be scaled in proportion to the wavelength used to perform observations, while keeping the same refractive index [12]. If the proportion of the change of scale is respected, then the same scattering behaviors as real dust are reproduced. The advantages of using this technique is the control of orientation, size, shape, structure and refractive index of the measured dust analogs [13].

Both techniques have advantages and disadvantages which are discussed in detail in this thesis (Section 1.4), giving complementary scattering information. However, if the objective is to understand the scattering parameters of specific controlled geometric structures (aggregates and grains of dust analogs) in a wide range of wavelengths, the best choice is to use the microwave scattering experiment with 3D printed analogs (centimeter sizes). This is a unique possibility that can be achieved with our laboratory experiment at CCRM in Marseille (for more details on this setup see Section 1.5).

Hence, during my PhD I aimed to study the scattering parameters such as the phase function, the degree of linear polarization and other Mueller matrix elements of protoplanetary dust analogs in the Mie scattering range. These scattering parameters were calculated with measurements performed in our microwave scattering experiment. The analogs were fabricated with three different morphologies: fractal aggregates and two irregular grain families, using additive manufacturing (3D printing). The goal was to understand their scattering properties based on their scattering parameters and thus give insights to understand the indirect information that is gathered with scattered light observations. Notice that this is the first time that scattering parameters of protoplanetary dust analogs are retrieved, using microwave scattering experiments, and controlling their geometry and refractive index with additive manufacturing.

In this manuscript, I first present in Chapter 1 the state of art about planetary formation and electromagnetic scattering theory, emphasizing on the protoplanetary stage and the scattering parameters, respectively. Then the two laboratory techniques, light scattering and microwave scattering techniques, are discussed and compared,

and at the end our microwave scattering experiment is presented. Finally, in order to do the microwave analogy of protoplanetary dust, I describe this analogy from two points of views, size and material (refractive index). Ultimately, the microwave analogy assumptions, that were considered to perform the scattering measurements, are pointed out.

Second, in Chapter 2, I present the scattering parameters retrieved for the first morphology, fractal aggregates, in which three main studies are conducted: i) scattering parameters averaged over several orientations of our aggregates at different wavelengths, ii) scattering parameters including a size distribution and finally iii) the estimation of the fractal dimension based on the phase function.

Third, in Chapter 3, I present the scattering parameters retrieved for two irregular grain families: the first family for which grains are generated with a synthetic roughness and the second family for which grains have a natural roughness taken from the tomography of a meteorite. With both families two main studies are conducted: i) scattering parameters averaged over several orientations of our grains at different wavelengths and ii) scattering parameters including a size distribution. At the end, a comparison between the scattering parameters of the three morphologies is presented, where the most discriminant scattering parameters of each morphology are identified. Lastly, conclusions of all three morphologies properties and prospects for future works are discussed.

This thesis was made with the collaboration of Julien Milli (IPAG), Jean-Baptiste Renard (LPC2E), Hervé Tortel and Christelle Eyraud (Institut Fresnel), Pascal Rannou (GSMA), Azar Maalouf and Vincent Laur (Lab-STICC), Jean-Marie Felio (IUSTI), Cécile Leroux and Arnaud Coudreuse (CTTM). This project was financially supported by CNRS, France, as part of its 80|PRIME cross-disciplinary programme, by the French National Research Agency in the framework of the Investissements d'Avenir program (ANR-15-IDEX-02), through the funding of the Cross-disciplinary Project "Origins of Life" of Université de Grenoble-Alpes and by GdR Suie.

Résumé version longue

La formation planétaire débute par l'agglomération de poussières circumstellaires pour former des corps plus gros et finalement des planètes. Cependant, cette croissance n'est pas entièrement comprise et le modèle standard du scénario d'accrétion [1, 2] fait face à différentes barrières de croissance [3]. Chaque jour il y a de plus en plus d'exoplanètes qui sont découvertes, avec aujourd'hui un total de 5113 exoplanètes (le 11 juillet 2022, http://exoplanet.eu), néanmoins leurs mécanismes de formation ne sont pas bien connus.

Plusieurs scénarios ont été proposés pour surmonter ces barrières comme par exemple des instabilités de type gravitationnelle ou de l'écoulement. Cependant, ces instabilités représentent des mécanismes qui arrivent dans des conditions très spécifiques, en laissant la barrière de dérive radial sans la résoudre [4]. D'autres solutions ont été proposées comme des poussières irrégulières, c.à.d. des agrégats fractals ou des grains, au lieu des poussières sphériques compactes qui avaient été étudiés les premières aussi vu de la simplicité des modèles. En effet, les propriétés optiques de la poussière avaient été modélisées avec la théorie de Mie ou en condiérants des distributions de sphères creuses [6]. Toutefois, les simulations de la diffusion par ces sphères n'ont pas le même comportement que les observations de la lumière diffusée par les disques protoplanétaires [7], ce qui démontre la nécessité de considérer des poussières irrégulières.

Les télescopes actuels permettent d'observer les disques protoplanétaires en lumière diffusée (voir Figure 0.1) et d'obtenir ainsi des informations indirectes. Mais comment interpréter ces informations pour remonter à la morphologie de ces poussières et comment ces barrières peuvent-elles être dépassées ? Comment faire sans informations directes sur la poussière ? Pour faire avancer ces connaissances, deux types d'expériences en laboratoire peuvent reproduire l'analogie de la diffusion de cette poussière, donc dans des conditions expérimentales contrôlées, afin de réaliser des interprétations à partir des caractéristiques de diffusion d'objets connus.

Ces expériences sont la diffusion de la lumière avec une source laser et l'autre avec des micro-ondes. Les deux permettent d'obtenir les paramètres de diffusion via les éléments de la matrice de Mueller. En effet, la compréhension de ces paramètres aide à la compréhension des caractéristiques des analogues tels que leurs composition, taille et morphologie. Ainsi les mesures en laboratoire donnent des pistes pour interpréter les observations.

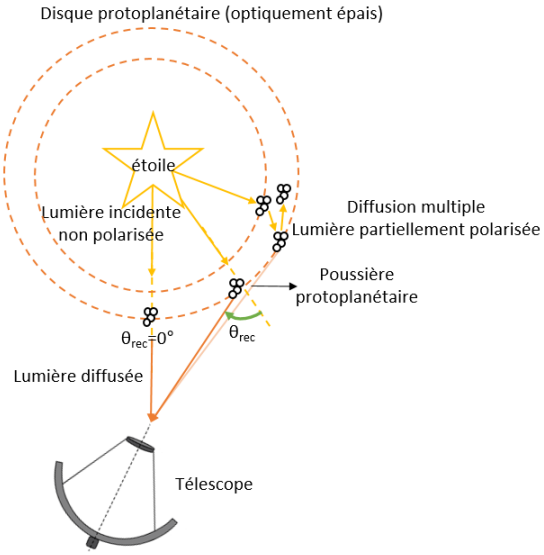

Figure 0.1: Schéma des mesures protoplanétaires avec deux types de sources qui rencontrent des poussières et produisent de la lumière diffusée. Cette diffusion est détectée par les télescopes à différents angles de réception (θ_{rec}).

Les expériences de laboratoire faites avec une source laser étudient des particules de l'ordre millimétrique ou submillimétrique, cela veut dire une diffusion de Mie/géométrique. Généralement, ces particules sont éjectées par un générateur d'aérosol dont les mesures sont faites avec des nuages de particules [8]. Les particules peuvent également être en lévitation ultrasonique [10] ou en micro-gravité [11], ce qui permet d'obtenir des mesures de particules aléatoirement orientées ou parfois des orientations contrôlées. Malheureusement, les principaux inconvénients de ces techniques sont: une géométrie non contrôlée des analogues qui donne accès à des paramètres de diffusion inconnus difficiles à interpréter. De plus, les agrégats de petite taille ont tendance à se coller les uns aux autres à cause de l'éjection d'air ou de la lévitation, ce qui rend impossible la mesure des nuages ou des grains bien séparée sans avoir de perturbation due à la diffusion des grains voisins.

L'autre type d'expérience utilise des antennes donc des mesures en multi-longueur d'onde. La taille des particules est d'ordre du millimètres/centimètres, cela veut dire une diffusion de Rayleigh/Mie. Grâce à la taille des particules, elles sont posées avec des positions fixées dans des systèmes stables. Le principe de cette technique est l'invariance par changement d'échelle des équations de Maxwell, ce qui permet de reproduire des phénomènes de diffusion similaires aux vraies particules (poussière protoplanétaires). Ainsi, la particule peut avoir une taille nanométrique ou kilométrique et son analogue une taille centimétrique, simplement en respectant le paramètre de taille et l'indice de réfraction originale (analogie micro-onde) [12]. Cette technique fournit également un contrôle d'orientation de l'analogue. Ainsi, les deux types de techniques ont des avantages et des inconvénients (voir Section 1.4)

ce qui donne des informations de diffusion complémentaires. Néanmoins, lorsqu'il s'agit d'étudier les paramètres de diffusion des analogues ayant des géométries contrôlées (analogues des agrégats ou grains de poussière) et de les mesurer à différentes longueurs d'ondes, le meilleur compromis est l'utilisation de l'analogie micro-onde et la fabrication d'analogues par impression 3D (analogues centimétriques).

De ce fait, au travers de cette thèse, on cherche à fournir des outils réalistes pour interpréter les observations de disques protoplanétaires en mettant à profit des expériences de diffusion en micro-ondes. Des analogues de poussière contrôlés géométriquement et utilisant un indice de réfraction similaire au silicate astronomique [14], grâce à la fabrication additive, ont été mis à profit. Les dimensions de ces analogues ont été choisies pour conserver le rapport dimension sur longueur d'onde, ce qui permet de reproduire des phénomènes de diffusion similaires aux observations de diffusion de la poussière protoplanétaire.

Dans cette thèse, j'ai étudié différents paramètres caractéristiques tels que la fonction de phase, le degré de polarisation linéaire et d'autres éléments de la matrice de Mueller avec trois morphologies de poussières : des agrégats fractals, et deux familles de grains ayant différents types de rugosité. L'objectif principal est de comprendre ces différents paramètres et de donner des idées et/ou des outils qui permettent de mieux appréhender les informations indirectes contenues dans les signaux diffusés par la poussière protoplanétaire.

Les analogues ont été mesurés dans la chambre anéchoïque du Centre Commun de Ressources en Microondes (CCRM) en utilisant des longueurs d'onde de 16,7 mm à 100 mm (voir la Section 1.5 pour plus de détails sur notre système de mesure). La configuration expérimentale principalement utilisée est celle où la diffusion comprend la zone de diffusion avant (voir Figure 0.2).

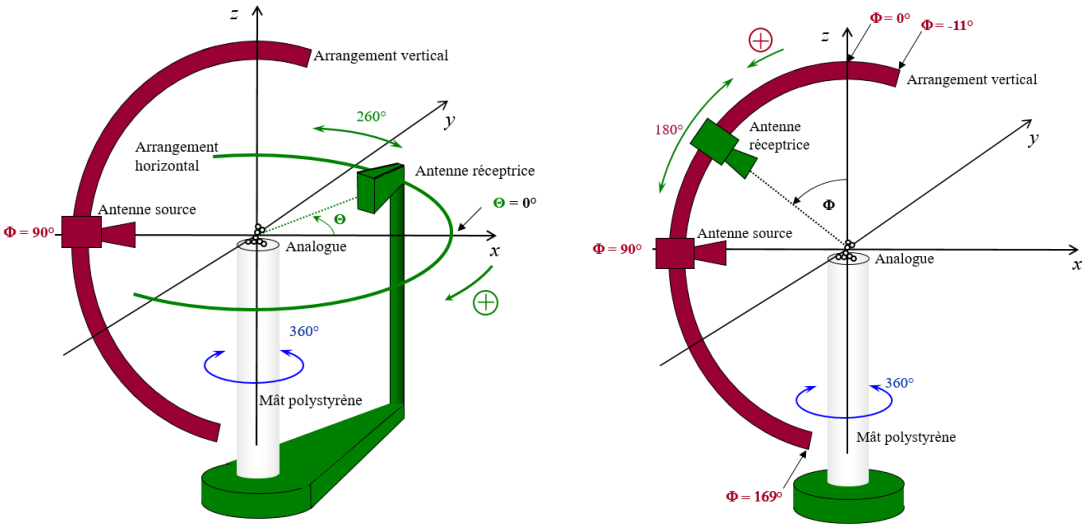

(a) Configuration - diffusion vers l'avant

(b) Configuration - diffusion vers l'arrière

Figure 0.2: Installation expérimentale dans deux types de configurations.

De plus, des simulations numériques ont été réalisées, principalement avec la méthode des éléments finis [15] pour une validation croisée avec les mesures. Les hypothèses de base sur les poussières pour faire l'analogie avec les mesures et la simulation numérique sont : un milieu macroscopiquement isotrope et symétrique [16] avec des poussières aléatoirement orientées et sans interaction. Ces hypothèses ainsi que des antennes utilisées dans une polarisation horizontale (pour les deux antennes) et après verticale, permettent de mesurer 6 éléments de la matrice de Mueller: S_{11}, S_{12}, S_{22}, S_{33}, S_{34} et S_{44}. Les différences en incluant la polarisation croisée ou non, pour ces 6 éléments, sont négligeables. Néanmoins, dans le cas de S_{22}, l'inclusion de la polarisation croisée est nécessaire pour pouvoir faire après la normalisation avec S_{11} . Si la polarisation croisée n'est pas incluse, $S_{22} = S_{11}$. Ainsi, ces éléments décrits en termes des éléments de la matrice de Jones sont :

$$\begin{aligned}
S_{11} &= \frac{1}{2}\left(|S_1|^2 + |S_2|^2\right), \\
S_{22} &= \frac{1}{2}\left(|S_2|^2 + |S_1|^2 - |S_4|^2 - |S_3|^2\right), \\
S_{12} &= \frac{1}{2}\left(|S_2|^2 - |S_1|^2\right), \\
S_{33} &= S_{44} = \Re\left\{S_1 S_2^*\right\}, \\
S_{34} &= \Im\left\{S_2 S_1^*\right\}.
\end{aligned} \tag{0.1}$$

A partir de ces éléments, les paramètres de diffusion ont été calculés, la fonction de phase (moyenne de S_{11} sur différentes orientations, $< S_{11} >$), le degré de polarisation linéaire (division entre les moyennes $DPL = \frac{-<S_{12}>}{<S_{11}>}$), et aussi $\frac{<S_{22}>}{<S_{11}>}$, $\frac{<S_{34}>}{<S_{11}>}$ et $\frac{<S_{44}>}{<S_{11}>}$. Il faut remarquer que tous les éléments peuvent être retrouvés avec les mesures sauf S_{22} qui contient la polarisation croisée donc retrouvable avec les simulations.

1. Agrégats fractals:

La première morphologie étudiée a été celle des agrégats fractals (voir le chapitre 2). Nos agrégats ont été générés avec un logiciel d'agrégation par diffusion, c.à.d. agrégation du type monomère-groupe des monomères, dénommé Diffusion Limited Aggregation (DLA) [17]. Sept agrégats ont été générés avec 74 monomères, correspondant à différentes dimensions fractales comprises entre $D_f = 1.5$ (très poreux) et $D_f = 2.8$ (très compact). Les paramètres de taille ($X = 2\pi R_{max}/\lambda$, étant R_{max} le rayon de la sphère inclusive et λ l'onde incidente) de ces agrégats sont entre $X_{agg} = 0.97$ à $X_{agg} = 19.60$, et pour les monomères entre $X_{mon} = 0.97$ à $X_{agg} = 1.04$. Après leur génération virtuelle, ils ont été imprimés avec une résine, ayant un indice proche du silicate astronomique [14] (indice de réfraction des agrégats $1.7 + 0.03i$), par stéréolithographie avec la collaboration du Centre de Transfert de Technologie du Mans (CTTM).

- Deux types d'études sur les paramètres de diffusion des agrégats ont été effec-

tués. La première étude avec des paramètres de diffusion moyennés à partir des différentes orientations des agrégats et différentes longueurs d'onde (ou paramètres de taille). La Figure 0.3 montre un exemple de ces paramètres de l'agrégat Ag_DLA_Df2.0_N74_1. Les mêmes paramètres ont été obtenus pour les autres sept agrégats. Grâce au changement du X_{mon}, on a observé une cohérence entre les paramètres obtenus par mesure et par simulation. De plus, les paramètres des agrégats poreux ($D_f \leq 2$) présentent des comportements de diffusion de Rayleigh tandis que les agrégats compacts ont des comportements de type pseudo-sphérique. Par ailleurs, $\frac{<S_{34}>}{<S_{11}>}$ et $\frac{<S_{44}>}{<S_{11}>}$ ont validés le même comportement de diffusion qui a été observé au travers de la fonction de phase et du DPL. Alors que $\frac{<S_{22}>}{<S_{11}>}$ (qui est lié à la sphéricité) a donné des informations supplémentaires pour identifier les agrégats les plus poreux ($D_f \leq 1.7$), les agrégats intermédiaires ($D_f = 2.0$ à 2.5) et l'agrégat le plus compact ($D_f = 2.8$).

- Dans la deuxième étude, pour simuler une distribution de taille, une loi de puissance a été appliquée sur X_{mon} des différents paramètres de diffusion, avec des indices de $n_s = 3.5$ (distribution supposée pour la poussière protoplanétaires), $n_s = 2$ et $n_s = 5$ (les deux dernières afin d'étudier l'effet du changement de n_s sur les paramètres de diffusion). La Figure 0.4 présent les paramètres de diffusion retrouvés à $n_s = 3.5$ pour cinq de nos agrégats en ayant différentes D_f. Grâce a notre expérience de diffusion en micro-ondes, nous avons pu analyser les paramètres de diffusion avec ou sans la distribution de taille. Cela nous a permis de comprendre quels étaient les phénomènes mis en jeu pour retrouver les paramètres finaux, y compris l'effet de la distribution. D'ailleurs, les différences entre les agrégats de différentes D_f et avec un nombre fixe de monomères peuvent être identifiée par: i) la largeur à mi-hauteur et les remontés dans la rétrodiffusion de la fonction de phase, ii) le niveau maximal du DPL et de sa branche négative dans la rétrodiffusion, iii) les niveaux de $\frac{<S_{22}>}{<S_{11}>}$, iv) la régularité de la courbe $\frac{<S_{44}>}{<S_{11}>}$ et v) le comportement constant autour d'une valeur nulle de la courbe $\frac{<S_{34}>}{<S_{11}>}$. Cependant, si le nombre de monomères n'est pas fixe (cas des agrégats dans la nature, i.e. poussière protoplanétaire), les niveau maximal du DPL et leur angle de diffusion peuvent permettre de différencier les agrégats poreux des agrégats compacts, même si le nombre de monomères change, car l'effet de la dépolarisation est complètement lié à la morphologie (sphère) et au couplage interne entre monomères. Donc le DLP peut être analysée conjointement avec $\frac{<S_{22}>}{<S_{11}>}$ qui est liée à la sphéricité des agrégats.

- Finalement, dans la troisième étude, la dimension fractale des agrégats a été déterminée à partir de la fonction de phase représentée dans l'espace q ($q = 2k\sin(\theta/2)$). Parmi toutes les méthodes présentées dans la littérature, la méthode la plus prometteuse est une méthode originale que nous avons proposé, la méthode de Butterworth. Cependant, d'autres cas test sont nécessaires pour valider le domaine d'application de cette méthode. De plus, il serait important

d'augmenter la taille de nos agrégats ainsi que leur nombre de monomères pour augmenter la fractalité et diminuer les oscillations de la pente de la fonction de phase pour permettre une estimation plus fiable de la dimension fractale.

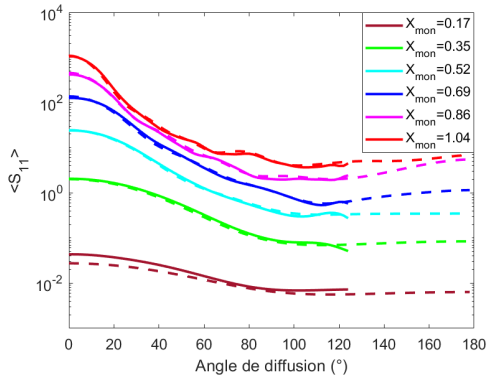

(a) Fonction de phase

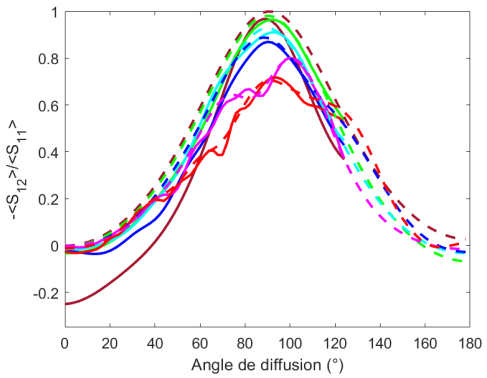

(b) Degré de polarisation linéaire

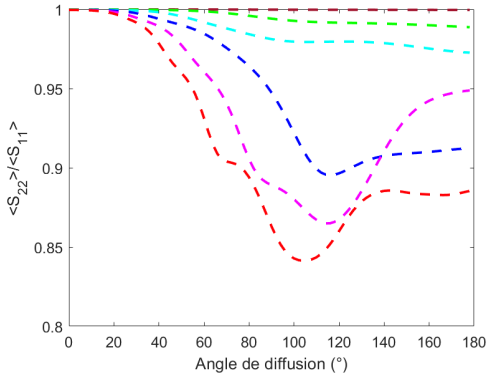

(c) S_{22} normalisé

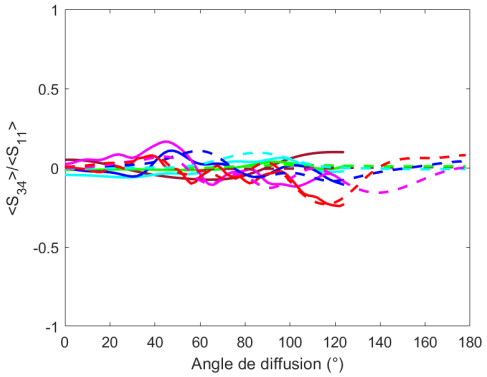

(d) S_{34} normalisé

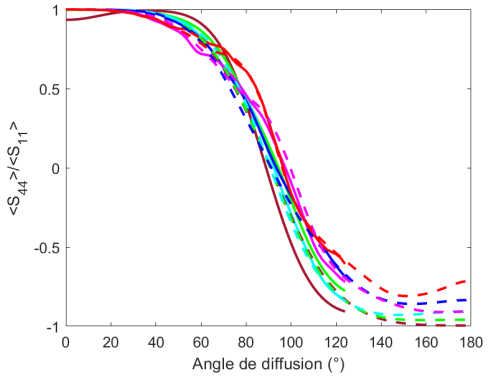

(e) S_{44} normalisé

Figure 0.3: Mesures (lignes continues) et simulations numériques (lignes discontinues) des paramètres de diffusion de l'agrégat Ag_DLA_Df2.0_N74_1 (dimension fractale 2) à différents paramètres de taille X_{mon}.

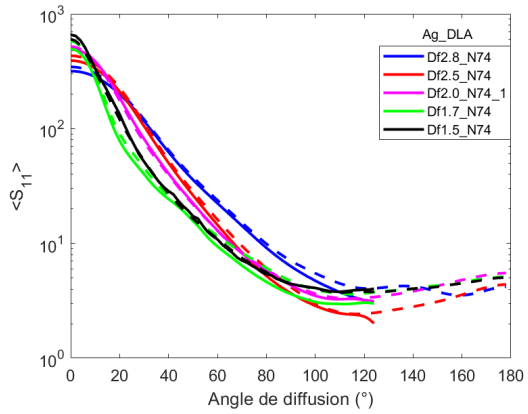

(a) Fonction de phase

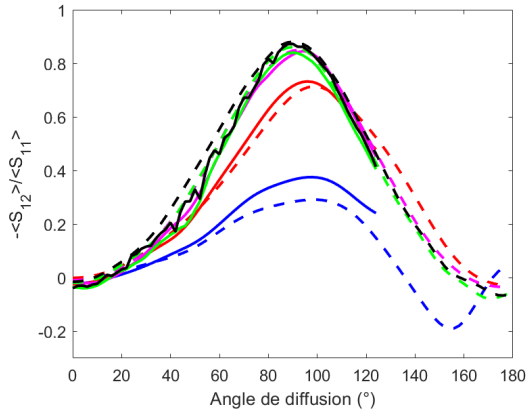

(b) Degré de polarisation linéaire

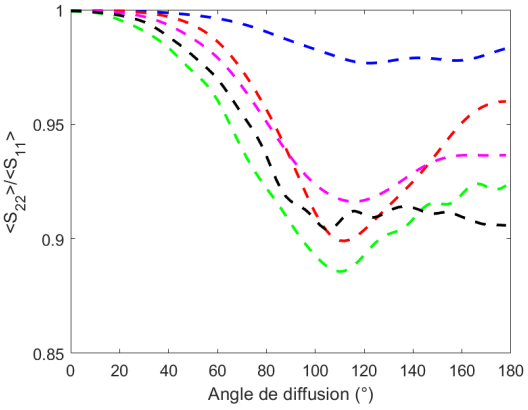

(c) S_{22} normalisé

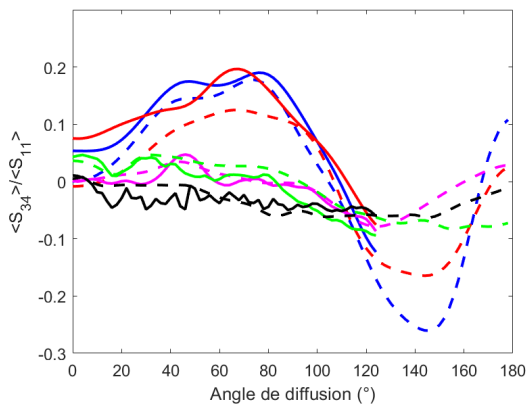

(d) S_{34} normalisé

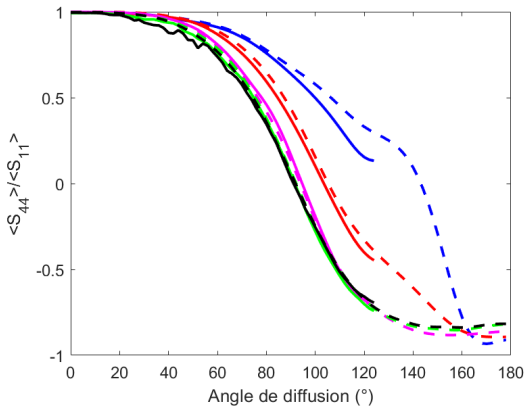

(e) S_{44} normalisé

Figure 0.4: Mesures (lignes continues) et simulations numériques (lignes discontinues) des paramètres de diffusion des agrégats avec une distribution de taille en loi de puissance $n_s = 3.5$.

2. Première famille des grains:

La deuxième morphologie étudiée a été les grains irréguliers (voir chapitre 3) fabriqués avec une rugosité contrôlée. Pour cela, des sphères qui ont été initialement maillées avec des triangles et ensuite la distance entre le centre de la sphère et le sommet de chaque triangle a été perturbé avec des rayon aléatoires. Six grains, ayant des rugosités différentes dès $r = 2.6\%$ à $r = 13.2\%$, ont été générés virtuellement. Ils ont ensuite été imprimés par stéréolithographie (collaboration CCTM) avec le même indice de réfraction que les agrégats ayant un paramètre de taille de 1.07 à $X = 7.73$. Les deux mêmes études des paramètres de diffusion, ont été réalisés pour les grains.

- Selon les paramètres de diffusion retrouvés dans la première étude, le DLP a démontré d'avoir la meilleure sensibilité au changement de la rugosité des grains. Leurs différences ont été mises en évidence avec l'amplitude d'oscillation du DLP, ainsi le DLP des grains les plus rugueux a les amplitudes les plus petites tandis que le moins rugueux a les amplitudes les plus grandes. De plus, grâce au paramètre $\frac{<S_{22}>}{<S_{11}>}$, on a pu identifier quel grain était le plus sphérique, qui présente des niveaux autour de 1 contrairement aux moins sphériques qui a des niveaux inférieurs à 1. Ce comportement a été validé avec notre calcul de sphéricité réalisé à partir des fichiers 3D des grains et qui ont montré le même ordre des courbes $\frac{<S_{22}>}{<S_{11}>}$ selon leurs valeurs de rugosité.

- La deuxième étude, basé sur les paramètres de diffusion avec des distributions de taille, a démontré que les remontés de la fonction de phase en rétrodiffusion et les niveaux maximum du DLP peuvent donner des informations sur la rugosité des différents grains à un même n_s. De même, $\frac{<S_{22}>}{<S_{11}>}$ a de nouveau montré sa dépendance avec la sphéricité des grains. En somme, ces trois paramètres peuvent donner des idées de la rugosité/sphéricité et donc de la morphologie de nos grains.

3. Deuxième famille des grains

La troisième morphologie étudiée a été une autre famille de grains irréguliers mais cette fois-ci avec une rugosité naturelle (voir chapitre 3). La morphologie de ces grains a été obtenu par tomographie assistée par ordinateur à partir d'une chondrite (météorite rocheuse), laquelle est composée de chondres et d'inclusions réfractaires. Au total quatre analogues de chondres et d'une inclusion réfractaire ont été réalisées en 3D (Collaboration avec Yves Marrocchi). Cette fois, les grains ont été imprimés par dépôt de fil fondu, ce qui permet de bénéficier de plus de matériaux et des réalisation de dimensions plus importantes (collaboration avec Azar Maalouf et Jean-Marie Felio). Les chondres ont un paramètre de taille entre $X = 1.03$ et $X = 9.19$, et une rugosité entre $r = 5.04\%$ et $r = 13.26\%$. L'inclusion a un paramètre de taille dès $X = 3.59$ à $X = 21.53$ et une rugosité de $r = 24.05$.

- Les deux mêmes études pour retrouver les paramètres de diffusion ont été réalisées. Toutefois, les paramètres ont été calculés seulement à partir de mesures

car ces analogues présentent une rugosité naturelle difficile à mailler avec précision pour produire des simulations fiables. Donc, parmi les cinq paramètres de diffusion, quatre ont été retrouvés uniquement avec des mesures: la fonction de phase, le DPL, $\frac{<S_{34}>}{<S_{11}>}$ et $\frac{<S_{44}>}{<S_{11}>}$ (voir Figure 0.5 qui présent un exemple des paramètres de la chondre C0_PLA_orange_r5.04). Tous ces paramètres ont présentés le même comportement avec l'augmentation de la rugosité que ce soit pour les chondrules ou pour l'inclusion, c.à.d. lorsque la rugosité augmente les amplitudes d'oscillations diminuent. Le DLP a démontré plus de sensibilité que les autres paramètres pour identifier les chondres. En effet, ce paramètre est lié à la dépolarisation et donc à la rugosité de chaque chondre.

- La deuxième étude (paramètres de diffusion retrouvés avec une distribution de taille) a montré une différenciation des grains grâce au DLP et $\frac{<S_{44}>}{<S_{11}>}$. Le DLP a présenté différents niveaux maximums en fonction de la rugosité des chondres, et un angle de diffusion correspondant un maximum plus grand pour l'inclusion que pour les chondres. D'autre part, $\frac{<S_{44}>}{<S_{11}>}$ à montré une organisation aux alentours de 124° qui est lié aussi à la rugosité des chondres (voir Figure 0.6).

Finalement, les paramètres de diffusion des trois morphologies ont été comparés à $n_s = 3.5$. Grâce au DLP, on a pu différentier les agrégats des deux familles de grains. Comme perceptive, il serait intéressant de faire des mesures dans la zone de rétrodiffusion, surtout pour la deuxième famille de grains pour vérifier si ses paramètres de diffusion sont bien distincts de la première famille de grains.

En conclusion, nos résultats ont prouvé que le contrôle de la géométrie, de l'indice de réfraction et de l'orientation de nos analogues est essentiel pour interpréter leurs propriétés de diffusion, fournissant des mesures de diffusion uniques grâce à notre expérience micro-ondes au CCRM et grâce à la fabrication additive. De plus, ces résultats suggèrent que les porosités de nos agrégats et la rugosité de nos grains compacts affectent clairement et de manière spécifique leurs propriétés de diffusion. Par ailleurs, j'ai montré l'intérêt de poursuivre le développement instrumental des télescopes pour obtenir d'autres paramètres que l'intensité totale diffusée (fonction de phase) et le degré de polarisation linéaire. En effet, les autres paramètres de diffusion peuvent donner plus d'indices sur la morphologie des poussières des disques protoplanétaires. Enfin, comme premiers prologement de ces études je propose d'augmenter la taille des analogues et de tester d'autres indices de réfraction qui existent dans les disques, afin d'obtenir des paramètres de diffusion plus proches des observations. Il serait également intéressant d'effectuer des mesures à des angles plus proches de la rétrodiffusion.

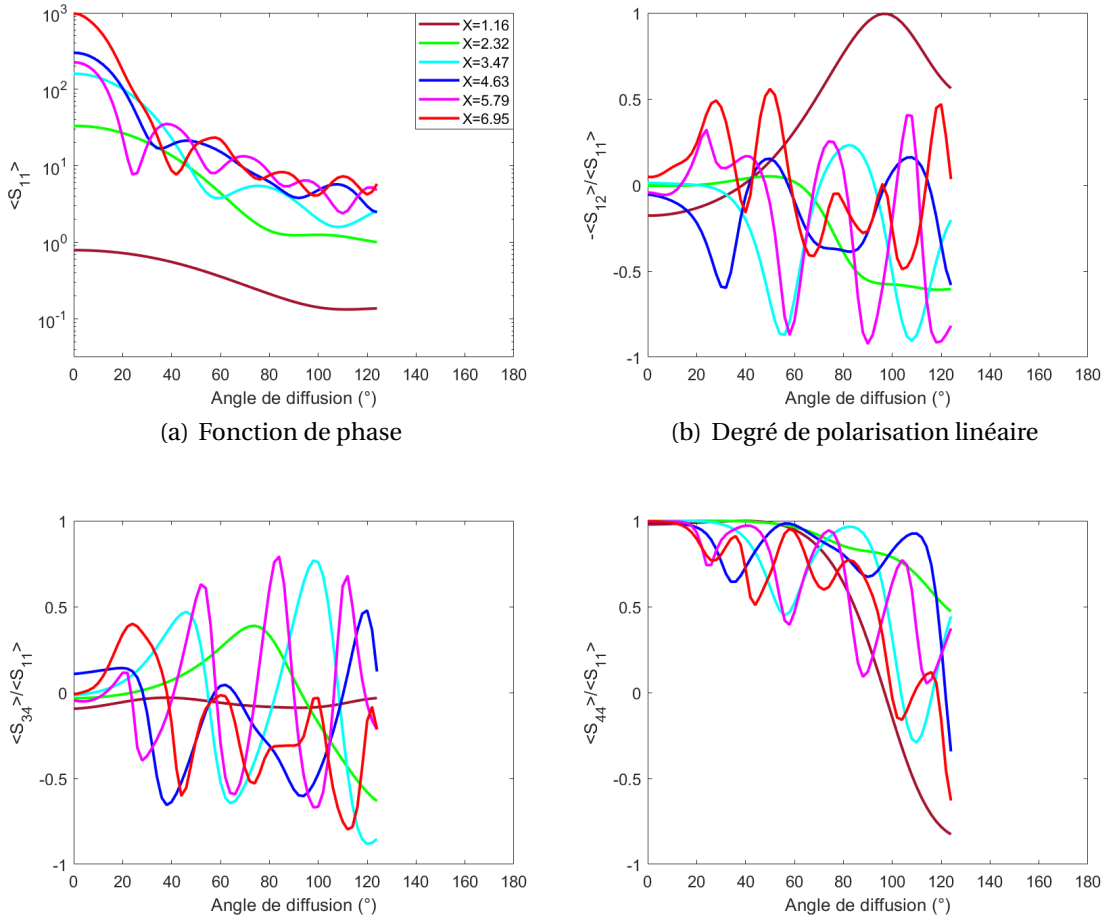

(a) Fonction de phase

(b) Degré de polarisation linéaire

(c) S_{34} normalisé

(d) S_{44} normalisé

Figure 0.5: Mesures (lignes continues) des paramètres de diffusion de la chondre C0_-PLA_orange_r5.04 à différents paramètres de taille X.

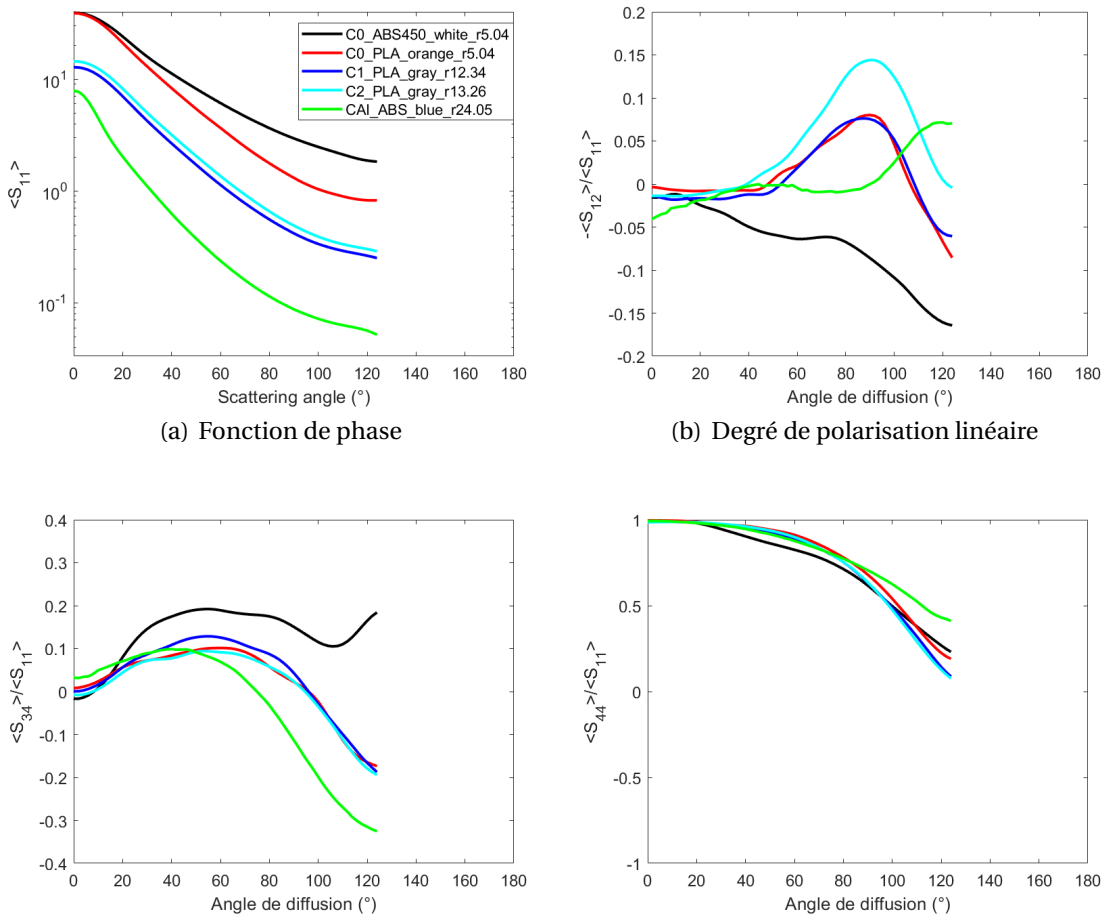

(a) Fonction de phase

(b) Degré de polarisation linéaire

(c) S_{34} normalisé

(d) S_{44} normalisé

Figure 0.6: Mesures (lignes continues) des paramètres de diffusion des chondres et CAI avec une distribution de taille en loi de puissance $n_s = 3.5$.

1 State of the art

Sommaire

1.1 Introduction . . . 41
1.2 Stellar and planetary formation . . . 41
1.2.1 Formation . . . 42
1.2.2 Empirical evolutionary sequence . . . 43
1.2.3 Protoplanetary disk . . . 45
1.2.3.1 General characteristics of PPD . . . 45
1.2.3.2 Aggregation of dust . . . 48
1.2.3.3 PPD observations . . . 53
1.3 Electromagnetic scattering theory . . . 58
1.3.1 Electromagnetic wave . . . 61
1.3.2 Stokes parameters . . . 62
1.3.3 Amplitude scattering matrix or Jones matrix . . . 66
1.3.4 Scattering matrix or Mueller matrix . . . 68
1.3.5 Scattering parameters to be studied . . . 70
1.3.6 Conclusions . . . 71
1.4 Laboratory techniques for measuring scattering parameters . . . 71
1.4.1 Microwave scattering technique . . . 72
1.4.1.1 Microwave scattering experiment in SUNYA laboratory 72
1.4.1.2 Microwave scattering experiment at Bochum University 73
1.4.1.3 Microwave scattering experiment at the University of Florida . . . 74
1.4.2 Light scattering technique . . . 75
1.4.2.1 Multicolor light scattering experiment at Bochum University . . . 76
1.4.2.2 Scatterometer at the University of Helsinki . . . 77
1.4.2.3 Amsterdam light scattering experiment at the University of Amsterdam . . . 78
1.4.2.4 Granada light scattering experiment in the Instituto de Astrofísica de Andalucía . . . 79
1.4.2.5 PROGRA2 experiment . . . 81
1.4.3 Summary . . . 83
1.5 Microwave scattering experiment at CCRM . . . 85
1.5.1 Anechoic chamber facility . . . 85

1.5.2 Experimental setup 86
1.5.2.1 Forward scattering zone 87
1.5.2.2 Backward scattering zone 88
1.5.3 Measurements 89
1.6 Numerical simulations 90
1.7 Microwave analogy of protoplanetary dust 91
1.7.1 Size analogy 92
1.7.2 Material analogy 93
1.7.3 Microwave analogy assumptions 97
1.8 Conclusions 99

1.1 Introduction

Planetary formation is a highly debated subject, where there is still missing information to understand the whole growth process to form planets. Within the stage of protoplanetary disks, dust grows forming different morphologies, e.g., aggregates and pebbles. However, the mechanisms that describe this dust growth face some problems known as the growth barriers that are yet to be resolved. In order to understand more how these dust particles grow, indirect information on their structure can be obtained with observations of scattered light of dust of protoplanetary disks. To interpret these observations, laboratory scattering measurements and numerical simulations can give some clues by using analogs of protoplanetary dust particles and thus help in the comprehension of dust growth in planetary formation. During my thesis, I aimed to understand the scattering properties of different protoplanetary dust analogs using laboratory scattering measurements, this being the first time using the microwave scattering technique and geometrically controlled dust analogs.

In this chapter I first present an overview of the stellar and planetary formation, and then more specifically the protoplanetary stage is detailed. Then, I describe the scattering theory on which this study is based. Third, I discuss the different laboratories that can be used to obtain these scattering measurements. And finally, I describe the laboratory scattering experiment that I used during my PhD to obtain the scattering parameters of protoplanetary dust analogs.

1.2 Stellar and planetary formation

Within the stellar and planetary formation, protoplanetary disks are within one of the stages of this formation. The following section outlines this formation. Then a detailed description of protoplanetary disks and constraints of dust aggregation is presented, the main subject of this study being protoplanetary dust.

1.2.1 Formation

1. The prestellar phase:

   The stars and planets formation occur in the interstellar medium, in molecular clouds, where 99% of the baryonic matter is gas (from this gas 76% is hydrogen (H) and 22% is helium (He)) and 1% is dust [4]). The contraction of these molecular clouds leads to over dense regions, known as dense cores. Some of these dense cores can evolve to form even denser regions out of which individual stars form, named prestellar cores (prestellar phase) [18]. Due to different mechanisms that produce the lost of the internal support of the core, i.e. loss of stability, (e.g., ambipolar diffusion [19], dissipation of turbulence [20, 21], and other internal and external perturbations as pressure [22]), the prestellar core follows a gravitational collapse and thus the beginning of the protostellar phase.

2. The protostellar phase:

   The protostellar phase is where the main accretion happens. In this phase the protostar has a smaller mass compared to its envelope. However, due to the accretion of the envelope material onto the protostar, as well as the material ejection (i.e., jets and outflows [23]), the mass of the protostar increases until exceeding the mass of the envelope. The accretion comes to an end when all the envelope material is accreted/ejected.

   It is important to note that the surrounding protostar material is contained in an envelope but also into an accretion disk. Indeed, protostellar cores are rotating systems inherited from their molecular clouds. Therefore, to preserve the angular momentum of this rotation, particles of the envelope rotate. Yet, due to the centrifugal force, the material that is rotating in the equatorial plane is not able to be accreted by the protostar, leading to the accumulation of material in the equatorial plane and thus forming a circumstellar disk [24]. These circumstellar disks are thought to be found even before, in the prestellar phase, as was shown for example by a survey of 16 protostellar disks in which 11 of them presented a better reproduction of models with observations by including dust continuum emission envelope models and circumstellar disk models [25].

3. The pre-main-sequence phase:

   After the accretion/ejection of the envelope material, the protostar is only surrounded by the circumstellar disk, starting the pre-main-sequence phase. The circumstellar disk, which is composed of dust and gaz, is slowly acretted (with a rate between 10^{-11} to $10^{-8} M_{\odot}\ /yr$, where $M_{\odot}$ is the solar mass, while pre-main-sequence stars have a rate between 10^{-8} to $10^{-6} M_{\odot}\ /yr$ [26]) by the pre-main object (which has already accumulated 90% of its final mass). These circumstellar disks host the grains that will grow and form planets (protoplanetary disks). Notice that this is the phase in which this thesis will be focused on.

The pre-main object is not enough hot to be into a radiative equilibrium, therefore it undergoes into a quasi-static contraction that will last a Kelvin-Helmholtz timescale [27]. The beginning of this contraction states the birth of the stellar embryo, known as the birthline in the Hertzprung-Rusell diagram, appearing as a visible object [28]. During the contraction, the temperature of the pre-main-sequence star progressively increases up to 10^6 and 10^7K (temperatures to burn deuterium and hydrogen, respectevely) thanks to the excess of the gravitational energy during the contraction and the photospheric radiation. In parallel, the disk losses its gas, becoming an optically thin circumstellar disk (Debris disk) [29].

Finally, when the pre-main-sequence object arrive to 10^7K, the thermonuclear combustion of hydrogen starts and so the main-sequence object appears (adult star).

1.2.2 Empirical evolutionary sequence

The evolution of young stellar objects, described previously from the protostellar phase to the pre-main-sequence phase, can be classified in an empirical way, based on observations of the mass distribution surrounding the stellar object, the velocity distribution of the disk gas, and the non-stellar radiative flux. In the case of the mass and temperature distribution, they can be inferred by modeling the spectral energy distribution (SED). Protostellar SED is divided in four classes. Within this classes, Class I to Class II were first defined by Lada in [30]. Then Class 0 was implemented by Andre, Ward-Thompson, and Barsony in [31]. This classification is shown in Figure 1.1, considering the bolometric temperature (which is the temperature of a blackbody whose SED has the same average frequency [32]), the mass of the envelope (M_{env} compared to the stellar mass M_*) and the disk mass (M_{Disk} compared to the solar mass, $M_\odot$, and Jupiter mass, $M_{Jupiter}$). Additionally, the time is defined since the formation of the protostellar object or collapse of the dense core ($t = 0$). The classes are described from Class 0 (the youngest stars) to class III (The most evolved stars) as follows:

1. Class 0: the protostellar mass is smaller than the envelope mass. This protostellar object is surrounded by the cold material of the envelope, which emits as a cold blackbody in the millimeter wavelengths (thermal emission of cold dust). Red arrows coming out of the protostellar object represent the jets and outflows, and dark blue arrows represent the accretion.

2. Class I: the protostellar mass becomes greater than the envelope mass. There is an increase in the protostellar object temperature. At this stage, the protostellar core is detectable at millimeter to near infrared wavelengths, and the infrared excess infers the presence of a disk.

3. Class II: the envelope has dissipated almost completely. The spectrum is caused by two objects, one from the pre-main-sequence star (which can be a T Tauri star with 1 to 2 $M_\odot$ [33] or Ae/Be Herbig star with 2 to 8 $M_\odot$ [34]) acting as black bodies with a maximum at the near infrared, and the other from the spectrum coming from the re-emission, material of the protoplanetary disk (with a mass of $0.01 M_\odot$) emitting at longer wavelengths (infrared excess). This is the stage where this thesis is focused on.

4. Class III: the spectrum of the star dominates in the near infrared and as the temperature of the star increases, the peak shifts toward visible wavelengths. An optically thin disk is formed around the star, with a detectable mass, smaller than the Jupiter mass.

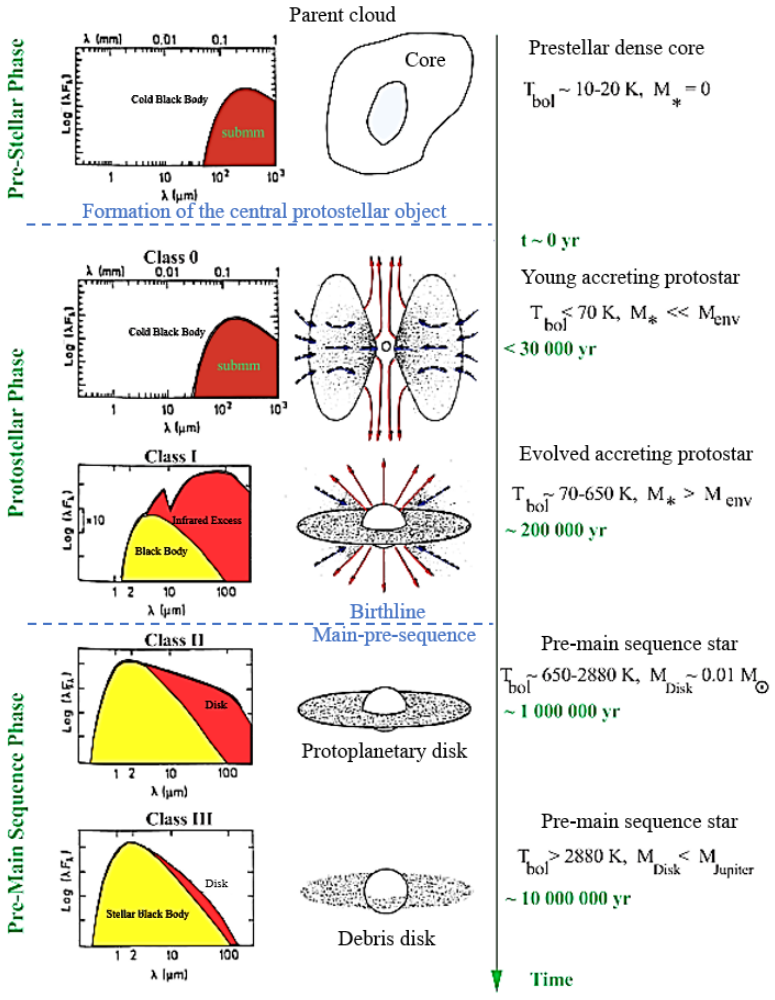

Figure 1.1: Empirical evolutionary sequence based on the shape of SED, the bolometric temperature and the disk mass [taken and modified from 35].

1.2.3 Protoplanetary disk

As it was previously seen, protoplanetary disk (PPD) and its pre-main-sequence star have a spectral Class II. At this stage, the formed thick disk is made of dust and gas, and the dust accretion is taking place for the formation of pebbles, planetesimals and planets. This accretion is described by the core accretion scenario model [1, 2] which is the most popular explanation for the origin of gas giant planets of the Solar System, i.e., Jupiter and Saturn. This model begins first with a core (protoplanet) that grows at a fixed disk radius by accreting dust and planetesimals whose orbits cross. Note that the core is surrounded by a near-hydrostatic gaseous envelope. As the core becomes more massive, it attracts more gas and solids that will fall later into the envelope. After reaching its critical mass, the envelope enters in a runaway growth (mainly accreting gas). At the end of this stage (due to disk dissipation or the opening of a disk gap), a giant planet is formed. The problem with this model is that the timescale to form giant planets is longer than the disk lifetime (around $1-3 Myr$) [36]. For this reason, different subjects as instabilities (which is an alternative mechanism to form planets in a faster way), dust growth processes, dust morphologies, etc, are being studied to reduce the growth timescales. In this thesis I will focus on the study of dust morphology in protoplanetary disks. Hence, in this section I will first describe the main characteristics of protoplanetary disks, and then I will focus on protoplanetary dust: dust transport, dust growth and dust barriers, and finally, how can we get information on the dust of these protoplanetary disks with scattering observations.

1.2.3.1 General characteristics of PPD

Radius: one approach to estimate the protoplanetary disk radius is to define an effective size r_j, defined as the radius that encircles a fixed fraction of the luminosity L from tracer j. In this way, based on mm continuum observations (for mm-sized dust) of 200 disks, $r_{mm} \approx 10-500$ AU (r_{mm} encircling $0.9 L_{mm}$) [36]. For smaller grains (µm-sized dust), the scattered images demonstrate that these particles are distributed out of greater distances than mm-sized grains (which is expected since small grains are predicted to be well coupled to the gas). In the case of the disk gas, the CO line emission is used to estimate the radius, having $r_{CO} \approx 100-500$ AU (based on a survey of 22 Lupus disks [37]).

Mass: the mass disk can be defined assuming an emission that arises in an optically thin, isothermal portion of the disk. In this way, the observed flux (F_ν) is directly related to the disk mass (M_{disk}, considering the gas and dust of the disk), as follows:

$$M_{disk} = \frac{d^2 F_\nu}{\kappa_\nu B_\nu(T_c)}, \tag{1.1}$$

where d is the distance to the source, κ_ν is the opacity, and $B_\nu(T_c)$ is the Planck function at a characteristic temperature T_c.

In order to have an idea of the protoplanetary disk mass values, some examples of mass estimations are presented as follows based on observations of different molecular clouds. One of the first large survey to measure this mass, was made with the observations of protoplanetary disks of the Ophiuchi molecular cloud [38]. In this survey, protoplanetary disk masses were estimated between 0.001 to 0.1 $M_{\odot}$. Another survey in the Taurus-Auriga star formation region, detected 74 objects of Class II, observed with sub-millimeter wavelengths, presenting a mean mass of $0.003 M_{\odot}$ [39]. A recent survey in the Serpens star-forming region, presented the mass disk of 235 protoplanetary disks, having a mean mass around $0.00005 M_{\odot}$ (calculated based on the full version of Table 1 in [40]).

Structure: PPD are studied around pre-main-sequence stars of approximately $\leq 3Myr$ old [36] to $\leq 17Myr$ old [41]. At this stage, the structure of this geometrically thin disk flares, i.e. as the radius of the disk (r) and the vertical scale height (thickness of the disk, h) increase.

Assuming that gas is at hydrostatic equilibrium, the vertical structure can be described by the pressure gradient that takes into account the gas density (ρ) and the vertical component of gravity (g_z) [42]:

$$\frac{dP}{dz} = -\rho g_z, \tag{1.2}$$

where the vertical component of gravity can be described as follows:

$$g_z = \frac{GM_*}{d^2}\sin(\theta) = \frac{GM_*}{d^3}z, \tag{1.3}$$

G being the gravitational constant, M_* the stellar mass, z the height above the mid-plane of the disk and d the distance from the stellar object to z (see Figure 1.2). The pressure gradient (Equation 1.2), points outwards.

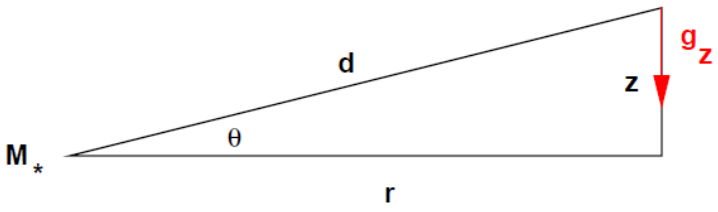

Figure 1.2: Vertical structure of protoplanetary disk considering a vertical hydrostatic equilibrium (taken from [42]).

Considering a geometrically thin disk ($z/r << 1$) and assuming a vertically isothermal disk, the hydrostatic equilibrium is recalculated with the sound speed constant (c_s) and solved, obtaining the vertical scale height [42]:

$$h(r) = \frac{c_s}{\sqrt{GM_*/r^3}}, \tag{1.4}$$

this equation shows that h increases with the distance from the star r.

On the other hand, the radial structure of the disk is defined by the radial surface density. Assuming a thin, viscous disk, the time evolution of the surface density is [43]:

$$\frac{\partial \Sigma}{\partial t} = \frac{3}{r}\frac{\partial}{\partial r}\left[r^{1/2}\frac{\partial}{\partial r}\left(\nu \Sigma r^{1/2}\right)\right], \tag{1.5}$$

where t is the time and ν is the viscosity of the disk. This surface density was characterized as a power law profile $\Sigma \propto R^{-p}$ (for $R \leq R_{out}$, where R_{out} is the outer radius of the disk), if the viscosity could also be written as a power law [44]. However, a pure power law could not match with observations. For this reason, the surface density was later redefined with a power law profile including an exponential taper (the disk does not have a sharp edge as described by a power law) [45] based on [46]:

$$\Sigma(R) \propto \frac{R}{R_c}^{-\gamma} exp\left[-\left(\frac{R}{R_c}\right)^{(2-\gamma)}\right], \tag{1.6}$$

where R_c is a characteristic radius that delineates where the Σ profile begins to steepen significantly from a power law and γ specifies the radial dependence of the disk viscosity ($\nu \propto R^{\gamma}$). However, this surface density profiles are under discussion and measurements of disk densities based on observations remain in an exploratory phase, as shown for example in [47]. Additionally, the previous profiles consider smooth disks and it has been shown that disks are not smooth, i.e. there are cavities and other substructures (see Section 5.1 in [41] for a summary in substructures).

Finally another element that affects the disk structure is its temperature (thermal structure), where the main irradiation on dust is made by the host star. Notice that the disk temperature is mainly controlled by dust (dust opacities affect a large electromagnetic spectrum, dominating the absorption of the stellar light and thus the thermal emission. Hence, we can assume that dust and gas have the same temperature). The classical way to constrain the temperature distribution is with SED modeling, where the temperature profile of a flared disk was defined as [48]:

$$T_{disk}(r) \propto r^{-1/2}, \tag{1.7}$$

affecting the radial profile of the disk and showing how the disk temperature decreases while the radius of the disk increases. Yet, the disk temperature also varies with altitude, $T_{disk}(z)$. Indeed, temperature decreases from surface layers of the disk (outer upper/lower layers) to the midplane [49]. This is caused by the fact that stellar radiation can not penetrate the midplane due to the disk opacity. Lastly, recent works have been modeling the temperature profile based on observations of opti-

cally thick molecular emission lines (i.e., CO and CN), as shown for example in [50, 51].

Dust and gas composition: initially, disk composition is 99% gas and 1% dust but as gas accretion occurs (and small dust particles are coupled to gas), these percentages evolve. For the gas, the most abundant gaseous species is H_2, followed by CO, H_2O and other less abundant molecular species that are detected in very small percentages [52, 53].

In terms of protoplanetary dust composition, the main components are silicates: amorphous silicates, olivine and pyroxene, and crystalline silicates, forsterite and enstantite, or just silica [54]. The presence of crystalline silicates is due to the transformation of amorphous silicates because of thermal annealing and condensation in the inner disk or shock heating in the outer disk [53]. Other minor components are carbons, polycyclic aromatic hydrocarbons [55], ices [56] and other minerals.

Dust size: The radius size of these small grains is around 0.1µm to 10µm [52] and thanks to agglomeration during this protoplanetary stage, the dust can range from submicrometer to centimeter scales [42]. Based on the mentioned radius size range, it has been suggested that protoplanetary dust has a power law size distribution with exponent −3.5 which is the same as for Debris disks [57, 58], the submicrometer-sized dust being more abundant than dust in tenths of micrometers (see Equation 1.8). This size distribution, in Debris disks, results from a steady-state evolution supposing an infinite collisional cascade producing submicrometer dust sizes.

$$n(a) \propto a^{2-3q}, \tag{1.8}$$

where a is the radius of the dust, $q = 11/6$ is the population mass index giving a final exponent of −3.5. The size of dust can vary depending on the disk. As previously mentioned protoplanetary dust size ranges from 0.1µm to 10µm. For simplicity we consider in this study a minimal size of 0.1µm.

1.2.3.2 Aggregation of dust

The aggregation of dust takes place thanks to the dust transport and growth mechanisms, both described in the following section and based on [59].

Dust transport in PPD:

1. Drag force: dust is embedded in a gaseous disk, producing an aerodynamic drag force (F_D, see Equation 1.9) when particles move throughout (i.e. gas friction opposing to the motion of particles) [42]:

$$F_D = -\frac{1}{2} C_D \pi a^2 \rho v^2, \tag{1.9}$$

where C_D is the drag coefficient, a the radius of a spherical dustt particle, ρ the density of the gas and v the speed of the particle relative to the gas. This drag force not only depends on the gas and particles motion but on the size of the particle, giving two drag regimes: the Epstein regime (small particles interact in the gas in a free-molecular-flow regime) and Stokes regime (a flow structure develops around larger particles). Particles in both regimes, having radius up to centimeters, are affected by this drag force, being coupled with the gas (when the Stokes number St is < 1, $St = \Omega_k \tau_s$, where Ω_k is the Keplerian orbital velocity and τ_s is the stopping or friction time).

2. Radial drift: the radial motion of dust in the disk is caused by the differential velocity between gas and dust. Gas is subjected to gravitational, centrifugal and pressure forces while dust is only subjected to gravitational and centrifugal forces, thus gas has a sub-Keplerian orbital velocity due to the pressure force and dust has a Keplerian velocity (Ω_k). As dust has a larger velocity compared to the gas, dust experiences a drag force due to the gas, causing a loss in the dust angular momentum and drifting inward (toward the pre-main-sequence star). However, the radial drift is not always inward, if the sign of the gas pressure gradient changes, dust will not be drifted inward, instead it will be pushed outward.

3. Dust trapping: the problem with the radial drift is that particles should move inward in a small fraction of the protoplanetary disk life time. Only if the gas pressure gradient is locally reversed, being positive or zero (it is normally negative making particles move inward), there will not be a radial motion to inner regions but particles will be drifted outward. However, if a local gas pressure maximum is created (by vortices, planets clearing gaps or other magneto-hydrodynamic mechanisms), the gas pressure gradient will have opposite signs on both sides of the maximum, creating a dust trapping (dust piles up) called pressure bumps [60, 61].

4. Meridional flows and radial mixing: viscous evolution of gas drags particles inward with radial gas velocity (advection transport of particles), as long as particles are well coupled to the gas (which means $St < 1$). If the gas velocity in a region has some inward motion, then the gas velocity can be positive at the midplane, producing a meridional flow pattern and allowing to transport dust particles outwards. However, this process is weaker than the inward radial drift, thus it does not explain the presence of millimeter sized particles in the outer regions of the disk. Additionally to this meridional flow pattern, the gas is considered as turbulent, hence this turbulent stirring creates radial mixing of dust particles.

5. Vertical mixing and settling: vertical mixing of dust can be possible if dust has larger sizes ($St > 1$), producing a partial decoupling from the gas and having

damped vertical oscillations due to its orbital motion and gas drag force. During this vertical mixing the vertical component of the gravitational acceleration and the deceleration of the drag force create a settling velocity (v_{sett}) to the midplane: $v_{sett} = St\Omega_K z$. This settling increases with particles size and height. In this way, while large particles settle and grow in the midplane, it is expected that small dust stays in the upper layers (surface) of the disk.

Dust growth in PPD:

Transport mechanisms of dust, previously explained, lead to differential vertical and radial motion of dust. These movements cause two growth processes: grain-grain collision (that is related to relative velocities), and condensation. During the growth process the primordial dust particles, known as monomers, stick together forming aggregates. This whole phenomenon of aggregation depends on the composition of dust, the monomer size distribution, the structure of aggregates, the impact parameter (b is defined as the projected distance between the centers of mass of the aggregates in the direction perpendicular to the collision velocity, if $b = 0$ there is a head-on collision between aggregates and if $b = b_{max}$ there is a grazing collision [62]) and impact velocity.

The first growth process, grain-grain collision, has two important elements which are the collision frequency and the collisional outcomes. The first element, collision frequency, depends on the relative velocities of grains. These relative velocities are originated by the different sizes of the particles and thus relative motions. As the size difference between particles increases, relative motions increases (particles of similar sizes have similar Stokes numbers and thus same velocities). Examples of these relatives velocities are the vertical settling relative velocity, radial drift relative velocity and turbulent relative velocity. All of them are affected by the Stokes number, velocities being small for particles having $St < 1$ and reaching higher values for $St > 1$. These relative velocities can also be larger if the Stokes number difference between the colliding particles increase (up to $St = 1$). Another motion is the Brownian motion that produces relative random velocities affecting specifically small particles (sub-micrometer sizes).

The second element of collision, the collisional outcomes, have been retrieved with laboratory and microgravity experiments performed during the last 30 years. There are two types of outcomes depending on the size of the colliding particles, supposing that particles are composed of only silica, which is in fact one of the most abundant components of protoplanetary dust (see Figure 1.3) [63]:

- Outcomes for similar-sized dust: size ratio between the two colliding particles is around one, producing different collisional outcomes, i.e., sticking, bouncing, fragmentation and abrasion. **Sticking** occurs when the collision energy is smaller than the van-der-Waals energy. The sticking leads to different regimes, i.e., hit-and-stick regime when there are small impact velocities (producing fractal dimensions between $1.1 \leq D_f \geq 2.0$) and compaction regime for higher impact

velocities (producing fractal dimensions $D_f < 3.0$). **Bouncing** happens when the energy dissipation of the collision is insufficient to stick and not large enough to destroy the colliding particles. **Fragmentation** is when the threshold velocity (for impact velocities $\gtrsim 1 m/s$ depending on the particle size) is exceeded leading to the destruction of particles. And finally, **abrasion** occurs when cm-sized aggregates, having bouncing collisions, lose mass in very small quantities (1000 collisions are needed to completely destroy these centimetric particles).

- Outcomes for small projectiles hitting larger target particles: the difference of colliding particle size (size ratios $\neq 1$) produces three additional outcomes: mass transfer, cratering and erosion. Above a certain velocity threshold, not only fragmentation can take place but also a **mass transfer** of the small hitting particle to the larger dust target. However, if the size of the hitting particles increases, keeping the same velocity that in the mass transfer outcome, then there will be a lost mass of the dust target by **cratering**. On the contrary, if the size of the hitting particle decreases, at the same impact velocity as the two previous outcomes, then an **erosion** effect will occur.

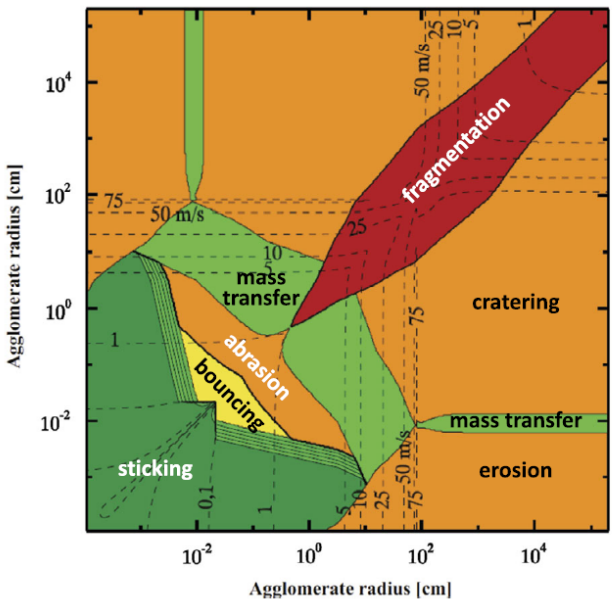

Figure 1.3: Collisional outcomes for silica colliding particles at a distance of 1 AU [taken from 63].

The second growth process, condensation, is a mechanism in which gas condensates on the surface of grains, creating ice mantles. However, this process is limited by the quantity of material in the gas phase. Indeed, there is not enough condensed gas to grow dust/ice mantles on every grain surface (there is no continuous source of condensable material) and continue with this mechanism in an indefinite growth

process. Thus, the limited gas material goes preferentially onto small particles because the accretion of this condensed gas is a surface process and the dust surface area is larger for small particles compared to their volume than large particles. Therefore this mechanism happens at small scales (microscopical grains) but it does not solve the growth barriers for larger grains to reach to planetesimal sizes (km-sized solids). Notice that as well as condensation, evaporation takes place, producing the opposite effect.

Growth barriers in PPD:

Within the different mechanisms of transport and growth of dust there are still some constraints that have not yet been solved for pebbles (mm to cm sizes): the growth barriers [3], i.e. the bouncing barrier, the drift barrier and the fragmentation barrier. The bouncing barrier happens at the bouncing stage and it is the incapacity of pebbles to stick and grow rather than bounce between each other, inhibiting other growth process [63]. The fragmentation barrier occurs when the impact velocity increases when particle size increases, shattering particles and making impossible the transition from pebbles to planetesimals (km sizes). Finally, the drift barrier is associated with a dust transport process, radial drift, in which dust is coupled with gas bringing all dust inwards to the pre-main-sequence star [64] and sublimating all dust unless there is an instability. However, instabilities (i.e.,streaming and gravitational instabilities) are mechanisms that happen at very specific/unique conditions, and the drift barrier prevails. Nonetheless observations proved that planetesimals and planets exist, thus, there is a problem in the core accretion model.

For example, for the gravitational instability to happen and form giant planets, very massive ($M_{disk} = 0.25 M_*$) and cold disks (with fast cooling time of $t_{cool} = 5\Omega^{-1}$, where Ω is the angular frequency) are needed [65, 66, 67]. On the other hand, the streaming instability occurs at local gas pressure maximum zones. For this instability to happen, two favorable conditions, to form planetesimals from pebbles, must be satisfied. First, dust is slightly coupled to gas and the higher the Stokes number the higher is the instability [68] ($St > 0.01$[69]). Second, dust-to-gas ratios in the midplane must be larger than 1 [68]. When dust-to-gas rations reaches this value, drift velocities of dust particles are slowed down, generating particle-density enhancements. Hence, particles are piled up collapsing (due to self-gravity) and forming larger particles up to planetesimals [70].

However, for these instabilities to happen, stringent conditions need to be satisfied as previously mentioned. Thus, other possibilities to solve the growth barriers and therefore the planet forming timescales of models need to be studied. As for example, dust morphologies. Indeed, the different models that describe the dust transport and dust growth consider spherical dust particles which actually is a very strong assumption. Lets see in the following section which type of PPD observations can help us to obtain more information about this dust morphology.

1.2.3.3 PPD observations

A summary of the general characteristics of PPD is presented on Figure 1.4. On the right side there are the different dust sizes that can be found in protoplanetary disks and the telescopes that are able to observe them, based on their wavelengths. The distribution of particles is also schematized, larger particles are settled on the midplane while smaller particles are at the surface of the disk. On the left side, there is a representation of dust transport and growth processes.

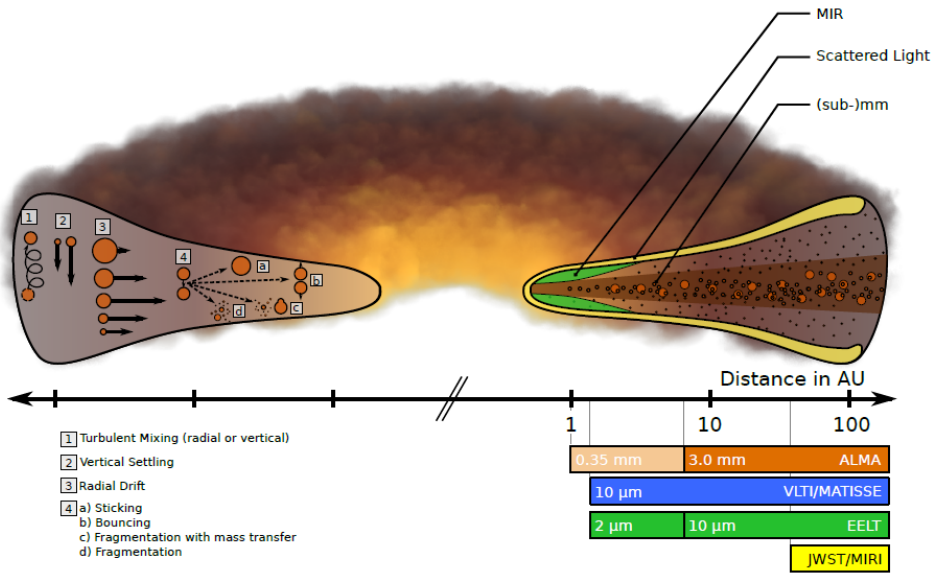

Figure 1.4: Representation of a protoplanetary disk with its transport and growth processes (on the right) as well as dust sizes (on the left) [taken from 59].

In order to understand more the accretion process of these sub-micrometer to centimeter particles (from dust to pebbles), it is important to study the morphology of this dust. Indirect information on the dust morphology can be retrieved with observations of protoplanetary disks with different telescopes at millimeter, near-infrared and optical wavelengths, i.e., Atacama Large Millimeter Array (ALMA), Very Large Telescope (VLT), James Webb Space Telescope (JWST) and Hubble Space Telescope (HST); as well as with centimeter wavelengths, i.e., Square Kilometre Array (SKA) and Very Large Array (VLA).

For representing the case in which protoplanetary dust particles are measured with telescopes, lets first imagine the situation and then understand it based on the scattering theory (explained in Section 1.3). Imagine a protoplanetary disk, with a center pre-main-sequence star emitting non-polarized light (first source) in all directions. This radiation encounters different dust particles that compose the disk. After encountering dust, this non-polarized light can follow several transformations due to absorption, scattering and multiple scattering (between dust) [71, 72], transforming the first source in a second source, this time of partially polarized light. Then, thanks

to telescopes, the scattered light coming from these dusts can be detected (see Figure 1.5).

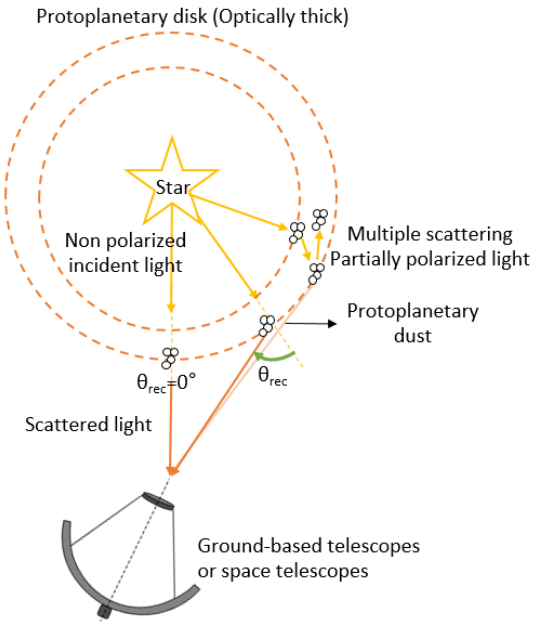

Figure 1.5: Scheme to represent the two types of sources that encounter dust in protoplanetary disks, producing scattered light that is detected by telescopes at different angles of reception (θ_{rec}).

After detection, scattered images of protoplanetary disks are reconstructed as shown in Figure 1.6 [73], where different protoplanetary disks at different positions can be seen. Notice that these scattered images present a main challenge at the optical and NIR wavelenghts, which is the contrast of the disk compared to the host star [36]. In fact, scattered light from the disk is significantly fainter than the star. Thus, in order to obtain only the scattered light of the disk, a coronagraphic mask is necessary to remove the stellar emission.

Another technique to obtain only the scattered light coming from the disk is using a polarization differential imaging (PDI). By using a polarizing beam-splitter in the telescope instrument, the incoming light is divided and perpendicular polarized [see Section 7.2.3 in 74]. The subtraction of these two linearly polarized components gives the polarized emission coming from the disk while the unpolarized light coming from the host star is vanished. The way to characterize this polarized light in the PDI is by using the Stokes formalism, where the Stokes vector describes the different states of polarization (see Section 1.3.2 for a detail explanation). Based on the Stokes vector, I represent the total intensity, Q and U the linear polarization, and V the circular polarization. Combining Q and U, the polarized intensity ($\sqrt{Q^2+U^2}$) can be calculated (see Equations 1 for Q and Equation 2 for U in [75]). From the polarized

intensity, U can be neglected since it is a signal dominated by noise and instrumental or reduction artifacts (when considering single scattering). However, in [76] was probed that PPDs that are observed under high inclination, present multiple scattering and therefore U cannot be neglected. After retrieving the polarized intensity, this last one can be divided by the total intensity giving the degree of polarization (including Q and U in the polarized intensity) or the degree of linear polarization (including only Q in the polarized intensity). Hence, with nowadays scattered light and polarimetric observations, the total intensity and the polarized intensity can be retrieved and therefore the degree of linear polarization of the disk is computed (see Figure 1.7 where these three scattering parameters were retrieved with observations of disk LkCa15 with VLT/SPHERE).

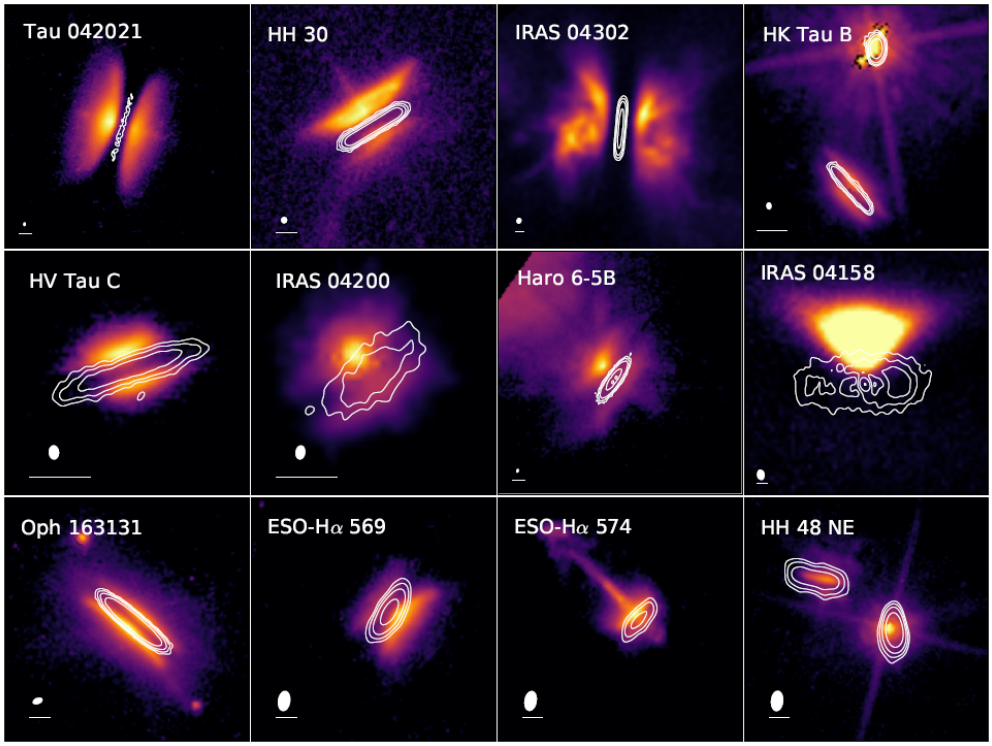

Figure 1.6: Images of protoplanetary disks seen in scattered light with HST (color images) at NIR wavelengths for all sources, except for IRAS 04200, Oph 163131, ESO-Hα 574 and HK Tau B which are at optical wavelengths; and with ALMA (continuum images in white contours) at band 7 for all sources, except for Oph 163131 which is at band 6 [taken from 73].

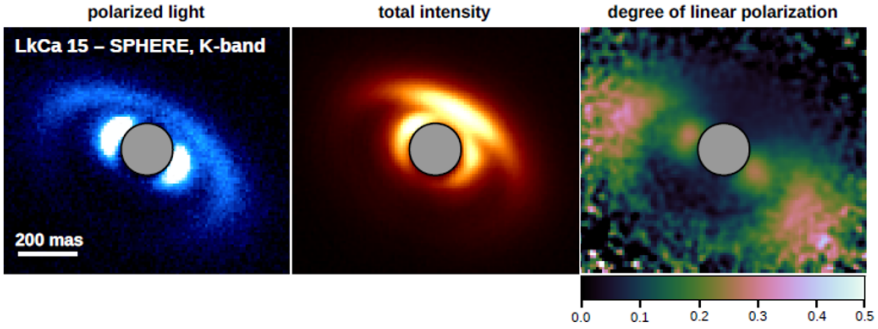

Figure 1.7: Images of disk LkCa15 presented in polarized intensity (left image) , total intensity (middle image) and the computed degree of linear polarization (right image). Note that the color map of the total intensity is 10 times larger than for the polarized intensity and the gray circle in the middle is the coronographic mask [taken from 41].

The fact of being able to model protoplanetary disks and retrieving similar disk as observations probes that we understand the different properties and components of itself. However, there is still a lot of work to do to obtain the exact observed disks based on current models. Indeed, evidences that protoplanetary disk observations are not reproducible with models of the same population of spherical dust, as shown for example in [77, 78], probes that we need to consider other dust morphologies. For this reason, it is of outmost importance to study and understand the signatures of this dust through their scattering parameters. But how can we pass from the scattering parameters of dust (i.e., total intensity, degree of linear polarization, etc) to the observations in scattered light of disks which include all the interactions between dust particles (also represented in terms of total intensity, polarized intensity, degree of linear polarization, etc)? To solve this question two steps are necessary: first, the scattering parameters of dust must be obtained. This can be done with laboratory measurements or simulations. Second, taking into account these dust scattering parameters and other interactions (as for example interactions between dust, interactions between dust and gas, and absorption of dust), we can use the radiative transfer to model protoplanetary disks. Indeed, these disks are optically thick and to obtain their scattering parameters a radiative transfer is necessary to model the whole disk. Therefore, using radiative transfer codes, synthetic images of protoplanetary disks are retrieved. Then, synthetic images can be compared to observations seen in scattered light and in this way constrain the possible morphologies of this dust (see Figure 1.8).

During my thesis I focused on the first step, aiming to obtain the scattering parameters as a function of the scattering angles of dust of different morphologies, using laboratory measurements (microwave analogy) and simulations. The scattering parameters that I studied are the phase function (intensity in terms of the scattering angles), the degree of linear polarization and some others that cannot be observed directly but instead to be used, as prospects, in transfer radiative codes. Herein, we

are interested in studying the scattering parameters in the Mie scattering regime (see following section, Figure 1.11). The reasons for this choice are: i) we aim to study the scattering behavior at the scale of the photon-dust interaction, ii) the smallest dust can be easily simulated in the Rayleigh regime, thus we can ignore them and iii) the size distribution of protoplanetary dust is assumed to be a power law distribution which gives more weight to small sized-dust, hence we assume a small contribution of large sized-dust. Therefore, the zone of our interest to study the morphology of dust with the scattering parameters is in the Mie scattering regime.

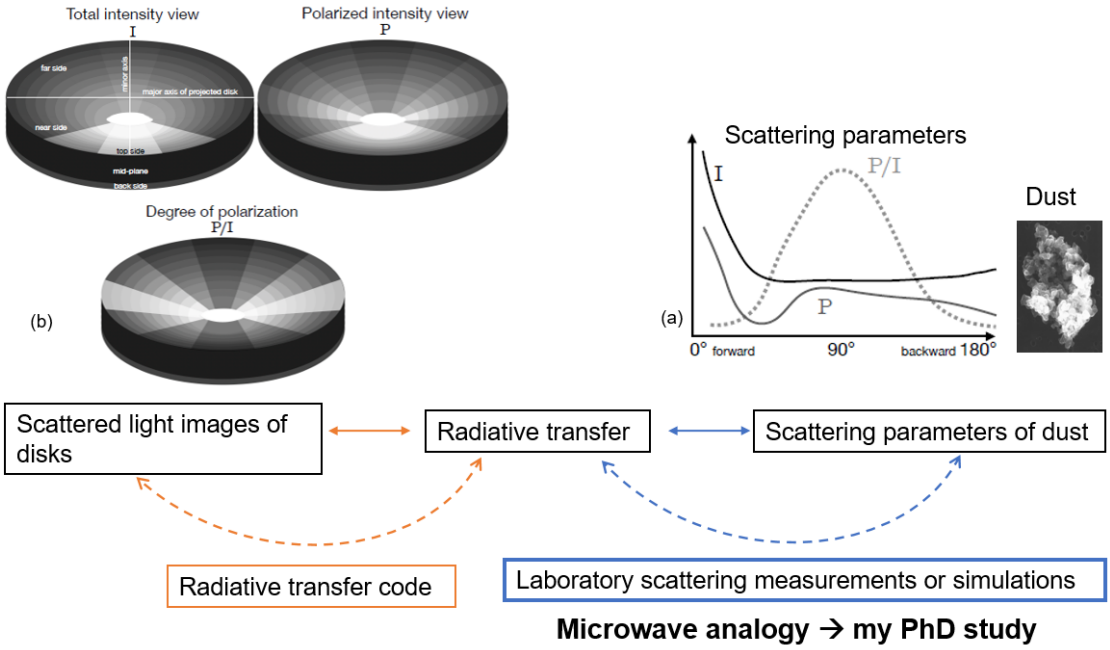

Figure 1.8: Scheme for passing from (a) the scattering parameters of dust to (b) the same parameters of protoplanetary disk. Images (a) and (b) were taken from [41].

Notice that disks that are more evolved in their formation, as it is the case for debris disks, their scattering parameters as a function of scattering angles (2D diagrams), can be retrieved from observations without using a radiative transfer code. Indeed, debris disks are optically thin, gas is already dissipated (as previously explained in Section 1.2.1). Therefore, examples as intensity diagrams in 2D (named in this manuscript as phase functions) of these disks, as shown in Figure 1.9, are retrieved. Since the main objective of my thesis is to obtain the scattering parameters in 2D of dust and not to obtain the synthetic scattered images of protoplanetary disks in 3D, in Chapters 2 and 3, comparisons with scattering parameters of a debris disk are performed, as a first approach to validate our results (as well as comparisons with other laboratory measurements and simulations).

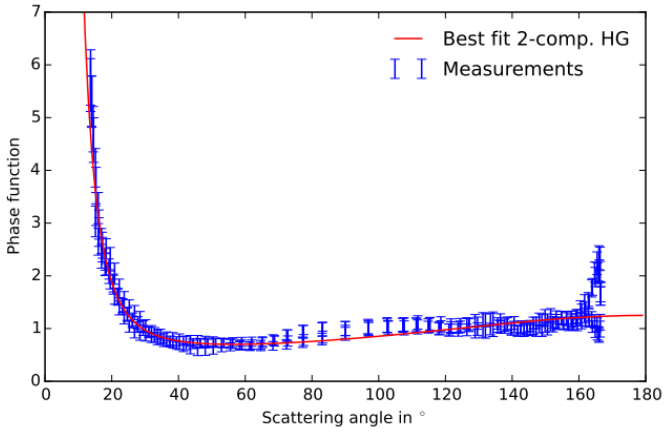

Figure 1.9: Phase function of disk HR4796A based on observations in scattered light taken from [78]. The phase function is represented over the scattering angles from 13.6° to 166.6°.

The following section is focused on the electromagnetic scattering theory, Stokes formalism and the scattering parameters of interest in this study.

1.3 Electromagnetic scattering theory

The phenomenon of scattering happens when an electromagnetic wave encounters an object called the obstacle or target. So when the wave "gets in contact", the object electric charges oscillate due to the electric field of the incident wave. This first process is called excitation. In addition, accelerated electric charges radiate electromagnetic energy which is a secondary radiation, this second process is called re-radiation. Thus, the scattering is composed of an excitation and a re-radiation. It is important to note that the excitation can transform the electromagnetic energy into other types of energies like thermal energy, which is called absorption. In this way, scattering and absorption are related processes that happen at the same time [79].

It is important to clarify that the host media in which the obstacle is found is supposed to be homogeneous (indeed, all media scatter light because of the heterogeneity of the system under consideration but for simplicity we will consider it as homogeneous, which means that the atomic and molecular composition of the medium is negligible compared to the incident wavelength), isotropic and non absorbing. In this way, the present work studies the scattering phenomenon of a particle in this host medium. Furthermore, the composition of the particle is assumed to be stated in macroscopic terms which means that it is defined with optical constants which depends on the frequency. Another important assumption is that the frequency of the incident wave is the same as the scattered wave, i.e. elastic scattering (no loss of energy when the wave encounters the object).

If there is a single particle, divided in small imaginary regions, and submitted to an

incident wave (oscillating field), there will be an induction of a dipole moment in each region. Therefore, those regions will be dipoles oscillating at the same frequency as the incident wave, scattering a secondary radiation (see Figure 1.10)

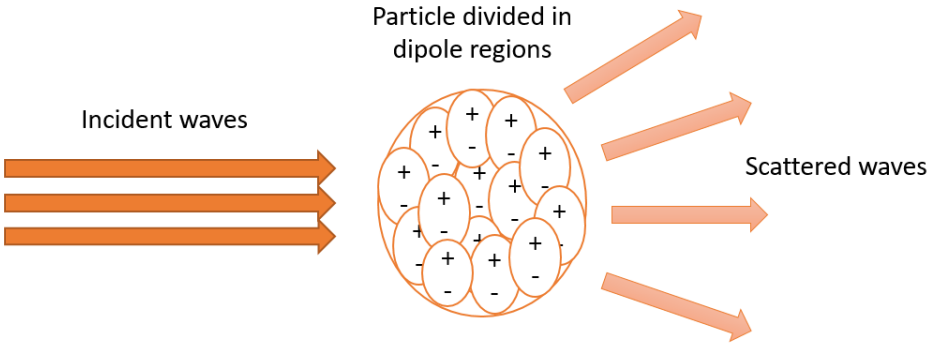

Figure 1.10: Electromagnetic scattering for a single particle.

On the other hand, if there is a collection of particles, like it is in the case of aggregates, constituent particles of the aggregate will be electromagnetically coupled which means that each constituent particle is excited by the incident field plus the scattered field of other constituent particles (coupling) [79, 80]. If there is a group of aggregates then there will be also electromagnetic coupling between aggregates, know as multiple scattering.

Based on this scattering process, the incident field interacts with a particle or a collection of particles and the scattered field will contain information related to that particle(s), i.e. size, shape, material and structure [13]. Furthermore, the relation between the wavelength and the particle size is important and it is usually expressed with the size parameter:

$$X = \frac{2\pi r}{\lambda}, \tag{1.10}$$

where r is the radius of a spherical particle or the radius that includes a collection of particles and λ is the wavelength in the medium. The size parameter can be separated in four different scattering regimes: geometric optics ($r >> \lambda$), Mie scattering ($r \approx \lambda$), Rayleigh scattering ($r << \lambda$) and negligible scattering regimes [81] (see Figure 1.11). In this thesis we are interested in the Mie scattering regime.

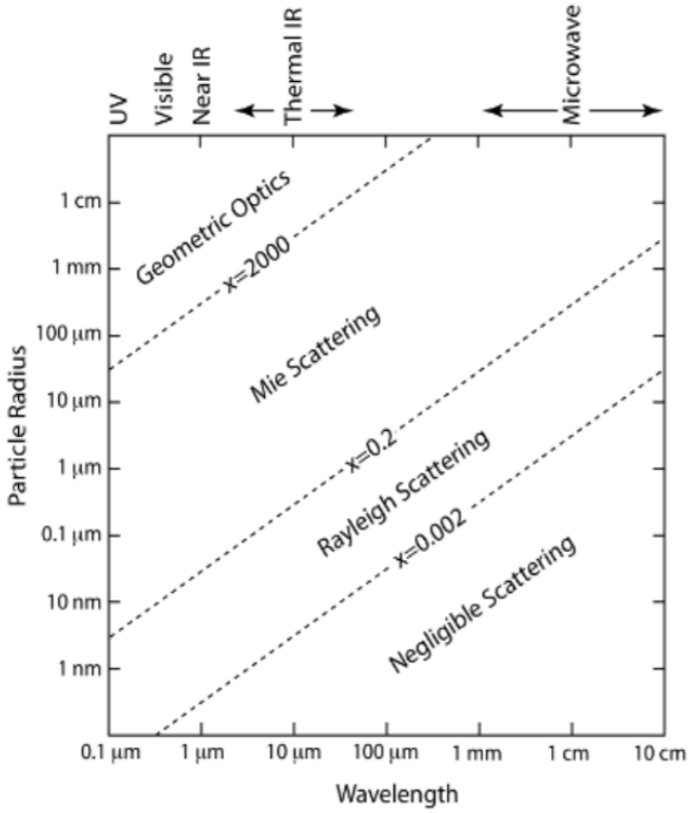

Figure 1.11: Scattering regimes depending on the particle radius and the wavelength [taken and modified from 81].

Depending on the information that is apriori known about the field and the object, the interaction between the wave and the particle can give different information, giving rise to two kinds of problems: the direct and inverse scattering problems. The direct problem is the determination of the scattered field for a known object. This means, the observer knows the shape, the size and the composition of the object and after applying an electromagnetic wave (with a specific polarization and frequency), the observer obtains (with measurements or numerical simulations) the unknown scattered field corresponding to the object under study. On the other hand, the inverse problem allows the determination of the object properties from the known scattered field of the object. Thus, the goal of the inverse problem is to obtain an electromagnetic characterization of the studied object, like its permittivity, degree of polarization, etc, that gives information on its shape, size and composition, from a controlled electromagnetic wave [79].

For our case study, the analysis of this scattered field will give us clues to interpret the scattered waves observed from protoplanetary disks and thus deduce the scattering properties of protoplanetary dust (inverse problem), based on the knowledge developed with our laboratory experiments and simulations (direct problem).

1.3.1 Electromagnetic wave

To understand the electromagnetic scattering phenomenon, it is necessary to first define the electromagnetic wave that interacts with the object. The following description and notation are from [79], unless stated otherwise (from Section 1.3.1 to Section 1.3.4).

Consider a complex electric field for a time-harmonic plane electromagnetic wave, propagating along the z direction:

$$\mathbf{E} = Re\{\mathbf{E}_c\} = Re(\mathbf{A} + i\mathbf{B})e^{(ikz - i\omega t)}, \tag{1.11}$$

E_c being the complex electric field, $\mathbf{A}$ and $\mathbf{B}$ real vectors (independent of the position), $i^2 = -1$, k the wave number, z the distance from the source to the object, ω the angular frequency and t the time. Using the Euler's formula, Equation 1.11, takes the form:

$$\mathbf{E} = \mathbf{A}\cos(kz - \omega t) - \mathbf{B}\sin(kz - \omega t), \tag{1.12}$$

if Equation 1.12 is in a specific plane $z = 0$, it is transformed as:

$$\mathbf{E} = \mathbf{A}\cos(\omega t) - \mathbf{B}\sin(\omega t). \tag{1.13}$$

Equation 1.13 is known as the vibration ellipse (see Figure 1.12) and it describes the state of polarization of an electromagnetic wave, which is one of the characteristics of the wave. It is necessary to understand polarization because scattering is one of the mechanism which influences polarization of electromagnetic waves.

From Equation 1.13, three cases appear: a linear polarized wave (if $\mathbf{A} = 0$ or $\mathbf{B} = 0$), a circular polarized wave (if $|\mathbf{A}| = |\mathbf{B}|$ and $\mathbf{A} \cdot \mathbf{B} = 0$) and an elliptically polarized wave (Equation 1.13).

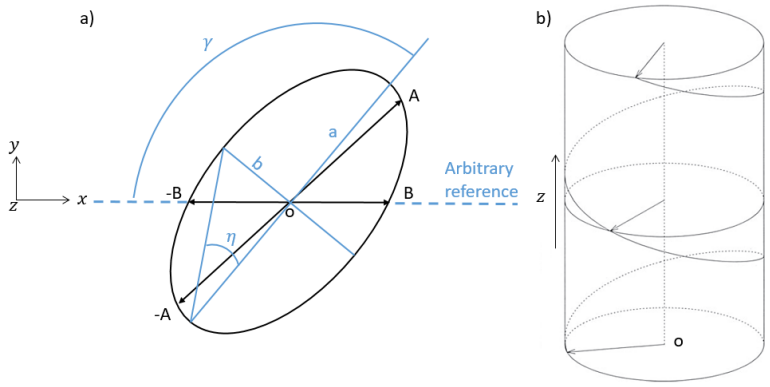

Figure 1.12: a) Vibration ellipse viewed from the plane xy with its amplitudes A and B (see Equation 1.13), semimajor axis a, semiminor axis b, angles γ and η (see Equation 1.16); b) Vibration ellipse viewed in the z direction.

The vibration ellipse can rotate in two directions, clockwise (right-handed rotation of the ellipse viewed by an observer who is looking toward the source) and anticlock-

wise: this characteristic is called handedness. Another characteristic is the ellipticity which is the length of the semiminor axis (a) of the ellipse divided by the length of the semimajor axis (b). Finally, the last property is the azimuth that is the angle (γ) between the semimajor axis and an arbitrary reference (see Figure 1.12 for a, b and γ). These three characteristics plus the irradiance (also known as intensity or flux, which is the energy per unit area and time [Wm^{-2}] represented by I or the magnitude of the Poynting vector) form the ellipsometric parameters.

1.3.2 Stokes parameters

Even though the ellipsometric parameters describe a monochromatic wave, they are not appropriate to understand the transformations of polarized waves and they are not directly measurable by most of the optical instruments (not intensity but handedness, ellipticity and azimuth angle). Accordingly, Stokes defined the Stokes polarization parameters, which are measurable or observable quantities, in 1852 [82].

Lets consider a monochromatic wave defined by an electric field $\mathbf{E}$ in two orthogonal components:

$$\mathbf{E} = \mathbf{E}_0 e^{(ikz - i\omega t)}, \tag{1.14}$$

where $\mathbf{E}_0 = E_\parallel \mathbf{e}_\parallel + E_\perp \mathbf{e}_\perp$ in which the amplitudes are $E_\parallel = a_{m\parallel} e^{i\delta_\parallel}$ and $E_\perp = a_{m\perp} e^{-i\delta_\perp}$ and the orthogonal bases are $\mathbf{e}_\parallel$ and $\mathbf{e}_\perp$. Based on the above equation, four cases appear giving birth to the Stokes parameters:

1. Whatever the wave (incident or scattered wave of the object) its intensity can be written as $E_\parallel E_\parallel^* + E_\perp E_\perp^*$, giving the first Stokes parameter I.

2. When there is a horizontal polarization, the amplitude of the wave is $E_\parallel$ and the measurable quantity, the intensity ($I_\parallel$), is $E_\parallel E_\parallel^*$. On the contrary, if there is a vertical polarization, the amplitude of the wave is $E_\perp$, and the intensity ($I_\perp$) is $E_\perp E_\perp^*$. The difference between these two intensities, $E_\parallel E_\parallel^* - E_\perp E_\perp^*$, gives the second Stokes parameter Q.

3. When there is a linear polarization of 45°, the orthogonal basis should change for convenience, thereby the orthogonal basis are:

   $$\mathbf{e}_+ = \tfrac{1}{\sqrt{2}}\left(\mathbf{e}_\parallel + \mathbf{e}_\perp\right) \text{ and } \mathbf{e}_- = \tfrac{1}{\sqrt{2}}\left(\mathbf{e}_\parallel - \mathbf{e}_\perp\right),$$

   the electric field is $\mathbf{E}_0 = E_+ \mathbf{e}_+ + E_- \mathbf{e}_-$ and the amplitudes are:

   $$E_+ = \tfrac{(E_\parallel + E_\perp)}{\sqrt{2}} \text{ and } E_- = \tfrac{(E_\parallel - E_\perp)}{\sqrt{2}}.$$

   If there is a 45° polarization, the amplitude is E_+ and the intensity is:

   $$I_+ = (E_\parallel E_\parallel^* + E_\parallel E_\perp^* + E_\perp E_\parallel^* + E_\perp E_\perp^*)/2.$$

On the other hand, if the polarization is −45°, the amplitude is E_- and the intensity is:

$$I_- = (E_\parallel E_\parallel^* - E_\parallel E_\perp^* - E_\perp E_\parallel^* + E_\perp E_\perp^*)/2.$$

The difference between $I_+ - I_-$ gives the third Stokes parameter U which is $E_\parallel E_\perp^* + E_\perp E_\parallel^*$.

4. The last case is for circular polarization. It is also convenient to define another orthogonal basis:

$$\mathbf{e}_R = \frac{1}{\sqrt{2}}\left(\mathbf{e}_\parallel + i\mathbf{e}_\perp\right) \text{ and } \mathbf{e}_L = \frac{1}{\sqrt{2}}\left(\mathbf{e}_\parallel - i\mathbf{e}_\perp\right).$$

Based on the basis noted above, the field is defined as $\mathbf{E}_0 = E_R\mathbf{e}_R + E_L\mathbf{e}_L$ where R represents the right circular polarization and L, the left circular polarization. The amplitudes are:

$$E_R = \frac{(E_\parallel + iE_\perp)}{\sqrt{2}} \text{ and } E_L = \frac{(E_\parallel + iE_\perp)}{\sqrt{2}}.$$

If there is a right circular polarization, the amplitude is E_R and the intensity is:

$$I_R = (E_\parallel E_\parallel^* - iE_\parallel^* E_\perp + iE_\perp^* E_\parallel + E_\perp E_\perp^*)/2.$$

On the other side, if there is a left circular polarization, the amplitude is E_L and the intensity is:

$$I_L = (E_\parallel E_\parallel^* + iE_\perp E_\parallel^* - iE_\parallel E_\perp^* + E_\perp E_\perp^*)/2.$$

Subtracting $I_R - I_L = i(E_\perp^* E_\parallel - E_\parallel^* E_\perp)$, the last Stokes parameter appear, V.

In this way, the Stokes parameters are:

$$\begin{aligned} I &= E_\parallel E_\parallel^* + E_\perp E_\perp^* = a_{m\parallel}^2 + a_{m\perp}^2, \\ Q &= E_\parallel E_\parallel^* - E_\perp E_\perp^* = a_{m\parallel}^2 - a_{m\perp}^2, \\ U &= E_\parallel E_\perp^* + E_\perp E_\parallel^* = 2a_{m\parallel}a_{m\perp}\cos(\delta), \\ V &= i(E_\perp^* E_\parallel - E_\parallel^* E_\perp) = 2a_{m\parallel}a_{m\perp}\sin(\delta), \end{aligned} \tag{1.15}$$

where $*$ represents the complex conjugate.

These four parameters can also be described in terms of the ellipsometric parameters (see Figure 1.12) as follows:

$$\begin{aligned} I &= c^2, \\ Q &= c^2 \cos(2\eta)\cos(2\gamma), \\ U &= c^2 \cos(2\eta)\sin(2\gamma), \\ V &= c^2 \sin(2\eta), \end{aligned} \tag{1.16}$$

in which $c^2 = a^2 + b^2$ is the quadratic sum of the semimajor axis and semiminor axis, γ is the angle between $0 \leq \gamma \leq \pi$ and η is the angle between $\frac{-\pi}{4} \leq \eta \leq \frac{\pi}{4}$ of the vibration ellipse.

The Stokes parameters are organized in a vector called the Stokes vector **I** (intensity vector), where all quantities are measurable and its unit is $\left[\frac{W}{m^2}\right]$

$$\mathbf{I} = \begin{pmatrix} I \\ Q \\ U \\ V \end{pmatrix}. \tag{1.17}$$

Based on the Stokes vector, the different states of polarization can be defined as shown in Figure 1.13 in which the vector is normalized to the unity.

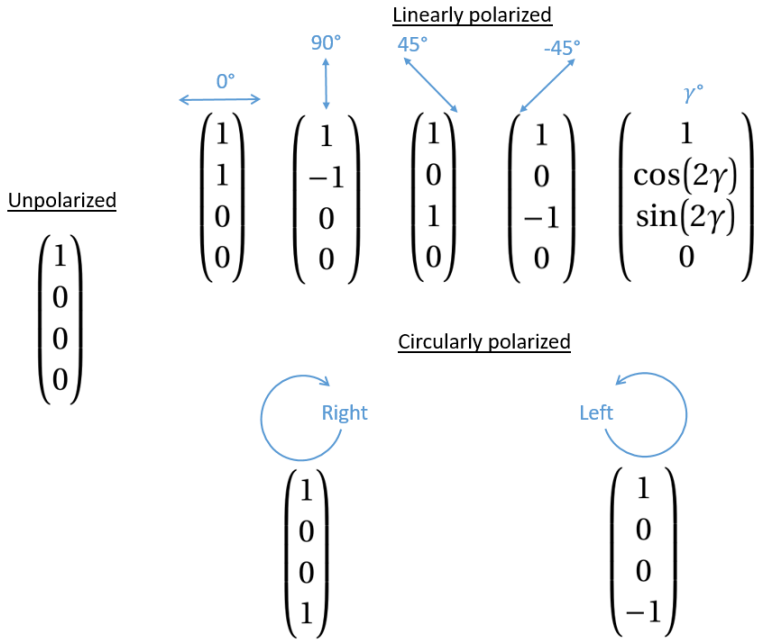

Figure 1.13: Basic states of polarization represented by the Stokes vector. Note that the horizontal and vertical polarizations have inverse signs in the standard astronomical convention (see Figure 1 in [83]).

At the beginning of this section, the wave was supposed to be a monochromatic

wave, yet the Stokes parameters can also represent quasi-monochromatic waves and non polarized waves [79, 84]:

- If the wave is monochromatic, it means $E_\parallel$ and $E_\perp$ (the complex amplitudes of the electric field) are completely correlated, so the radiation is totally polarized. The Stokes vector in the Equation 1.15 and the parameters are related as follows:

$$I^2 = Q^2 + U^2 + V^2. \tag{1.18}$$

- If the wave is quasi-monochromatic, it means $E_\parallel$ and $E_\perp$ are partially correlated so the radiation is partially polarized. Stokes parameters takes the form:

$$\begin{aligned} I &= \left\langle E_\parallel E_\parallel^* + E_\perp E_\perp^* \right\rangle = \left\langle a_\parallel^2 \right\rangle + \left\langle a_\perp^2 \right\rangle, \\ Q &= \left\langle E_\parallel E_\parallel^* - E_\perp E_\perp^* \right\rangle = \left\langle a_\parallel^2 \right\rangle - \left\langle a_\perp^2 \right\rangle, \\ U &= \left\langle E_\parallel E_\perp^* + E_\perp E_\parallel^* \right\rangle = \left\langle 2 a_\parallel a_\perp \cos(\delta) \right\rangle, \\ V &= i \left\langle E_\perp^* E_\parallel - E_\parallel^* E_\perp \right\rangle = \left\langle 2 a_\parallel a_\perp \sin(\delta) \right\rangle. \end{aligned} \tag{1.19}$$

  The brackets $\langle\rangle$ represent time averages in which the interval is much longer than the period, $2\pi/\omega$.

  Additionally, the identity that relates them is:

$$I^2 \geq Q^2 + U^2 + V^2. \tag{1.20}$$

- If the wave is unpolarized, $E_\parallel$ and $E_\perp$ are totally uncorrelated so the time average is null for any time shift and orthogonal direction couple. The Stokes parameters take the form $Q = U = V = 0$.

If there are two or more waves propagating in the same direction and knowing that there is no relation between the phases of each separate wave (incoherence), thanks to the incoherent additivity rule, the intensities of these two waves can be added up to form a total intensity. Using this rule, the Stokes vectors of each wave can be added up. Moreover, this rule also provides the possibility of separating the Stokes vectors in an incoherent sum of unpolarized waves and totally polarized waves [84] as shown below [82]:

$$\begin{pmatrix} I \\ Q \\ U \\ V \end{pmatrix} = (1-P)\begin{pmatrix} I-(Q^2+U^2+V^2)^{1/2} \\ 0 \\ 0 \\ 0 \end{pmatrix} + (P)\begin{pmatrix} (Q^2+U^2+V^2)^{1/2} \\ Q \\ U \\ V \end{pmatrix}, 0 \leq P \leq 1. \quad (1.21)$$

Equations 1.20 and 1.21 lead to the equation of the degree of polarization:

$$P = \frac{(Q^2+U^2+V^2)^{1/2}}{I}. \quad (1.22)$$

The degree of polarization is a value between 0 and 1. $P = 1$ is when the wave is totally polarized and $P = 0$ when the wave is totally unpolarized, e.i., for light coming from the star. A more specific degree of polarization is the degree of linear polarization (Equation 1.23), where the parameter V is not included because it is related to the circular polarization:

$$P_l = \frac{(Q^2+U^2)^{1/2}}{I}. \quad (1.23)$$

There is another degree of linear polarization in which U is eliminated (for an incident unpolarized wave, this means considering a single scattering for protoplanetary dust as previously discussed in Section 1.2.3.3 and not a multiple scattering between dust particles) but it is called in the same way [80]:

$$P_s = \frac{-Q}{I}. \quad (1.24)$$

Note that in the following chapters, I will refer to this Equation 1.24 as the degree of linear polarization (DLP).

Finally, the degree of circular polarization is defined in Equation 1.25, where parameters V and Q are not taken into account.

$$P_c = \frac{V}{I}. \quad (1.25)$$

1.3.3 Amplitude scattering matrix or Jones matrix

This thesis is interested in the scattering of an elastic wave by a particle. There are two ways of describing this phenomenon: with the amplitude scattering matrix (using the two components of the electric field) or with the scattering matrix (using the Stokes vector, see Section 1.3.4). In this study, we have access to the incident and scattered fields with our laboratory scattering measurements, thus we also have access to the amplitude scattering matrix, also known as the Jones matrix (see Section 1.5). Note that the amplitude scattering matrix **S** is known as the Jones matrix in the optical domain and the Sinclair matrix in the radar domain.

Consider a plane harmonic electromagnetic wave that is scattered by a particle. The plane between the incident direction of propagation and the scattered direction is called the scattering plane. Based on this plane, the electromagnetic incident and scattered fields can be decomposed into two orthogonal components, a parallel component and perpendicular one to the scattering plane (see Figure 1.14). Therefore, the incident electric field is:

$$\mathbf{E}_i = (E_{0\parallel}\mathbf{e}_{\parallel i} + E_{0\perp}\mathbf{e}_{\perp i})e^{(ikz-i\omega t)} = E_{\parallel i}\mathbf{e}_{\parallel i} + E_{\perp i}\mathbf{e}_{\perp i}, \tag{1.26}$$

where $\mathbf{e}_{\parallel i}$ and $\mathbf{e}_{\perp i}$ are the orthonormal basis vectors, $k = 2\pi n/\lambda$ is the complex wavenumber in the medium surrounding the object, n is the refractive index in the surrounding medium and λ is the wavelength of the incident wave. $E_{\parallel i}$ and $E_{\perp i}$ are the complex amplitudes of the incident wave. The scattered electric field, in the far field region (at a large distance r from the object, $kr >> 1$), is defined as:

$$\mathbf{E}_s = E_{\parallel s}\mathbf{e}_{\parallel s} + E_{\perp s}\mathbf{e}_{\perp s}. \tag{1.27}$$

It is important to note that $\mathbf{e}_{\parallel s}$ and $\mathbf{e}_{\perp s}$ form a different set of orthonormal basis vectors only used for the scattered wave. The complex amplitudes of the scattered wave are $E_{\parallel s}$ and $E_{\perp s}$.

Finally, the amplitudes of the incident wave and the amplitudes of the scattered wave are linearly related by the amplitude scattering matrix or Jones matrix as follows:

$$\begin{pmatrix} E_{\parallel s} \\ E_{\perp s} \end{pmatrix} = \frac{e^{ik(r-z)}}{-ikr} \begin{pmatrix} S_2 & S_3 \\ S_4 & S_1 \end{pmatrix} \begin{pmatrix} E_{\parallel i} \\ E_{\perp i} \end{pmatrix}, \tag{1.28}$$

where S_1, S_2, S_3 and S_4 are the complex elements of the amplitude scattering matrix and depend on the scattering angle θ, the distance to the source z and the distance to the detector r.

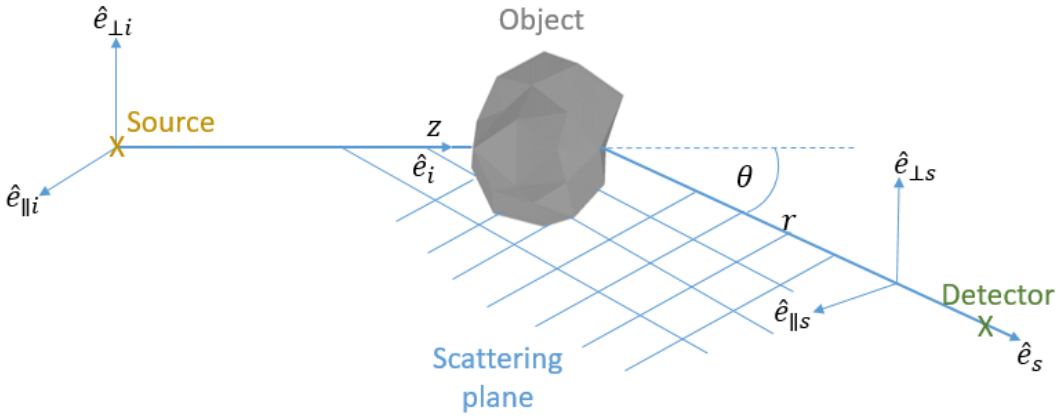

Figure 1.14: Incident and scattered electric fields described by their perpendicular and parallel components to the scattering plane [based on 84].

If the incident wave is totally polarized, parallel to the scattering plane $\mathbf{e}_{\parallel i}$, the only incident complex amplitude will be $E_{\parallel i}$. This means only the elements S_2 and S_4, from Equation 1.28, remain. In this case, two types of scattered waves can be produced: parallel $\mathbf{e}_{\parallel s}$ or perpendicular $\mathbf{e}_{\perp s}$ to the scattering plane. $S_2 E_{\parallel i}$ will be equal to $E_{\parallel s}$ producing a co-polarization and $S_4 E_{\parallel i}$ will be equal to $E_{\perp s}$ producing a cross-polarization.

Now let us suppose a totally polarized wave but this time perpendicular $\mathbf{e}_{\perp i}$ to the scattering plane. Using again Equation 1.28, two cases will be produced. The first one, $S_3 E_{\perp i}$ equals to $E_{\parallel s}$ producing a cross-polarization. The second one, $S_1 E_{\perp i}$ equals to $E_{\perp s}$ producing a co-polarization.

To summarize the two previous paragraphs, S_1 and S_2 are the co-polarized elements and S_3 and S_4 are the cross-polarized elements of the amplitude scattering matrix .

Experimentally, to obtain the amplitude scattering matrix, the amplitude and phase of the scattered waves should be measured. These measurements might be done in all directions for two incident orthogonal polarization states (i.e., horizontal (parallel) and vertical (perpendicular) polarization). This kind of measurements can be done in our anechoic chamber (see Section 1.4.1 and 1.5).

1.3.4 Scattering matrix or Mueller matrix

The other mathematical way to describe scattering is with the scattering matrix $\mathbf{S}_{(i,j)}$, also known as the Mueller matrix in the optical domain or the Kennaugh matrix in the radar domain. This matrix is obtained based on Equation 1.28 that shows the relations between the incident and the scattered waves, using the Stokes parameters shown in Equation 1.19 [79, 80]:

$$\begin{pmatrix} I_s \\ Q_s \\ U_s \\ V_s \end{pmatrix} = \frac{1}{k^2 r^2} \begin{pmatrix} S_{11} & S_{12} & S_{13} & S_{14} \\ S_{21} & S_{22} & S_{23} & S_{24} \\ S_{31} & S_{32} & S_{33} & S_{34} \\ S_{41} & S_{42} & S_{43} & S_{44} \end{pmatrix} \begin{pmatrix} I_i \\ Q_i \\ U_i \\ V_i \end{pmatrix}. \tag{1.29}$$

The elements of the Mueller or scattering matrix S_{ij} are dimensionless quantities contrary to the Jones matrix (or amplitude scattering matrix) in which its elements are complex quantities. These Mueller matrix elements can be obtained with light scattering experiments (see Section 1.4.2), but also with our microwave scattering experiment. This latter is possible thanks to the relations between the Jones matrix elements and the Mueller matrix elements that are used in this study and shown in the following equations [79]:

$$
\begin{aligned}
S_{11} &= \frac{1}{2}\left(|S_1|^2 + |S_2|^2 + |S_3|^2 + |S_4|^2\right), \\
S_{12} &= \frac{1}{2}\left(|S_2|^2 - |S_1|^2 + |S_4|^2 - |S_3|^2\right), \\
S_{13} &= \Re\left\{S_2 S_3^* + S_1 S_4^*\right\}, \\
S_{14} &= \Im\left\{S_2 S_3^* - S_1 S_4^*\right\}, \\
S_{21} &= \frac{1}{2}\left(|S_2|^2 - |S_1|^2 - |S_4|^2 + |S_3|^2\right), \\
S_{22} &= \frac{1}{2}\left(|S_2|^2 + |S_1|^2 - |S_4|^2 - |S_3|^2\right), \\
S_{23} &= \Re\left\{S_2 S_3^* - S_1 S_4^*\right\}, \\
S_{24} &= \Im\left\{S_2 S_3^* + S_1 S_4^*\right\}, \\
S_{31} &= \Re\left\{S_2 S_4^* + S_1 S_3^*\right\}, \\
S_{32} &= \Re\left\{S_2 S_4^* - S_1 S_3^*\right\}, \\
S_{33} &= \Re\left\{S_1 S_2^* + S_3 S_4^*\right\}, \\
S_{34} &= \Im\left\{S_2 S_1^* + S_4 S_3^*\right\}, \\
S_{41} &= \Im\left\{S_2^* S_4 + S_3^* S_1\right\}, \\
S_{42} &= \Im\left\{S_2^* S_4 - S_3^* S_1\right\}, \\
S_{43} &= \Im\left\{S_1 S_2^* - S_3 S_4^*\right\}, \\
S_{44} &= \Re\left\{S_1 S_2^* - S_3 S_4^*\right\}.
\end{aligned}
\tag{1.30}
$$

At the left side of the equations, there are the scattering matrix elements (or Mueller matrix elements), and at the right side, there are the amplitude scattering matrix elements (or Jones matrix elements).

In the case of a single particle, the equations defined in 1.30, from the 16 elements S_{ij}, at least 7 are independent real quantities: the 4 modules of the complex amplitudes and 3 phase differences of S_1, S_2, S_3 and S_4. This means that from the 16 equations, only 9 relations can be established. In the case of a collection of particles, the scattering matrix can be the sum of all particle scattering matrices only if coupling is negligible, otherwise interactions between them should be included. With laboratory measurements, coupling is measured, thus no approximations need to be done.

The element S_{11} in a normalized scattering matrix is known as the phase function p and represents the angular distribution of the scattered wave by an object at a given wavelength. This quantity p is related with the differential scattering cross-section dC_{sca}, which is included inside the definition of scattering cross section C_{sca} as follows [85]:

$$
C_{sca} = \int_{4\pi} d\hat{\mathbf{r}} \frac{dC_{sca}}{d\Omega}. \tag{1.31}
$$

Therefore, the phase function is [85]:

$$p = \frac{4\pi}{C_{sca}} \frac{dC_{sca}}{d\Omega}, \tag{1.32}$$

where $\frac{dC_{sca}}{d\Omega}$ should not be interpreted as a derivative but as the electromagnetic power scattered into a unit solid angle $d\Omega$ in a given direction per unit incident intensity.

The term p satisfies the following normalization condition [85]:

$$\frac{1}{4\pi} \int_{4\pi} p d\Omega = \frac{1}{2} \int_0^{\pi} p(\theta) \sin(\theta) d\theta = 1, \tag{1.33}$$

where $d\Omega$ is the differential solid angle defined as $d\Omega = \sin(\theta) d\theta d\phi$.

In terms of the amplitude scattering matrix, the phase function is:

$$p = S_{11} = \frac{1}{2} \left(|S_1|^2 + |S_2|^2 + |S_3|^2 + |S_4|^2 \right). \tag{1.34}$$

Dust particles in protoplanetary disks are supposed to be randomly oriented, thus in terms of the Mueller matrix this is equivalent as supposing particles with reciprocity and mirror symmetries. Applying these two symmetries (for more information about these symmetries see [80]), Equation 1.30 is transformed to:

$$\begin{pmatrix} I_s \\ Q_s \\ U_s \\ V_s \end{pmatrix} = \frac{1}{k^2 r^2} \begin{pmatrix} S_{11} & S_{12} & 0 & 0 \\ S_{12} & S_{22} & 0 & 0 \\ 0 & 0 & S_{33} & S_{34} \\ 0 & 0 & -S_{34} & S_{44} \end{pmatrix} \begin{pmatrix} I_i \\ Q_i \\ U_i \\ V_i \end{pmatrix}. \tag{1.35}$$

1.3.5 Scattering parameters to be studied

After considering the mentioned symmetries, there are 6 nonzero independent scattering matrix elements. Based on these elements, several scattering parameters can be defined: the phase function, the degree of linear polarization (DLP), the non-sphericity, the degree of circular polarization (DCP), and other Mueller elements normalized by S_{11}.

The phase function p is the element S_{11} of the Mueller matrix and in terms of the Jones matrix elements, it is defined in Equation 1.34. The degree of linear polarization expressed in Equation 1.24 can also be expressed in terms of Jones and Mueller matrix elements. When light is totally parallel polarized, the intensity is $I_{\parallel}$:

$$I_{\parallel} = S_{11} + S_{12} = |S_2|^2, \tag{1.36}$$

and when light is totally perpendicular polarized, the intensity is $I_{\perp}$:

$$I_{\perp} = S_{11} - S_{12} = |S_1|^2, \tag{1.37}$$

then, relating Equations 1.36 and 1.37 with 1.24, the degree of linear polarization is

($I_S = S_{11} I_i$, $Q_S = S_{12} I_i$ and $U = V = 0$):

$$P_s = \frac{-Q}{I} = \frac{I_\perp - I_\parallel}{I_\perp + I_\parallel} = -\frac{S_{12}}{S_{11}} = \frac{|S_1|^2 - |S_2|^2}{|S_1|^2 + |S_2|^2}. \tag{1.38}$$

Moreover, element S_{22} normalized with the phase function S_{11}, gives $\frac{S_{22}}{S_{11}}$, which is sensitive to the non-sphericity of a particle. Indeed, one indicator of asphericity is the degree to which the depolarization ratio ($\Delta = 1 - \frac{S_{22}}{S_{11}}$) diverges from zero. Additionally, spherical particles follow $S_{11} = S_{22}$ and $S_{33} = S_{44}$; these relations are known as the Mie symmetries [79]. Thus, these elements help to identify the presence or absence of spherical symmetries.

Furthermore, $\frac{S_{44}}{S_{11}}$ is proportional to the degree of circular polarization as shown in Equation 14.5 in [79]. Finally, $\frac{S_{34}}{S_{11}}$ is present when the particle scatters with a polarization of 45°.

1.3.6 Conclusions

In conclusion, the Mueller and Jones matrices are mathematical representations of an incident wave that is transformed into a scattered wave, after encountering an object. During this process, the wave suffers changes in its state of polarization and gives birth to the scattering phenomenon. This scattering phenomenon provides information about the encountered particle based on different scattering parameters: the phase function, degree of linear polarization (DLP), spherical symmetries, degree of circular polarization (DCP), and some other normalized Mueller matrix elements.

These Mueller matrix elements are related to the observables obtained with telescopes (scattered Stokes vectors) from circumstellar disks. Therefore, certain dust properties are encoded within the Mueller matrix and this is the kind of information we would like to analyze. However, observations are not enough to interpret protoplanetary dust properties. For this reason, it is important to explore the scattering properties of protoplanetary dust analogs with laboratory scattering measurements. Based on these measurements, different scattering parameters can be obtained and the particle shape, material and orientation can be controlled. The following section presents the different laboratory experiments that can be used to retrieve these Mueller matrix elements.

1.4 Laboratory techniques for measuring scattering parameters

There are two main ways of measuring the scattering parameters of an object which depend on the type of instrument used for producing and measuring the emitted and scattered wave. If the source is a laser and the detector is a photomultiplier, then it is the light scattering technique. If the source and detector are antennas, then it

is the microwave scattering technique. These two types of techniques are going to be discussed in this section, specifying the most relevant authors in the scattering domain and the main characteristics of both techniques.

1.4.1 Microwave scattering technique

The microwave scattering technique relies on the scale invariance rule (SIR). This rule states that analog particles can have the same scattering properties as real particles if the analog electromagnetic system has geometrical dimensions that are scaled in proportion to the incident wavelength, while keeping the same complex refractive index [12]. To respect this proportion, the use of the size parameter is essential, defined as the ratio between the particle size to the incident wavelength (defined in Equation 1.10). Thereby, if the size parameter and the refractive index are respected, then the analog has the same scattering properties as the real particles. The advantage of this rule is that real particles of different sizes that are measured with different wavelengths can be reproduced using microwaves and scaling the size of the analog compared to the real particle. Therefore, scattering observations with near-infrared or optical wavelengths of (sub)micrometer dust particles can be reproduced with this technique.

1.4.1.1 Microwave scattering experiment in SUNYA laboratory

In the 1950s J. M. Greenberg was the first to construct a microwave scattering facility in the X-band (frequency of 9.43GHz and wavelength of 3.18cm) at Sunya Laboratory in New York city. The measurements were made with an apparatus that had a Pound-stabilized klystron as the microwave source and connected to a horn-type radiator as the transmitting aperture. After the wave encountered the target, the receiving aperture was a circular parabolic reflector connected to a crystal detector and a DC-amplifier. The target was suspended in the air by thin nylon lines at a distance of 40 ft from the transmitter and 30 ft from the receiver. The X axis of the target was fixed by a synchro motor and this information was sent to the plotter or recorded, while the Y axis information was gathered by the DC-amplifier. At the end, the plotter received these two entries [86]. The following figure illustrates the experimental setup.

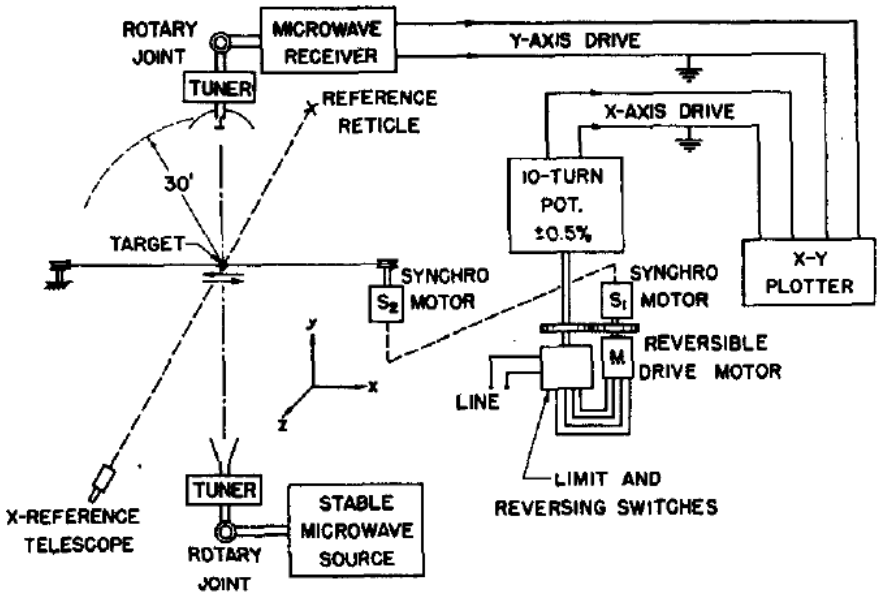

Figure 1.15: Microwave scattering setup at SUNYA laboratory [taken from 86].

The main interest of Greenberg was the scattering measurements of interstellar analog materials. He measured the scattering of different objects like spheres, spheroids and cylinders, where their sizes were at the same scale as the wavelength, for a size parameter ranging from $X = 1.25$ to $X = 5$. The analog materials were Lucite or Plexiglas representing the refractive index of silicates of approximately $n = 1.6$. The measurements were done at scattering angles ranging from 0° to 170° [86].

1.4.1.2 Microwave scattering experiment at Bochum University

Later in the 1970s R. H. Giese built a microwave scattering facility at Bochum University in the Ka-band (at a frequency of 35 GHz and a wavelength of 8.57mm). The sizes of the particles that could be analyzed were between 0.5λ to 10λ, corresponding to particles in the optical range from 0.25µm to 5µm. If there was the necessity to analyze particle sizes between 20µm to 150µm, a laser apparatus was used instead. The scattering angles were between 15° to 170° which later evolved to angles from 0° to 175° [87].

The microwave setting is shown in Figure 1.16, where the signal was produced by a phase-locker Gunn oscillator, operating at a frequency of 35 GHz. Then three branches were splitted from the transmitter, where the first was a phase reference, the second was acting as a compensation for the scattering noise and the last one was for power monitoring. The transmitting antenna was fixed while the receiving antenna could sweep all the scattering angles. Both antennas could change in different states of polarization and with four combinations between them, they could produce all the scattering matrix elements. After the phase adjustment between E_x and E_y (previously

named as $E_{\parallel}$ and $E_{\perp}$), the signal x and y could be taken, representing the real and imaginary parts of each scattering matrix element [88].

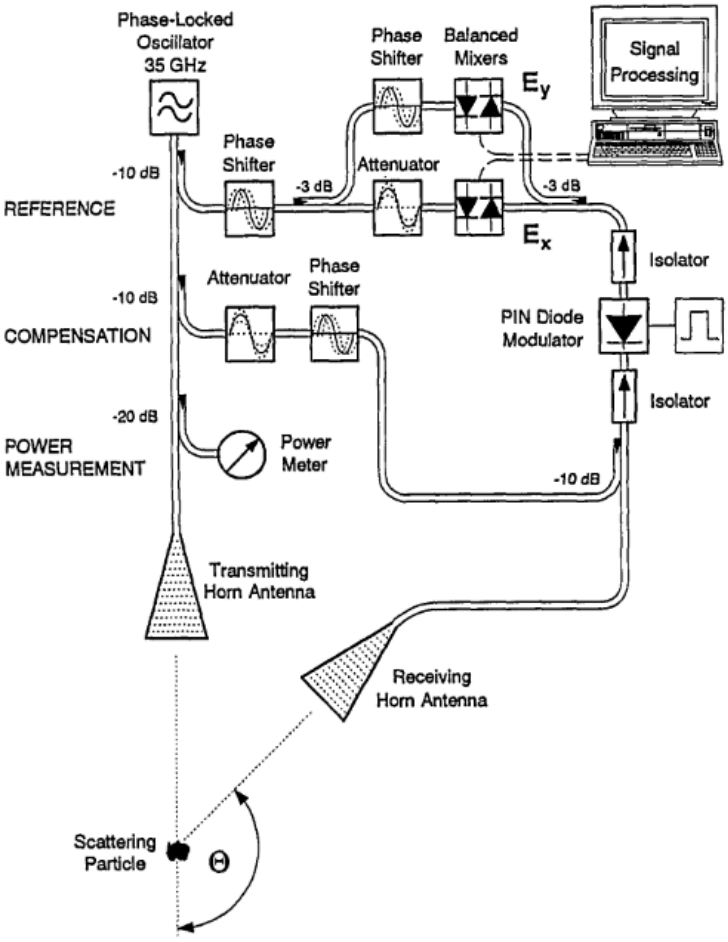

Figure 1.16: Microwave scattering setup at Bochum University [taken from 88].

Giese was interested by the study of interplanetary dust particles like dielectric and absorbing non-spherical particles (cubes, concave and convex particles) as well as fluffy [89] and compact particles. Most of his work was focused at refractive indices between $m = 1.4 - 0.05i$ to $m = 1.7 - 0.015i$ and size parameters between $X \approx 0.5$ to $X \approx 40$ [90, 89, 91, 13, 87].

1.4.1.3 Microwave scattering experiment at the University of Florida

In 1995 the microwave scattering facility at the University of Florida started being functional. Different from the other two previous facilities, this one had the possibility to work with more than just one wave, in the w-band from 75 GHz to 110 GHz (from a wavelength of 2.7 to 4 mm). The transmitting and receiving horn antennas were

connected to a Network analyzer assembly for generating the selected wavelengths and analyzing the signals. In addition, both antennas had a front Fresnel lens and a polarizer. The Fresnel lens was used to produce a planar wavefront and the polarizer was used to produce perpendicular or parallel polarization to the scattering plane. With four combinations of polarization, the intensity and phase of the waves were obtained. The receiving antenna could move all along the scattering angles from 0° to 168° [92]. Figure 1.17 illustrates the described setup.

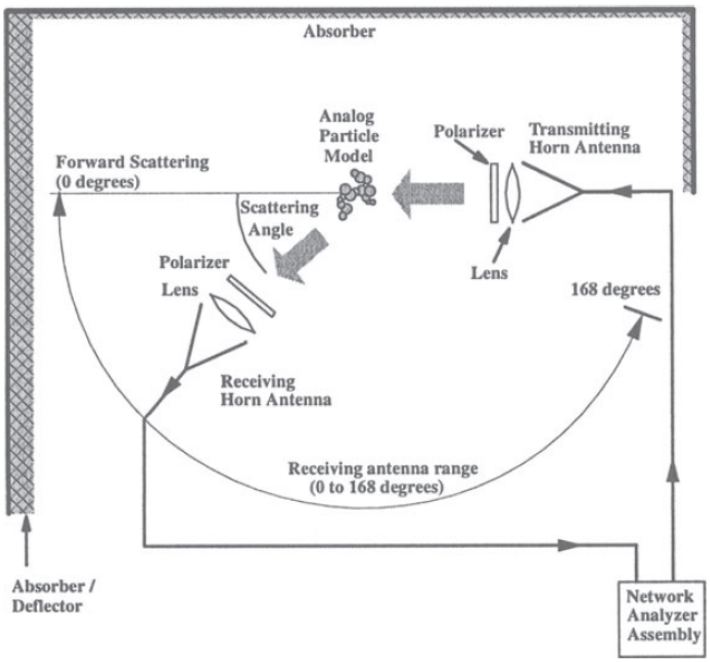

Figure 1.17: Microwave scattering setup at the University of Florida [taken from 92].

The first object model that was studied in this laboratory by B. A .S Gustafson, was the bird's nest structures which consisted of two concentric cylinders made of two different analog materials, i.e., Plexiglas and Eccofoam, representing silicate and ice. The idea was to represent aggregated interstellar grains [93]. Other materials were BK7 glass, acrylic, polysterene and nylon having refractive indices between $m = 1.61 - 0.004i$ to $m = 2.518 - 0.023i$. Different types of particle shapes like spheres, spheroids, disks and rods were analyzed [94]. Other measurements were made on inhomogeneous particles with inclusions, where the refractive index was calculated with the Mixing rule [95]. The apparatus was adapted to measure size parameter from $X \approx 0.4$ to $X \approx 200$ [96].

1.4.2 Light scattering technique

Contrary to the microwave scattering technique, light scattering technique directly measures micrometer/millimeter dust particles at optical wavelengths.

1.4.2.1 Multicolor light scattering experiment at Bochum University

At Bochum University, there was another experiment for measuring scattering properties of dust particles [87]. The experiment was based on a laser apparatus and it was known as the multicolor light scattering experiment (see Figure 1.18). The purpose of this experiment was to study larger single particles compared to the microwave scattering experiment of the same University, between $X \approx 40$ to $X \approx 300$. There were four different colours (blue $\lambda = 476\,\text{nm}$, green $\lambda = 531\,\text{nm}$, yellow $\lambda = 568\,\text{nm}$ and red $\lambda = 676\,\text{nm}$) emitted by a Krypton Ion laser. After the laser, a pockels cell was placed to turn the linear light 90° and then the light was encountered with a suspended particle (suspension by electrodynamic balance of charged particles). The scattered light was passed through a polarizing beam splitter prism which divided the two orthogonal polarized components of the scattering light. Finally, the light was detected by two photomultipliers, measuring the co and cross-polarization [87].

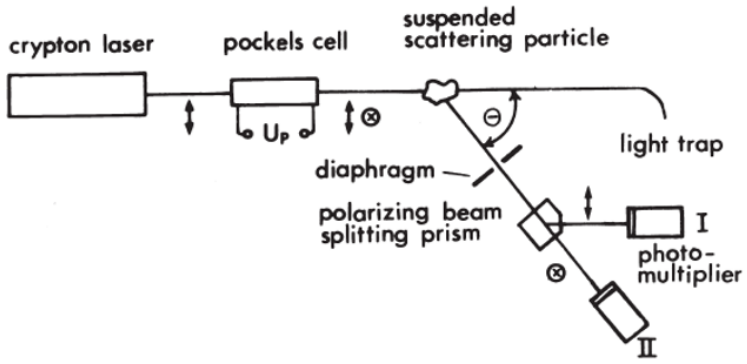

Figure 1.18: Multicolor light scattering setup at Bochum University [taken from 87].

The main idea with this setup was to analyze the effect of different wavelengths (or colors) on the same particle to identify different scattering informations of the object, as the wavelength is affected by different size details of the target.

Additionally, another light scattering experiment was the photopolarimeter for rapid particle analysis (see Figure 1.19). Composed of a laser and a half-wave plate to change the polarization, the particle was by four sensors. The first one was positioned at 5° for the forward scattering intensity to determine the size, the second and third ones were at 90° measuring the co and cross scattered components, and finally, the last sensor was at 175° to measure the backscattering.

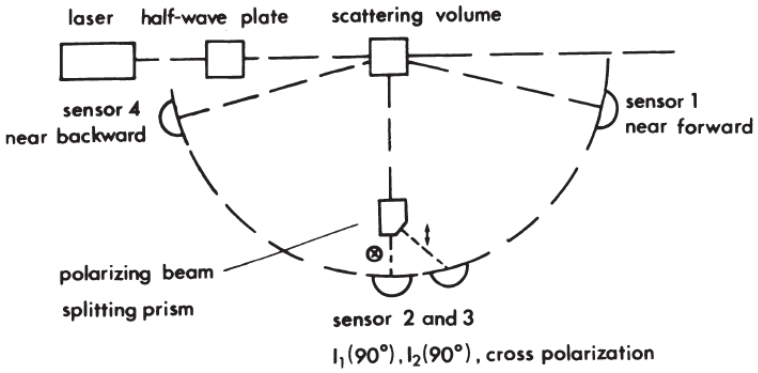

Figure 1.19: Photopolarimeter setup at Bochum University [taken from 87].

1.4.2.2 Scatterometer at the University of Helsinki

At the University of Helsinki, K. Muinonen has been studying and using the discrete-dipole approximation (DDA) which is a wave optics method for simulating the electromagnetic scattering of different particle shapes that can be anisotropic and/or inhomogeneous. For comparing the simulation results, his group has developed an scatterometer (see Figure 1.20) which measures scattered light at different wavelengths, for particles in the micrometer to millimeter size scale. The instrument is composed of several photomultiplier tubes used as detectors, a ultrasonic levitator for the samples and a Argon-krypton laser as the light source, which includes 12 different wavelengths from 465 nm to 676 nm. Measurements are performed in the azimuthal angle around 360°, except from 11° to −11° which is a dead zone [97]. In this previous study, two measurements are presented, the calibration sphere ($r = 2.5$mm) which is a big sample for the levitator so it is measured in a fixed position at a wavelength of 514 nm ($X \approx 30560$) and a Chelyabinsk LL5 chondrite particle ($X \approx 12224$) measured in the levitator.

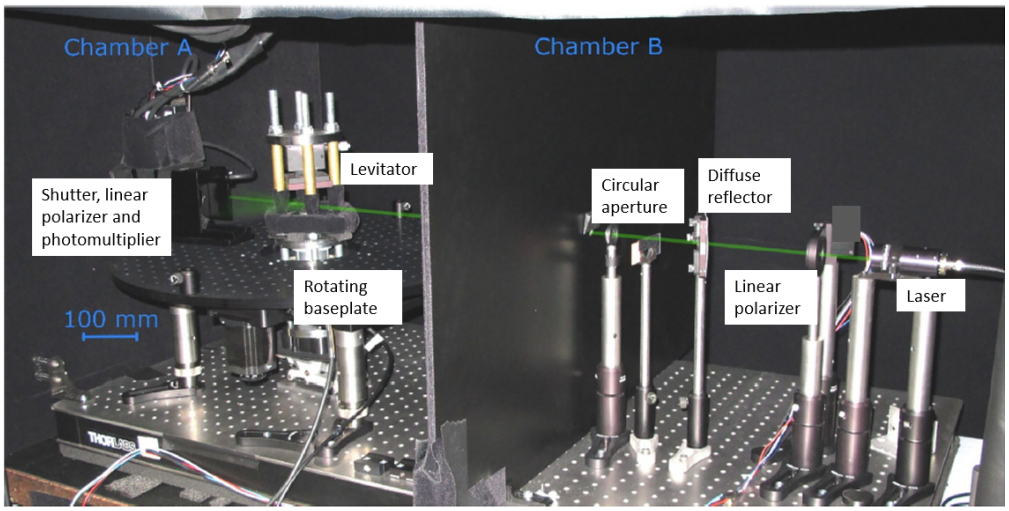

Figure 1.20: Scatterometer setup at the University of Helsinki [taken and modified from 97].

One of the main light scattering studies of K. Muinonen is about internal inhomogeneities and surface roughness of large cosmic dust particles with samples of hematite, white clay and water ice (with refractive indices from $m = 1.6 + 0.00001\,i$ to $m = 3 + 0.01\,i$), which are materials that can be found on Mars, comets and asteroids [98]. Other studies are on the reflectance spectra of meteorite samples [99], where the main components are olivine, pyroxene and iron (materials that are also found in chondrites). As well as, studies of space weathering effects of olive grains with nano inclusions performed with the reflectance spectra [100].

In general, this group is mainly interested in the study of interplanetary and dust particles, using different methods like DDA and the scatterometer instrument which later evolved into the 4π Scatterometer [10] and ray optics codes for the reflectance.

1.4.2.3 Amsterdam light scattering experiment at the University of Amsterdam

In the 1980s a light scattering setup was built at the Astronomical Institute of the University of Amsterdam in J. W. Hovenier's group. During the existence of this experimental setup, there was also the creation of the Amsterdam Light Scattering Database in 1989. Nevertheless, the experiment was closed in 2009, as well as the database [8].

This apparatus was based on the device developed by Hunt and Huffman presented in [101]. It worked with two types of lasers, an He-Ne laser (λ = 632.8nm) and an He-Cd laser (λ = 441.6nm). Then light was passed through a polarizer (P) and an electro-optic modulator (EOM). After this, light encountered randomly oriented particles produced by an aerosol jet stream and scattered light was passed through a quarter-wave plate (Q), an analyzer (A) and finally it was detected by a photomultiplier (that could measure around the scattering angles from 5° to 173°). The ensemble of modulator plus lock-in amplifier was used to retrieve all the elements of the scattering

matrix. Additionally, a monitor was used to correct variations of the aerosol stream [102] (see Figure 1.21).

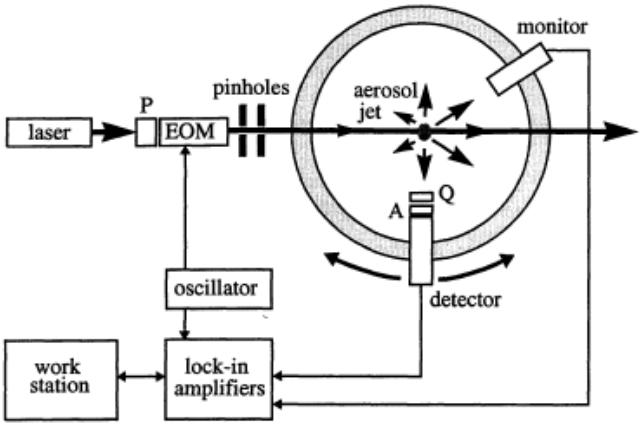

Figure 1.21: Light scattering setup at the Astronomical Institute of the University of Amsterdam [taken from 102].

Different studies were made thanks to the measurements performed with this instrument in the micrometer range scale with size parameters between $X \approx 8$ to $X \approx 163$ [for more information see 103]. One of their research works was on mineral terrestrial aerosol particles (feldspar, red clay, quartz, loess, Pinatubo and Lokon volcanic ashes, and Sahara sand with refractive indices between $m = 1.5 + 0.00001\,i$ to $m = 1.7 + 0.001\,i$) with sizes between 0.1µm to 100µm of diameter. The objective was to analyze the light scattering properties of different sizes and complex refractive indices of irregular particles. The experimental results were compared with simulations (ray optics methods using Gaussian random shapes for representing the minerals) and in general there was a good agreement between measurements and computations. Moreover, even if the study was about terrestrial minerals, in the discussion, they presented the importance of their results for astronomical objects (which are also composed of silicates), specifically circumstellar dust shells [102]. Others subjects of interest were the light scattering properties of aerosols, volcanic ashes, planetary atmospheres and cosmic dust particles.

1.4.2.4 Granada light scattering experiment in the Instituto de Astrofísica de Andalucía

The Granada light scattering setup known as IAA setup was built at the Instituto de Astrofísica de Andalucía. The device was based on the Amsterdam light scattering instrument that was explained in 1.4.2.3 but with several improvements. The upgrades are: i) the blockage of the laser beam in backward and forward directions, allowing a larger scattering angle range ($3° - 177°$), ii) corrections in the background signals, producing better measurements at small and big scattering angles iii) and finally, light

source change for a tunable argon-krypton laser, having 5 different wavelengths (483, 488, 520, 568 and 647 nm) where size parameters are from $X \approx 20$ to $X \approx 380$ [for more information see database https://www.iaa.csic.es/scattering/ which is the fusion between the Amsterdam database and Granada database 103].

The IAA apparatus emits light with a linearly polarized continuous-wave tunable argon-kripton laser, then light passes through a filter wheel (FW), polarizer (p) and electro-optic modulator (M). Light is scattered by the target particles that are ejected by a nebulizer (for water droplets) or an aerosol generator. Later, scattered light passes thought a quarter-wave plate (Q) and an analyzer (A) and then it arrives to a photomultiplier detector (PM). This last instrument helps to produce left and right circular polarizations which together produce unpolarized light. The monitor is also a photomultiplier tube but it is used to correct the variations in the aerosol stream (see Figure 1.22). It is important to know that the optical components are positioned at special angles to polarize light and produce all the scattering matrix elements [104].

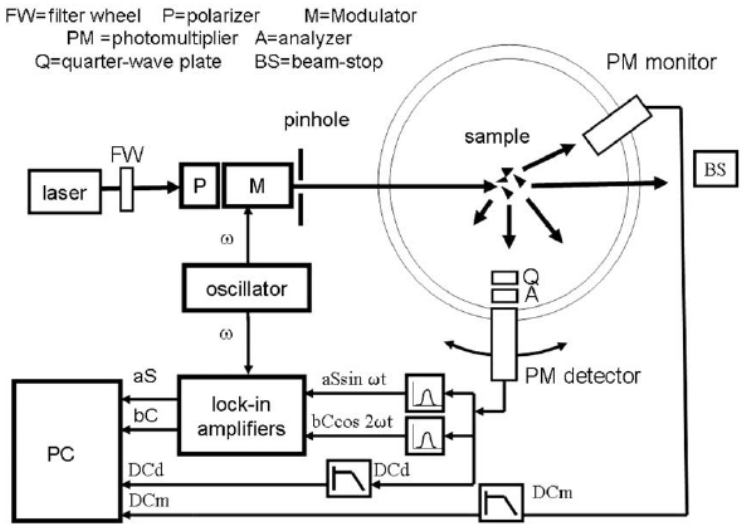

Figure 1.22: Granada light scattering setup at the Instituto de Astrofísica de Andalucía [taken from 104].

One of the main research subjects of this group is the scattering properties of cosmic dust particles. In [105] two kinds of irregular particles were studied, both with high refractive indices: hematite ($m = 3.0 + 10^{-1}i$ to $3.0 + 10^{-2}i$) which is a material that is found in Mars and rutile ($m = 2.73 + 0i$) which is present in oxygen-rich circumstellar shells. In [106], light scattering measurements were performed for fluffy aggregates composed of magnesiosilica, ferrosilica and alumina which are cosmic dust that can be found in circumstellar and interplanetary environments.

Also in [107], measurements of the phase function were done for three irregular millimeter-sized cosmic dust grains: enstatite, quartz and volcanic material (from Mount Etna). At side and backscattering angles, enhancements of the phase function

were found for these particles. These enhancements were also found in the phase function of the Fomalhaut and HR 4796A dust rings.

Moreover, in [108], the phase function and degree of linear polarization of four carbonaceous chondrites, two silicate minerals and one organic powder (with sizes ranging from sub-microns to hundreds of microns) were studied, these samples being analogs of cometary dust. Finally, in [9], the study of the phase function and the degree of linear polarization of three millimeter compact cosmic dust analogs was presented, the analogs being charcoal, Mg-Fe aluminiosilicate and quartzite.

The previous papers are some of the examples of the studied cosmic dust particles or analogs that have been measured by this group with refractive indices between $m = 1.54 + 0i$ to $m = 3 + 0.1i$.

1.4.2.5 PROGRA2 experiment

The PROGRA2 experiment, acronym that stands for Propriétés Optiques des Grains Astronomiques et Atmosphériques, in english Optical properties of astronomic and atmospheric grains, started operating in 1994. The PROGRA2 experiment was created by two french universities LPC2E and LATMOS, where the scientific director is Jean-Baptiste Renard. This experiment was made to perform polarimetric measurements of clouds of particles that are in the submicrometer and micrometer range at different wavelengths and of any composition (see database in https://www.icare.univ-lille.fr/progra2/). Three different setups are used:

1. PROGRA2 in levitation: the particles are lifted by an air draught inside a vial (that is in a rotating plataform) where a laser (source) points inside. Usually the particles float with random movements from 1 second to tens of seconds. The laser can be in the visible wavelength range, thus the setup is called PROGRA2-VIS, using two wavelengths λ = 543.5nm and λ = 632.8nm. Or the setup is called PROGRA2-IR, using a laser in the infrared range $\lambda = 1.5 - 1.6$µm. After the light encounters the cloud of particles, the scattered light goes to a beam-splitter separating the parallel and perpendicular scattered components, both components being collected by two CCD cameras. These two cameras are fixed at 90° one from the other, hence, the platform that contains the vial is in charge of rotating the sample for measuring at different phase angles from $\alpha = 5°$ to 165° (where α is the phase angle and it is related to the scattering angle θ as follows $180° - \alpha = \theta$). With this collected data, the polarization of the scattered light can be extracted, yet not the phase function. For the phase function, a third camera is needed as a reference to obtain the scattered light in the vial at the same phase angle (fixed at $\alpha = 90°$). Hence, the phase function is derived by the addition of the parallel and perpendicular scattered components and divided by the reference leading to results in arbitrary units without the need of an absolute calibration [11]. The PROGRA2 setup is shown in Figure 1.23.

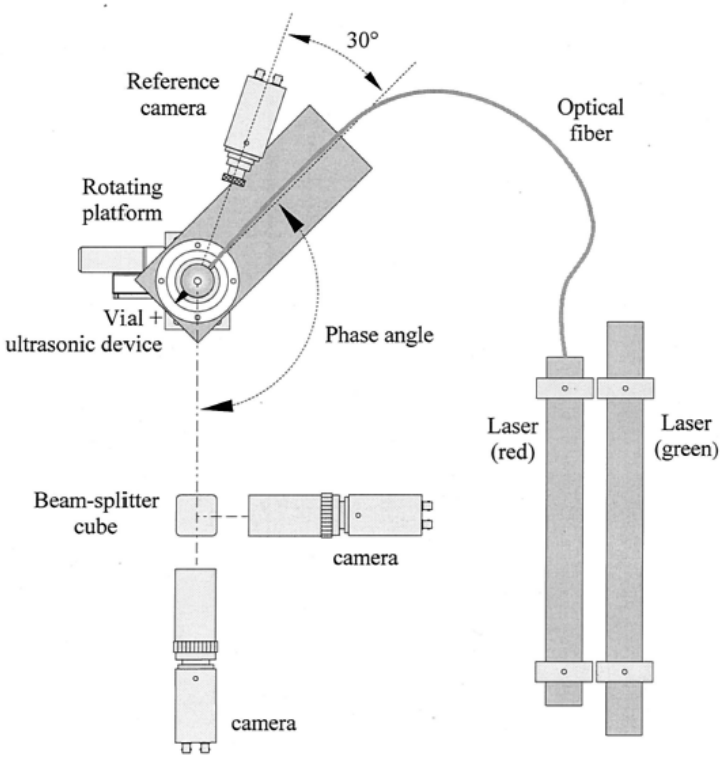

Figure 1.23: PROGRA2 setup at visible wavelengths [taken from 11].

2. PROGRA2 in microgravity: the particles are lifted with parabolic flights having a microgravity phase of approximately 22 seconds where they can float with random movements. The experimental setup is the same as presented in Figure 1.23, the only difference being the type of vial. For microgravity experiments, a vacuum-vial is used (see Figure 1.24). This setup is specific for large samples that can not be suspended with air levitation (particle diameter> 20µm), while with air levitation, it is adapted for fluffy aggregates or lightweight particles.

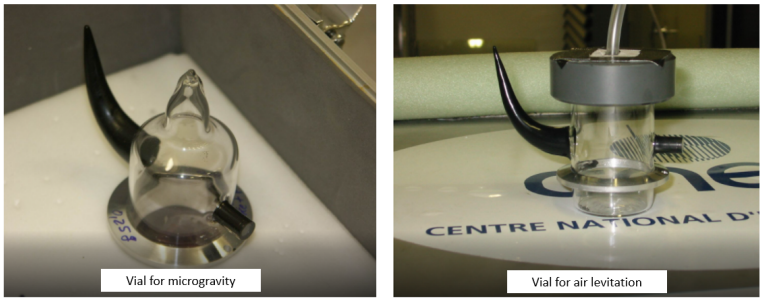

Figure 1.24: PROGRA2 vials [taken and modified from PROGRA2 database].

3. PROGRA2-SURF experiment: this experiment is adapted to measure grains that

are deposited in layers (type of deposition: random ballistic deposition). The setup (see Figure 1.25) is composed of a laser that works in the visible range at $\lambda = 543.5$nm and $\lambda = 632.8$nm. The laser is connected to an optical fiber and this fiber is fixed to a rotating arm. After the laser beam encounters the sample, a beam-splitter divides the two scattered components that are collected by two CDD cameras. The beam-splitter and the two cameras are also fixed on a rotating arm, measuring from a phase angle of 6° to 140°- 160° [109].

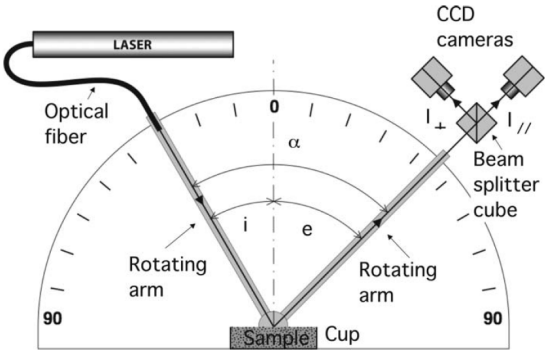

Figure 1.25: PROGRA2-surf setup [taken from 109].

In general, the images that are taken by the PROGRA2 cameras are used to build the intensity and the polarization maps pixel by pixel. This imaging allows to measure the polarization coming from individual grains, dense clouds, aggregates and groups of aggregates. The size parameters of the particles that can be measured by PROGRA2 are: for aggregates around $X = 5-11560$, for constituent particles $X = 0.14-5.7$ and for deposited particles $X = 49645-115605$. The main subject of research of this group is interstellar dust particles (cometary/asteroidal analogs, lunar analogs, mars analogs), earth atmosphere (different kinds of soots, volcanic ashes) and other atmospheric dust particles (e.g., Titan's atmosphere), which include morphologies like aggregates or grains (rough particles) and materials like alumina, silicates (enstatite, forsterite) and others minerals mixed with carbons (refractive indices ranges from $m = 1.11 + 0.08i$ to $m = 2 + 1i$) [110, 111, 112, 113, 109, 114].

1.4.3 Summary

Table 1.1 presents a general comparison between the microwave and light scattering laboratory techniques that measure scattering quantities in order to infer the scattering properties.

The microwave scattering technique has two main advantages. First, it can gather the amplitude and the phase of the scattered wave, offering more information of the scattering phenomenon than just the intensities. Second, the wavelength range is

	Light scattering technique	**Microwave scattering technique**
Measurement (scattering quantities)	Measurements of the Mueller/scattering matrix elements that are related to the intensities of the scattered wave.	Measurements of the the Jones/amplitude scattering matrix elements that are related to the amplitude and the phase of the scattered wave.
Size of the setup	Distance from the detector to the sample is of the order of centimeters.	Distance from the detector to the sample is of the order of meters.
Wavelength range	Measurements are done with one or few visible wavelengths depending on the laser.	Measurements are done with antennas so there is a large range of wavelengths that can be used.
Target positioning system	The targets are lifted in randomly orientation thanks to different systems (e.g. acoustic levitation, aerosol jet stream, microgravity). Additionally, some setups have also a pedestal to measure in fixed positions or controlled acoustic levitator.	The targets are positioned in a stable oriented system. In order to obtain a randomly oriented particle, the target position has to be changed as many times as necessary.
Target size	Micrometer to millimeter.	Millimeter to centimeter.
Target size parameter	$10 \lesssim X \lesssim 10000$ Geometric and part of Mie scattering range. Advantage of having a larger size parameter range.	$0.5 \lesssim X \lesssim 200$ Mie scattering range.
Target material	Refractive indices $1.1 < n < 3$ and $0.00001i < k < 1i$	Refractive indices $1.4 < n < 2.5$ and $0 < k < 0.25i$

Table 1.1: Comparison between light scattering and microwave scattering techniques.

larger thanks to the fact that measurements are performed with antennas. On the other hand, the light scattering technique has a smaller experimental setup size and particles can be measured in random orientation and in some cases, in fixed position, which is an advantage compared to the microwave scattering technique that can only perform measurements for a fixed target position. However, if measurements need to be performed in a fixed position, the microwave scattering technique appears more accurate. Both techniques can measure different target sizes, thus different scattering regimes, and different target materials, depending on the final application, yet the light scattering technique can measure a larger size parameter range.

As can be seen, both techniques have advantages and disadvantages. Thus, these techniques give complementary scattering information. However, if the objective is to understand the scattering properties of specific controlled geometric structures in a wide range of wavelengths, the best compromise is to use the microwave analogy (microwave scattering technique) with 3D printed particles (centimeter-sized particles). This is a unique possibility that can be achieved with our laboratory experiment. The details of the experimental setup and how measurements are performed is explained in the following section. Additionally, the realizations of our dust analogs by 3D printing are explained in Chapters 2 and 3, depending on the sample type.

1.5 Microwave scattering experiment at CCRM

Our measurements are performed in the anechoic chamber of Centre Commun de Ressources en Micro-Ondes (CCRM) in Marseille. This anechoic chamber is in a Faraday cage where different microwave devices allow the generation, transmission and reception of microwave signals. This section is focused on the description of the anechoic chamber facility, setup and the steps to perform the scattering measurements.

1.5.1 Anechoic chamber facility

The anechoic chamber facility was built in 1996 in Marseille. The whole structure is inside a Faraday cage of dimensions 14.5m x 6.5m x 6.5m to shield the interior from external electric fields. This way, measurements are not perturbed by external sources. Inside the chamber, there are pyramidal absorbing foams that attenuate at least 40 dB for frequencies equal or greater than 1 GHz (see Figure 1.26).

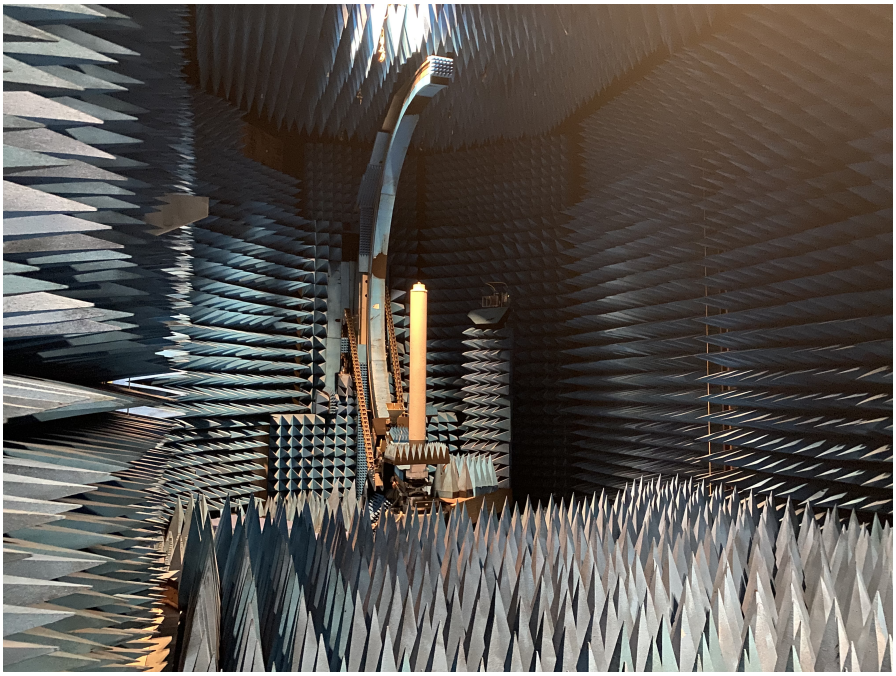

Figure 1.26: Photo of anechoic chamber CCRM.

This anechoic chamber is equipped with microwave devices that can perform measurements at wavelengths between 100 mm to 7.5mm (frequencies between 3 GHz to 40 GHz), but for this study wavelengths will be selected between 100 mm to 16.7mm (frequencies between 3 GHz to 18 GHz).

1.5.2 Experimental setup

In order to perform measurements, several microwave devices are needed for the generation, the transmission and the reception. First, for the generation, a reference synthesizer (R&S SMB100A) generates a continuous wave signal of frequency $F_B = 1$ to 18 GHz. Second, the signal propagates into a coaxial cable to a reference coupler. This coupler delivers the transmitting signal to the transmitting antenna (DRG horn antenna) and also to the 20 dB attenuator. The coupler and the attenuator guarantee an attenuation of 40 dB so the signal can be delivered to the reference mixer (NSI-RF-5945), without damaging this latter with high amplitude signals. The reference mixer scales the reference signal (RF) from GHz to an intermediate frequency (IF) of 20 MHz. This scaling is possible thanks to a local oscillator synthetizer (R&S SMB100A), producing a local oscillation frequency $F_{LO} = F_B - 20\,\text{MHz}$. The local oscillation frequency is transmitted to the mixer through a Digital Frequency Converter (DFC). That way, the IF signal named a_1 that was generated by the transmitting mixer is transmitted to the Vector Network Analyzer (VNA, R&S ZNB4) through the DFC.

Third, for the reception, the receiving antenna (DRG horn antenna) detects the signal and a coaxial cable sends the signal to the test mixer (NSI-RF-5945). This mixer

does exactly the same as the transmitting mixer but for the received signal. After mixing the received signal and combining it with the one from the oscillator, a test signal b_2 is transmitted to the VNA. The VNA calculates the ratio $\frac{b_2}{a_1}$ in amplitude and phase (see Figure 1.27 for the setup of the devices at CCRM). All these devices allow to perform measurements between 2 GHz to 18 GHz [for more information see 115].

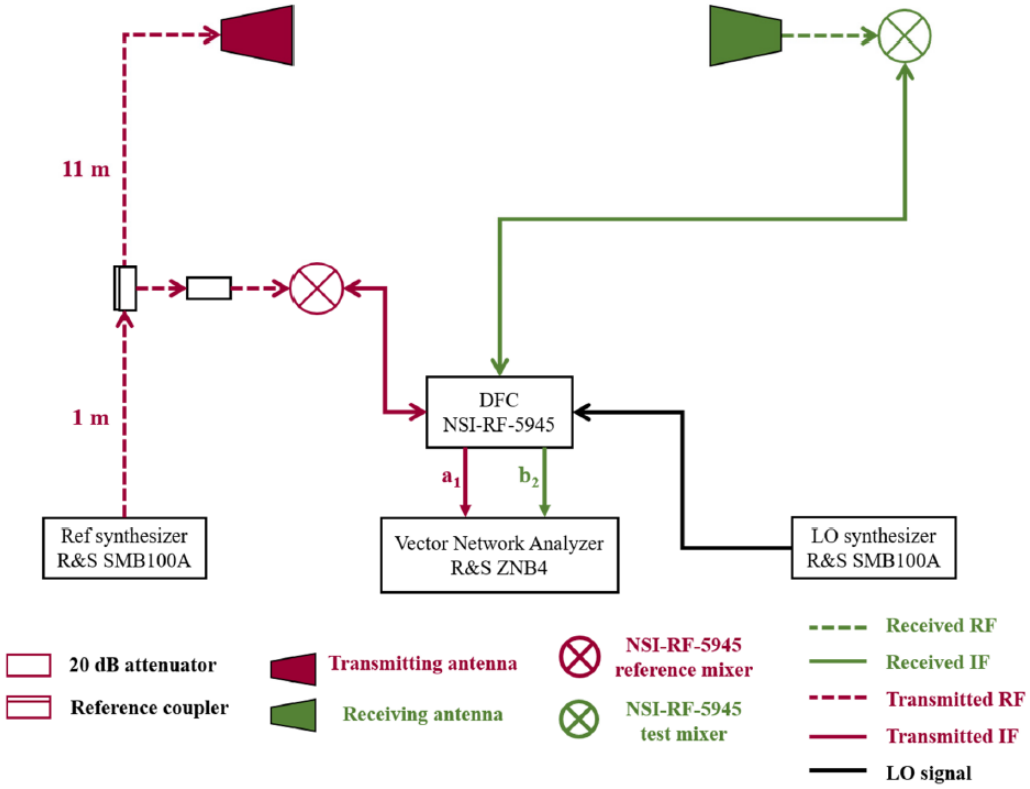

Figure 1.27: Setup of microwaves devices at CCRM [taken from 115].

Emitting and receiving antennas are both linearly polarized and used at the same states of polarization, horizontal and then vertical. Two types of configurations are used during measurements: forward and backward configuration which corresponds to scattering angles (θ) from 0° to 130° with the horizontal arrangement (see Section 1.5.2.1) and from 120° to 168° with the vertical arrangement (see Section 1.5.2.2), respectively [116].

1.5.2.1 Forward scattering zone

Each sample is laid on a expanded polystyrene mast (transparent material for the used wavelengths) that can be 360° rotated all around its symmetry axis. Furthermore, each sample can be placed on the mast at different positions, giving thus other orientations. For one chosen position, the receiving antenna is moved in the forward zone from $\theta = 130°$ to $-130°$ in the scattering plane and then the polystyrene mast (on which

the sample is placed) turns 10° to restart the receiving antenna measurements. The emitting antenna is always positioned at the same place pn the vertical arrangement at $\Phi = 90°$ (see Figure 1.28).

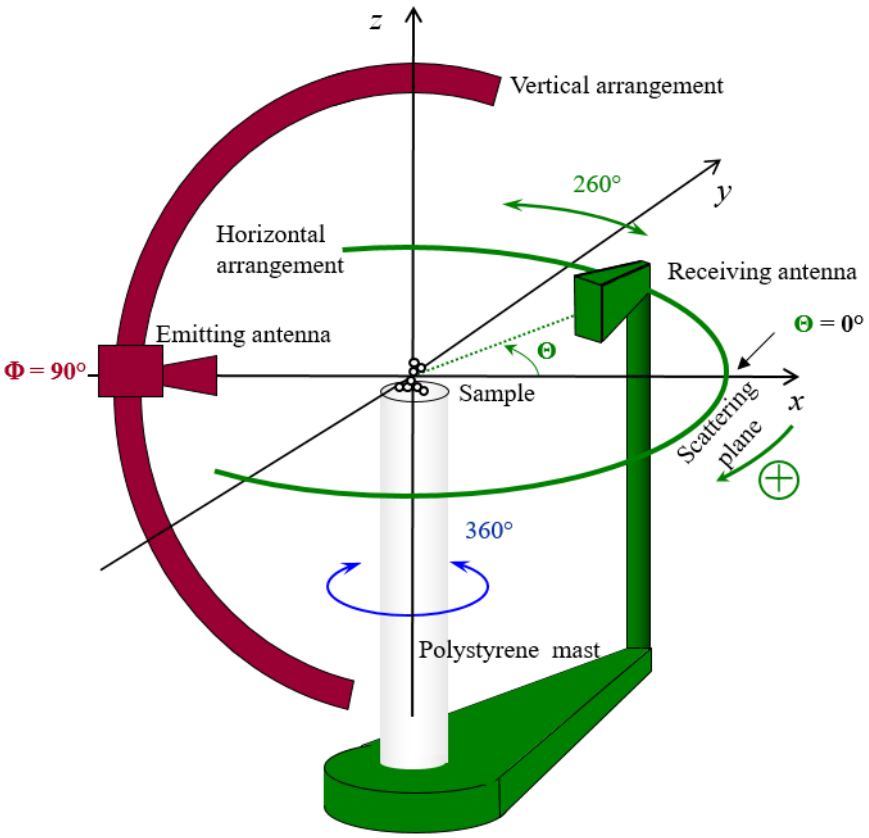

Figure 1.28: Forward experimental setup where the emitting antenna is fixed at the vertical arrangement while the receiving antenna moves on the horizontal arrangement [taken from 117].

1.5.2.2 Backward scattering zone

The samples are similarly laid on a polystyrene mast that turns all around its symmetry axis, as for the forward scattering zone. The difference is only in the position of the receiving antenna. In this case, the emitting antenna is placed at the same point on the vertical arrangement but the receiving antenna is moved through the vertical arrangement (from $\Phi = -11°$ to $\Phi = 78°$ and from $\Phi = 102°$ to $\Phi = 168°$ backward zone) for each 10° of rotation of the polystyrene mast (see Figure 1.29).

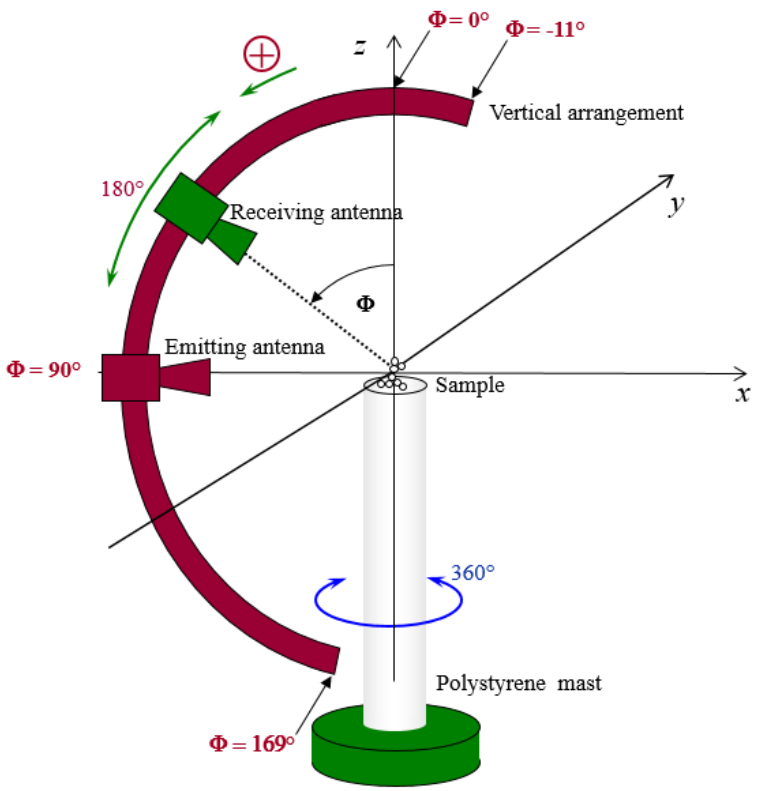

Figure 1.29: Backward experimental setup where the emitting antenna is also fixed while the receiving antenna moves on the vertical arrangement [taken from 117].

1.5.3 Measurements

The receiving antenna measures two different complex transmission coefficients to finally obtain the scattered field: the first one, where there is no sample, the second one, in presence of a sample. Measurements are later calibrated with a metallic sphere measurement, turning the transmission values into incident field values $\mathbf{E_i}$ (without the sample) and total field values $\mathbf{E_t}$ (with the sample). This calibration considers an illumination of magnitude 1 and phase 0° at the center of the sample. After obtaining the electric fields, drift errors are treated with a drift correction procedure [118, 119] applying a complex correction coefficient to the total field, and so the subtraction between the total field and the incident field is made, giving the scattered field, $\mathbf{E_s} = \mathbf{E_t} - \mathbf{E_i}$.

Additionally, another post-processing is applied, an angular low pass filter [119], which uses the deduction of the spatial bandwidth of the scattered field with two elements: the wavelength and the bounding sphere of the sample. Indeed, in [119] is demonstrated that the angular spectrum of the Fourier transform of the scattered field cannot be more than $X^2/2$, where X is the sample size parameter that depends on radius of the bounding sphere and the used wavelength. Thus, signals larger than

$X^2/2$ are cut off. Finally, once the post-processed scattered values are obtained, the average intensities (average over the different orientations of the sample) of the Jones matrix elements can be calculated. Knowing that the antennas are configured either in horizontal or vertical polarization, the only two Jones matrix elements that can be calculated are the co-polarized elements, S_1 and S_2. These two elements, expressed in terms of Mueller matrix elements, give the possibility to calculate different scattering parameters, e.g., the phase function, degree of linear polarization, and others that are specific depending on the type of sample.

The main assumptions for our measurements are:

1. The host media is supposed to be homogeneous, isotropic and non-absorbing.
2. The incident wave is a time-harmonic locally plane electromagnetic wave and quasi-monochromatic.
3. Elastic scattering: the frequency of the incident wave is the same as the scattered wave.
4. The composition of the sample is assumed to be stated in macroscopic terms.

It is important to note that the CCRM setup is able to do other type of measurements, i.e., radar cross section measurements, that are not specified in this study but is an advantage to determinate other characteristics like the inner structure of a sample. For example, radar measurements in CCRM of an analog of Itokawa asteroid can give information of its inner structure [120].

1.6 Numerical simulations

In order to compare measurements with numerical simulations, our group has developed two homemade codes based on two rigorous methods: Finite Element Method (FEM) [15] and Method of Moment (MoM) [121].

These codes have been compared to other methods like the superposition T-Matrix method [122] and DDA [123]. In [121], measurements and numerical methods such as the superposition T-matrix method, DDA and MoM were compared in amplitude and phase of the scattered field for an aggregate, giving comparable results for different frequencies or wavelengths. Furthermore, in [115], measurements and numerical simulations of the scattered field of spheroids in T-matrix and FEM gave also equivalent results in terms of intensity and phase. These results proved the validation of our simulation methods compared to other models and our measurements.

For the FEM, the weak form of the vectorial Helmholtz equation is used to compute the electromagnetic field. A scattered field formulation is implemented and the electric field is discretized onto basis functions associated to edges of tetrahedrons, resulting from unstructured mesh of the domain [15]. With a discretization of an order of $\lambda/10$, $2\text{x}10^6$ degrees of freedom (DOF) can be typically obtained. The sparse linear

system obtained is solved thanks to dedicated sparse linear solvers like MUMPS in [124] or Pardiso in [125]. The scattered far-field is then computed (for all the scattering angles and wavelengths) with the help of a classical near-field to far-field transform.

On the other hand, the MoM solves the observation equation which is a 3D integral involving: the free-space dyadic Green function, the contrast, which is the difference between the square of the wave number at a determined point and the square of the wave number in vacuum, and the total field. Then the field inside the object, which is expressed as the addition between the incident field and some coupling terms, is computed (for all the scattering angles and wavelengths) with the coupling equation [121]. It is numerically resolved with a 1D-FFT-method, exploiting the block-Toeplitz structure of the free-space dyadic Green function [120].

In conclusion, with the microwave scattering experiment at CCRM and numerical simulations (FEM and MoM), we can obtain the scattered field of a chosen sample having the Jones matrix elements and thus the Mueller matrix elements, and for this specific study, at 16 different wavelengths from $\lambda = 16{,}7\,\text{mm}$ to $100\,\text{mm}$ (frequencies between $18\,\text{GHz}$ to $3\,\text{GHz}$). Measurements can be done in two scattering zones, retrieving scattering information about the sample from $\theta = 0°$ to $168°$. On the other hand, FEM and MoM simulations can retrieve all the scattering information for angles up to 180°.

The specific sizes and materials of samples depend on the application, in this case, protoplanetary dust, sizes and materials are going to be discussed in the following section.

1.7 Microwave analogy of protoplanetary dust

As previously explained in Section 1.4, the microwave analogy relies on the scale invariance rule (SIR). Thereby, the size parameter and the refractive index of the real particle should be conserved in order to have the same scattering properties for the analog particle (see Figure 1.30 for an example of a real particle of size a and its analog particle that has been multiplied by a factor f in size, fa, and incident wavelength, $f\lambda$, while conserving the same refractive index).

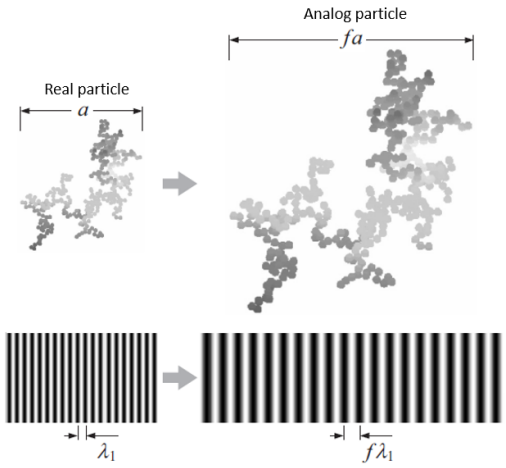

Figure 1.30: Scale invariance rule [taken and modified from 85].

It should be noted that the scaling can be applied to produce larger analogs as it is the case for the previous example or smaller analogs, for example centimetric analogs of trees [115].

1.7.1 Size analogy

In the case of protoplanetary dust, we suppose that dust particle sizes are at orders of sub-micrometers to micrometers (radius from $r_{real} = 0.1\mu m$ to $r_{real} = 10\mu m$) and that the scattered waves are observed in the optical, NIR and millimetric wavelength ranges (see Section 1.2.3 for more information). This means that the size parameter of dust particles ranges from $X_{min\_real} = 0.0002$ to $X_{max\_real} = 157.08$, see Table 1.2.

Dust radius (μm)		**Wavelengths** (μm)			**Size parameter**	
r_{min}	r_{max}	Range	λ_{min}	λ_{max}	X_{min}	X_{max}
0.1	10	Millimetric	300	2600	0.0002	0.21
		NIR	1	2.5	0.25	62.83
		Optical	0.4	0.7	0.90	157.08

Table 1.2: Parameters of protoplanetary dust.

Based on Table 1.2, if we respect the maximum and minimum size parameters, and knowing that with the anechoic chamber we can measure objects with size of the order of centimeters (from $r_{analog} = 1\,cm$ to $r_{analog} = 20\,cm$), then the wavelengths that should be used in the anechoic chamber, in order to measure all the sizes of protoplanetary dust, are from $\lambda = 0.4mm$ to $\lambda = 6.28 \times 10^6 mm$ (frequencies between $4.7 \times 10^{-5} GHz$ to $750\,GHz$). However, as it was previously mentioned, the maximum wavelength range of CCRM setup is from $\lambda = 7.5mm$ to $\lambda = 100\,mm$ (frequencies between $40\,GHz$ to $3\,GHz$), meaning that with our setup we can cover size parameters

from $X_{min\_analog} = 0.6$ to $X_{max\_analog} = 167.6$, which is a large range of the protoplanetary dust size parameter (see Table 1.3). Notice that these different size parameters can be achieved with the different wavelengths but also with 3D printed analogs of different sizes, which is the advantage of using the microwave analogy together with the 3D printing or additive manufacturing.

Dust radius (mm)		**Wavelengths (mm)**		**Size parameter**	
r_{min}	r_{max}	λ_{min}	λ_{max}	X_{min}	X_{max}
10	200	7.5	100	0.63	167.6

Table 1.3: Parameters of protoplanetary dust analogs that can be achieved with CCRM setup.

For this current study, measurements are performed at a smaller wavelength range than what can be achieved with the CCRM setup. Measurements are at wavelengths of $\lambda = 16.7$mm to $\lambda = 100$ mm (frequencies between 18 GHz to 3 GHz) and in general 3D printed dust analog sizes are of orders of $r_{analog} = 1$ cm to $r_{analog} = 10$ cm. Thus, analog parameters for this specific study are presented in Table 1.4.

Dust radius (mm)		**Wavelengths (mm)**		**Size parameter**	
r_{min}	r_{max}	λ_{min}	λ_{max}	X_{min}	X_{max}
10	100	16.7	100	0.63	37.62

Table 1.4: Parameters of protoplanetary dust analogs for this specific study.

1.7.2 Material analogy

The composition of protoplanetary dust is mainly silicates and in lower percentages ice, carbons and other minerals (explained in Section 1.2.3). In order to make a microwave analogy, the complex refractive index ($m = n + ik$) must be kept the same, meaning that if the protoplanetary dust is observed at a certain wavelength, the analog must have the same refractive index at the wavelength of the microwave devices.

I made a bibliographical study in order to summarize the refractive indices of silicates, ice and carbon. Figure 1.31 shows the different materials with their corresponding refractive indices, real and imaginary parts (for permittivity see Figure 1.32). Three different types of materials are presented: first, analog materials used in laboratory scattered measurements; second, natural materials from samples found in Earth and used as analogs for laboratory scattered measurements or simulations; third, astronomical materials where their refractive indices have been accepted by the astronomical community and that are shown in the infrared band (700 nm - 1 mm) and millimetric ALMA bands (band 3: 2.7 – 3 mm, band 6: 1.2 – 1.4mm, band 7: 0.85mm).

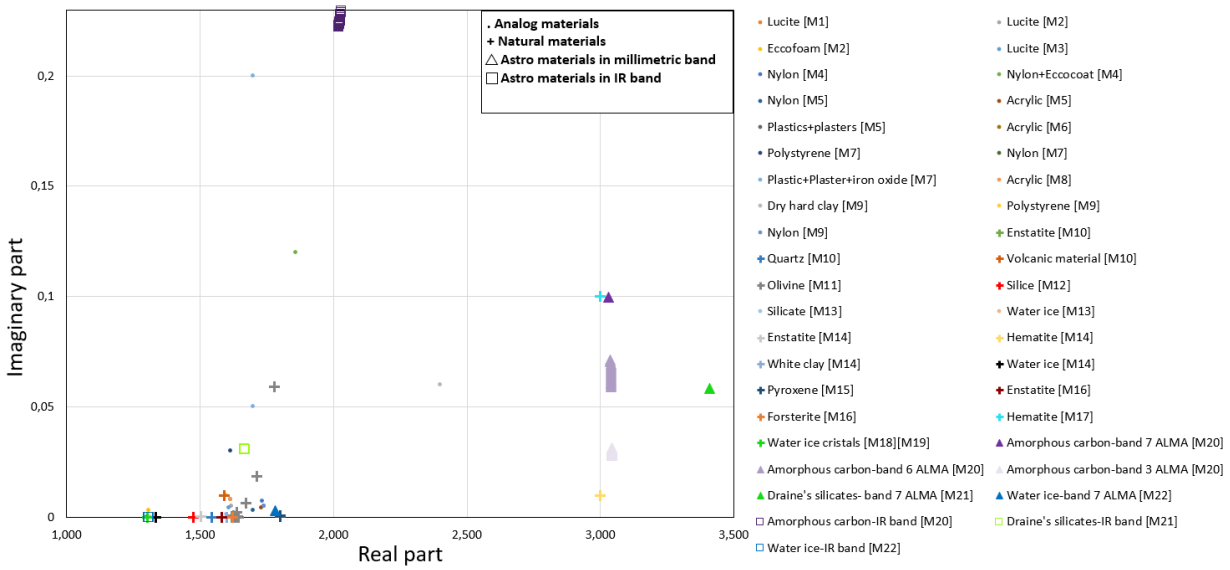

Figure 1.31: Bibliographical study of refractive index of protoplanetary dust (these specific references are at the end of this section with a prefix M for material properties).

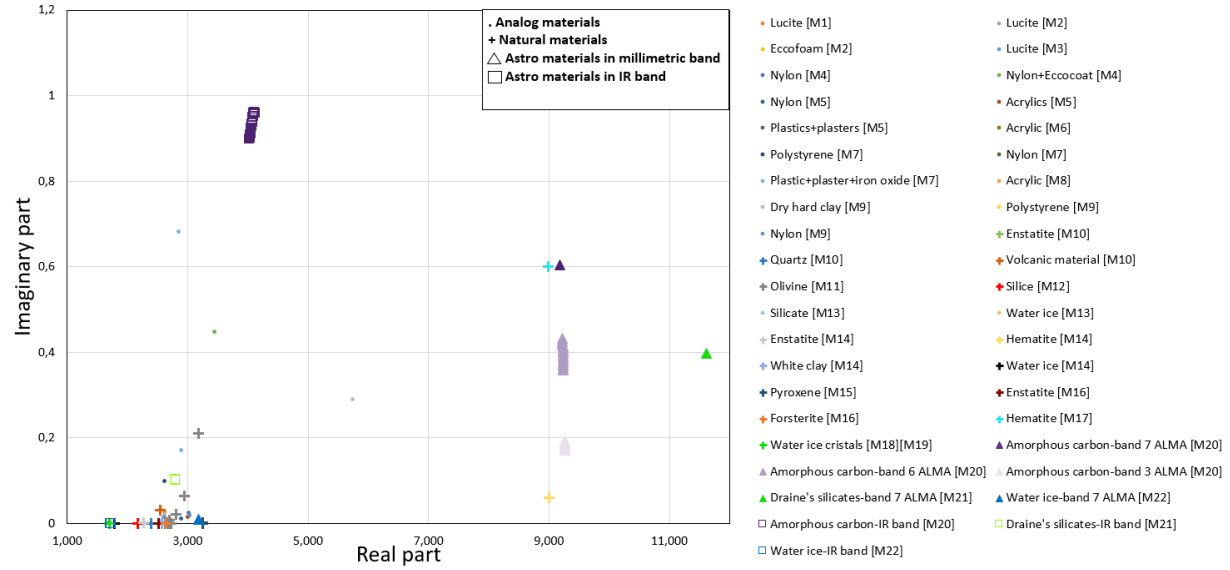

Figure 1.32: Bibliographical study of permittivity of protoplanetary dust (these specific references are at the end of this section with a prefix M for material properties).

As can be seen in Figure 1.31, most of the materials are assembled around real parts of $n = 1.3 - 1.8$ (real permittivity $\varepsilon' = 1.7 - 3.2$) and imaginary parts of $k = 0 - 0.05$ (imaginary permittivity $\varepsilon'' = 0 - 0.2$). Exceptions can be seen for the amorphous carbon, in IR and millimetric bands, presenting larger refractive indices.

Based on this bibliographical study and knowing that the most abundant materials are silicate minerals, this thesis will be focused on the simplest scenario which is to suppose that all dust is made of silicate, this being the first approach to produce 3D printed protoplanetary dust analogs. For this reason, our analog materials will have refractive index values close to the astronomical silicate [14] (see Figure 1.33).

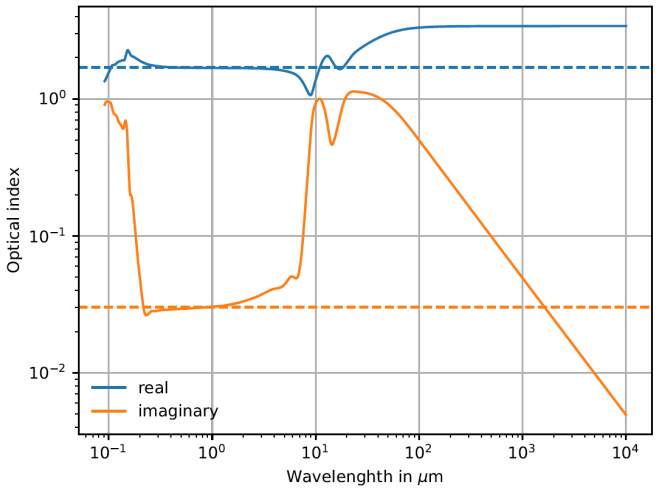

Figure 1.33: Refractive index of the astronomical silicate.

As shown in the following two chapters, the analog materials were chosen based on two criteria. First, our analogs need to have similar refractive indices to the astronomical silicate, and second, they need to be able to be printed by means of additive manufacturing.

In conclusion, it is possible to produce dust analogs with the desired size and material. Furthermore, these dust analogs can be measured in the CCRM facility, having the advantage of controlling their orientation, geometry and optical index. It should be noted that this is the first time that protoplanetary dust analogs are 3D printed and measured using the microwave scattering technique.

[M1] J. M. Greenberg, N. E. Pedersen, and J. C. Pedersen. “Microwave analog to the scattering of light by nonspherical particles”. In: *Journal of Applied Physics* 32.2 (1961), pp. 233–242. ISSN: 00218979. DOI: 10.1063/1.1735984.

[M2] B. Å. S. Gustafson. “Scattering by ensemble of small particles experiment, theory and applications”. In: *Reports of the Lund Observatory* 17 (1980).

[M3] D. W. Schuerman, R. T. Wang, B. Å. S. Gustafson, et al. “Systematic studies of light scattering 1: Particle shape”. In: *Applied Optics* 20 (1981), pp. 4039–4050. ISSN: 0003-6935. DOI: 10.1364/ao.21.000369.

[M4] R. H. Zerull, B. Å. S. Gustafson, K. Schulz, et al. “Scattering by aggregates with and without an absorbing mantle: microwave analog experiments”. In: *Applied Optics* 32 (1993), p. 4088. ISSN: 0003-6935. DOI: 10.1364/ao.32.004088.

[M5] B. Å. S. Gustafson. "Microwave analog to light scattering measurements: A modern implementation of a proven method to achieve precise control". In: *Journal of Quantitative Spectroscopy and Radiative Transfer* 55.5 (1996), pp. 663–672. ISSN: 00224073. DOI: 10.1016/0022-4073(96)00009-X.

[M6] Y. L. Xu and B. Å. S. Gustafson. "Experimental and theoretical results of light scattering by aggregates of spheres". In: *Applied Optics* 36.30 (1997), p. 8026. ISSN: 0003-6935. DOI: 10.1364/ao.36.008026.

[M7] B. Å. S. Gustafson, L. Kolokolova, J. E. Thomas-Osip, et al. "Scattering by complex systems II: Results from microwave measurements". In: *Formation and Evolution of Solids in Space*. Springer, Dordrecht, 1999, pp. 549–563. ISBN: 978-94-011-4806-1. DOI: https://doi.org/10.1007/978-94-011-4806-1_34.

[M8] Y. L. Xu and B. Å. S. Gustafson. "A generalized multiparticle Mie-solution: Further experimental verification". In: *Journal of Quantitative Spectroscopy and Radiative Transfer* 70 (2001), pp. 395–419. ISSN: 00224073. DOI: 10.1016/S0022-4073(01)00019-X.

[M9] L. Kolokolova and B. Å. S. Gustafson. "Scattering by inhomogenous particles: Microwave analog experiments and comparison to effective medium theories". In: *Journal of Quantitative Spectroscopy and Radiative Transfer* 70 (2001), pp. 611–625. ISSN: 00224073. DOI: 10.1016/S0022-4073(01)00033-4.

[M10] O. Muñoz, F. Moreno, F. Vargas-Martín, et al. "Experimental Phase Functions of Millimeter-sized Cosmic Dust Grains". In: *The Astrophysical Journal* 846.1 (2017), p. 85. ISSN: 1538-4357. DOI: 10.3847/1538-4357/aa7ff2.

[M11] A. Penttilä, T. Väisänen, J. Markkanen, et al. "Rigorous light-scattering simulations of nanophase iron space-weathering effects on reflectance spectra of olivine grains". In: *Icarus* 345 (2020), p. 113727. ISSN: 10902643. DOI: 10.1016/j.icarus.2020.113727.

[M12] J. Mroczka, M. Woźniak, and F. R. A. Onofri. "Algorithms and methods for analysis of the optical structure factor of fractal aggregates". In: *Metrology and Measurement Systems* 19.3 (2012), pp. 459–470. ISSN: 08608229. DOI: 10.2478/v10178-012-0039-2.

[M13] A. Penttilä, E. Zubko, K. Lumme, et al. "Comparison between discrete dipole implementations and exact techniques". In: *Journal of Quantitative Spectroscopy and Radiative Transfer* 106 (2007), pp. 417–436. ISSN: 00224073. DOI: 10.1016/j.jqsrt.2007.01.026.

[M14] J. Escobar-Cerezo, C. Palmer, O. Muñoz, et al. "Scattering Properties of Large Irregular Cosmic Dust Particles at Visible Wavelengths". In: *The Astrophysical Journal* 838 (2017), pp. 1–17. ISSN: 1538-4357. DOI: 10.3847/1538-4357/aa6303.

[M15] J. Martikainen, A. Penttilä, M. Gritsevich, et al. “Spectral modeling of meteorites at UV-vis-NIR wavelengths”. In: *Journal of Quantitative Spectroscopy and Radiative Transfer* 204 (2018), pp. 144–151. ISSN: 00224073. DOI: 10.1016/j.jqsrt.2017.09.017.

[M16] E. Frattin, O. Muñoz, F. Moreno, et al. “Experimental phase function and degree of linear polarization of cometary dust analogues”. In: *Monthly Notices of the Royal Astronomical Society* 484 (2019), pp. 2198–2211. ISSN: 13652966. DOI: 10.1093/mnras/stz129. arXiv: 1901.05975.

[M17] M. Kahnert, T. Nousiainen, and P. Mauno. “On the impact of non-sphericity and small-scale surface roughness on the optical properties of hematite aerosols”. In: *Journal of Quantitative Spectroscopy and Radiative Transfer* 112 (2011), pp. 1815–1824. ISSN: 00224073. DOI: 10.1016/j.jqsrt.2011.01.022.

[M18] C. Liu, R. L. Panetta, and P. Yang. “The effective equivalence of geometric irregularity and surface roughness in determining particle single-scattering properties”. In: *Optics Express* 22.19 (2014), pp. 23620–23627. ISSN: 1094-4087. DOI: 10.1364/oe.22.023620.

[M19] J. Zhang, L. Bi, J. Liu, et al. “Optical scattering simulation of ice particles with surface roughness modeled using the Edwards-Wilkinson equation”. In: *Journal of Quantitative Spectroscopy and Radiative Transfer* 178 (2016), pp. 325–335. ISSN: 00224073. DOI: 10.1016/j.jqsrt.2016.02.013.

[M20] F. Rouleau and P. G. Martin. “Shape and clustering effects on the optical properties of amorphous carbon”. In: *The Astrophysical Journal* 377 (1991), pp. 526–540. DOI: 10.1086/170382.

[M21] B. T. Draine and H. M. Lee. “Optical properties of interstellar graphite and silicate grains”. In: *The Astrophysical Journal* 285 (1984), pp. 89–108. DOI: https://doi.org/10.1086/165385.

[M22] J. B. Pollack, D. Hollenbach, S. Beckwith, et al. “Composition and radiative properties of grains in molecular clouds and accretion disks”. In: *The Astrophysical Journal* 421 (1994), pp. 615–639. DOI: 10.1086/173677.

1.7.3 Microwave analogy assumptions

Knowing that we are able to reproduce part of the size parameters of protoplanetary dust and conserve a similar refractive index, several assumptions for the analog measurements need to be stated in order to mimic the same conditions as with protoplanetary dust particles:

1. Dusts are considered sufficiently far from each other to not produce interference between each other. Thus, samples in the anechoic chamber are measured one by one.

2. Dust is considered randomly oriented in protoplanetary disks and not preferentially orientated. For this reason, each sample is considered as one object and its measured scattered field is the average of a sufficient number of orientations [126].

3. There are different sizes of dust, for this study we assume sizes from 0.1µm to 10µm in protoplanetary disks, with a size distribution. For measurements in the anechoic chamber, one representative sample is measured at multiple wavelengths which is equivalent to having multiple samples of one object with different sizes at one wavelength.

With laboratory scattering experiments (previously described in Section 1.4), the analogy of this protoplanetary scenario (sketched in Figure 1.5), can be made. The analogy can be made using three main components: an electromagnetic source (laser or antenna), dust analogs and a detector. However, depending on the type of technique (i.e., light or microwave scattering technique) to obtain the Mueller matrix elements and thus the scattering parameters of interest (see Equation 1.35 for randomly oriented particles and Section 1.3.5 for the scattering parameters), different measurements need to be performed.

For the microwave analogy, which is the technique used in this study, there are several substeps, described as follows, to retrieve the scattering parameters of analogs of protoplanetary dust (remember that this thesis is focused on the first step (a) of the scheme presented in Figure 1.8):

1. The emitting and receiving antennas must be used in four linear states of polarization: both horizontally, both vertically, and two cross-polarizations (one vertical and the other horizontal and vice versa). This must be done for the incident field (measurement without sample) and total field (measurement with sample), explained in Section 1.5.3.

2. After performing the four states of polarizations, the four Jones matrix elements can be retrieved.

3. From these four Jones matrix elements, the six Mueller matrix elements of interest for randomly oriented particles can be calculated (see Equations 1.28 and 1.30).

4. Based on these six Mueller matrix elements, the scattering parameters of interest can be calculated (see Section 1.3.5).

The six Mueller matrix elements that are retrieved, means that the incident source is unpolarized, finding the elements of the first column of the Mueller matrix and therefore the phase function and the degree of linear polarization. The other four remaining elements are retrieved for a source that is partially polarized, and based on them, the other scattering parameters of interest are retrieved. Therefore, we can

retrieve the scattering parameters of protoplanetary dust analogs for a non-polarized incident source and a partially polarized source which is the case described in Figure 1.5.

Remember that the second step (b) (described in Figure 1.8) is out of the limits of the main objective of this thesis. For this second step, Mueller matrix elements need to be put inside a 3D radiative transfer code as inputs to model the scattered light in dense dusty media (protoplanetary disks), then the output is a synthetic image of the scattered disk, and finally synthetic images can be compared with observations of protoplanetary disks.

As previously explained in Section 1.2.3.3, in order to know if our measurements are consistent, comparisons between our retrieved scattering parameters can be done with other circumstellar disks that are not optically thick, i.e. debris disks, where the phase function and the degree of linear polarization are presented as a function of the scattering angles (2D diagrams). However, other Mueller matrix elements such as S_{22}, S_{33}, S_{34} and S_{44} are not possible to be compared because this type of disk is considered optically thin and so multiple scattering that produces incident partially polarized light is negligible, thus only incident non-polarized light coming from the star is taken into account. If only non-polarized light acts as the incident source, then, S_{22}, S_{33}, S_{34} and S_{44} become zero, which is the case for debris disks. For this reason, only the phase function and the degree of linear polarization of debris disks are possible to be compared with our results. Other comparisons can be done with other objects that were involved in the formation of the Solar System as with comets which also have the phase function and the degree of linear polarization. Finally, comparisons with existing laboratory measurements and numerical simulations of the scattering parameters of aggregates and grains can be performed.

On the other hand, if measurements are performed with the light scattering technique, then more states of polarization, not just four linear polarizations as with the microwave scattering technique, need to be used [see Table 1 in 104] in order to find the six Mueller matrix elements of interest S_{11}, S_{12}, S_{22}, S_{33}, S_{34}, S_{44}. Therefore, using the microwave scattering technique is simpler and we can calculate the Mueller matrix elements and thus the scattering parameters of protoplanetary dust interest with just four states of polarization. This latter is possible because with the microwave scattering technique we can retrieve the whole complex scattered field, phase and amplitude, then this can be expressed in terms of the Jones matrix elements and thanks to the passage equations the Mueller matrix elements are retrieved to finally obtain the scattering parameters.

1.8 Conclusions

There is an evident need to understand in more detail the accretion processes during the protoplanetary stage where different barriers are presented in the current accretion model. Barriers that are present because protoplanetary dust has been always

considered as compact an spherical. Information on these protoplanetary disks is obtained with observations of scattered light. However this does not give direct information on the morphology of protoplanetary dust. A way to understand and go further in the interpretation of these observations and obtain some information about dust is with the help of laboratory scattering experiments. As previously described in this first chapter, two techniques are used for this purpose, the microwave scattering technique and the light scattering technique.

The main objective of this thesis is to use the microwave scattering technique (microwave analogy) in order to study different scattering properties of protoplanetary dust analogs and to give clues to interpret the protoplanetary scattered observations. This latter will give some tools to understand the accretion scenario. Compared to others techniques, the microwave scattering technique in which this study is based on, has enormous advantages. First, with this technique we can retrieve the complex scattered field, having the phase and the amplitude, and leading to the Mueller matrix elements and scattering parameters of interest. This latter can be achieved with only four states of polarizations. Second, the centimeter-sized analogs allow a physical control of the particle orientation (we can manually control the position of centimeter-sized analogs). Third, the fabrication of 3D printed analogs gives a total geometrical and material control, which leads to an easier analysis of the scattering parameters and the interpretation of these parameters leads to the scattering properties.

The present study is focused on the scattering parameters of 3 types of protoplanetary dust analogs : fractal aggregates presented in Chapter 2, and two families of irregular grains in Chapter 3.

2 Fractal aggregates

Sommaire

2.1 Introduction . . . 102
2.2 Fractal definition . . . 105
2.3 Analogs of dust aggregates . . . 106
2.3.1 Virtual generation . . . 106
2.3.2 3D-printing by stereolithography . . . 108
2.3.3 Aggregate size analogy . . . 109
2.4 Scattering properties of fractal-like aggregates . . . 110
2.4.1 Setup parameters . . . 111
2.4.1.1 Number of necessary measurements . . . 111
2.4.1.2 Method of simulation and co and cross terms . . . 113
2.4.1.3 Forward and backward measurements . . . 115
2.4.2 Aggregates with average orientation . . . 116
2.4.2.1 Phase function . . . 116
2.4.2.2 Degree of linear polarization . . . 123
2.4.2.3 Conclusions . . . 128
2.4.2.4 Other scattering parameters . . . 129
2.4.2.5 Conclusions . . . 133
2.4.3 Aggregates with average orientation and size distribution effect 136
2.4.3.1 Probability distribution . . . 136
2.4.3.2 Phase function . . . 137
2.4.3.3 Degree of linear polarization . . . 140
2.4.3.4 Other scattering parameters . . . 142
2.4.3.5 Conclusions . . . 145
2.4.4 Direct comparison of scattering parameters found in the literature 146
2.4.4.1 Laboratory measurements . . . 147
2.4.4.2 Numerical simulations . . . 148
2.4.4.3 Observations . . . 151
2.4.4.4 Conclusions . . . 152
2.5 Estimation of fractal dimension . . . 153
2.5.1 D_f estimation methods . . . 153
2.5.1.1 Fractal zone definition . . . 154
2.5.1.2 D_f estimation from the fractal zone . . . 155
2.5.1.3 D_f estimation by Butterworth filter . . . 156

2.5.2 Estimated fractal dimension with our aggregates phase functions 158
2.5.2.1 Phase functions of aggregates with average orientation and with different D_f . . . 158
2.5.2.2 Phase functions of aggregates with average orientation and with same D_f . . . 163
2.5.2.3 Phase functions of aggregates with average orientation including a size distribution effect . . . 166
2.5.2.4 Conclusions . . . 169
2.6 Conclusions . . . 170

2.1 Introduction

The process by which dust grains from the interstellar medium evolve during the collapse of a molecular cloud, and grow in a protoplanetary disk to form pebbles, boulders and finally planetesimals or planets still faces many open questions [see 59, for a review]. Several theoretical scenarios are proposed to overcome the physical barriers to grain growth and many are tested against laboratory experiments [see 63, for a review]. Fractal aggregates and irregular solid grains have been proposed as the outcome of the dust growth process and their presence was confirmed by the observations of cometary dust in the Solar System [e.g. 127, 128, based on recent results from the Rosetta and previous missions]. However, observational evidence in protoplanetary disks is still missing, despite tremendous progress in high-angular resolution instruments in the (sub)millimeter, near-infrared and optical ranges. Sensitive panchromatic observations of disks at high-angular resolution are now routinely produced by facilities such as ALMA, SPHERE, or GPI, but most interpretations do not consider aggregates and still rely on compact spherical particles. As a first step to provide more realistic tools to interpret protoplanetary disk observations and study grain growth in those disks, we study here the scattering properties with the interpretation of the scattering parameters of small fractal dust aggregates made of 74 monomers.

Fractal aggregates are characterized by their porosity or their fractal dimension D_f as these two parameters are closely related [129]. The fractal dimension D_f ranges from 1 for a very fluffy or porous particle to 3 for a compact sphere. The size parameter $X_{agg} = 2\pi R/\lambda$ is another important descriptive parameter, where R can be the radius of the sphere enclosing the aggregate and λ the incident wavelength or R can also be the gyration radius. These aggregate characteristics directly influence their scattering parameters, such as phase function, degree of linear polarization, and other Mueller matrix elements, and therefore their scattering properties.

Scattering properties of aggregates have been studied since the seventies to analyze different dust particles, e.g. interstellar dust particles, soot particles and aerosols in planet atmospheres. Two different laboratory measurement techniques have been used to better understand these properties: light scattering and microwave scattering techniques.

Light scattering technique uses optical sources to study particles in the (sub) millimeter size range, therefore with size parameters larger than 1. These particles can be ejected by an aerosol generator so measurements are done for a cloud of particles [8]. Particles large enough (mm sizes) can be positioned on a holder and measured individually [9]. Other light scattering instruments use levitation, in this case ultrasonic levitation, having the advantage to make 4π measurements for single targets at visible wavelengths as is the case of the 4π Scatterometer [10]. Or even using microgravity levitation during parabolic flights as in the case of PROGRA2 experiment operating in visible and infrared wavelengths for particles that are larger than 20 μm [130], but as aggregates tend to stick in these flights, an air levitation experiment is used, covering sizes from submicrons to tens of microns and fluffy-like aggregates (of sizes around microns to millimeters with 90% of porosity) [111]. In [11] the study of clouds of irregular particles of silicon carbide grains and desert sand aggregates gave a better understanding of their brightness and polarisation phase functions. A more specific study of the analysis of polarisation and maximum polarisation of fluffy aggregates composed of silica and carbon was published in [110], in [112] with highly porous aggregates of similar materials and in [113] with different silicates and mixtures of carbon.

Unfortunately, light scattering experiments are facing challenges: uncontrolled aggregate geometries, which leads to unknown parameters during measurement and therefore results that are difficult to interpret; small size parameter aggregates which tends to stick together with air ejections and levitation due to Van der Waals forces, making difficult to measure a cloud of aggregates sufficiently separated or even one isolated grain without the contribution of neighboring grains [11].

Another way of obtaining scattering parameters is to take advantage of the microwave analogy, which relies on the scale invariance rule (SIR) to measure objects that in reality are very big (kilometer scales) or small like it is the case of our study for the (sub)micrometer protoplanetary dust. In Maxwell's equations, the SIR states that an electromagnetic system will give equivalent scattering results at any frequency if all geometrical dimensions are scaled in proportion, while keeping the complex refractive index identical [131, 16, 12]. The first particle analogs to be fabricated were inspired by stratospheric dust aggregates collected by high-altitude-flying U2 spy-planes [132, 133]. These analogs were measured in the microwave scattering facility of Bochum University. They were fabricated with size parameters between $X_{agg} = 20$ to $X_{agg} = 32$ [89] and matched with the flux of zodiacal lights measured by Helios and Pioneer space probes. However the geometry of these analogs was not controlled which produced scattering parameters difficult to interpret and thus scattering properties.

Microwave measurements of the scattering phase function and degree of linear polarization of aggregates made of identical monomers followed: assembly of spherical monomers with monomer size parameter ranging from $X_{mon} = 0.58$ (Rayleigh scattering) to $X_{mon} = 7.86$ [88, 134, 135] ; assembly of spheres, sphereoids and cylinders monomers with monomer size parameter ranging from $X_{mon} = 0.51$ to $X_{mon} = 21.1$ [136, 96]. The main conclusion of these works was that the more packed the aggregate,

the wider the forward scattering peak of the phase function. Unfortunately, the fractal dimensions of the aggregates used in the aforementioned microwave studies were unknown.

Scattering parameters of protoplanetary aggregates can also be simulated (see for example [137, 138, 139] where different scattering approximate methods, e.g. Discrete Dipole Approximation (DDA) and T-Matrix method, were used). Studies on simulated scattering properties of aggregates of interplanetary dust particles and cometary particles are found in [140, 141, 142, 143]. Similar numerical studies have been performed for aerosols and atmospheric applications [144, 145, 146]. Yet, aggregates used in these numerical methods are discretized in dipoles which is an approximation of the object that scatters and therefore these scattering simulations need to be compared with scattering measurements.

Although several measurements and theoretical scattering studies of aggregates exist, the need remains for more results, in particular to differentiate aggregates and irregular polydisperse particles, as well as to study large particles of (sub)micrometer sizes and aggregates containing thousands of monomers with a realistic size distribution or even larger irregular particles below the geometric optics regime [147]. The aim of this chapter is therefore to provide laboratory measurements, using the microwave scattering technique, of the scattering parameters of protoplanetary dust aggregates whose fractal dimensions, geometries and refractive indices are fully controlled. Together with these measurements and their interpretation (giving the scattering properties), we also provide finite element method (FEM) simulations of the same aggregate particles for cross validation.

The present chapter studies numerically and experimentally the scattering parameters, i.e. phase function, degree of linear polarization and other Mueller matrix elements, of seven different protoplanetary analog aggregates, with wavelengths ranging from 100 mm to 16.7mm (in frequency, from 3 GHz to 18 GHz), leading to sizes parameters ranging from $X_{agg} = 1$ and $X_{agg} = 20$. These aggregates are defined by their fractal dimensions D_f of 1.5, 1.7, 2.0, 2.5 and 2.8. The main advantage of using this microwave scattering technique with aggregates fabricated with additive manufacturing is that the geometry and the refractive index of our analogs are controlled to high accuracy. This thesis is based on our group previous studies in which several scattering field measurements (magnitude and phase) of different aggregates were performed, using different manufacturing methods from sticking monomer by monomer to using additive manufacturing techniques [148, 149, 121, 150].

In this chapter I first make a brief introduction of the fractal definition. Then, I describe how the analog aggregates of protoplanetary dust were fabricated by a collaboration with Centre de Transfert de Technologie du Mans (CTTM). I present and analyze the scattering parameters that were obtained based on scattering measurements and numerical simulations for our aggregates. Finally, I make an estimation of the fractal dimension of aggregates based on their phase function using different methods and proposing a new one. At the end, I present the conclusions and prospects for future works for this first studied morphology, aggregates.

2.2 Fractal definition

The definition of the fractal dimension D_f, was first given by Mandelbrot in [151] who defined this dimension different to what was explained by the mathematicians until the 19th century. Based on the euclidean space, the dimension D is an integer number being 1 for a line, 2 for a plane and 3 for a 3D structure. However, Mandelbrot defined D_f as a set of fractional and integer numbers, from 1 to 3 included.

The main characteristic of these fractal objects, that can be described by D_f, is the invariance of their structures under changes of scale, meaning that there is always the same structure even by zooming infinitely in or out. This concept is called self-similarity and it is not present for euclidean objects; for example if a sphere (euclidean object of $D = 3$) is zoomed in, there are no other small spheres, actually there is just a part of the surface of that sphere. But if we take an aggregate composed of an infinite number of spheres even if the scale is changed, we always find the same elementary structure, spheres, known as monomers. The characteristics of a fractal aggregate are related by a single equation named the fractal equation:

$$N = k_0 (R_g / a)^{D_f}, \tag{2.1}$$

where N is the number of monomers, k_0 the fractal prefactor (or proportionality constant), R_g the gyration radius (which is the mean-squared value of the distances between the aggregate center of mass and the geometric center of each monomer), a the monomer radius and D_f the fractal dimension.

However if that aggregate does not have an infinite number of monomers, called mathematically a bounded set, it will be also self-similar with the union of N non-overlapping identical subsets. Thus, the aggregate is still fractal but with a finite number of monomers (see Figure 2.1).

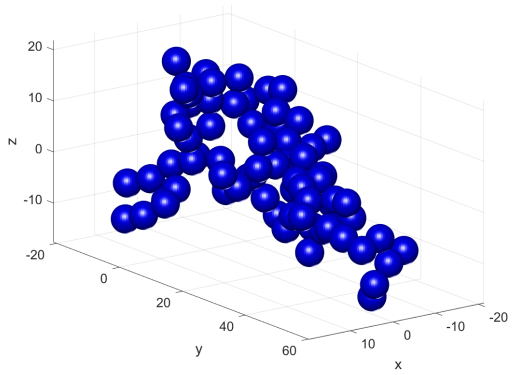

Figure 2.1: Example of one of our fractal-like aggregates created with DLA algorithm [17] with a fractal dimension of 1.7, number of monomers 74 and radius of gyration of 23.93mm.

Based on this definition of finite fractal aggregates of identical monomers which are also known as fractal-like aggregates, the following section is focused on the fabrication of these aggregates being analogs of protoplanetary dust.

2.3 Analogs of dust aggregates

The evolution of dust particles in protoplanetary disks is complex and involves several processes. The structure and shape of a particle retain the record of its evolution, in particular its collisional history. Yet, very little direct information is available on the particle structures and shapes in disks and observing their scattering signatures will allow significant progress in our understanding of dust evolution. To do so, one must first understand the typical signatures of different families of particles. Here we will focus on fractal aggregates.

Herein different types of aggregates are generated with fractal dimensions ranging from 2.8 (compact) to 1.5 (fluffy, porous), see Table 2.1. This range of fractal dimensions covers the outcome of dust growth by collisions of individual monomers with clusters and by collisions between clusters. For comparison, Ballistic Particle-Cluster Aggregation (BPCA) results in aggregates with high fractal dimensions, typically larger than 2.5, while Ballistic Cluster-Cluster Aggregation (BCCA) yields objects with fractal dimensions typically smaller than 2 [152] for slow collisional velocities.

To produce these analogs two steps were necessary; first, their virtual generation and second, 3D printing. The details for these two steps are described in the following sections.

2.3.1 Virtual generation

Nature uses different types of aggregation giving birth to a variety of different fractal dimensions as previously explained. To generate a large range of fractal dimensions, all aggregates were generated with a tunable Diffusion Limited Aggregation software DLA created by [17], in which, at each monomer-cluster aggregation scheme, the algorithm verifies if the fractal dimension is correct, if it is not the case, the monomer is eliminated and another monomer will diffuse toward the seed. Thus, this software is able to produce different fractal dimensions that are presented in nature thanks to BPCA or BCCA.

Three input parameters are necessary to describe the particles: the fractal dimension of the aggregate, the number of monomers included in the particle, and the radius of the monomers. All monomers are spherical and for this study they have the same size (monodisperse). These parameters are related based on the fractal equation (see Equation 2.1). All aggregates were fabricated with $N = 74$ monomers, with a monomer radius of $a = 2.5$mm. The reason behind the choice of 74 monomers is purely historical, indeed our previous group work started working with 74 monomers because it was the maximum quantity of monomers that they decided to stick [149],

before fabricating them with 3D printing techniques. The DLA software assumes a single point of contact between each monomer, i.e., no overlapping. The fractal prefactor is set to $k_0 = 1.593$ in order to have aggregates that can achieve the highest possible compactness in a 3D space (fractal prefactor with this value correspond to monodisperse compact aggregates [153], thus we have the possibility to produce fluffy aggregates up to very compact aggregates being able to produce all the fractal dimensions that we want). This prefactor value, which depends on the compactness factor and the fractal dimension of the particle [see Equation 16 of 154], is set constant in the DLA software. Specific information of each aggregate is given in Table 2.1.

In Figure 2.2 and Table 2.1, the names of each analog are made of a string specifying first that they are aggregates generated with DLA (Ag_DLA), followed by their fractal dimension (Df) and the number of monomers (N). When several realizations with the same parameters are made, an additional index is added at the end (see, e.g., aggregates of fractal dimension $D_f = 2$, where the index goes from 1 to 3, Ag_DLA_-Df2.0_N74_index). In [126], we used a different naming convention. The names used in that paper are recalled in the first column of Table 2.1 for reference.

The values of the numerical fractal dimensions are also given in Table 2.1 as well as the radius of gyration (which was calculated by the software). Other parameters are the radius of the bounding sphere R_m (it is the smallest sphere in which each aggregate fits inside) and the size parameter of each aggregate X_{agg} which was calculated with the radius of the bounding sphere at the minimum and maximum wavelengths. Moreover, the porosity, P_{R_g}, was estimated as the subtraction to unity of the ratio between the volume of the material in the aggregate (V) and the volume of a sphere calculated with the radius of gyration (V_s) as shown in Equation 2.2 based on [129], values are in Table 2.1.

$$P_{R_g} = 1 - \left(\frac{V}{V_s}\right), \tag{2.2}$$

where $V_s = \frac{4}{3}\pi R_c^3$ and $R_c = \sqrt{\frac{5}{3}} R_g$ [155].

Finally, the material packing density, ρ, was calculated and defined as the ratio of the aggregate volume to the total volume of the bounding sphere [taken by 156].

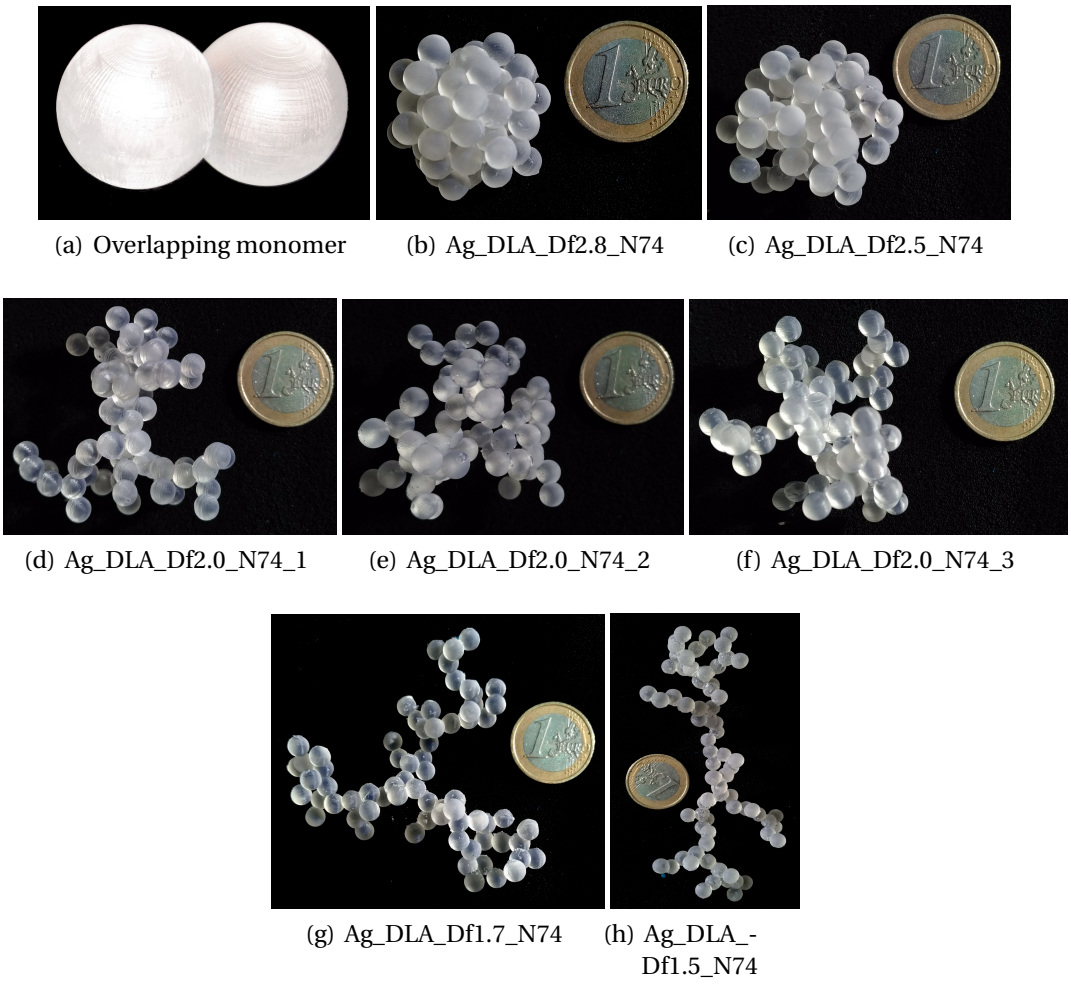

(a) Overlapping monomer (b) Ag_DLA_Df2.8_N74 (c) Ag_DLA_Df2.5_N74

(d) Ag_DLA_Df2.0_N74_1 (e) Ag_DLA_Df2.0_N74_2 (f) Ag_DLA_Df2.0_N74_3

(g) Ag_DLA_Df1.7_N74 (h) Ag_DLA_-Df1.5_N74

Figure 2.2: 3D printed aggregates, using the SLA technique, with their corresponding technical name (second column of Table 2.1).

2.3.2 3D-printing by stereolithography

After the virtual generation, aggregates were fabricated using an additive manufacturing process named stereolithography (SLA). SLA has the advantage of its good accuracy and surface finish compared to other 3D printing methods (the first time our group used this technique to print aggregates was in [150]). The resolution of SLA printer (collaboration with Centre de Transfert de Technologie du Mans (CTTM)) used for these aggregates is of 25 µm for each photo-polymerized layer and the maximum dimensions that this printer is able to print are 64 mm x 40 mm x 134 mm.

The principle of SLA is to photopolymerize the liquid acrylic resin, layer by layer. The solidification is done thanks to a UV laser. The resin that was used to print aggregates has a refractive index of $1.7 + i0.03$ at our working wavelengths which is close to the

Aggregate	Aggregate technical name	Numerical fractal dimension	Radius of gyration (mm)-R_g	Radius of the bounding sphere (mm)-R_m
AgC232	Ag_DLA_Df1.5_N74	1.5	32.30	51.98
AgC233	Ag_DLA_Df1.7_N74	1.7	23.92	36.58
AgC185	Ag_DLA_Df2.0_N74_1	2.0	17.03	26.20
AgC2211	Ag_DLA_Df2.0_N74_2	2.0	17.03	26.54
AgC2221	Ag_DLA_Df2.0_N74_3	2.0	17.03	26.00
AgC186	Ag_DLA_Df2.5_N74	2.5	11.60	18.19
AgC187	Ag_DLA_Df2.8_N74	2.8	9.83	15.49

Aggregate technical name	Size parameter of the aggregate λ = 16.7 mm to λ = 100 mm			Porosity % -P_{R_g}	Material packing density-ρ
Ag_DLA_Df1.5_N74	19.60	to	3.27	97.91	0.011
Ag_DLA_Df1.7_N74	13.80	to	2.30	94.90	0.031
Ag_DLA_Df2.0_N74_1	9.88	to	1.65	85.68	0.085
Ag_DLA_Df2.0_N74_2	10.01	to	1.67	85.83	0.081
Ag_DLA_Df2.0_N74_3	9.81	to	1.63	85.83	0.086
Ag_DLA_Df2.5_N74	6.86	to	1.14	54.78	0.252
Ag_DLA_Df2.8_N74	5.84	to	0.97	25.88	0.407

Table 2.1: Analog aggregate properties with monomer size parameter from X_{mon} = 1.04 (λ = 16.7 mm) to X_{mon} = 0.17 (λ = 100 mm).

index of astronomical silicate without any metallic or mineral inclusions. Draine and Lee astronomical silicate has same values from λ = 0.2 to 3µm (for more information see [14]).

It is important to note that the monomer radius used by the DLA software was different from the one chosen at the moment of the printing. The virtual generation of aggregates was at one point of contact between monomers, however, printing monomers with this condition is not possible because there is no mechanical strength. For this reason, the monomer radius was increased by 10%, thus the actual radius used in practice to allow interpenetration was $a_{int} = a * 1.1$. Figure 2.2 presents the overlapping between monomers and the printed aggregates with SLA technique.

2.3.3 Aggregate size analogy

Knowing that the printed monomer radius is a_{int} = 2.75mm and wavelength ranges from 16.7mm to 100mm, the monomer size parameter ranges from X_{mon} = 1.04 to X_{mon} = 0.17, respectively. The monomer radius corresponding to the same size parameter at optical, NIR or millimeter (ALMA band 3 to 10) wavelengths is shown in Table 2.2. If the analogy is applied to the aggregate size, the minimum aggregate size parameter is 0.97 and the maximum 19.60. Thus, the aggregate radius corresponding to the same size parameter at optical, NIR or millimeter (ALMA band 3 to 10) range is shown in Table 2.2.

Range name	Wavelength	Radius of protoplanetary monomer	Radius of protoplanetary aggregate
Optical (nm)	400 to 700	11 to 115	65 to 2180
NIR (µm)	1.00 to 2.50	0.028 to 0.412	0.155 to 7.78
Millimeter (mm)	0.30 to 2.60	0.008 to 0.428	0.046 to 8.09

Table 2.2: Monomer and aggregate radius corresponding to different wavelength ranges (units are noted in the first column).

2.4 Scattering properties of fractal-like aggregates

In order to obtain the scattering properties of the seven fractal-like aggregates, measurements were performed in the anechoic chamber of CCRM (described in Section 1.5.2), using wavelengths between 100 mm to 16.7mm (corresponding to frequencies of 3 GHz to 18 GHz). Scattering measurements were obtained for all aggregates in the forward zone, which was the main experimental configuration used during this thesis (for an explanation of the experimental setup see Section 1.5.2). Additionally, numerical simulations were made based on our two methods MoM and FEM (presented in Section 1.6), using the same geometric file of the 3D objects as the one used for 3D printing. Both methods have advantages and disadvantages, for example for the simulation of Ag_DLA_Df2.0_N74_1, MoM needs less memory (2 GB) but more running time (from 1 hour to 2 hours depending on the frequency), on the contrary, FEM is faster (10 min for each frequency) but the needed memory is 70 GB. Although there are these differences, both methods gave very similar scattering behaviors as can be seen in Figure 2.5. Based on these consistent results, we decided to choose one of them which was FEM based on its better discretization of the scatterer (aggregates composed of spheres) in tetrahedrons and not in cubes as MoM do, taking advantage here of the conformal mesh properties of FEM.

All our results are based on the assumption of having a macroscopically isotropic and symmetric medium [16] and random orientation of non-interacting aggregates. Thus, the Mueller matrix that describes this situation is shown in Equation 1.35. When cross-polarized terms are negligible, it is possible to simplify the Mueller matrix expressions. However, there is just one exception for S_{22} where the inclusion of the cross-polarized elements is essential to then be able to normalize by S_{11}. If this inclusion is not made, then $S_{22} = S_{11}$ (see Section 2.4.1.2 and Figure 2.6). Therefore, the 6 Mueller matrix elements of Equation 1.30 can be re-described as follows:

$$
\begin{aligned}
S_{11} &= \frac{1}{2}\left(|S_1|^2 + |S_2|^2\right), \\
S_{22} &= \frac{1}{2}\left(|S_2|^2 + |S_1|^2 - |S_4|^2 - |S_3|^2\right), \\
S_{12} &= \frac{1}{2}\left(|S_2|^2 - |S_1|^2\right), \\
S_{33} &= S_{44} = \Re\left\{S_1 S_2^*\right\}, \\
S_{34} &= \Im\left\{S_2 S_1^*\right\}.
\end{aligned}
\tag{2.3}
$$

Based on these experimental and computational tools previously mentioned, we measured and simulated the scattering response of aggregates, then I compared measurements with numerical simulations, and I calculated the Mueller matrix elements obtaining different scattering parameters, i.e. the phase function (S_{11}), the degree of linear polarization (DLP, $-S_{12}/S_{11}$) and the normalized elements S_{22}, S_{34} and S_{44}. The interpretation of these parameters gave the scattering properties of these fractal-like aggregates.

2.4.1 Setup parameters

In this section I describe: i) the number of necessary measurements per aggregate, ii) the method of simulation, iii) the effect of including or not the cross-polarized elements on the different scattering parameters and iv) the zone where measurements could be performed.

2.4.1.1 Number of necessary measurements

A collaborative study to obtain the number of necessary measurements and orientations to retrieve the mean scattering phase function and DLP of randomly oriented aggregates was made in [126]. For a fixed position of an aggregate, the receiving antenna measures from −130° to 130° with steps of 2° giving 131 measurements. Additionally, the support where the aggregate is placed, rotates each 10° all around 360° for each receiving antenna measurement, providing 36 orientations (see Figure 2.3). Thus, at each frequency, there is a total of 4716 measurements. Based on this information, we calculated the quantity of necessary orientations to achieve the lowest error percentage or best accuracy of convergence of the phase function and DLP (see an example in Figure 2.4 for the calculus of the phase function, named brightness, and DLP, named polarization, of aggregate Ag_DLA_Df2.0_N74_1 at $\lambda = 23\,\text{mm}$). Note that the same analysis was done for all aggregates at the wavelengths of interest and in order to obtain the lowest desired error percentage, the corresponding maximum number of measurements of all wavelengths was taken. For an accuracy of 1% for the phase function and 0.5% for the DLP, a total of 72 orientations were necessary for all aggregates except for Ag_DLA_Df1.7_N74 and Ag_DLA_Df1.5_N74 with 108 orientations.

The same number of orientations was used to find the other scattering parameters of interest. Note that numerical simulations were made with the same amount of orientations to have comparable computational and experimental results. Yet the position of the aggregate is not exactly known and this could introduce differences between measurements and numerical simulations.

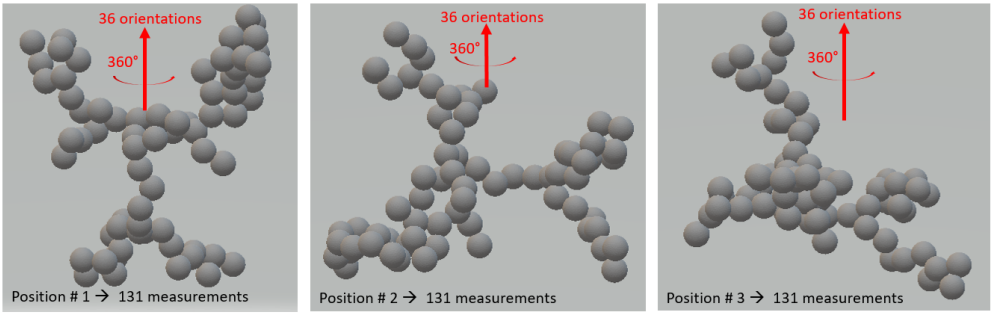

Figure 2.3: Example of necessary number of orientations and positions of aggregate Ag_DLA_Df1.7_N74 to obtain mean scattering parameters. A total of 108 orientations were necessary for this aggregate.

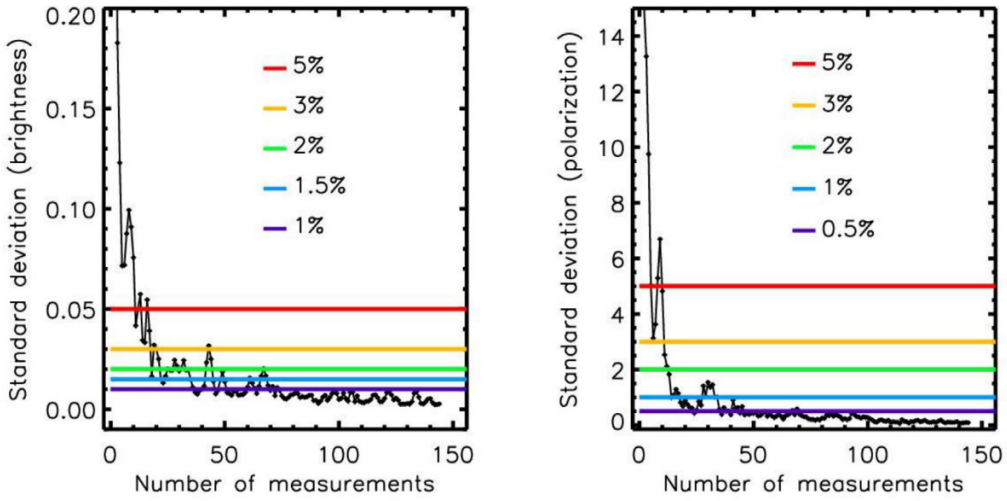

Figure 2.4: Example of necessary number of measurements of aggregate Ag_DLA_-Df2.0_N74_1 at $\lambda = 23\,\text{mm}$, $X_{agg} = 7.14$ and $X_{mon} = 0.75$ [taken from 126].

All results of phase function and DLP were obtained by averaging its different values of the same aggregate at multiple orientations. This means that we averaged first the total intensity phase function $< S_{11} >$ and the polarized intensity phase function $< S_{12} >$ before dividing one by the other to find the average DLP, $\frac{-<S_{12}>}{<S_{11}>}$. In the case of DLP the average was done before the division because the observables (S_{12} and S_{11}) in protoplanetary disks are already averaged in terms of orientations (i.e., supposing that

we observe the intensity, S_{11}, and polarized intensity, S_{12}, of a population of randomly oriented dust particles). Similarly to DLP, the other scattering parameters $\frac{<S_{22}>}{<S_{11}>}$, $\frac{<S_{34}>}{<S_{11}>}$ and $\frac{<S_{44}>}{<S_{11}>}$, were also averaged and calculated.

2.4.1.2 Method of simulation and co and cross terms

As previously mentioned, MoM and FEM methods were compared as shown in Figure 2.5 proving an excellent agreement between both models with the superposition of curves. Based on the discretization that each model has, i.e., tetrahedrons for FEM and cubes for MoM, and the morphology of our aggregates composed of spherical monomers, FEM method was selected to perform all the numerical simulations in this study.

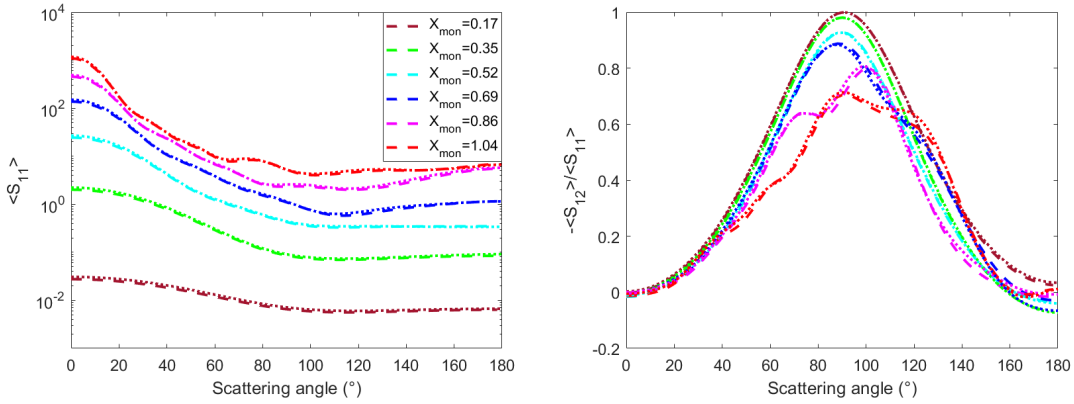

(a) Phase function (b) DLP

Figure 2.5: Comparison between FEM (dashed lines) and MoM (dotted lines) numerical simulations at six different wavelengths (100 mm, 50 mm, 33.3mm, 25 mm, 20 mm and 16.7mm) indicated in terms of monomers size parameter, from $X_{mon} = 0.17$ to $X_{mon} = 1.04$ for Ag_DLA_Df2.0_N74_1.

FEM numerical simulations were also used to verify the effect of cross-polarized elements (Jones elements S_3 and S_4) on Mueller matrix elements of all aggregates. In Figure 2.6, the six scattering parameters based on Mueller matrix elements with (dashed-dotted lines) and without (dashed lines) cross-polarization are represented for aggregate Ag_DLA_Df2.0_N74_1. For all scattering parameters, the differences between including or not the cross-polarization terms (S_3 and S_4) increase when the size of the scatterer increases (or X_{mon}). However, these differences are negligible, thus we will not take into account cross-polarized elements for our Mueller matrix elements, except for $\frac{<S_{22}>}{<S_{11}>}$. In the case of $\frac{<S_{22}>}{<S_{11}>}$, notice that $< S_{22} >$ without cross-polarization becomes $< S_{11} >$, thus the ratio between these two Mueller matrix elements equals 1 (see all dashed lines that are superposed at 1 in Figure 2.6.c). Thus, for $\frac{<S_{22}>}{<S_{11}>}$, cross-

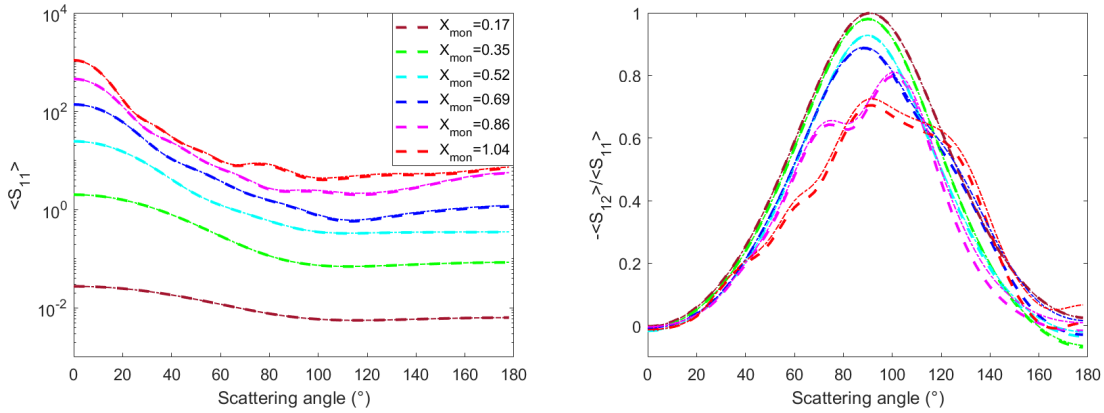

(a) Phase function

(b) DLP

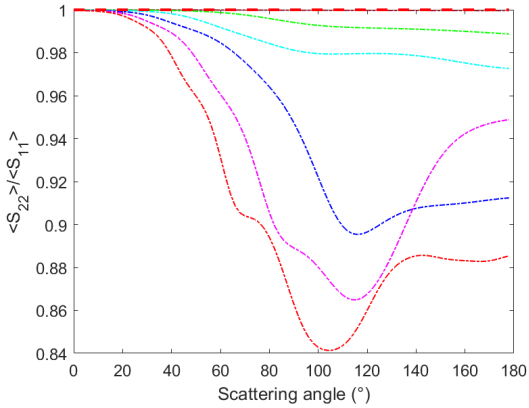

(c) Normalized S_{22}

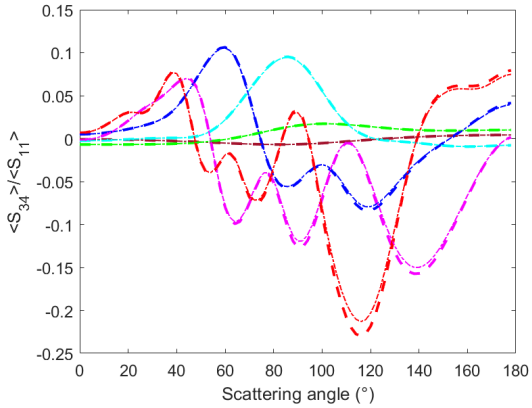

(d) Normalized S_{34}

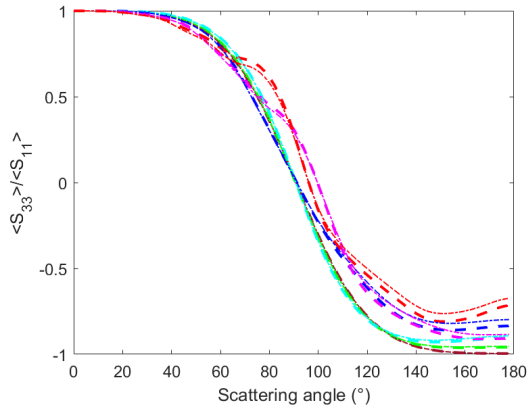

(e) Normalized S_{33}

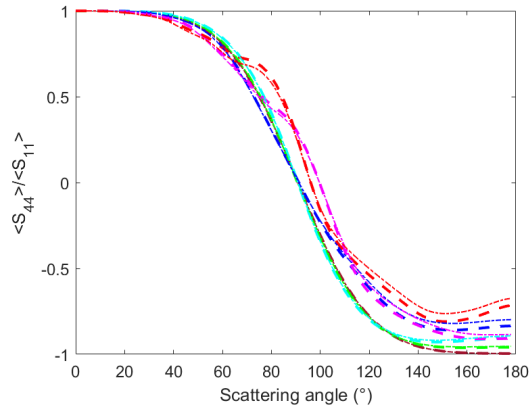

(f) Normalized S_{44}

Figure 2.6: FEM numerical simulations of Ag_DLA_Df2.0_N74_1, considering co-polarized Jones matrix elements (dashed lines) and co-polarized plus cross-polarized elements (dashed-dotted lines), from $X_{mon} = 0.17$ to $X_{mon} = 1.04$.

polarized elements are necessary to be able to analyze it, if not the ratio becomes 1 all along the scattering angles.

Furthermore, the behavior of $\frac{<S_{33}>}{<S_{11}>}$ and $\frac{<S_{44}>}{<S_{11}>}$, with the inclusion and not of cross-polarized elements, shows that these two scattering parameters (see Figure 2.6.e and Figure 2.6.f) are identical with co-polarized elements (dashed lines) and with the inclusion of cross-polarized elements (dashed-dotted lines). For these reasons, from now on the numerical simulation results are going to be represented in terms of co-polarized elements for all scattering parameters, except for $\frac{<S_{22}>}{<S_{11}>}$ (as written in Equation 2.3). Note that the fact that we will not take into account the cross-polarized elements for the phase function, DLP, $\frac{<S_{34}>}{<S_{11}>}$ and $\frac{<S_{44}>}{<S_{11}>}$ might produce a slight shift of curves but the shape is conserved (identical).

2.4.1.3 Forward and backward measurements

We have verified that the Mueller matrix elements of interest do not depend whether we use the cross-polarized elements or not. The only exception is for $< S_{22} >$ where the inclusion of the cross-polarized elements is necessary in order to avoid a constant ratio of 1 for $\frac{<S_{22}>}{<S_{11}>}$. Based on this findings, measurements were performed with only co-polarized elements, i.e, antennas at the same linearly state of polarization. Moreover, most of our measurements were performed in the forward zone obtaining scattering parameters that were represented from 0° up to 130°. This decision was made based on the fact that backward configuration has a lower accuracy due to coupling between antennas and it would multiple by a factor of two the measurement time by analog. Thus, Figure 2.7 presents an exceptional case with measurements at forward and backward configuration for Ag_DLA_Df2.0_N74_1. As can be seen in this figure, solid curves in the backward and forward zone do not present a continuity. This is due to the coupling of antennas at backward scattering angles. Indeed, in order to perform backward measurements emitting and receiving antennas need to be very close and this leads to mutual coupling where the emission that should be radiated away to the analog is instead absorbed by the receiving antenna, acting as noise. For these reasons, for the rest of aggregates, the backscattering analysis will be based on FEM numerical simulations.

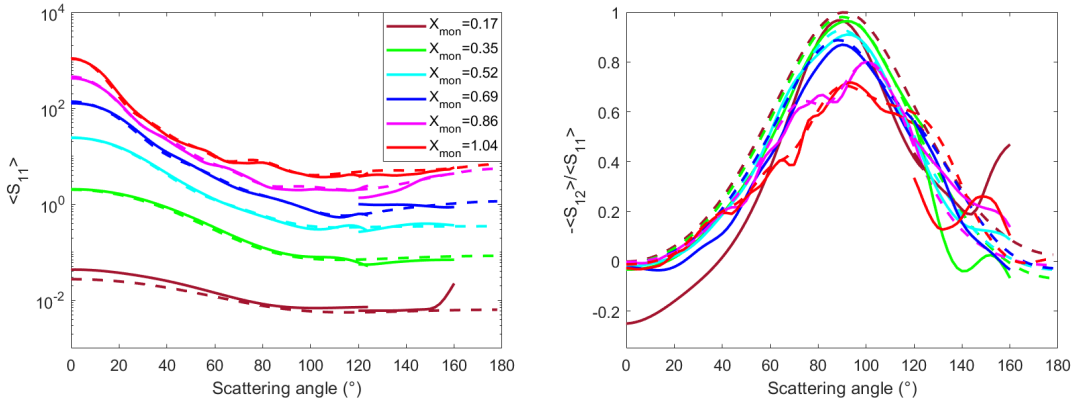

(a) Phase function (b) DLP

Figure 2.7: Measurements in the forward and backward zone (solid lines) and numerical simulations (dashed lines) of Ag_DLA_Df2.0_N74_1, from $X_{mon} = 0.17$ to $X_{mon} = 1.04$.

After verifying the different setup parameters, the Mueller matrix elements for all our aggregates were used to calculate the scattering parameters and then analyze them. Two types of scattering results are presented in the following sections: first, scattering parameters of aggregates with average orientation (Section 2.4.2) and second scattering parameters of aggregates with average orientation plus size distribution effect (Section 2.4.3).

2.4.2 Aggregates with average orientation

2.4.2.1 Phase function

Phase functions of aggregates with average orientation of different D_f are presented in Figure 2.8 at different wavelengths or X_{mon}. The levels of phase functions are consistent with size parameter X_{mon} and X_{agg}. Higher values of size parameters represent higher cross sections $Q_{sca}\pi a^2$ and so larger intensity of scattered light. For this reason, levels of the phase function curves at $X_{mon} = 0.17$ are the lowest for all aggregates and the highest at $X_{mon} = 1.04$. Moreover, Ag_DLA_Df1.5_N74 has the largest bounding radius thus the levels of its curves are larger compared to the rest of aggregates.

The measured phase functions shown in Figure 2.8 are calibrated and thus their quantitative value is significant. Numerical simulations and measurements have the same absolute values and curve shape, being both directly comparable. A comparison criterion was developed in order to estimate quantitatively the difference between our measurements and computations. Indeed, this comparison was the way we chose to have an idea of the systematic error of our experimental measurements, since a real quantification of the systematic error takes a lot of time and this has not yet been

done in the CCRM anechoic chamber. Thus, as this quantification goes out of the limits of this thesis, we measured the systematic error with the comparison between measurements and FEM simulations.

To estimate the difference between measurements and FEM simulations a Root Mean Square Deviation ($RMSD$) estimator was chosen, supposing the simulation as the reference. This criterion was normalized with the Interquartile Range (IQR) which is the difference of the 75th percentile ($Q3$) and the 25th percentile ($Q1$). Thus, the RMSD with the normalization is:

$$RMSD_{IQR} = \frac{RMSD}{(Q3 - Q1)}. \tag{2.4}$$

Furthermore, as the phase functions are represented with a logarithmic scale, this criterion is calculated on the logarithm of this quantity. The $RMSD_{IQR}$ is presented in Figure 2.9 for the phase function. The increasing values of the $RMSD_{IQR}$ obtained when the wavelength decreases (upper horizontal axes) are nothing but normal, but that the high values obtained at the large wavelengths are due to two different phenomena. First, from the experimental point of view, the scattered signals are very low and thus more sensitive to noise (especially with the calibration target of 20 mm which is small compared to the large wavelengths and thus more sensitive to noise). Second, from the numerical point of view, the chosen box where the fields are computed begins to be too small to have a distance, object-bounding box, larger than $\lambda/2$ for such large wavelengths. Thus, we cannot suppose that on the bounding of the box there is a far-field.

Additionally, the gray line (in Figure 2.9) represents the comparison between an exact Mie calculus for a solid sphere with a refractive index of $1.7 + i0.03$ (same that of the aggregates) and the simulation of the same sphere with FEM. Thus, taking Mie computations as reference, the obtained criterion values give a good idea of the minimal values that may be obtained with such FEM computations.

In general, the forward-scattering peak of the phase function is a proper characteristic of the overall dimension of the aggregate and demonstrates how constructive interference dominates compared to other bumps [as it was shown in 88]. These bumps represents the distribution of matter or structural information within aggregates. This is the case if bumps are still present after averaging enough the orientation of the aggregate [88]. This can be easily seen if the aggregate has a fractal dimension closer to 3, a sphere, for which its distribution of matter is symmetric and so the bumps will be well-defined, representing constructive interference at the same scattering angles. An example of this is shown in Figure 2.8.a, for Ag_DLA_Df2.8_N74, which has almost the same fractal dimension as a sphere.

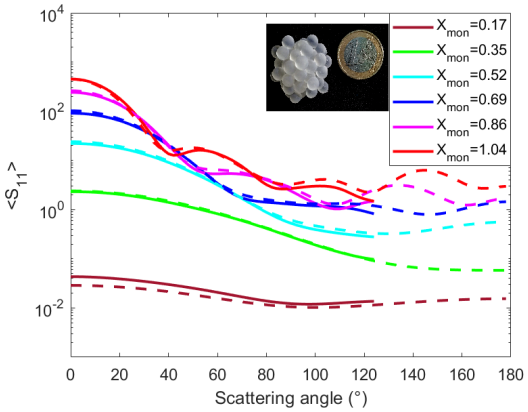

(a) Ag_DLA_Df2.8_N74

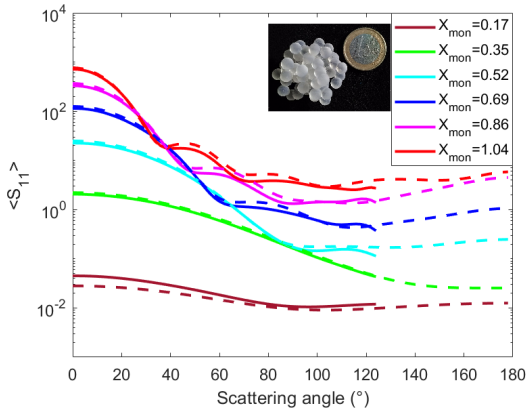

(b) Ag_DLA_Df2.5_N74

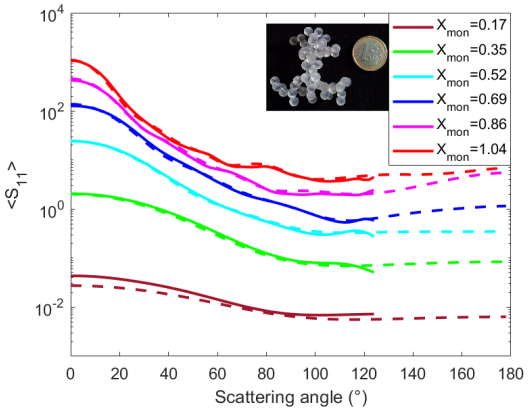

(c) Ag_DLA_Df2.0_N74_1

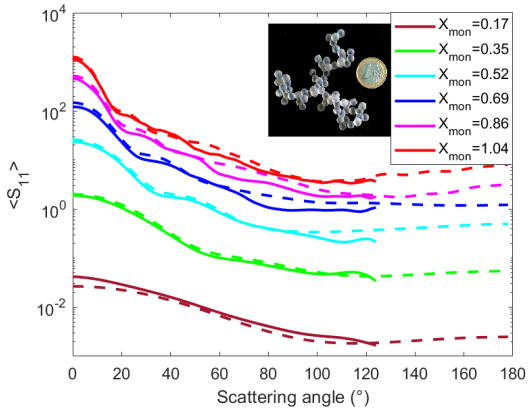

(d) Ag_DLA_Df1.7_N74

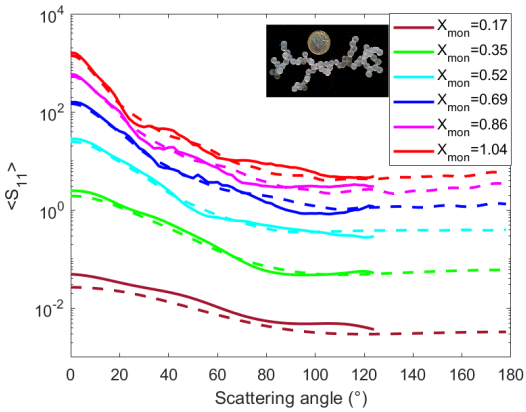

(e) Ag_DLA_Df1.5_N74

Figure 2.8: Phase function of aggregates with different fractal dimensions, measurements (solid lines) and numerical simulations (dashed lines), from $X_{mon} = 0.17$ to $X_{mon} = 1.04$.

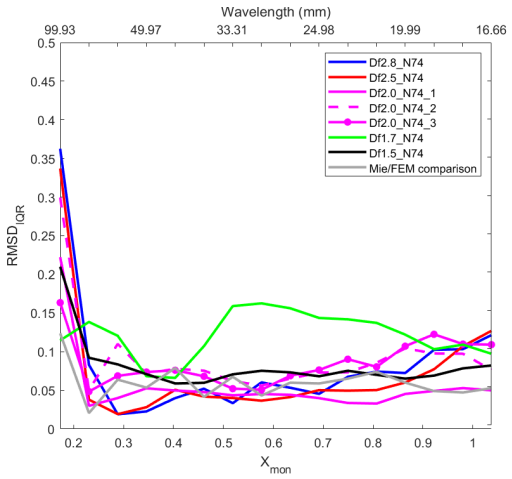

Figure 2.9: Normalized root mean square deviations on the log of the phase function plotted for all the measured aggregates, taking their FEM numerical simulation as reference. The gray line is a comparison of the Mie simulation versus FEM numerical simulation with a sphere of 32.5mm in diameter.

The phase function of Ag_DLA_Df2.8_N74 has defined peaks and valleys at high X_{mon} for the forward-scattering peak and bumps. At $X_{mon} = 1.04$, $X_{mon} = 0.86$ and $X_{mon} = 0.69$, the monomer size is about the same size as the wavelength and the aggregate size parameter is about five to four times the wavelength. Hence, the whole aggregate size is close to λ and so the behavior is that of Mie scattering. On the contrary, size parameters from $X_{mon} = 0.17$ to $X_{mon} = 0.52$ have only the forward-scattering peak, corresponding to $X_{agg} = 0.97$ to $X_{agg} = 2.92$, respectively. As the size of the whole aggregate has decreased compared to the wavelength, the scattering becomes almost isotropic, thereby there is only the forward-scattering peak for the phase function.

It is important to notice that as all our aggregates have the same refractive index for a given monomer size parameter, changes in the phase function are entirely attributable to changes in the structure of the whole aggregate. For this reason, when $X_{mon} << 1$ (Rayleigh regime), e.g. $X_{mon} = 0.17$ (see Figure 2.10), all our aggregates are small compared to the wavelength and thus their phase function, curve shape, is similar. They all have the forward scattering peak, presenting differences in their width. On the contrary, at $X_{mon} = 1.04$, as the fractal dimension increases toward 2.8 the bumps are well-defined and slowly disappear as the fractal dimensions decreases to 1.5.

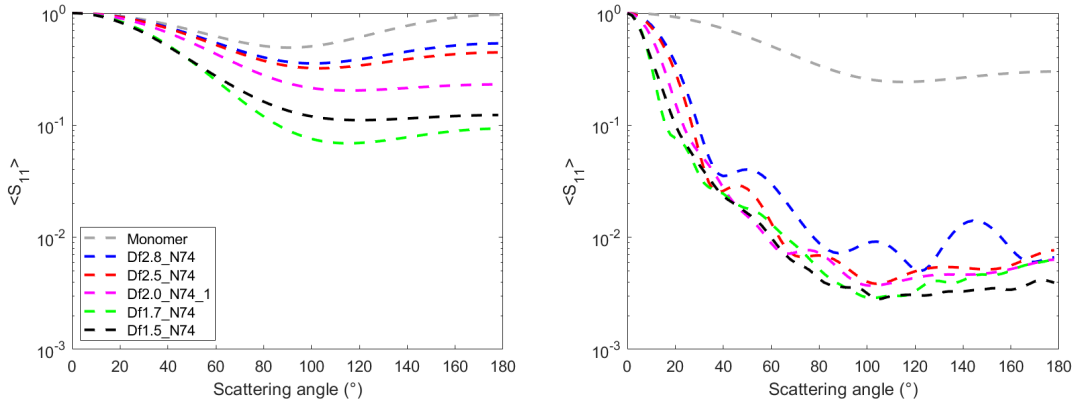

(a) Phase function at $X_{mon} = 0.17$

(b) Phase function at $X_{mon} = 1.04$

Figure 2.10: FEM numerical simulations of normalized phase function of aggregates with different fractal dimensions at $X_{mon} = 0.17$ and $X_{mon} = 1.04$. The gray line is the Mie simulation for a sphere with the same radius as that of a monomer.

Another analysis that can be done is comparing the phase function of aggregates having the same fractal dimension. Figure 2.11 presents the phase function of another two aggregates of $D_f = 2$ which were generated using the same software and parameters ($N = 74$, $K_0 = 1.593$, $a_{int} = a1.1$) but as the software creates random positions of each monomer, each type of aggregate is completely unique. Comparing aggregates having the same fractal dimension, it is shown that even if all three aggregates (Ag_DLA_Df2.0_N74_1, Ag_DLA_Df2.0_N74_2 and Ag_DLA_Df2.0_N74_3) were generated with different monomer configurations, phase function curves at the same X_{mon} present similar forward-scattering peaks and same levels. The aggregate that has a little difference in terms of the width of the phase function forward-scattering peak is Ag_DLA_Df2.0_N74_1 compared to the other two aggregates. In brief, these three aggregates present similar scattering properties as can be seen in Figure 2.12 for superposed phase functions.

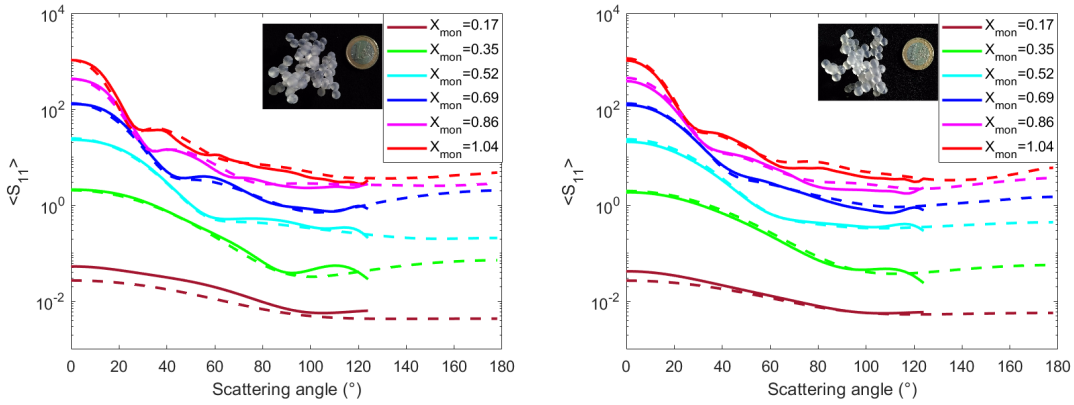

(a) Ag_DLA_Df2.0_N74_2 (b) Ag_DLA_Df2.0_N74_3

Figure 2.11: Phase function of aggregates having the same fractal dimension $D_f = 2.0$, measurements (solid lines) and numerical simulations (dashed lines), from $X_{mon} = 0.17$ to $X_{mon} = 1.04$.

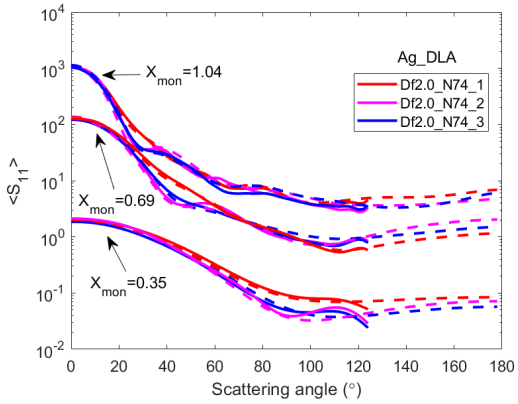

Figure 2.12: Measurements (solid lines) and numerical simulations (dashed lines) of the scattering phase function of three aggregates having the same fractal dimension $D_f = 2$, at different X_{mon}.

Based on the phase function, an important element that can be calculated is the half-width at half-maximum (HWHM). Table 2.3 shows the evolution of HWHM of the phase function of all aggregates at different X_{mon}. From $X_{mon} = 0.35$ to 1.04, at each size parameter, there is a decrease of the width from the biggest to the smallest fractal dimension which was the expected behavior because the forward-scattering peak width is inversely proportional to the size of the object [79]. Thus, as the object becomes smaller or at least its bounding sphere (from fluffy aggregates to compact aggregates) becomes smaller, the forward-scattering peak becomes wider.

At $X_{mon} = 0.17$, width values for all aggregates are around an average of 55,5° for measurements and 57,5° for simulations, which is mainly due to the size of wave-

lengths compared to all the sizes of aggregates (small aggregates compared to the wavelength, Rayleigh behavior).

X_{mon} / Ag_DLA	Df2.8_N74	Df2.5_N74	Df2.0_N74_1	Df1.7_N74	Df1.5_N74
0.17	56 (54)	52 (56)	54 (58)	60 (58)	50 (54)
0.35	78 (80)	78 (80)	56 (56)	40 (42)	48 (46)
0.52	64 (62)	60 (58)	48 (46)	32 (32)	38 (36)
0.69	50 (46)	46 (46)	46 (44)	28 (26)	32 (32)
0.86	42 (40)	36 (36)	36 (34)	32 (32)	26 (30)
1.04	32 (32)	30 (30)	30 (28)	26 (26)	22 (28)

X_{mon} / Ag_DLA	Df2.0_N74_1	Df2.0_N74_2	Df2.0_N74_3
0.17	54 (58)	64 (62)	54 (60)
0.35	56 (56)	58 (58)	56 (60)
0.52	48 (46)	40 (42)	42 (42)
0.69	46 (44)	34 (34)	36 (34)
0.86	36 (34)	28 (26)	30 (28)
1.04	30 (28)	24 (18)	26 (22)

Table 2.3: HWHM of phase function in degrees at different X_{mon} for different fractal dimensions. Measured values (numerical values).

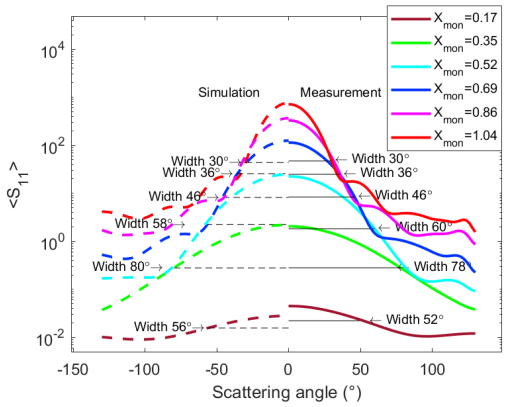

Figure 2.13: Example of measured (solid lines) and numerical (dashed lines) HWHM of the phase function of Ag_DLA_Df2.5_N74.

Another analysis that can be done based on Table 2.3 is to study for each aggregate how the width decreases at different X_{mon}, from 0.35 to 1.04. For example, Ag_DLA_-Df2.8_N74 has a measured HWHM from 78° (numerical 80°) to 32° (numerical 32°). All aggregates present this decrease because as wavelength get smaller, the size of the object compared to the wavelength is bigger, and so the forward-scattering peak will be narrowed. This effect is illustrated in Figure 2.13 for aggregate Ag_DLA_Df2.5_N74 comparing the numerical simulation and measurements and in Figure 2.14 comparing all aggregates HWHM in terms of the inverse of aggregates size parameter, showing the linearity of this behavior.

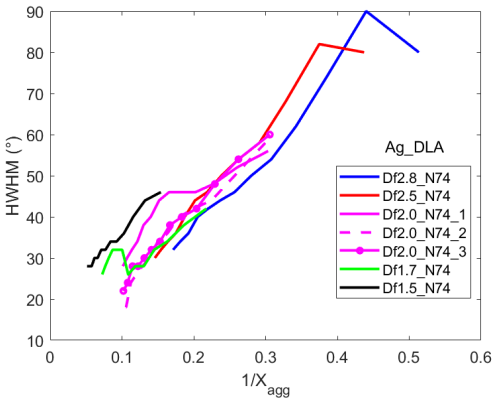

Figure 2.14: Numerical HWHM of the phase function for all aggregates with their corresponding inverse X_{agg}, from $\lambda = 50$ to 16.7 mm.

2.4.2.2 Degree of linear polarization

The degree of linear polarization (named in [117] as DOP, named herein DLP to be more precise) of aggregates with average orientation of different D_f are presented in Figure 2.15 at different wavelengths or X_{mon}. Numerical simulations and measurements of DLP are quantitatively compared with our comparison criterion. Similar to the phase function, the $RMSD_{IQR}$ was calculated for the DLP as shown in Figure 2.16. In general, the levels of $RMSD_{IQR}$ for DLP are larger for all aggregates than for the phase function. This is due to the sensitivity of DLP as it is the division of two Mueller matrix elements. Additionally, Ag_DLA_Df2.8_N74 has more discrepancies than other aggregates, arriving to levels of 0.5 which we think that might be caused by its compactness. Indeed this aggregate is almost a sphere, thus it has a pseudo-sphere behavior in which at large X_{mon} it produces multiple DLP oscillations contrary to fluffier structures.

In general, all aggregates DLP in Figure 2.15 have a bell shape at $X_{mon} = 0.17$ and $X_{mon} = 0.35$ because when $X_{mon} << 1$ (Rayleigh regime), e.g. $X_{mon} = 0.17$, our aggregates are small compared to the wavelength and so the DLP has a maximum level of 1 without any depolarization as it is the case of a sphere in the Rayleigh regime. For example, in Figure 2.15.a for Ag_DLA_Df2.8_N74 and in Figure 2.17.a for all aggregates, the Mie simulation for a sphere with the same size as that of a monomer is presented in gray line, showing a polarization at 1, thus no depolarization. On the contrary, as monomer size parameter increases, different behaviors for each aggregate are shown. For Ag_DLA_Df2.8_N74, from $X_{mon} = 0.52$ to $X_{mon} = 1.04$ there is the presence of oscillations named as the pseudo-sphere behavior by [138]. These oscillations are also shown for Ag_DLA_Df2.5_N74 but with lower depolarization. For $D_f = 2$, Ag_DLA_-Df2.0_N74_1, oscillations are enveloped by the bell-shape behavior having DLP peak levels around 0.9 to 0.7. This phenomenon of Rayleigh-like behavior was also seen by [136, 106, 137, 146], the main cause being the small size of constituent particles or

monomers compared to the wavelength (subwavelength monomers). In this case all $X_{mon} < 1$ except for 1.04 where the bell-shape is deformed. Yet, there is another phenomenon that causes this Rayleigh-like behavior because all aggregates are composed of the same monomer, thus this behavior should happen in all aggregates which is not the case.

Indeed, as fractal dimension increases, coupling between monomers are going to be more important and so we verified that, at $D_f > 2$, there is coupling represented on the phase function bumps named as multiple scattering by [157]. This effect is also demonstrated with the DLP of Figure 2.17.b, where the polarization is not only a contribution of the primary structure (monomer), but additionally there is an effect of depolarization that we suggest is due to coupling between monomers. Hence, among all aggregates, Ag_DLA_Df2.8_N74 presents the largest depolarization and Ag_DLA_Df1.5_N74, the smallest. The Mie sphere simulation corresponding to the monomer (gray line), does not present any depolarization. In other words, the aggregates presenting a higher porosity (97.91% and 94.90%) will have higher levels of DLP while the least porous ones (Ag_DLA_Df2.8_N74 and Ag_DLA_Df2.5_-N74 with porosities of 25.88% and 54.78%, respectively) will have lower levels of DLP. This behavior was also seen by the simulations of amorphous silicate aggregates (refractive index of $1.689 + 0.0031i$ and $1.677 + 0.0044i$ at $\lambda = 0.45\mu$m and 0.65μm) containing $N = 2048$ in [143], and it was related to different porosities (between 59% to 98%) using different types of aggregation, i.e. Ballistic Cluster Cluster Agglomeration (BCCA), Ballistic Agglomeration (BA), Ballistic Agglomeration with 1 and 2 migrations (BAM1 and BAM2).

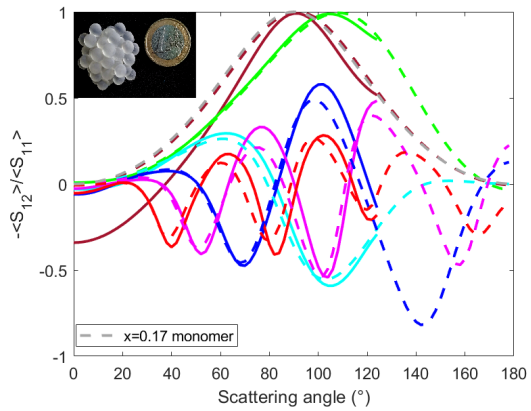

(a) Ag_DLA_Df2.8_N74

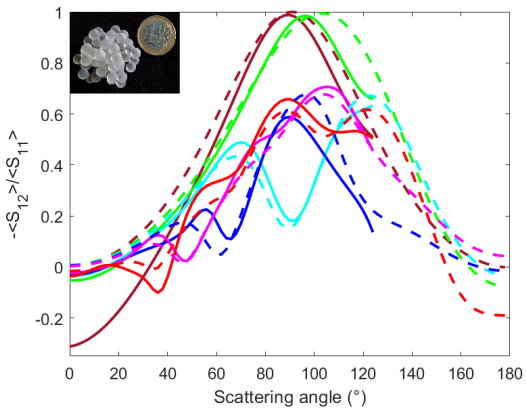

(b) Ag_DLA_Df2.5_N74

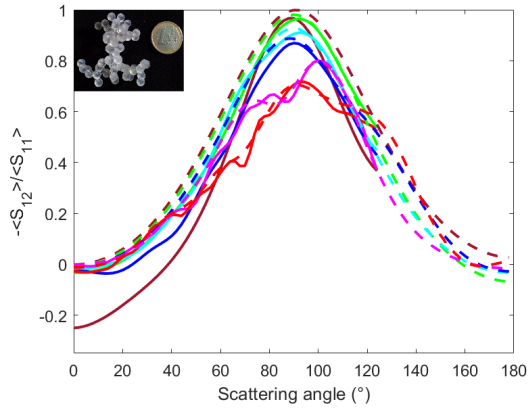

(c) Ag_DLA_Df2.0_N74_1

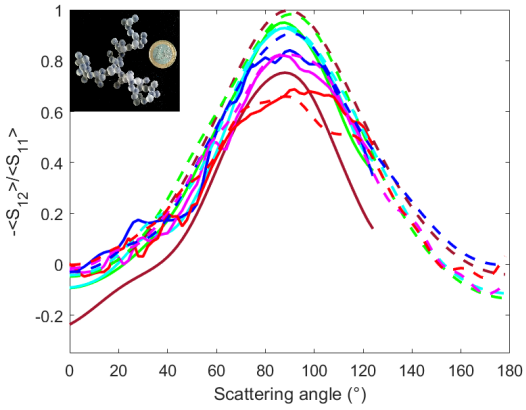

(d) Ag_DLA_Df1.7_N74

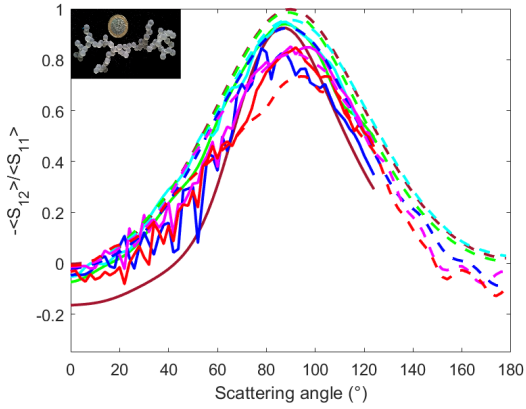

(e) Ag_DLA_Df1.5_N74

Figure 2.15: DLP of aggregates with different fractal dimensions, measurements (solid lines) and numerical simulations (dashed lines), from X_{mon} = 0.17 to X_{mon} = 1.04 (see the legend of Figure 2.8). Gray line in (a) is the Mie simulation for a sphere with the same size as that of a monomer.

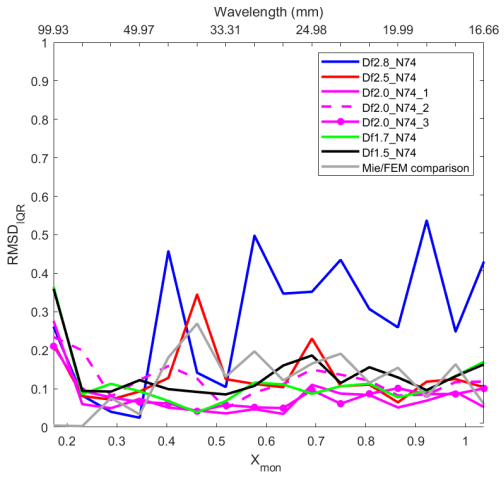

Figure 2.16: Normalized root mean square deviations on the DLP plotted for all the measured aggregates, taking their FEM numerical simulation as reference. The gray line is a comparison of the Mie simulation versus FEM numerical simulation with a sphere of 32.5mm in diameter.

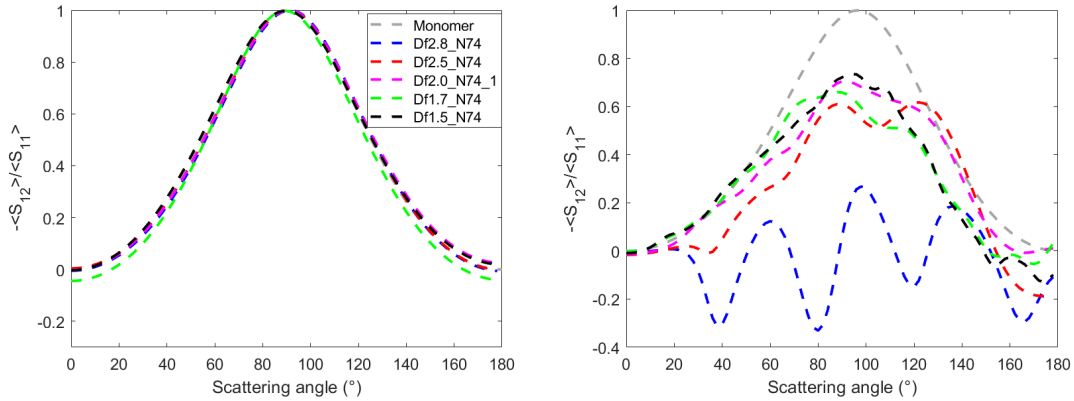

(a) DLP at $X_{mon} = 0.17$

(b) DLP at $X_{mon} = 1.04$

Figure 2.17: FEM numerical simulations of normalized DLP of aggregates with different fractal dimensions at $X_{mon} = 0.17$ and $X_{mon} = 1.04$. The gray line is a Mie simulation for a sphere with the same size as that of a monomer.

The DLP was also analyzed for aggregates having the same fractal dimension, $D_f = 2$ in Figure 2.18. Aggregates Ag_DLA_Df2.0_N74_1, Ag_DLA_Df2.0_N74_2 and Ag_DLA_-Df2.0_N74_3 are superposed at two different X_{mon} in Figure 2.19. As can be seen, at the same X_{mon}, all three aggregates have same levels and behaviors of DLP.

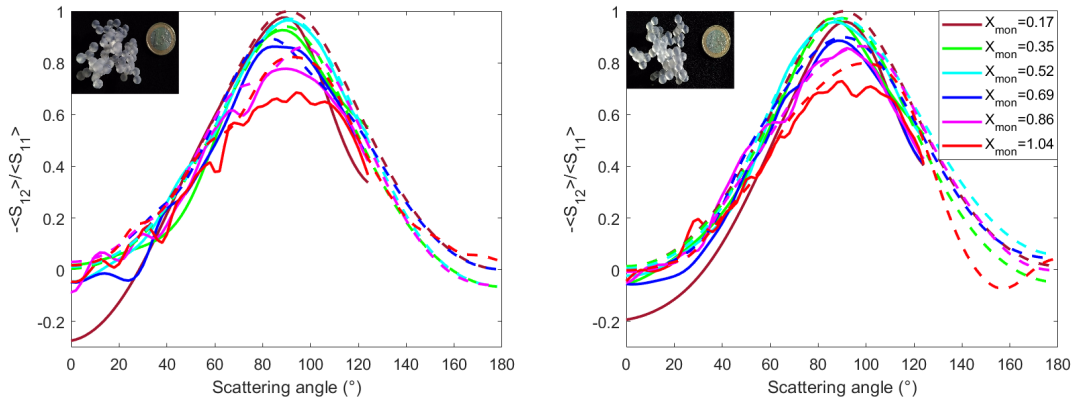

(a) Ag_DLA_Df2.0_N74_2 (b) Ag_DLA_Df2.0_N74_3

Figure 2.18: DLP of aggregates having the same fractal dimension $D_f = 2.0$, measurements (solid lines) and numerical simulations (dashed lines), from $X_{mon} = 0.17$ to $X_{mon} = 1.04$.

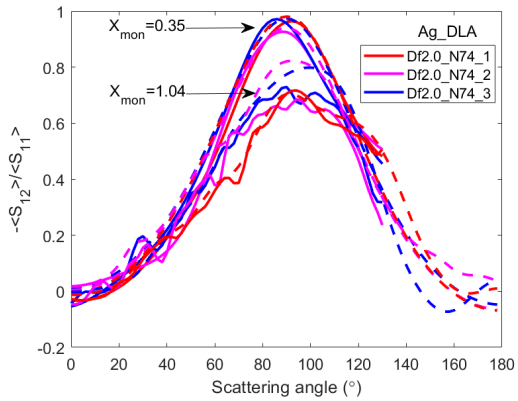

Figure 2.19: Measurements (solid lines) and numerical simulations (dashed lines) of DLP of three aggregates having the same fractal dimension $D_f = 2$ at different X_{mon}.

Another analysis that can be made based on DLP of different aggregates is to identify the angles where there is the maximum level of DLP at different X_{mon} for measurements and numerical simulations (see Table 2.4). It is important to note that all values have at least an uncertainty of 2° due to the angular sampling. The angles at maximum DLP are proposed to be analyzed at each X_{mon} for the different fractal dimensions. At $X_{mon} = 0.17$, all aggregates results for simulations and measurements have maximum DLP around 90°. However, at the other five size parameters, even if angles of maximum DLP are not to far from 90°, there is a tendency: large fractal dimensions ($D_f = 2.8$ and 2.5) have maximum DLP located at large scattering angles while small

fractal dimensions (D_f = 1.5) have maximum DLP located at smaller scattering angles. There is only one exception in which the maximum DLP of Ag_DLA_Df2.8_N74 has a smaller angle at X_{mon} = 0.52 than Ag_DLA_Df1.5_N74. This later can be seen in Figure 2.15.a (cyan line) where this DLP curve is in a transition between Mie-like behavior and a Rayleigh-like behavior giving this unusual scattering angle out of the expected behavior. Based on literature, DLP is mainly affected by monomers [113, 109, 114] so knowing that all the aggregates have the same monomer size and refractive index, the only difference that rest between them is their monomer organization. Large fractal dimensions (D_f = 2.8 and 2.5) have monomers that are closer together while fluffy aggregates ($D_f \leq 2$) have monomers that are farther from each other. The interaction between monomers creates a coupling, as previously explained. Thus, since the only difference between aggregates is their monomer positions we suppose that the difference of maximum levels of DLP (and corresponding scattering angle) from a big fractal dimension compared to a small fractal dimension is due to coupling effects. In other words, Ag_DLA_Df1.5_N74 has a DLP that is caused by monomers while Ag_DLA_Df2.8_N74 has a DLP that is caused by monomers plus the coupling between them, making the difference of angles between small and big fractal dimensions, and the difference between the levels of depolarizations.

X_{mon} / Ag_DLA	Df2.8_N74	Df2.5_N74	Df2.0_N74_1	Df1.7_N74	Df1.5_N74
0.17	92 (92)	90 (90)	88 (90)	88 (90)	86 (90)
0.35	104 (108)	96 (104)	92 (90)	88 (90)	88 (88)
0.52	62 (62)	124 (122)	92 (90)	88 (88)	88 (90)
0.69	102 (98)	90 (96)	90 (88)	90 (90)	78 (88)
0.86	124 (122)	106 (104)	100 (100)	86 (88)	90 (92)
1.04	102 (98)	90 (122)	94 (92)	92 (88)	92 (94)

X_{mon} / Ag_DLA	Df2.0_N74_1	Df2.0_N74_2	Df2.0_N74_3
0.17	88 (90)	88 (90)	92 (90)
0.35	92 (90)	88 (90)	86 (90)
0.52	92 (90)	90 (92)	88 (90)
0.69	90 (88)	84 (84)	88 (90)
0.86	100 (100)	90 (96)	92 (98)
1.04	94 (92)	94 (92)	90 (100)

Table 2.4: Angles in degrees corresponding to the maximum DLP at different X_{mon} for different fractal dimensions. Measured values (numerical values).

2.4.2.3 Conclusions

The main conclusions of our study of the phase function (Section 2.4.2.1) and the degree of linear polarization (Section 2.4.2.2) for aggregates with average orientation are:

1. The FEM numerical simulation and measurement results of the phase function and DLP for all of our aggregates were consistent. Simulations and measurements for both scattering parameters had similar behaviors and levels proving

a cross-validation. Based on our comparison criterion, the phase function had $RMSD_{IQR} \leq 0.35$ and for DLP, $RMSD_{IQR} \leq 0.5$.

2. All aggregates were generated and produced with the same refractive index, monomer size and controlled geometry allowing to compare the phase function and DLP with constant parameters. Based on this, at $X_{mon} = 0.17$, the phase function of all aggregates had the same shape of curve and level showing a Rayleigh behavior at $\lambda = 100$ mm. This behavior was also proven by the maximum DLP at the same wavelength presenting a value of ≈ 1 at 90° for all aggregates.

3. The three aggregates having a $D_f = 2$ presented a similar phase function and DLP. Levels and curve behaviors of both parameters were very close, especially between Ag_DLA_Df2.0_N74_2 and Ag_DLA_Df2.0_N74_3.

4. At $X_{mon} << 1$, the fractal dimension can be differentiated by the phase function width, while at $X_{mon} = 1$ the differences of depolarization in DLP can provide a notion of this fractal dimension.

5. HWHM of the phase function presented larger values for compact aggregates and smaller values for fluffier aggregates, which is a normal effect based on the diffraction theory.

6. The maximum DLP of porous aggregates has higher levels at the same wavelength than for compact aggregates as was already shown in literature.

7. The maximum DLP presented a tendency: as the fractal dimension increased, the value of the maximum was located at larger scattering angles, except at $X_{mon} = 0.52$ for Ag_DLA_Df2.8_N74 and Ag_DLA_Df1.5_N74. We suggest that this tendency is due to coupling effects between monomers since the only difference between aggregates is their monomers positions which create coupling.

It should be noted that in general, both scattering parameters, phase function and DLP, present a lot of little oscillations due to the fact that measurements and simulations are done for one object in multiple orientations and not with a size distribution of particles that would minimize these oscillations. For this reason, Section 2.4.3 is focused on the analysis of these two scattering parameters while adding a size distribution.

2.4.2.4 Other scattering parameters

The aim of this section is to study other scattering properties based on Mueller matrix elements $< S_{22} >$, $< S_{44} >$ and $< S_{34} >$ (Equation 2.3) in order to validate (or observe other) scattering behaviors that were (or not) seen for the same aggregates with the phase function and the DLP. These Mueller matrix elements are presented in literature

with the normalization of the phase function giving three scattering parameters: $\frac{<S_{22}>}{<S_{11}>}$ related to non-sphericity [79, 158], $\frac{<S_{44}>}{<S_{11}>}$ related to the degree of circular polarization [79] and $\frac{<S_{34}>}{<S_{11}>}$ related to the polarization at 45°. Note that with current observations made with telescopes, it is possible to obtain polarimetric images of protoplanetary disks, retrieving the phase function and the DLP of these optically thick disks [83]. Yet, other scattering parameters are still not possible to be retrieved with observations. Current developments to observe, for example, the degree of circular polarization are being done at the Very Large Telescope [159]. Thus, the scattering parameters that are presented in this section can be used for future comparisons with protoplanetary disk observations.

As previously explained in Section 2.4, $\frac{<S_{22}>}{<S_{11}>}$ is the only parameter for which the inclusion of cross-polarized elements is necessary. Thus for this parameter, results are only presented in terms of numerical simulations. Measurements with our microwave scattering experiment in CCRM can be performed to obtain the two Jones cross-polarized elements, yet the time per measurement of aggregate would double and there is a lower accuracy with these cross-polarized measurements. For this reason, I chose to forget about measuring this cross-polarization and I preferred to measure more samples. Thus $\frac{<S_{22}>}{<S_{11}>}$ is the only parameter that is fully based on numerical simulations. $\frac{<S_{22}>}{<S_{11}>}$ is correlated with depolarization as explained in [138]. As cross-polarization becomes more important, the phase function $< S_{11} >$ increases and $< S_{12} >$ decreases, thus the ratio $-\frac{<S_{12}>}{<S_{11}>}$ or DLP reduces. This is the case for irregular objects, contrary to a single sphere where cross-polarization does not happen. Therefore, $\frac{<S_{22}>}{<S_{11}>}$ gives information about the non-sphericity of an aggregate [160]. If $\frac{<S_{22}>}{<S_{11}>} = 1$ the object is spherical, and when $\frac{<S_{22}>}{<S_{11}>} < 1$ the object tends to be less spherical.

Figure 2.20 presents $\frac{<S_{22}>}{<S_{11}>}$ based on numerical simulations at different X_{mon} or wavelengths. At $X_{mon} = 0.17$, all aggregates have $\frac{<S_{22}>}{<S_{11}>}$ values around 1 all along the scattering angles, which was expected because the aggregate size is very small compared to the wavelength, so aggregates act like Rayleigh spheres. Yet, the difference of this parameter between aggregates starts being visible at $X_{mon} = 0.35$. At $X_{mon} = 1.04$, the most compact aggregate Ag_DLA_Df2.8_N74, has the lowest $\frac{<S_{22}>}{<S_{11}>}$ value of 0.88 while for the two least compact aggregates, $D_f = 1.7$ and $D_f = 1.5$, $\frac{<S_{22}>}{<S_{11}>}$ values are 0.73 and 0.78, respectively. Indeed, particles with smaller fractal dimensions are less spherical while compact aggregates are more spherical having smaller levels of cross-polarization and thus values of $\frac{<S_{22}>}{<S_{11}>}$ closer to 1. This general behavior is seen for all aggregates at $X_{mon} = 0.35$ (see Figure 2.21.a) where three groups can be identified: the most fluffly aggregates with $\frac{<S_{22}>}{<S_{11}>}$ values around 0.975, intermediate aggregates with values around 0.990 and the most compact aggregate with values of 0.998. Yet, for larger X_{mon}, this behavior fails for Ag_DLA_Df2.5_N74 for which $\frac{<S_{22}>}{<S_{11}>}$ levels are similar to the two most fluffy aggregates (see Figure 2.21.b). It is important to note that this parameter was also studied for the three aggregates with same fractal dimension $D_f = 2$ having similar levels and behaviors at different X_{mon}, proving the similarity in

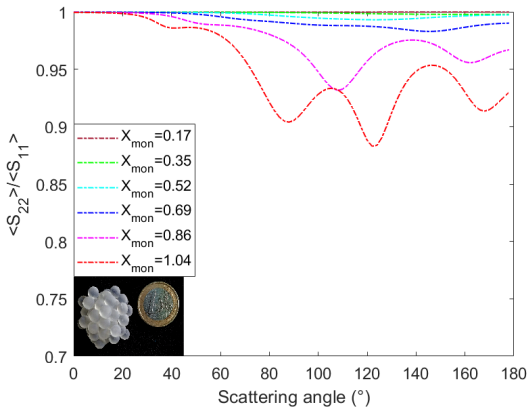

(a) Ag_DLA_Df2.8_N74

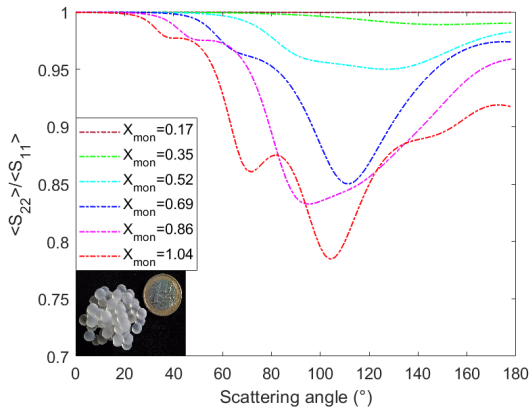

(b) Ag_DLA_Df2.5_N74

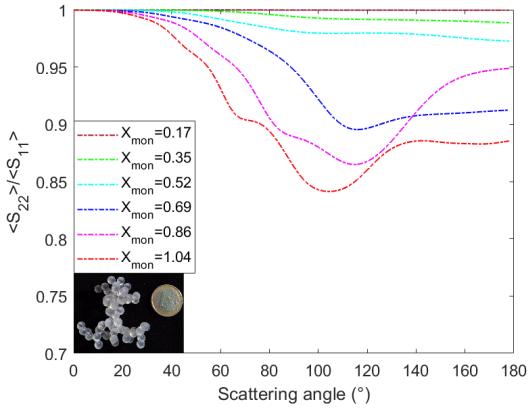

(c) Ag_DLA_Df2.0_N74_1

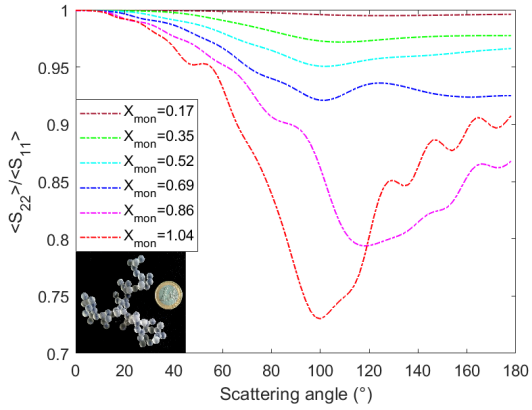

(d) Ag_DLA_Df1.7_N74

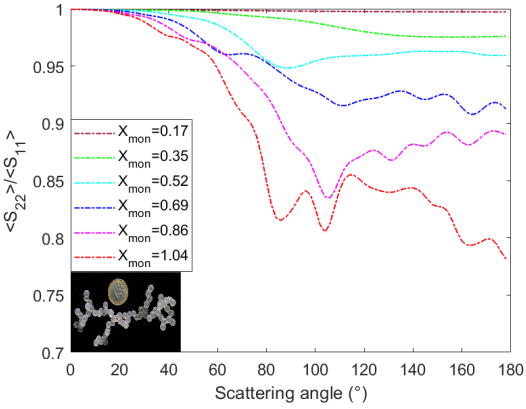

(e) Ag_DLA_Df1.5_N74

Figure 2.20: FEM numerical simulations of $< S_{22} > / < S_{11} >$ including co-polarized and cross-polarized elements of the Jones matrix of aggregates with different fractal dimensions, from $X_{mon} = 0.17$ to $X_{mon} = 1.04$.

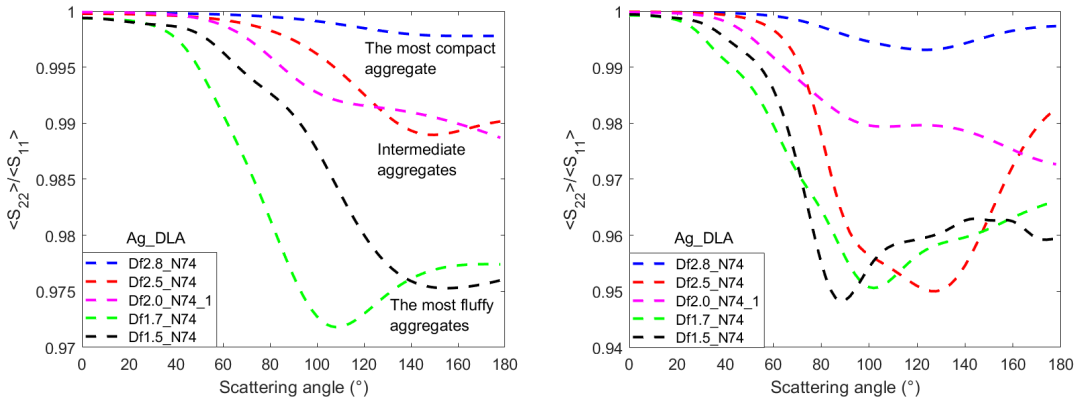

(a) $< S_{22} > / < S_{11} >$ at $X_{mon} = 0.35$ (b) $< S_{22} > / < S_{11} >$ at $X_{mon} = 0.52$

Figure 2.21: FEM numerical simulations of $< S_{22} > / < S_{11} >$ for aggregates with different fractal dimensions at $X_{mon} = 0.35$ and $X_{mon} = 0.52$.

their non-sphericity. The lowest $\frac{<S_{22}>}{<S_{11}>}$ values for the three are, at $X_{mon} = 1.04$, around 0.8 for Ag_DLA_Df2.0_N74_2 and Ag_DLA_Df2.0_N74_3 and around 0.84 for Ag_DLA_-Df2.0_N74_1. Therefore, with our numerical simulations, we can effectively show the sphericity of the aggregates based on $\frac{<S_{22}>}{<S_{11}>}$ levels and behaviors.

Another Mueller matrix element is $< S_{33} >$ which is equal to $< S_{44} >$ (explained in Section 2.4), and from now on we refer only to $< S_{44} >$. This element is measurable in the anechoic chamber of CCRM because it only needs the co-polarized elements. The ratio $\frac{<S_{44}>}{<S_{11}>}$ is proportional to the degree of circular polarization-DCP [see Equation 14.5 in 79] and it is shown in Figure 2.22 for all aggregates. $\frac{<S_{44}>}{<S_{11}>}$ for all aggregates present a Rayleigh behavior at $X_{mon} = 0.17$ having values around 1 at forward scattering angles up to 60° and smoothly decreasing toward -1 at backscattering angles. Behaviors of $\frac{<S_{44}>}{<S_{11}>}$ at larger monomer size parameters, $X_{mon} > 0.17$, depend on each aggregate (or D_f). $\frac{<S_{44}>}{<S_{11}>}$ of compact aggregates have important oscillations that increases with X_{mon}. On the contrary, $\frac{<S_{44}>}{<S_{11}>}$ of aggregates with $D_f \leq 2$ present almost no oscillations and only larger differences are seen at backscattering angles.

Additionally, $\frac{<S_{34}>}{<S_{11}>}$ shown in Figure 2.23 was measured and numerically simulated for all aggregates. At $X_{mon} = 0.17$, there is again an evidence of the Rayleigh behavior [85]. At this size parameter, $\frac{<S_{34}>}{<S_{11}>}$ of all aggregates have values very close to zero all along the scattering angles. For larger X_{mon}, compact aggregates, i.e., Ag_DLA_Df2.8_-N74 and Ag_DLA_Df2.5_N74, present $\frac{<S_{34}>}{<S_{11}>}$ with amplitudes of oscillations that are more important at middle scattering angles. In contrast, $\frac{<S_{34}>}{<S_{11}>}$ of fluffy aggregates show small oscillations around ± 0.2.

2.4.2.5 Conclusions

To conclude, these three scattering parameters $\frac{<S_{22}>}{<S_{11}>}$, $\frac{<S_{44}>}{<S_{11}>}$, and $\frac{<S_{34}>}{<S_{11}>}$ highlight some conclusions that were already seen with the phase function and the DLP: i) numerical simulations and measurements are consistent, ii) aggregates with $D_f = 2$ have similar scattering properties, iii) at $X_{mon} = 0.17$, scattering parameters of all aggregates have a Rayleigh behavior and iv) important differences within each scattering parameter can be seen at larger X_{mon} for different D_f. Additionally, $\frac{<S_{44}>}{<S_{11}>}$ and $\frac{<S_{34}>}{<S_{11}>}$ have obvious different behaviors at $X_{mon} > 0.17$ between compact aggregates ($D_f > 2$) and fluffy aggregates ($D_f \leq 2$). Compact aggregate curves have more oscillations while fluffy aggregate curves follow the Rayleigh behavior. Thus, these two parameters can give a notion if the aggregate has a fractal dimension smaller or bigger than 2. This latter is due to the behavior of the Mie sphere that compact aggregates have on these scattering parameters, as was already observed for DLP. Regarding $\frac{<S_{22}>}{<S_{11}>}$, there are more visible differences between one dimension to another, differentiating all five fractal dimensions in three groups at $X_{mon} = 0.35$, yet at other values of X_{mon} this distinction cannot be done because $\frac{<S_{22}>}{<S_{11}>}$ of aggregate Ag_DLA_Df2.5_N74 acts as a fluffy aggregate.

In sum, scattering parameters $\frac{<S_{44}>}{<S_{11}>}$ and $\frac{<S_{34}>}{<S_{11}>}$ validate the scattering behaviors that were already seen with the phase function and DLP for these aggregates. These four scattering parameters are able to be obtained with the microwave scattering experiment at the CCRM anechoic chamber . Instead, $\frac{<S_{22}>}{<S_{11}>}$ can give extra an information to identify between fluffy aggregates, intermediate aggregates and compact aggregates at $X_{mon} = 0.35$, but this parameter is more difficult to be measured and doubles the measurement time with our scattering experiment. Today telescopes can obtain polarimetric images, where phase function and DLP can be retrieved, as was previously mentioned. Therefore, with our measurements we can calculate the scattering parameters that can be obtained with telescopes. Being able to retrieve other scattering parameters, i.e $\frac{<S_{22}>}{<S_{11}>}$, $\frac{<S_{44}>}{<S_{11}>}$, and $\frac{<S_{34}>}{<S_{11}>}$, with our scattering experiment or numerical simulations is an advantage and may only be used for possible future comparisons with observations.

All these scattering parameters analyzed in Section 2.4.2 provide different or/and complementary information about the morphology of the aggregates, yet in order to do a complete analogy of protoplanetary dust a size distribution must be included as it is going to be shown in the following section.

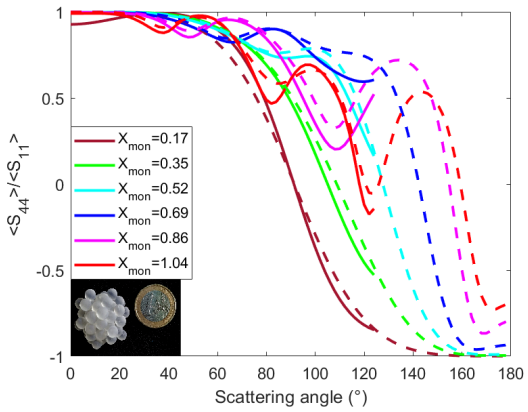

(a) Ag_DLA_Df2.8_N74

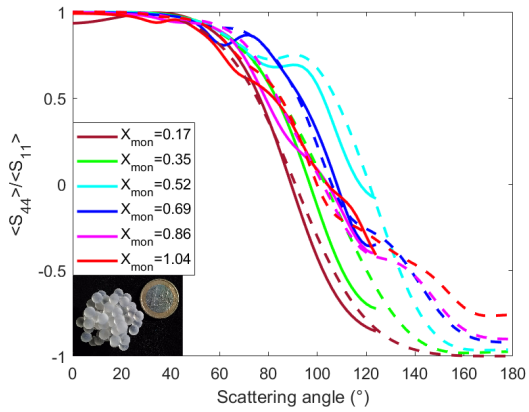

(b) Ag_DLA_Df2.5_N74

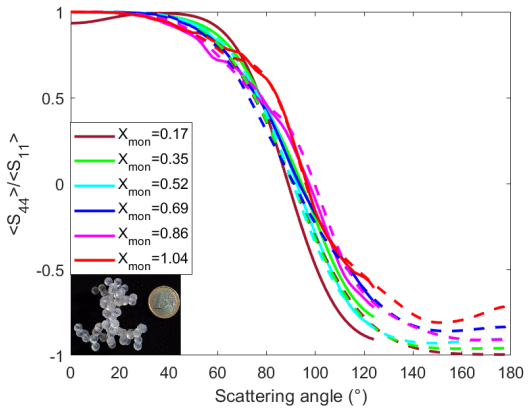

(c) Ag_DLA_Df2.0_N74_1

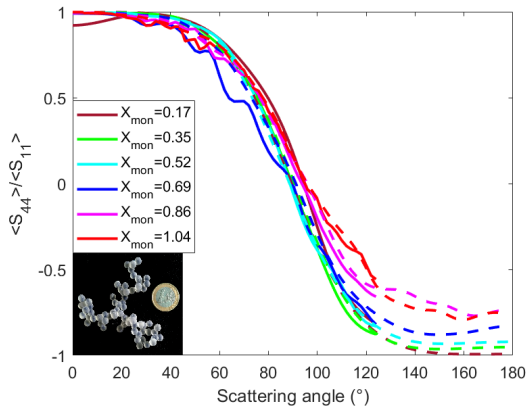

(d) Ag_DLA_Df1.7_N74

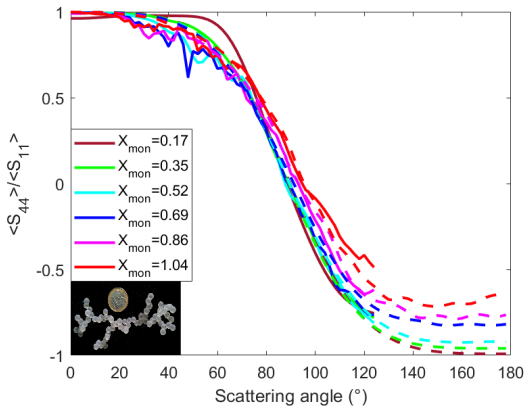

(e) Ag_DLA_Df1.5_N74

Figure 2.22: $< S_{44} > / < S_{11} >$ of aggregates with different fractal dimensions. Measurements (solid lines) and numerical simulations (dashed lines), from $X_{mon} = 0.17$ to $X_{mon} = 1.04$.

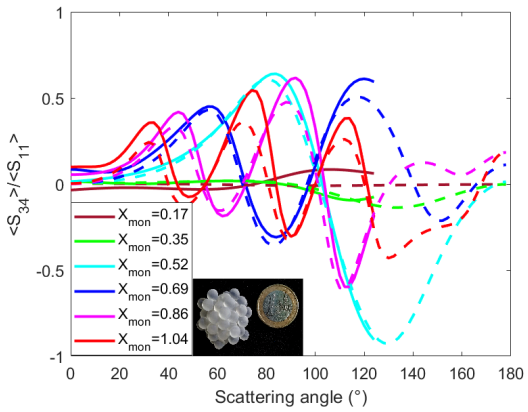

(a) Ag_DLA_Df2.8_N74

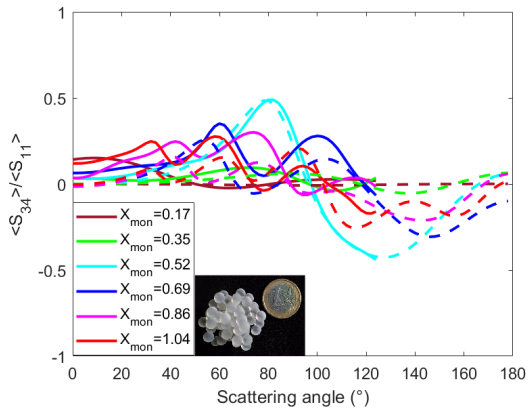

(b) Ag_DLA_Df2.5_N74

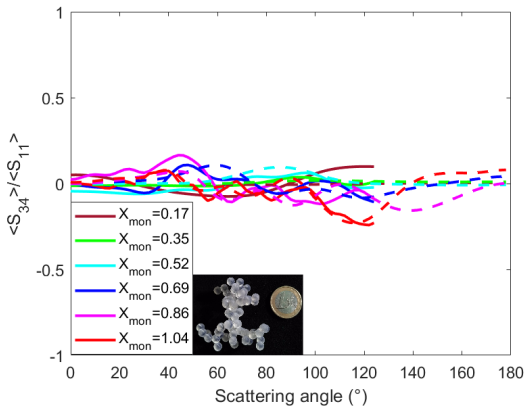

(c) Ag_DLA_Df2.0_N74_1

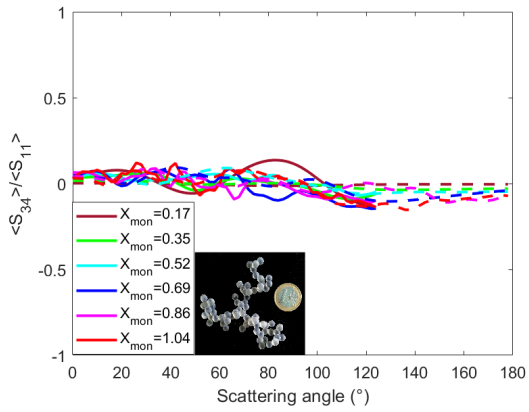

(d) Ag_DLA_Df1.7_N74

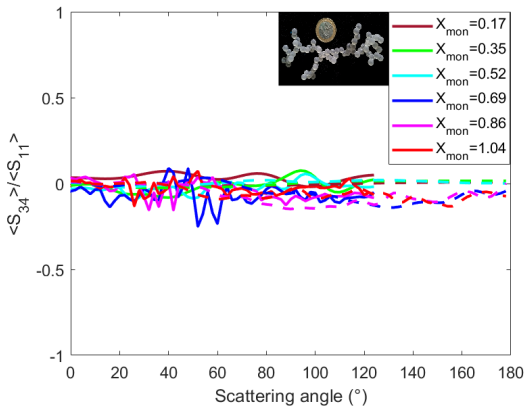

(e) Ag_DLA_Df1.5_N74

Figure 2.23: $< S_{34} > / < S_{11} >$ of aggregates with different fractal dimensions. Measurements (solid lines) and numerical simulations (dashed lines), from $X_{mon} = 0.17$ to $X_{mon} = 1.04$.

2.4.3 Aggregates with average orientation and size distribution effect

2.4.3.1 Probability distribution

Based on [52] and described in Section 1.2.3, we suppose protoplanetary dust sizes between 0.1µm to 10µm when considering optical and NIR data. This means that these particles cannot efficiently emit in the millimeter band. Even so, there are images of protoplanetary disks in ALMA band 3, $\lambda = 2.6$mm to 3.6mm, (see example of disk HL Tau observed in the ALMA Long Baseline Campaign [161]), implying the presence of dust sizes of orders of millimeters. However, dust of millimeter sizes are bad emitters at NIR and optical wavelengths, when considering a power law size distribution of index −3.5 [57] which gives more weigh to small particles. Therefore, if we are interested in NIR wavelengths, with this size distribution, the dust size we should take into account is between 0.1µm to 10µm, corresponding to size parameters of $X_{min} = 0.25$ to $X_{max} = 62.83$ (see Table 1.2).

During my PhD, size distribution was not directly applied to the radius but to the size parameter X_{mon} because we conserve the same aggregate but measured it at different wavelengths, i.e., the size of the monomer and aggregate changes compared to the wavelength. Thus, we have a population of 16 different monomer size parameters thanks to 16 wavelengths that were used for scattering measurements and simulations. With these measurements and simulations in multi-wavelengths, we can simulate a distribution of size written as $X_{mon}^{-3.5}$. Note that this simulation of size distribution scales the size of the monomer and whole aggregate, letting fixed the number of monomers and creating a population of homothetic aggregates. Thus we are applying an artificial size distribution that is called hereafter size distribution effect.

In order to do the microwave analogy and have the same scattering behavior as protoplanetary dust, we need to have the closest X_{min} of the protoplanetary dust population that we suppose. This X_{min} is of 0.25. We can achieve a similar value, when our simulations and measurements start at $\lambda = 60$ (5 GHz), obtaining $X_{mon} = 0.29$. Then the maximum protoplanetary size parameter $X_{max} = 62.83$ cannot be achieved by our analogs since the maximum that we have is $X_{mon} = 1.04$. Yet, with this size distribution effect, the probability of finding $X_{mon} = 1.04$ is of 0.07 (see probability of distribution in Equation 2.5), thus larger parameter sizes can be neglected because they are less likely to be present.

$$P(X) = \frac{X_{mon}^{-n_s}}{\frac{X_{max}^{-n_s+1} - X_{min}^{-n_s+1}}{-n_s+1}}, \tag{2.5}$$

where n_s is the index of the power law.

The same scattering parameters as the previous section were obtained including this size distribution effect $X_{mon}^{-3.5}$. Additionally, to have a complete analysis on how the index affects these scattering parameters, two more power law distributions with different indices were studied. Knowing that the supposed index is $n_s = 3.5$, we

decided to analyze the same scattering parameters at a lower and larger n_s, 2 and 5 (see Figure 2.24). The reason behind this decision is that a power law of $n_s = 3.5$ is a supposition not a certainty, hence different authors have been studying the scattering behavior at different indices. For example in [156], it was shown that size distribution ($1 < n_s < 4$) has a stronger impact on scattering behavior than the particle morphology. Therefore, the idea of this section is to give at the end some clues on which index and aggregate can give closer scattering behaviors directly comparable with other scattering laboratory results, numerical results and one circumstellar disk (see Section 2.4.4).

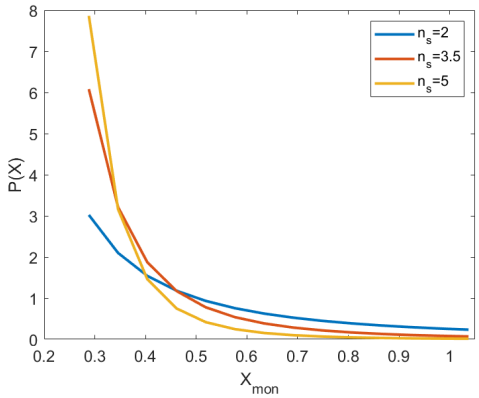

Figure 2.24: Probability distribution on the size parameter X_{mon}, from 0.29 to 1.04, with three different indices (see legend)

2.4.3.2 Phase function

After applying this size distribution effect of the three chosen indices, the scattering parameters were obtained. The phase function of all five aggregates corresponding to five different D_f is shown in Figure 2.25. Two main behaviors of the phase function are observed depending on the size distribution index. First, at $n_s = 2$, the forward scattering peak of the phase function of all aggregates presents a narrower HWHM compared to the other two phase functions obtained at larger n_s. There is a tendency that can be seen in Table 2.5, as n_s decreases from 5 to 2, the HWHM of the phase functions of all aggregates decreases. This behavior is due to fact that power law distributions with smaller n_s, i.e. 2, give more weight to larger X_{mon} and thus larger aggregate sizes. Therefore, as the size of the aggregate increases, the forward scattering peak narrows. Furthermore, it can be seen in Table 2.5 that for all three n_s, as the fractal dimension decreases, HWHM decreases too. Again, this is due to fact that large D_f, corresponding to compact aggregates, presents a smaller bounding sphere, compared to small D_f, which enlarges the forward scattering peak. The second observed behavior of the phase function is the enhancement of the backscattering, which is more important with $n_s = 2$ and $n_s = 3.5$ and decreases for $n_s = 5$. At all three

indices, from $D_f = 2.8$ to $D_f = 2.5$, the backscattering increases, and from $D_f = 2.5$ to $D_f = 1.5$, backscattering decreases. Thus, the fractal dimension with the most important enhancement is $D_f = 2.5$.

Comparing these phase functions with phase functions of previous section (without the size distribution effect see Figure 2.8 or see Figure 2.25.a curves named NSDE), several differences can be noted. First, characteristic bumps of phase functions of compact aggregates have disappeared (in Figure 2.25.a in brown line representing Ag_-DLA_Df2.8_N74 NDSE). As can be seen, all aggregates present smooth phase function curves when applying this size distribution effect. This latter was expected because applying this size distribution effect is averaging different sizes of the same aggregate thus averaging Rayleigh phase function behaviors of small X_{mon} with Mie behaviors of large X_{mon}. Moreover, little oscillations that were observed for porous aggregates without the size distribution (see Figure 2.25.a, gray line representing Ag_DLA_Df1.5_-N74 NDSE) also disappear with the size distribution effect because of the average. In brief, the size distribution effect smooths the phase functions of all aggregates. Second, the levels of the phase function in Figure 2.25 are organized from the most compact aggregate to the least compact. This levels are related to cross-sections thus, when the bounding radius of the aggregate is larger, then there will be larger scattered intensities. This behavior was also seen for aggregates without the size distribution effect. Nonetheless, one should apply caution in the interpretation of the scattered light from aggregates with different numbers of monomers since this changes the bounding radius and therefore it can be possible to find larger HWHM phase functions of compact aggregates with larger number of monomers than porous aggregates with smaller number of monomers. Hence, the level of the forward scattering peak of the phase function and its HWHM are not good parameters to identify from a porous aggregate to a compact aggregate when having aggregates with different numbers of monomers.

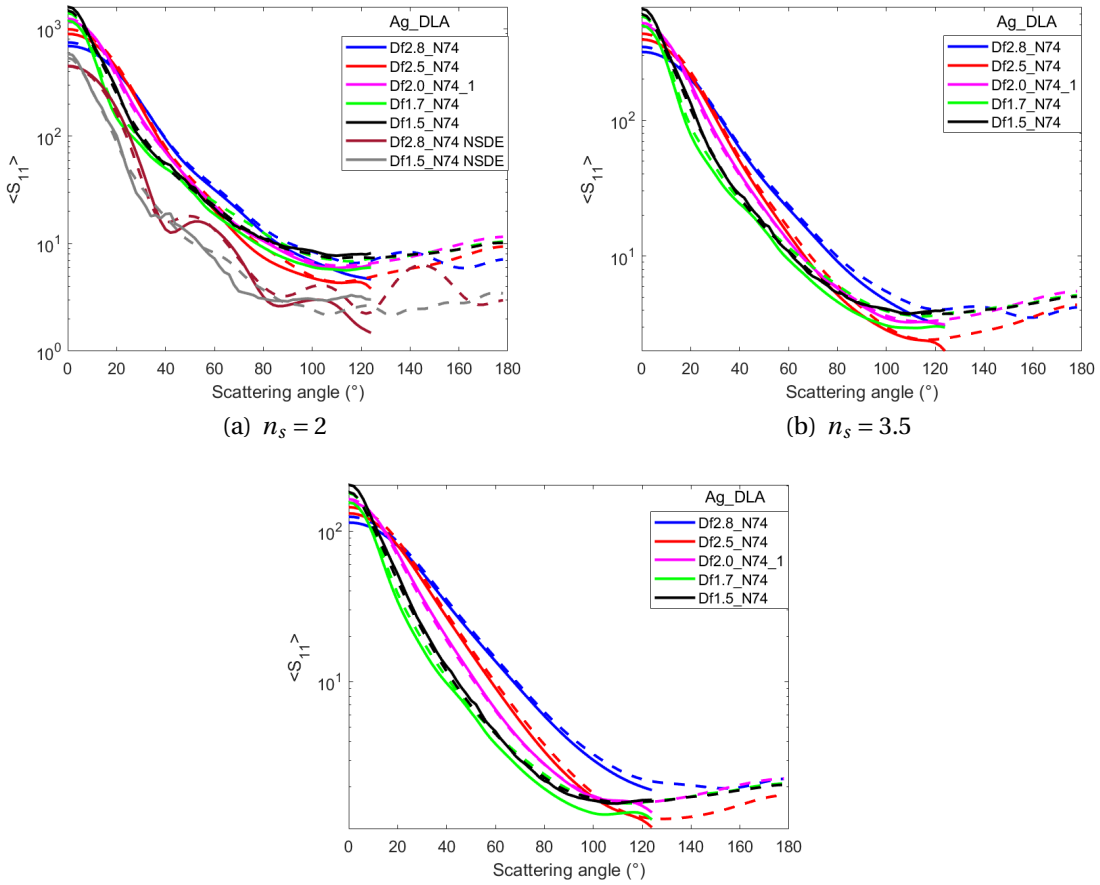

(a) $n_s = 2$ (b) $n_s = 3.5$

(c) $n_s = 5$

Figure 2.25: Phase function of aggregates with average orientation and with power law distributions of different n_s, measurements (solid lines) and numerical simulations (dashed lines). Figure (a) also presents the phase function of the most compact aggregate at $X_{mon} = 1.04$ (in brown) and most fluffy aggregate at $X_{mon} = 0.86$ (in gray) with No Size Distribution Effect (NSDE).

Being able to compare scattering measurements of aggregates wavelength by wavelength and then adding this size distribution effect is an advantage of our scattering experiment in CCRM. For example, if the index of the power law distribution need to be changed in the future, then data obtained with measurements and simulations do not need to change, the only change is on the index n_s to re-calculate the scattering parameter of interest.

n_s / Ag_DLA	Df2.8_N74	Df2.5_N74	Df2.0_N74_1	Df1.7_N74	Df1.5_N74
2	48 (46)	46 (42)	42 (36)	34 (28)	30 (30)
3.5	54 (52)	52 (48)	44 (40)	36 (30)	32 (32)
5	58 (58)	56 (54)	50 (42)	40 (32)	36 (34)

n_s / Ag_DLA	Df2.0_N74_1	Df2.0_N74_2	Df2.0_N74_3
2	42 (36)	36(30)	38(32)
3.5	44 (40)	40(34)	42(34)
5	50 (42)	46(40)	48(40)

Table 2.5: HWHM of phase function of aggregates with average orientation and with power law distributions of different n_s. Measured values (numerical values), both in degrees.

2.4.3.3 Degree of linear polarization

Figure 2.26 presents the degree of linear polarization of our aggregates. As can be seen, DLP curves present smoother behaviors compared to DLP of aggregates with only average orientation (see Figure 2.26.a with curves named NSDE). This smoothness is caused by the supplementary average of the size distribution effect as was also seen for the phase function curves.

One important characteristic of DLP is its maximum DLP levels. Compact aggregates, Ag_DLA_Df2.8_N74 and Ag_DLA_Df2.5_N74, present lower maximum DLP levels for the three chosen n_s. On the other hand, aggregates with $D_f \leq 2$ have superposed bell curves with similar maximum levels. This effect of D_f on the maximum DLP was also observed for DLP of aggregates with only average orientation (see Section 2.4.2.2). This latter showed that a bigger depolarization is due to coupling between monomers which decreases the maximum DLP levels of compact aggregates.

As n_s increases from 2 to 5, maximum levels of DLP increases for all aggregates as presented in Table 2.6, which is normal due to the important weight given to small X_{mon}, thus a tendency of Rayleigh behavior. Moreover, at each n_s, as fractal dimension decreases from $D_f = 2.8$ to $D_f = 1.5$, maximum levels increase. In general, maximum levels of DLP correspond to scattering angles between 90° for $D_f \leq 2$ to 100° for $D_f > 2$. This movement of scattering angles, corresponding to the maximum DLP and depending on D_f, was also showed for maximum DLP of aggregates with average orientation (see Table 2.4) but with more differences between scattering angles from one D_f to another.

Note that maximum levels of DLP and its corresponding scattering angles are related to the global structure (spherical or not spherical) of the aggregate but also to internal coupling (between monomers of a same aggregate). Spherical aggregates or compact aggregates depolarize less (as a sphere does) than fluffy aggregates, yet as compact aggregates have monomers that are assembled closer together, coupling is more important. Therefore the final depolarization increases for compact aggregates, presenting the lowest maximum levels of DLP among all aggregates. On the contrary, fluffy aggregates depolarize more because its level of sphericity decreases. However,

the coupling between monomers of fluffy aggregates is smaller than for compact aggregates, thus the sum of these two phenomenons (non sphericity + smaller coupling) creates a smaller depolarization compared to compact aggregates, and therefore presenting larger maximum levels. For this reason, even if the number of monomers is different from one compact aggregate to a fluffy aggregate (example that can happen in nature) their general structure (sphericity) and coupling might stay the same. Thus, based on DLP, we can differentiate between compact and fluffy aggregates without being affected by the number of monomers, contrary to the phase function. This is of high importance at the moment of choosing one scattering parameter that is more sensitive to distinguish between aggregates of different D_f without fixed number of monomers.

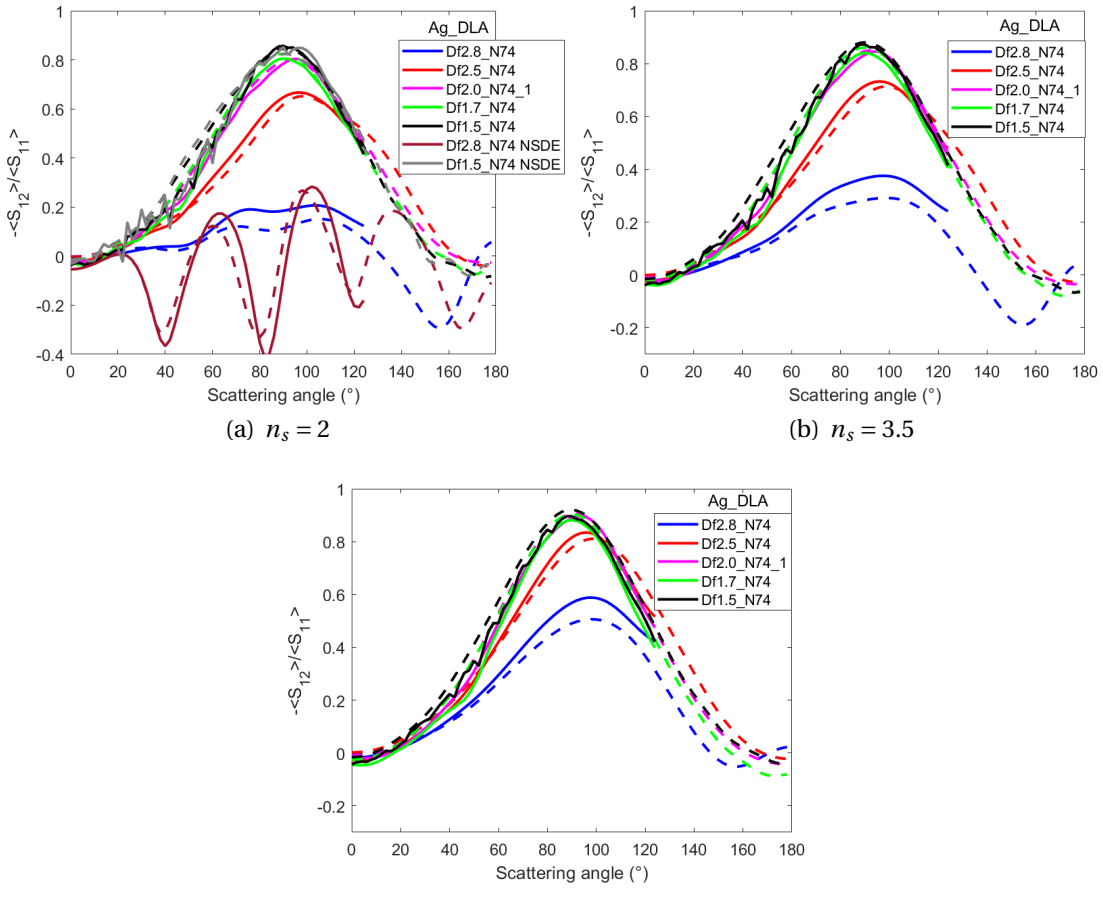

(a) $n_s = 2$

(b) $n_s = 3.5$

(c) $n_s = 5$

Figure 2.26: DLP of aggregates with average orientation and with power law distributions of different n_s, measurements (solid lines) and numerical simulations (dashed lines). Figure (a) also presents DLP of the most compact aggregate at $X_{mon} = 1.04$ (in brown) and most fluffy aggregate at $X_{mon} = 0.86$ (in gray) with No Size Distribution Effect (NSDE).

Finally, another observed characteristic of DLP is the negative polarization branch in the backscattering. This branch seen in Figure 2.26 is more prominent for Ag_DLA_-Df2.8_N74 compared to other aggregates, arriving to levels of −0.3 with $n_s = 2$ to levels of −0.05 with $n_s = 5$. Levels of negative polarization branches for other aggregates are always at similar values between 0 to −0.1.

n_s/ Ag_DLA	Df2.8_N74	Df2.5_N74	Df2.0_N74_1	Df1.7_N74	Df1.5_N74
2	0.21 (0.15)	0.67 (0.65)	0.80 (0.80)	0.81 (0.82)	0.86 (0.84)
3.5	0.38 (0.29)	0.73 (0.71)	0.85 (0.85)	0.84 (0.86)	0.87 (0.88)
5	0.59 (0.51)	0.83 (0.81)	0.90 (0.91)	0.88 (0.90)	0.90 (0.92)

n_s/ Ag_DLA	Df2.0_N74_1	Df2.0_N74_2	Df2.0_N74_3
2	0.80 (0.80)	0.80 (0.80)	0.84 (0.86)
3.5	0.85 (0.85)	0.85 (0.88)	0.87 (0.89)
5	0.90 (0.91)	0.89 (0.91)	0.91 (0.92)

Table 2.6: Levels of maximum DLP of aggregates with average orientation and with power law distributions of different n_s. Measured values (numerical values).

2.4.3.4 Other scattering parameters

Parameter $\frac{<S_{22}>}{<S_{11}>}$ is presented in Figure 2.27. As can be seen, levels of $\frac{<S_{22}>}{<S_{11}>}$ are larger with $n_s = 2$ for all aggregates compared to $n_s = 3.5$ and $n_s = 5$. This latter is expected due to the weight given to small size aggregates at $n_s = 5$, thus aggregates are smaller compared to the wavelength and so they act as Rayleigh spheres. Remember that when $\frac{<S_{22}>}{<S_{11}>}$ is closer to 1, it means the scattered object is more spherical. For $n_s = 2$ and $n_s = 3.5$, two groups of aggregates can be differentiated, one group being the most compact aggregate Ag_DLA_Df2.8_N74 with values of $\frac{<S_{22}>}{<S_{11}>}$ closer to 1 and the other group being the rest of the aggregates, thus less spherical. For $n_s = 5$, three groups can be differentiated: the first group with the most compact aggregate Ag_DLA_Df2.8_N74 with $\frac{<S_{22}>}{<S_{11}>}$ levels of approximately 1, the second group with aggregates of $D_f = 2.5$ and 2.0 and levels around 0.95, and the last group with aggregates of $D_f = 1.7$ and 1.5 and levels around 0.93. In short, with an index of 5 it is easier to identify aggregates of different fractal dimensions, yet the other two indices differentiate from the most compact $D_f = 2.8$ to the rest of fractal dimensions. This scattering parameter, that is related to sphericity, can be helpful at the moment of identifying aggregates of different D_f together with DLP. Finally, when comparing curves of this parameter with ot without the size distribution effect, curves of $\frac{<S_{22}>}{<S_{11}>}$ with the size distribution are smoother. This effect is also seen for the following two scattering parameters $\frac{<S_{44}>}{<S_{11}>}$ and $\frac{<S_{34}>}{<S_{11}>}$.

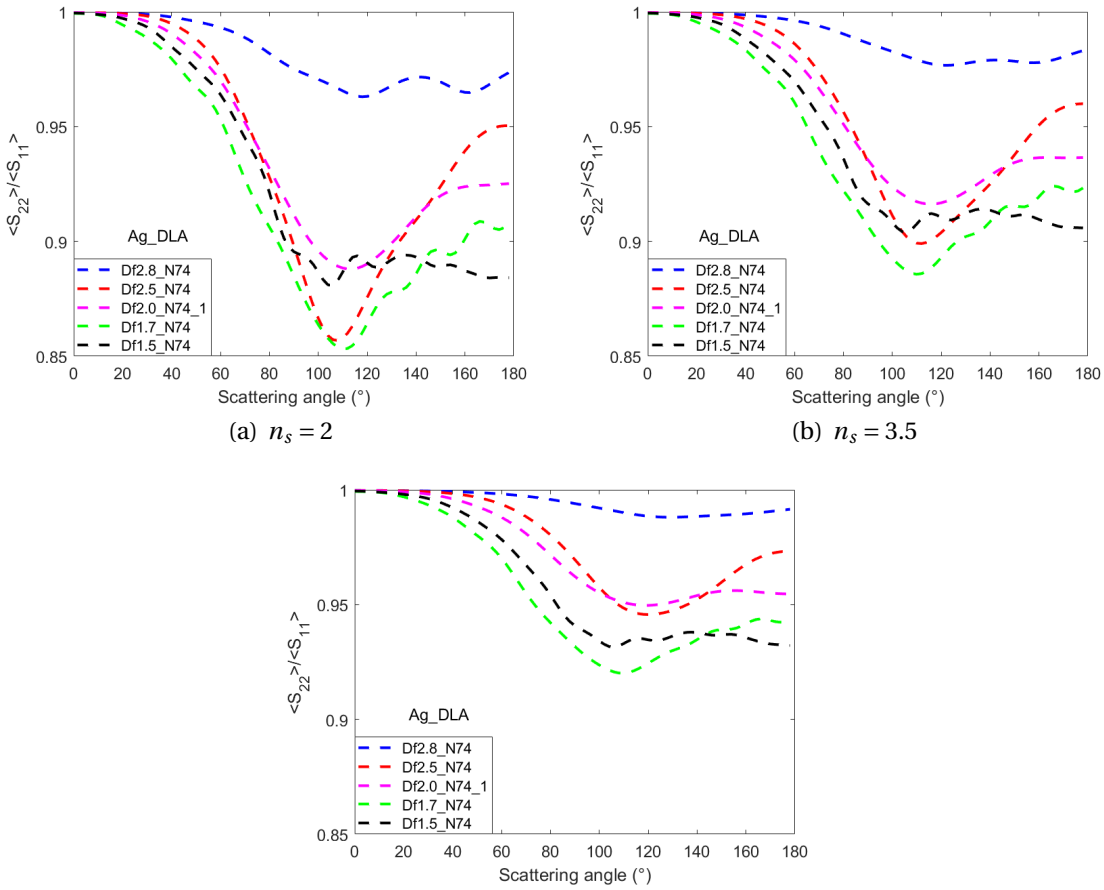

(a) $n_s = 2$ (b) $n_s = 3.5$

(c) $n_s = 5$

Figure 2.27: $< S_{22} > / < S_{11} >$ of aggregates with average orientation and with power law distributions of different n_s based on numerical simulations (dashed lines).

Parameter $\frac{<S_{44}>}{<S_{11}>}$ is presented in Figure 2.28. For all three indices, aggregates with $D_f \leq 2$ have the same Rayleigh behavior superposing all three curves. In the case of the two most compact aggregates, Ag_DLA_Df2.8_N74 and Ag_DLA_Df2.5_N74, differences of the curve shape between them and between the rest of aggregates are visible for all three n_s, specially at $n_s = 2$ where a characteristic bump for Ag_DLA_-Df2.8_N74 is present at 134°. This bump is also shown for other two n_s at the same scattering angle but with lower levels. Thus, this scattering parameter allows to make a difference between fluffy (Rayleigh behavior) and compact (Mie behavior) aggregates but also within compact aggregates like it was the case for DLP. Thus this parameter only validates the same scattering information already seen with DLP.

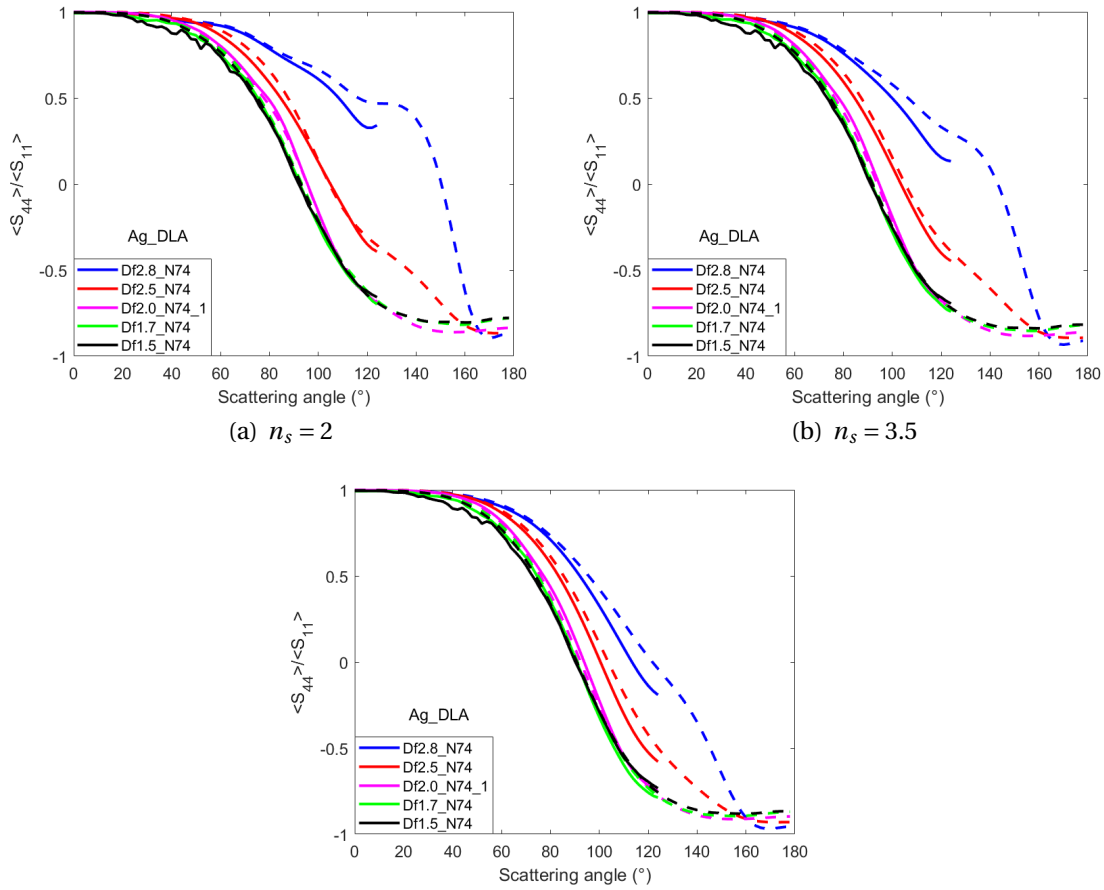

(a) $n_s = 2$ (b) $n_s = 3.5$

(c) $n_s = 5$

Figure 2.28: $< S_{44} > / < S_{11} >$ of aggregates with average orientation and with power law distributions of different n_s, measurements (solid lines) and numerical simulations (dashed lines).

Parameter $\frac{<S_{34}>}{<S_{11}>}$ shown in Figure 2.29, presents two main behaviors for aggregates with all three indices. The first behavior is related with compact aggregates where a positive and negative oscillation of ±0.2 is shown, being positive for scattering angles up to 120° and negative for backscattering angles. The second behavior is related to aggregates with $D_f \leq 2$, where $\frac{<S_{34}>}{<S_{11}>}$ values are around zero at all scattering angles. Even if these two behaviors are seen for all three indices, in general, oscillations are smoother and have smaller amplitudes when increasing index from $n_s = 2$ to $n_s = 5$ because weight is given to small aggregates thus Mie oscillations decrease. Using this scattering parameter allows us to differentiate between compact aggregates and fluffy aggregates, thus it does not add any extra information about the scattering behaviors compared to previous parameters.

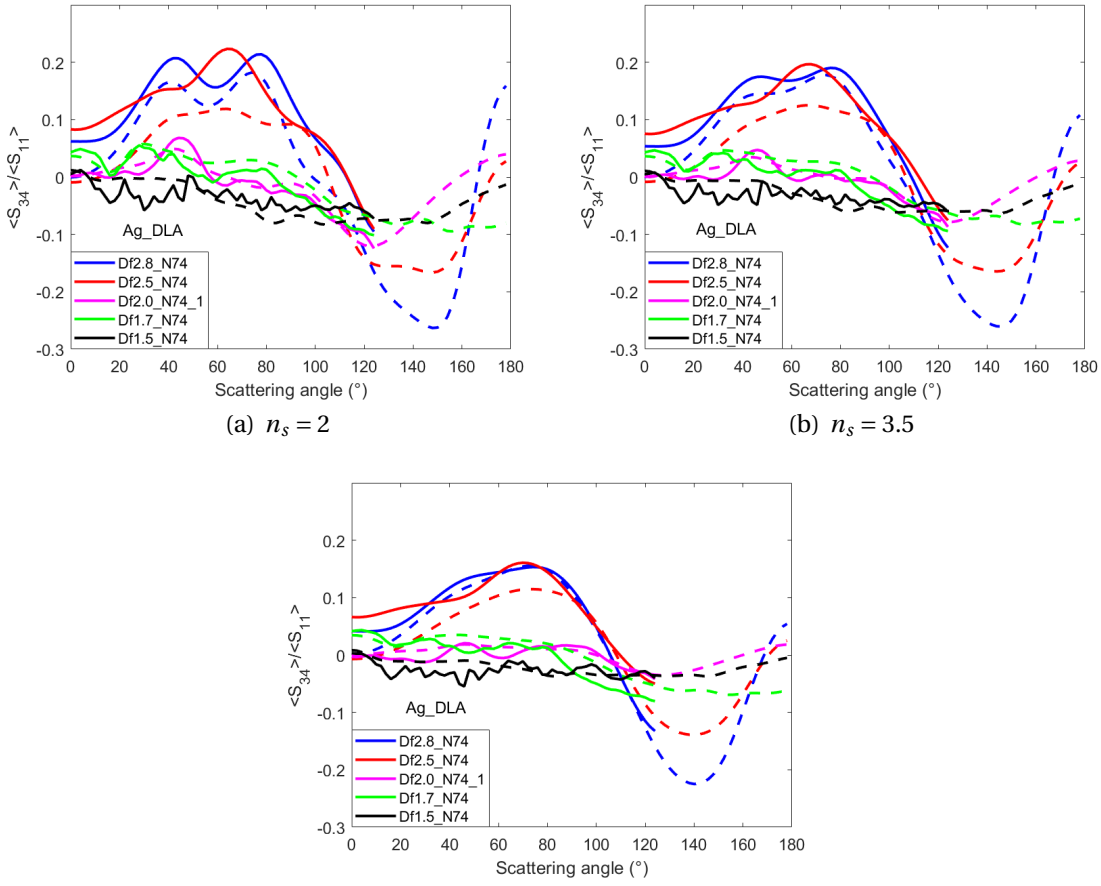

(a) $n_s = 2$ (b) $n_s = 3.5$

(c) $n_s = 5$

Figure 2.29: $< S_{34} > / < S_{11} >$ of aggregates with average orientation and with power law distributions of different n_s, measurements (solid lines) and numerical simulations (dashed lines).

2.4.3.5 Conclusions

In conclusion, we were able to compare scattering parameters of aggregates with and without the inclusion of the size distribution effect. Actually, since we have the individual measurements, analog by analog, and at different wavelengths, this gives us the possibility of constructing any distribution we want, which is an advantage of our scattering measurements and numerical simulations.

When comparing these scattering parameters without a size distribution effect and with the size distribution effect at $n_s = 3.5$ (used for protoplanetary dust), we observed that the smoothness of curves increases for all scattering parameters when applying the size distribution. This was expected since the size distribution is averaging even more the scattering parameters. Having these parameters without size distribution effect allowed us to understand which were the phenomena behind to obtain the

final scattering parameters including the effect of distribution. Note that this cannot be done when measuring a population of aggregates in a jet stream with light scattering technique because as a population, particles have already a determined size distribution and they do not have access to the individual measurements aggregate by aggregate.

Furthermore, all these scattering parameters can give complementary or validate information about the morphology of the aggregate, differentiating compact from fluffy aggregates. For example DLP showed how fluffy aggregates ($D_f \leq 2$) tend to have more a Rayleigh-like behavior while compact aggregates ($D_f > 2$) present a Mie-like behavior (residual oscillations of Mie after applying the size distribution). This was validated by $\frac{<S_{44}>}{<S_{11}>}$ and $\frac{<S_{34}>}{<S_{11}>}$.

Moreover, the difference between fractal dimensions of fixed number of monomers can be identified with: i) the HWHM and backscattering enhancement of the phase function, ii) maximum level of DLP and negative polarization branch, iii) the levels of $\frac{<S_{22}>}{<S_{11}>}$, iv) the smoothness of curve $\frac{<S_{44}>}{<S_{11}>}$, and v) the oscillation or flatness around zero of curve $\frac{<S_{34}>}{<S_{11}>}$. However, if the number of monomers is not fixed, which is the case in nature, i.e., with protoplanetary dust, from all these scattering parameters, DLP, levels of maximum DLP and its corresponding scattering angle can differentiate from porous aggregates to compact aggregates even if the number of monomers changes because the effect of depolarization is completely related to the morphology (sphericity) and coupling. DLP can be analyzed together with $\frac{<S_{22}>}{<S_{11}>}$ that is a scattering parameter directly related to sphericity.

To conclude which of the three indices of the power law size distribution is more adequate, a direct comparison with other laboratory scattering measurements of aggregates, numerical simulations of protoplanetary disks and observations of one circumstellar disk are proposed in the following section.

2.4.4 Direct comparison of scattering parameters found in the literature

After obtaining different scattering parameters which showed an excellent agreement between measurements and numerical simulations, direct comparisons with scattering parameters of aggregates with similar conditions found in different papers are made. Three types of comparisons are presented: with laboratory measurements, with numerical simulations and with observations of one circumstellar disk. Remember that in this PhD study we cannot make direct comparisons with protoplanetary disk images because, to create the synthetic images based on our Mueller matrix elements, a radiative transfer code needs to be used which is out of the limits of this study. This will be for future works.

2.4.4.1 Laboratory measurements

In [106] phase functions for cosmic dust analog aggregates ($X_{agg} \approx 5$) are retrieved and measured with light scattering technique. Samples 3 and 4 made of magnesiosilica have similar refractive index and size parameter to our aggregates (see Figure 2.30). These two samples have similar phase function shapes to Ag_DLA_Df1.7_N74 and Ag_DLA_Df1.5_N74 with size distribution effect of $n_s = 2$. Yet, there is a difference at small scattering angles around 5°.

Moreover, DLP shown in [106] presents maximum DLP levels of 0.8 for both samples which is also the case for aggregates Ag_DLA_Df1.7_N74 and Ag_DLA_Df1.5_N74 with $n_s = 2$ (see Figure 2.31), yet negative polarization branch values are larger for our aggregates (between −0.07 to −0.08 while in [106] values are around −0.02).

Additionally, general behavior and values of parameter $\frac{<S_{22}>}{<S11>}$ are also consistent with our results for the same two aggregates at $n_s = 2$, having values around 0.85 and 0.9 as shown herein (see Figure 2.32).

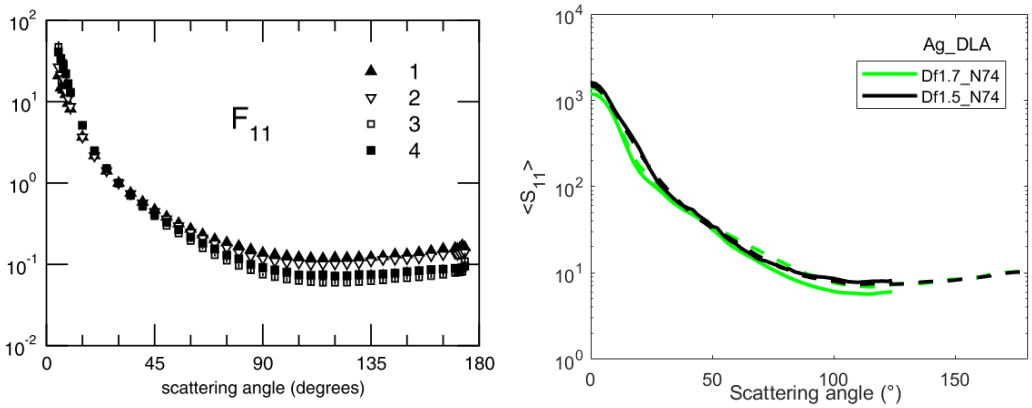

(a) Phase functions taken from [106]

(b) Our phase functions

Figure 2.30: Laboratory scattering measurements comparison of the phase function. (a) Phase function of samples 3 and 4 [see Figure 7 in 106], (b) phase function of our aggregates Ag_DLA_Df1.7_N74 and Ag_DLA_Df1.5_N74 with power law distribution effect of $n_s = 2$ for measurements (solid lines) and numerical simulations (dashed lines).

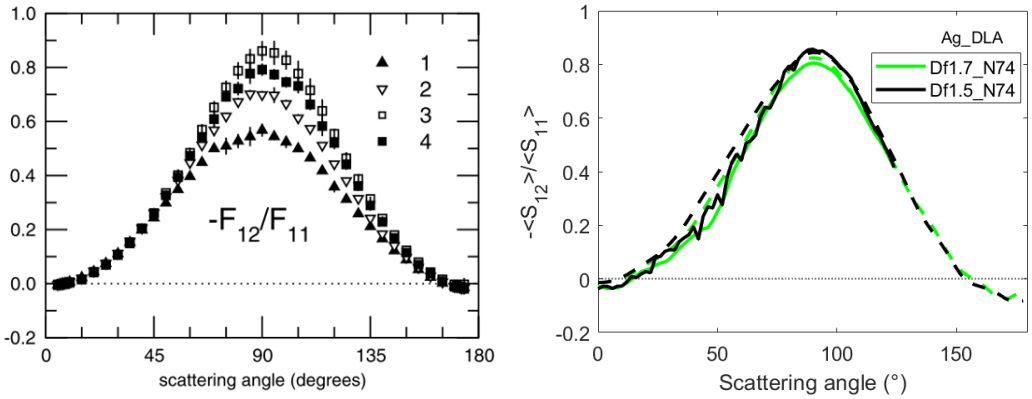

(a) DLP taken from [106] (b) Our DLP

Figure 2.31: Laboratory scattering measurements comparison of the DLP. (a) DLP of samples 3 and 4 [see Figure 7 in 106], (b) DLP of our aggregates Ag_DLA_Df1.7_N74 and Ag_DLA_Df1.5_N74 with power law distribution effect of $n_s = 2$ for measurements (solid lines) and numerical simulations (dashed lines).

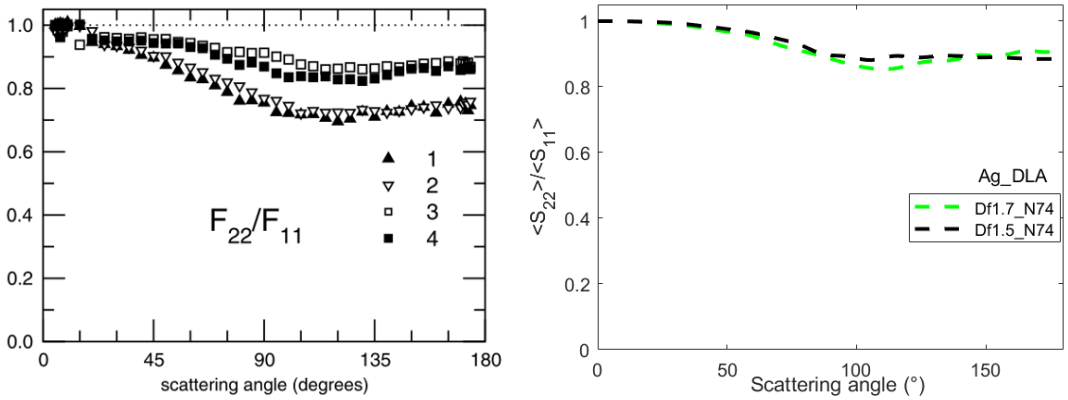

(a) $< S_{22} > / < S_{11} >$ taken from [106] (b) Our $< S_{22} > / < S_{11} >$

Figure 2.32: Laboratory scattering measurements comparison of $< S_{22} > / < S_{11} >$. (a) $< S_{22} > / < S_{11} >$ of samples 3 and 4 [see Figure 7 in 106], (b) $< S_{22} > / < S_{11} >$ of our aggregates Ag_DLA_Df1.7_N74 and Ag_DLA_Df1.5_N74 with power law distribution effect of $n_s = 2$ for measurements (solid lines) and numerical simulations (dashed lines).

2.4.4.2 Numerical simulations

In [137] DDA simulations are performed for compact dust aggregates of protoplanetary disks where phase functions of aggregates with $X_{agg} \approx 2.28$ (calculated with $r_v =$

0.2µm in [137] which is the radius of a sphere with the same material volume) have similarities with phase function of Ag_DLA_Df2.8_N74 with a size distribution effect of $n_s = 2$ (see Figure 2.33). These similarities are the shape and the levels of the phase function. The main cause for the existence of these similarities is the size parameter, indeed, in [137] $X_{agg} \approx 2.28$ and for our aggregate $X_{agg} = 1.62$ (which is the X_{agg} with the highest weight of the distribution), both presenting values that are close.

On the contrary, DLP in [137] for $r_v = 0.2$µm is not similar to our aggregate DLP. DLP in [137] has a higher maximum level of 0.55 compared to DLP of Ag_DLA_Df2.8_N74 which has a level of 0.21 for our measurements and 0.15 for our numerical simulations (see Figure 2.34). Additionally, DLP for aggregate Ag_DLA_Df2.8_N74 presents a prominent negative polarization branch which is not the case in [137], thus there is no resemblance in terms of DLP. The explanation behind this DLP difference is their shapes: our aggregate is more spherical, thus average Mie oscillations that produce a smaller DLP maximum and larger negative polarization branch.

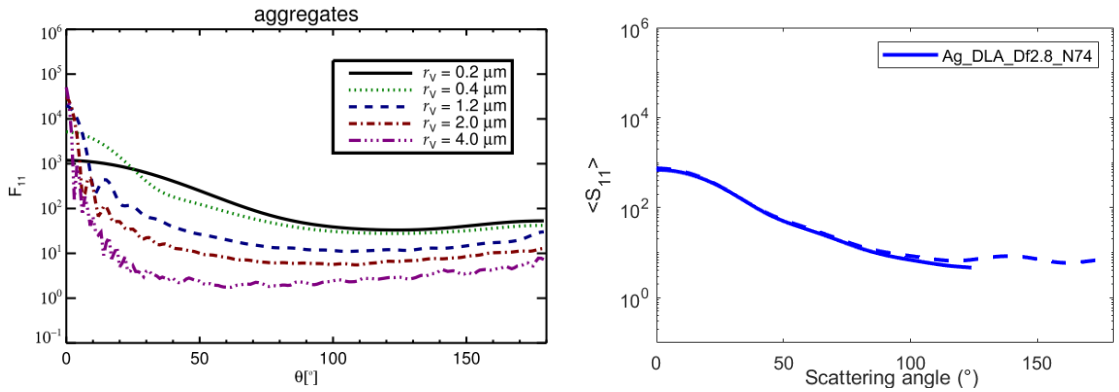

(a) Phase functions taken from [137]

(b) Our phase function

Figure 2.33: Numerical scattering comparison of the phase function. (a) Phase function of samples $r_v = 0.2$ [see Figure 4 in 137], (b) phase function of our aggregate Ag_DLA_Df2.8_N74 with power law distribution effect of $n_s = 2$ for measurements (solid lines) and numerical simulations (dashed lines).

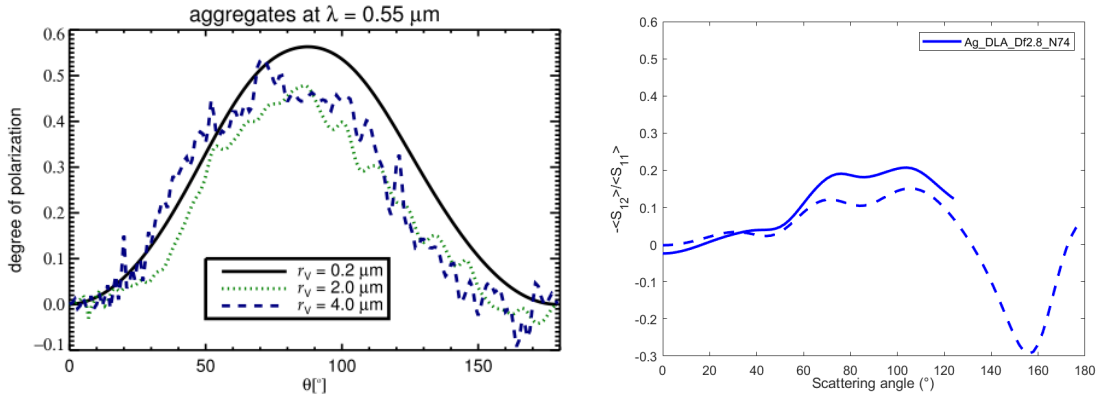

(a) DLP taken from [137]

(b) Our DLP

Figure 2.34: Numerical scattering comparison of the DLP. (a) DLP of sample $r_v = 0.2$ [see Figure 7 in 137], (b) DLP of our aggregate Ag_DLA_Df2.8_N74 with power law distribution effect of $n_s = 2$ for measurements (solid lines) and numerical simulations (dashed lines).

Additionally, in [146] simulations of aggregates with T-matrix method presented similar phase function shapes for 3 aggregate models (model 1, 2 and 3) with similar refractive index to our aggregates. Phase function shapes resemble our aggregates phase functions of Ag_DLA_Df2.8_N74, Ag_DLA_Df2.5_N74 and Ag_DLA_Df2.0_N74_-1 (mostly Ag_DLA_Df2.0_N74_1 to model 1) with a size distribution effect of $n_s = 5$. Yet, phase function levels are larger for our aggregates compared to [146] because of the difference in size parameter (see Figure 2.35). In our case at $n_s = 5$, the weight of the size distribution is more important for small particles, which means, aggregates measured/simulated at large wavelengths. The largest wavelength for our distribution is $\lambda = 60\,\text{mm}$, thus our aggregates have size parameters between $X_{agg} = 1.62$ to 2.75 while in [146] the size parameter is $X_{agg} = 1.18$ and 1.7. This difference leads to an order of difference between our phase function levels and the ones presented in [146].

In the case of DLP in [146], maximum levels are around 1. This is not the case for any of our aggregates with all three indices. Additionally, no negative polarization branch was indicated in [146] which is also not the case for all our aggregates with all three indices (as can be seen for example for $n_s = 3.5$ in Figure 2.36). The reason behind this DLP difference is that in [146] monomer radius ranges, in their power-law distribution, from 0.01 to 0.031, leading to $X_{mon} = 0.1 - 0.35$, while in our case, monomer size parameter is $X_{mon} = 0.3 - 1.04$. Therefore, in our case as monomers are bigger compared to the wavelength then coupling is more important, producing larger depolarizations and thus smaller levels of DLP. Hence, the similarities of phase function shapes (previous paragraph) and differences of maximum DLP levels are consistent with their similarities and differences of X_{agg} and X_{mon}.

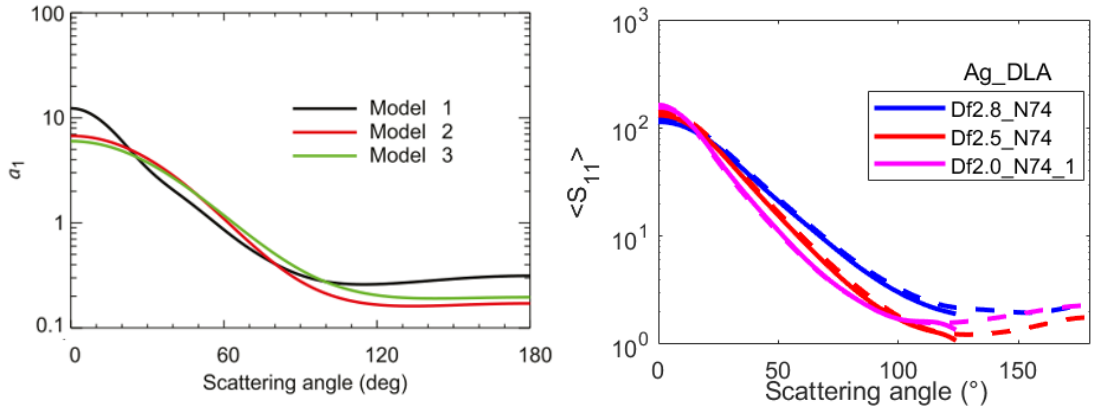

(a) Phase functions taken from [146] (b) Our phase function

Figure 2.35: Numerical scattering comparison of the phase function. (a) Phase function of models 1, 2 and 3 [see Figure 8 in 146], (b) phase functions of our aggregates with power law distribution effect of $n_s = 5$ for measurements (solid lines) and numerical simulations (dashed lines).

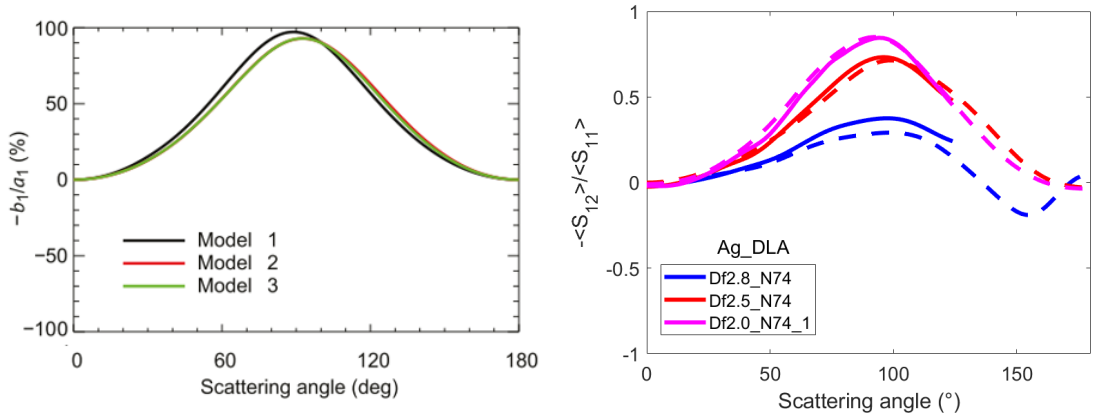

(a) Phase functions taken from [146] (b) Our phase function

Figure 2.36: Numerical scattering comparison of DLP. (a) DLP of models 1, 2 and 3 [see Figure 8 in 146], (b) DLP of our aggregates with power law distribution effect of $n_s = 3.5$ for measurements (solid lines) and numerical simulations (dashed lines).

2.4.4.3 Observations

Finally, observations of circumstellar disk HR4796A in [78], present a phase function with a very prominent forward scattering peak for scattering angles below 30° and then the phase function slowly increases from 40° to 166.6°, presenting an important

backscattering (see Figure 2.37). When comparing the phase function of our aggregates with the phase function of disk HR4796A, neither the forward peak nor the levels of the backscattering enhancement match, even when comparing with the narrowest aggregates phase functions obtained at $n_s = 2$. To obtain these two behaviors with our measurements, first, the size parameter of the aggregates need to be in the geometrical scattering so then the forward peak would be narrowed, as shown in [107] and compared with the debris disk Fomalhaut. And second, inclusions of materials with higher refractive index as hematite $m = 3+0.01i$ could also increase the backscattering enhancement shown in [98]. However, open questions are raised, as for example, is hematite sufficiently abundant in circumstellar disks to be considered? One approach, that can be made based on the abundances that are known today for protoplanetary dust, is to consider silicates with inclusions of amorphous carbon which is the second most abundant dust species after silicates. I suggest to explore these two possibilities, X and refractive index, for future fabrications of dust analogs.

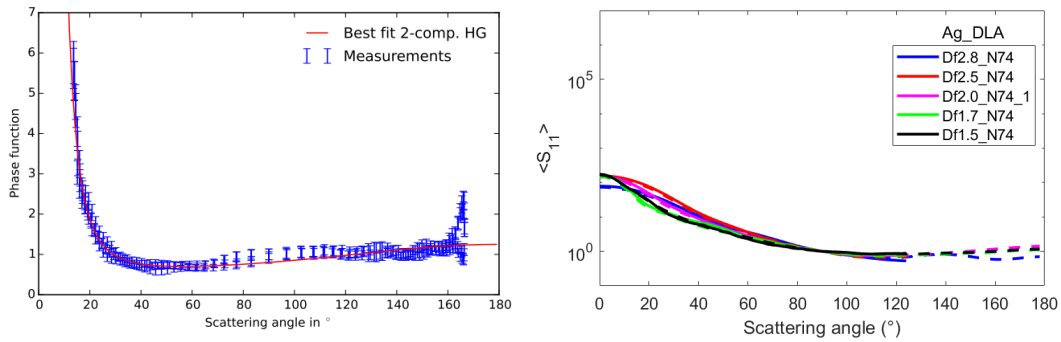

(a) Phase function taken from [78]

(b) Our phase function

Figure 2.37: Observational scattering comparison of phase function normalized at 90°. (a) Phase function of disk HR4796A [see Figure 17 in 78], (b) phase function of our aggregates with power law distribution effect of $n_s = 2$ for measurements (solid lines) and numerical simulations (dashed lines).

2.4.4.4 Conclusions

In summary, based on the presented comparisons with laboratory scattering measurements and numerical scattering simulations, similarities and differences found for the different scattering parameters are consistent with the refractive index and size parameter of our aggregates and the ones found in literature. Furthermore, the indices of the size distribution effect that better work are $n_s = 2$ and $n_s = 5$. However, none of the three indices match when doing the comparison with our phase functions and the one of circumstellar disk HR4796A. To be able to conclude if the index that is being supposed for dust in debris disk is correct, first the size parameter of aggregates needs to increase at orders of $X_{agg} = 100$ [107] to be in the geometrical scattering which can be achieved with our microwave scattering experiment in CCRM (see Table

1.3). Second, the refractive index should increase at orders of $m = 3 + 0.01i$ [98] which is a value coherent with the bibliographical material study (see Section 1.7.2) and possible to be 3D printed using additive manufacturing processes. This will produce phase functions that resemble to the phase functions of circumstellar disks (in this case debris disks), leading to possible conclusions on the power-law index that is used for dust.

2.5 Estimation of fractal dimension

Models of grain growth in protoplanetary disk have considered compact particles for simplicity but this produces growth barriers, i.e., shattering of dust or moving all dust to the star (explained in Section 1.2.3.2). In terms of scattering, this is as considering that these dusts are Mie spheres which is the classic approach. Nonetheless due to the different growth barriers, some authors proposed to use the Distribution of Hollow Spheres [6]. This latter gave better results than Mie spheres, yet it was still an approximation and scattering observations of disks suggested the presence of aggregates [78], leading to calculations of optical properties of aggregates in protoplanetary disks [137]. Based on this, the understanding of scattering properties of analogs of protoplanetary aggregates is of utmost importance. One important characteristic of fractal aggregates is the fractal dimension (D_f) defined in Section 2.2 and related to the morphology of the aggregate, i.e., its compactness or porosity. This characteristic can be estimated based on the scattered intensity (phase function) of aggregates. Hence, the purpose of this section is to determine the fractal dimension of our aggregates with their scattered intensities obtained with our microwave laboratory experiment and numerical simulations. The obtention of D_f with our scattered intensities will provide information to the IPAG group, that is in charge of observations of edge-on protoplanetary disks (disks that are oriented offering a vertical structure, for an example see Figure 1.6), to relate their scattering observations with our analog scattering measurements and thus relate them with the fractal dimension. Therefore this will help to understand how aggregates with different D_f are vertically settled in protoplanetary disks.

2.5.1 D_f estimation methods

Our aggregates were generated with a theoretical D_f, and we want to know if we can obtain their morphological characteristic D_f just with the scattering information. D_f can be estimated based on the scattered intensity averaged over all orientations of the aggregate (for our measurements in terms of the Mueller matrix is S_{11} or phase function). In [162], it is shown that the normalized scattered intensity represented in terms of q (called q-space) is equal to the structure factor $S(q)$ and this structure factor (see Equation 2.6 that is equal to the normalized phase function) carries information on the structure of the aggregate,

$$S(q) = N^{-2} S_{11}(q) = \frac{S_{11}(q)}{S_{11}(q=0)}, \tag{2.6}$$

where $q = 2k\sin(\theta/2)$ for an elastic scattering, k is the wave number and N is the number of monomers.

2.5.1.1 Fractal zone definition

When $S(q)$ is plotted, three different zones can be identified based on its asymptotic behavior (see Figure 2.38):

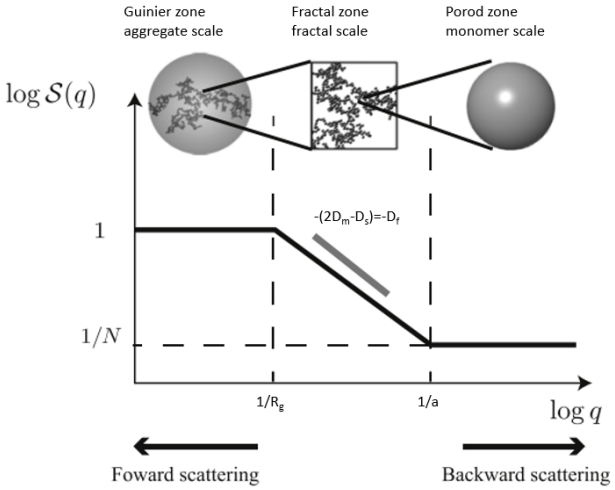

Figure 2.38: Structure factor in terms of q with its three corresponding zones.

1. Guinier zone: when $q < 1/R_g$, R_g being the radius of gyration. This zone depends on the overall size of the aggregate.

2. Fractal zone (or power-law): when $1/R_g < q < 1/a$, a being the radius of the monomer. This zone depends on the aggregate morphology and the slope is defined as $-(2D_m - D_s)$, where D_m is the mass dimension and D_f is the surface dimension. For an aggregate $D_f = D_m = D_s$, thus the slope estimates the fractal dimension.

3. Porod zone: when $q > 1/a$. This zone depends on the monomer size.

We focused on the fractal zone in order to obtain D_f based on the phase functions of our aggregates. However, this asymptotic behavior and analysis are based on scattering approximations. The structure factor of aggregates is calculated assuming

a Rayleigh-Gans-Debye scattering (RGD) which is an approximation of the Rayleigh theory that assumes [79]:

$$\begin{aligned} |m-1| &<< 1, \\ 2X_{mon}|m-1| &<< 1, \end{aligned} \tag{2.7}$$

where $m = n + ik$ is the complex refractive index of the monomer.

This RGD theory applied to fractal aggregates is known as RGDFA and is based on two approximations [145]:

1. The monomer radius of the aggregate is much smaller than the incident wavelength, $a << \lambda$.
2. Interactions between monomers are neglected which consist in neglecting internal coupling.

With our aggregates the ratio a/λ is between 0.03 to 0.16, thus they act as Rayleigh scatterers fulfilling the first approximation. Yet, the second approximation is not fulfilled because the internal coupling between monomers is visibly important, specially for compact aggregates as shown in the previous sections. Additionally, internal coupling increases with the refractive index (see Section 4.3 in [145] where the internal coupling parameter is affected by the refractive index) and ours are not close to 1. However, Sorensen et al. demonstrated in [145, 163] that even if this second approximation is not fulfilled, RGDFA theory is still applicable.

Thus, knowing that RGDFA is still applicable in our case, we can proceed to find the Fractal zone that was proposed by this approximation with our scattering phase functions to obtain D_f. Notice that our aggregates have a small number of monomers (74) and the level of fractality and self-similarity increases when $N \to \infty$, thus in this section I will study if these methods are still applicable in our case. Note that aggregation in nature, herein in protoplanetary disks, starts with small number of monomers, thus there is an interest to know if we can determine D_f for this real case.

2.5.1.2 D_f estimation from the fractal zone

This Fractal zone has been the subject of much discussion. Several authors have proposed different boundaries to delimit this zone depending on the type of aggregation or even the fractal dimension. The authors and their proposed zones to find the slope, $-D_f$, are:

1. Farias et al. [164] expressed that for randomly oriented fractal-like aggregates (for cluster-cluster type of aggregation) the Guinier zone and the Fractal zone are divided at $q = \sqrt{1.5D_f}$. This boundary was initially proposed by Dobbins and Megaridis in [165]. Note that an apriori knowledge of D_f is needed.

2. Oh et al. [166] proposed two Fractal zones depending on the type of aggregation: i) for monomer-cluster aggregation (DLA) the slope is found at $1/10a < q < 1/a$, and ii) for cluster-cluster aggregation (DLCA) the slope is found at $1/R_g < q < 1/a$.

3. Mroczka et al. [167] proposed two zones for aggregates with monomer-cluster aggregation: i) the first zone named First Slope Estimation (FSE) is suitable for all fractal dimensions, $q < 5/R_g$ and ii) the second zone based on [162] named Second Slope Estimation (SSE) is strictly for fractal dimensions between 1.6 to 2.0, $q > 5/R_g$.

Based on the previous list, there are 5 zones giving 5 methods, to determine the fractal dimension which are going to be used for the study of the phase function of our aggregates. Even if the type of aggregation that we used to generate our aggregates was monomer-cluster aggregation, we tested also the zones proposed for cluster-cluster aggregation in order to see if they were applicable for our case.

For Farias et al. and Oh et al. methods, the calculation of the slope was made inside the proposed boundaries by using a polynomial fitting of degree 1 (based on a least-square method).

For Mroczka et al. methods, the algorithm proposed in [167] was used. The main steps of this algorithm are: i) interpolation of the phase function curve to have 1000 points; ii) iteration step where a linear least square fitting is calculated between a portion of the phase function (windowed data) and polynomial of degree 1. The iteration stops when the norm of residuals (criteria curve) finds a local minimum in the criteria curve where the minimum must be two times smaller than the first local maximum; iii) if the local minimum satisfies the criteria, then it will be the central q position for the polynomial and therefore the slope; iv) if the criteria is not satisfied then the data that are inside the window need to be smaller and start over the calculation.

2.5.1.3 D_f estimation by Butterworth filter

It is important to note that our phase function curves in q-space present oscillations in the proposed Fractal zones, making difficult the determination of the slope. For this reason, we proposed a simple function, the Butterworth filter [168], that has the same asymptotic behavior as the structure factor in the Guinier and Fractal zone shown in Figure 2.38. This filter is expressed and named as BF in the following equation:

$$BF(q; a, q_0, n) = \frac{1}{1 + a^2 \left(\frac{q}{q_0}\right)^n}, \tag{2.8}$$

where a is the monomer radius, q_0 is the value of q at $BF = 0$ and n is the order of the filter which will be related to D_f. This filter is fitted with respect to a, q_0, n with the phase function curves and the best fit proposes an exponent n related to

D_f (see an example in Figure 2.39 of an oscillated curve where the filter was fitted). The relation between n and D_f needs first a learning stage in which each n is plotted in terms of the theoretical D_f to find the polynomial function that relates them. Therefore, two polynomial functions were found in this study: $g(n)$ for phase functions of aggregates with average orientation and $G(n)$ for phase functions of aggregates with average orientation and with size distribution effect (shown in Equation 2.12 and 2.9), both based on simulated data. For these two functions, the n obtained for five aggregates of five different D_f (Ag_DLA_Df2.8_N74, Ag_DLA_Df2.5_N74, Ag_DLA_-Df2.0_N74_1, Ag_DLA_Df1.7_N74 and Ag_DLA_Df1.5_N74) were used and plotted with the theoretical D_f, finding the polynomial functions (see Figure 2.40). Then, these functions were applied to these five aggregates simulations and measurements, here measurements being test cases. Moreover, these functions were applied to four more test cases (that were not used in the construction of the polynomials Ag_DLA_-Df2.0_N74_2 and Ag_DLA_Df2.0_N74_3, measurements and simulations). Note that this is a first learning stage. In fact, more phase functions of other aggregates need to be tested in order to validate $g(n)$ and $G(n)$. Once this validation is done, we will not need to know the theoretical D_f a priori. The advantage of this filter is that there is no need to know R_g or a because both are provided by the fitting of the Butterworth function with the whole phase function curve, while for the other methods, there is a necessity to know one or both values or even an a priori knowledge of D_f (once the relations are validated), as for example with Farias et al. method.

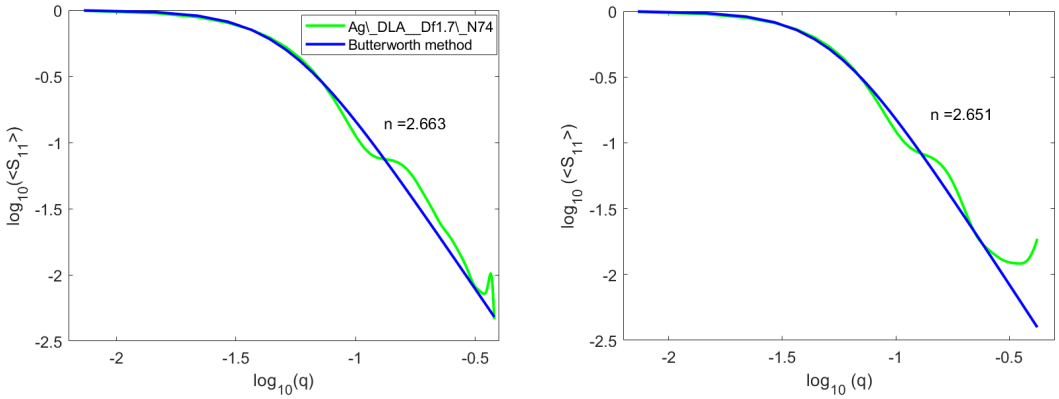

(a) Measurement (b) Simulation

Figure 2.39: Example of fitting between normalized phase function in q-space and Butterworth filter of Ag_DLA_Df1.7_N74 with average orientation at λ = 30 mm, corresponding to $X_{mon} = 0.58$.

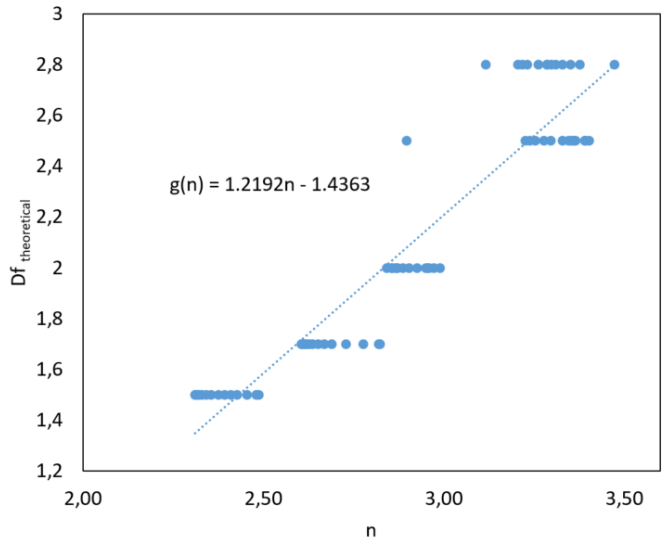

Figure 2.40: Polynomial function g(n) relating n found with Butterworth filter and theoretical D_f. Data points are based on simulated phase functions of aggregates with average orientation. The same procedure was made to find the relations for simulated phase functions of aggregates with average orientation including a size distribution effect ($G(n)$).

2.5.2 Estimated fractal dimension with our aggregates phase functions

The phase functions, based on measurements and simulations of all our aggregates, are normalized and studied in the q-space. In this study, 6 methods are applied to the phase function curves of our aggregates. These methods are named, from now on, with the last name of the first author of the paper where the zones were mentioned, followed by an abbreviation if there is more than one zone: Farias (corresponding to number 1 in list 2.5.1.2), Oh_DLA (corresponding to number 2 in list 2.5.1.2), Oh_DLCA (also corresponding to number 2 in list 2.5.1.2), Mroczka_FSE (corresponding to number 3 in list 2.5.1.2), Mroczka_SSE (also corresponding to number 3 in list 2.5.1.2). In the case of the proposed filter function, it is named Butterworth.

The following two sections study D_f, first, with phase functions of aggregates with average orientation, and second, with phase functions of aggregates with average orientation including a size distribution effect.

2.5.2.1 Phase functions of aggregates with average orientation and with different D_f

The estimation of D_f was first performed for phase functions of five aggregates (5 different fractal dimensions: Ag_DLA_Df2.8_N74, Ag_DLA_Df2.5_N74, Ag_DLA_Df2.0_N74_1, Ag_DLA_Df1.7_N74 and Ag_DLA_Df1.5_N74) with average orientation, for

monomer size parameters between $X_{mon} = 0.29$ to 1.04 (based on X_{min} and X_{max} of protoplanetary dust sizes explained in Section 2.4.3). Figure 2.41 presents an example of phase function in q-space of aggregate Ag_DLA_Df2.0_N74_1 where methods are applied showing the estimated D_f found at $X_{mon} = 0.58$. As can be seen for Farias, Oh_DLA and Oh_DLCA results, the fitting of polynomial with phase function curves is not well done because it takes into account the last portion of the curve which contains an oscillation, thus an incorrect estimation of D_f.

On the contrary, Mroczka_FSE method presents a slope exactly in the linear zone. However this method needs two inputs, the window size where data is analyzed and the step of this window to move all around the linear zone. This latter is an inconvenience because both inputs need to be carefully chosen to then obtain the zone where the criteria is satisfied (explained in the previous section). Moreover, the Mroczka_SSE method, which also has the same problems as Mroczka_FSE method, presents other difficulties. Phase function curves need to have values after the boundary $5/R_g$ because below this limit a fractal zone with a power law regime is not clearly observed [162]. This is the case for only certain aggregates at certain X_{mon} and for these ones the phase function curve in q-space is not linear, thus it is impossible to estimate D_f. For these reasons, both Mroczka methods are not used from now on.

Compared to previous methods, Butterworth method is more suitable for our phase functions, finding a Butterworth curve that synthetically damps the oscillations and gives an asymptotic behavior where the exponent n can be found (see Equation 2.8). After finding n at each X_{mon}, a relation between n and $D_{f\,theoretical}$ was calculated (learning stage previously explained). The relation is a linear polynomial function ($g(n)$) where the obtained n is evaluated and the function gives the D_f, as follows:

$$g(n) = 1.219n - 1.436, \tag{2.9}$$

where $g(n)$ is based on n found from simulations. For example, if $n = 2.96$, as shown in Figure 2.41, then $D_f = g(n) = 1.219(2.96) - 1.436$ which gives $D_f = 2.17$.

Note that after this learning stage where $g(n)$ is tested on measurements and also aggregates presented in Section 2.5.2.2, this relation needs to be applied to more test cases to verify if this relation actually gives the correct D_f without a priori knowledge of D_f.

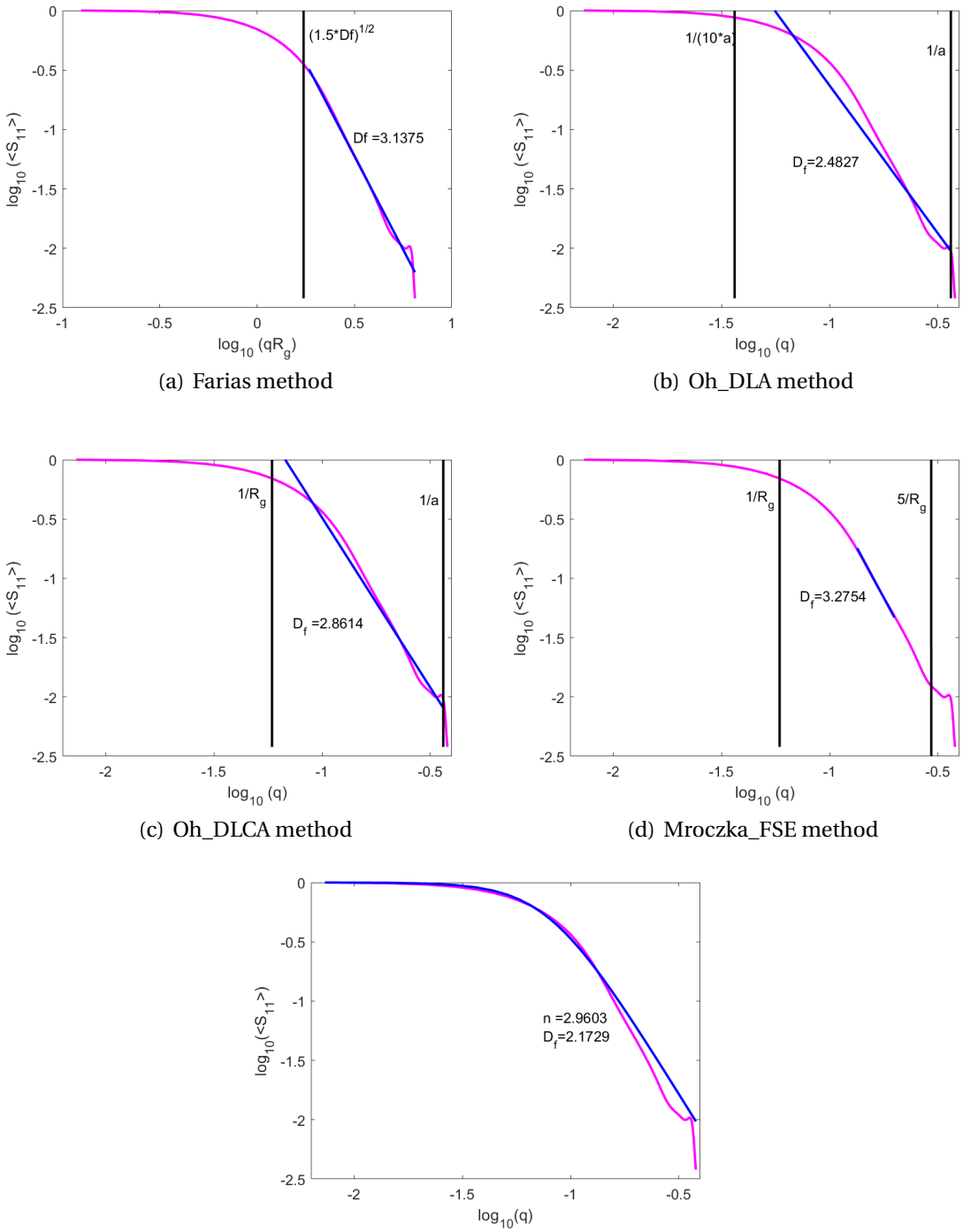

(a) Farias method

(b) Oh_DLA method

(c) Oh_DLCA method

(d) Mroczka_FSE method

(e) Butterworth method

Figure 2.41: Estimated D_f from measurements of normalized phase functions in q-space of Ag_DLA_Df2.0_N74_1 with different methods at $X_{mon} = 0.58$. Mrockza_SSE method does not give values because as can be seen in Figure (d) after $5/R_g$ there is not a linear zone to estimate D_f. Note that the theoretical D_f is included in the name of Ag_DLA_Df2.0_N74_1, thus $D_{f\,theoretical} = 2.0$.

Figure 2.42 shows the estimated D_f for Ag_DLA_Df2.0_N74_1 at different X_{mon}. Butterworth results have the lowest deviation from theoretical D_f. Futhermore, D_f obtained with measurements and simulations for this method are similar between each other. On the contrary, D_f obtained for other methods are not as stable as the Butterworth method. Estimations of D_f were also obtained for other aggregates. Table 2.7 summarizes these results presenting the mean fractal dimension $< D_f >$ (mean obtained from $X_{mon} = 0.29$ to $X_{mon} = 1.04$), the bias (see Equation 2.10), and the consistency (see Equation 2.11)

$$Bias = \left| < D_f > - D_{f\,theoretical} \right|, \tag{2.10}$$

$$Consistency = \frac{\sqrt{\langle (D_f - D_{f\,theoretical})^2 \rangle}}{D_{f\,theoretical}} \times 100\%. \tag{2.11}$$

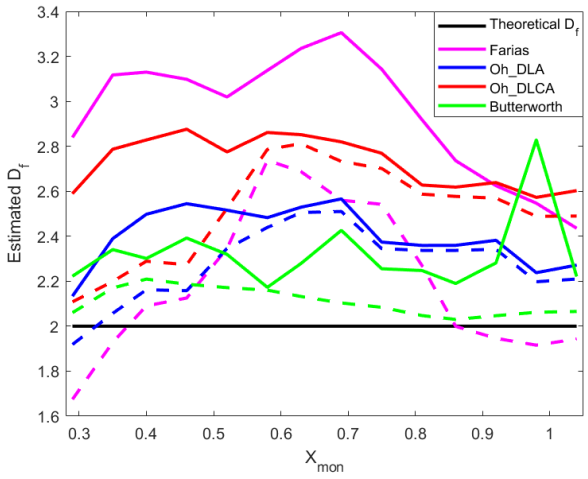

Figure 2.42: Estimated D_f from measurements (solid lines) and simulations (dashed lines) of phase functions in q-space of Ag_DLA_Df2.0_N74_1 with different methods, from $X_{mon} = 0.29$ to $X_{mon} = 1.04$.

For each aggregate in Table 2.7, the results that present the smallest bias are the obtained with the Butterworth method. Moreover, consistency of simulations and measurements have the smallest percentages compared to the consistency of other methods, proving the reliability and stability of this method (this can be also seen in Figure 2.42 green line). Conversely, Farias, Oh_DLA and Oh_DLCA results have more fluctuations (consistency percentages are larger) and between simulations and measurements, there is an important difference for Farias results (this will be discussed in the following section, see Figure 2.43.a.). Furthermore, results with these three methods have larger bias due to their boundaries that consider not only the linear zone of our phase functions but also oscillations. Thus, these three methods are not adapted to estimate D_f of our aggregates.

		Simulation			Measurement		
Ag_DLA	Method	$< D_f >$	Bias	Consistency %	$< D_f >$	Bias	Consistency %
Df2.8_N74	Farias	2.50	0.30	48.79	3.85	1.05	94.81
	Oh_DLA	2.35	0.45	21.26	2.32	0.48	21.18
	Oh_DLCA	3.27	0.47	31.38	3.46	0.66	33.84
	Butterworth	2.52	0.28	12.94	2.58	0.22	11.40
Df2.5_N74	Farias	2.69	0.19	49.81	3.99	1.49	95.12
	Oh_DLA	2.68	0.18	17.33	2.72	0.22	19.50
	Oh_DLCA	3.51	1.01	47.03	3.74	1.24	56.91
	Butterworth	2.58	0.08	6.86	2.59	0.09	8.95
Df2.0_N74_1	Farias	2.20	0.20	18.73	2.95	0.95	49.22
	Oh_DLA	2.28	0.28	16.01	2.40	0.40	21.08
	Oh_DLCA	2.51	0.51	27.62	2.73	0.73	36.91
	Butterworth	2.11	0.11	6.20	2.32	0.32	17.82
Df1.7_N74	Farias	1.78	0.08	10.69	2.21	0.51	30.15
	Oh_DLA	1.91	0.21	13.31	2.10	0.40	24.69
	Oh_DLCA	1.92	0.22	14.12	2.13	0.43	26.54
	Butterworth	1.83	0.13	9.29	1.91	0.21	15.81
Df1.5_N74	Farias	1.96	0.46	30.83	2.30	0.80	53.97
	Oh_DLA	2.01	0.51	34.96	2.24	0.74	49.62
	Oh_DLCA	1.98	0.48	32.60	2.19	0.69	46.25
	Butterworth	1.47	0.03	5.45	1.47	0.03	8.19

Table 2.7: Estimation of $< D_f >$ with its corresponding bias and consistency based on phase functions in q-space of aggregates with average orientation, from $X_{mon} = 0.29$ to $X_{mon} = 1.04$. For bias see Equation 2.10 and for consistency see Equation 2.11. The name of each aggregate contains $D_{f\,theoretical}$.

Two main problems are identified: first, the fractal zones of these methods were defined based on approximate numerical methods that calculated the scattered intensity without taking into account coupling between monomers, having asymptotic behaviors. This is not the case for our aggregates, in nature these interactions are present, and our measurements and simulations consider this coupling. Second, even by measuring only the linear zone of these phase functions, estimated D_f did not correspond to $D_{f\,theoretical}$. We suppose that phase functions in q-space of our aggregates are not enough averaged to estimate D_f because of the presence of oscillations (first hypothesis). Indeed, we think that we need more phase functions per aggregate/fractal dimension in order to increase the average. This may eliminate oscillations and therefore be able to estimate the slope. For this reason, a second study is made with three aggregates of $D_f = 2.0$ to average even more at a same fractal dimension (see Section 2.5.2.2) and then see if this first hypothesis is true. Additionally, an average of the phase functions obtained for each aggregate at different X_{mon} is made by applying the size distribution effect (see Section 2.5.2.3). The second hypothesis is that our aggregates are not enough large to be considered as fractals and thus estimate D_f. In order to increase the fractality, the number of monomers should increase. We will explore the first hypothesis in the following sections to understand if there is a problem of the average of the phase function that can be solved with multiple aggregates of the same fractal dimension.

2.5.2.2 Phase functions of aggregates with average orientation and with same D_f

A second study was made with three aggregates of same fractal dimension $D_f = 2$ (Ag_DLA_Df2.0_N74_1, Ag_DLA_Df2.0_N74_2 and Ag_DLA_Df2.0_N74_3). The phase functions of these aggregates were averaged and then D_f was estimated. This latter with the objective to verify if oscillations were produced by poor averaging of the phase function and thus the difficulty to estimate D_f. Figure 2.43 shows the estimation of D_f of average phase functions at $X_{mon} = 0.58$. Oscillations of phase function did not disappear after averaging phase functions of different aggregates with same fractal characteristics as we supposed. This caused an overestimation of D_f with Farias, Oh_DLA and Oh_DLCA methods. For Butterworth filter, the same $g(n)$ function was evaluated for n to calculate D_f (see Equation 2.9). Remember that $g(n)$ was built based on n obtained for simulated data of aggregates Ag_DLA_Df2.8_N74, Ag_DLA_Df2.5_N74, Ag_DLA_Df2.0_N74_1, Ag_DLA_Df1.7_N74 and Ag_DLA_Df1.5_N74, thus the average phase function of Ag_DLA_Df2.0_N74_1, Ag_DLA_Df2.0_N74_2 and Ag_DLA_Df2.0_N74_3 at 14 different wavelengths or X_{mon} are test cases of $g(n)$ to estimate D_f.

Figure 2.44 shows the estimated D_f from mean phase functions of three aggregates obtained between $X_{mon} = 0.29$ to $X_{mon} = 1.04$. Butterworth and Oh_DLA results have similar values for measurements and simulations. The mean fractal dimension, bias and consistency for these methods are presented in Table 2.8. Farias results have the

lowest consistency for simulations, yet due to oscillations of phase function that did not disappear after averaging, Farias, as well as, Oh_DLA and Oh_DLCA are not reliable methods. Actually, after averaging, the number of oscillations increases (comparing Figure 2.43 to Figure 2.41 an extra oscillation at $q = -0.8$ was added). This proves that averaging three aggregates is not enough to have a statistical average. The average should be done in the future with more than three aggregates phase functions with the same D_f. Another option is to increase the number of orientations per aggregate, this might also smooth phase functions curves of aggregates in q-space.

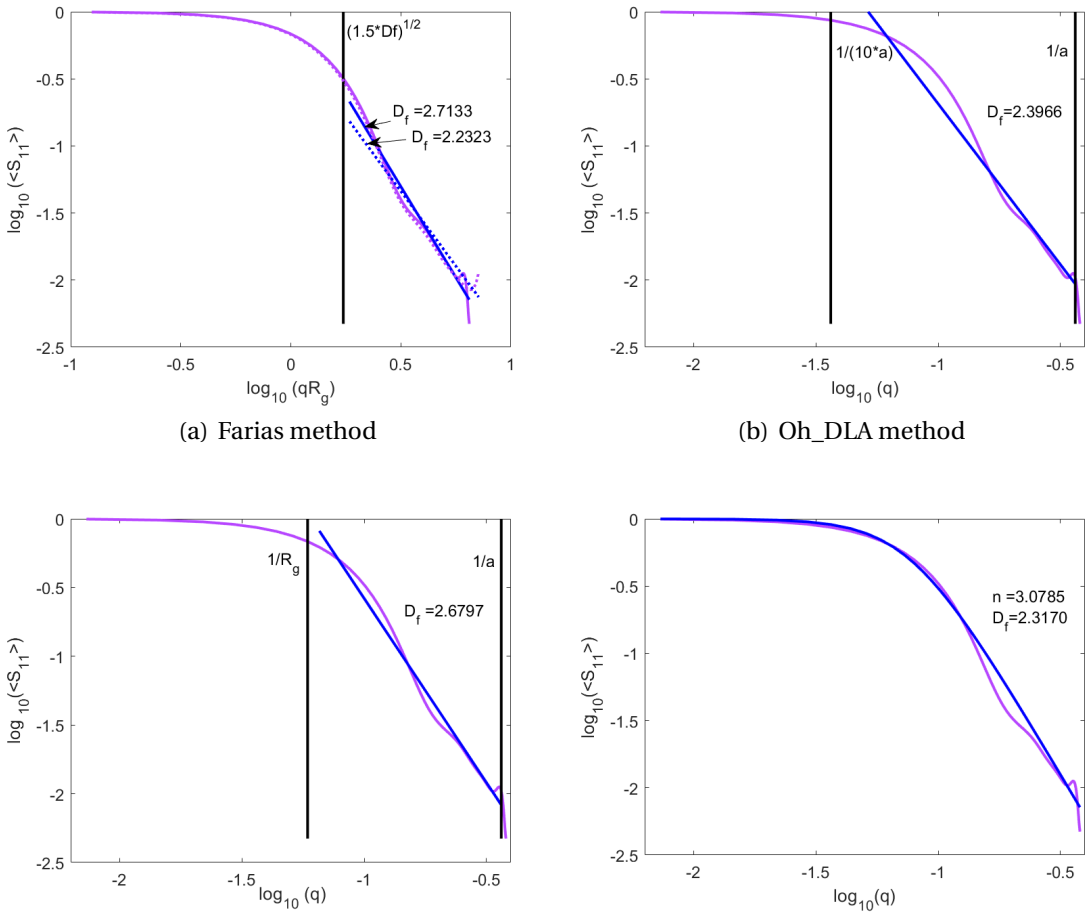

(a) Farias method

(b) Oh_DLA method

(c) Oh_DLCA method

(d) Butterworth method

Figure 2.43: Estimation of D_f from measurements of normalized mean phase functions in q-space of three aggregates with $D_{f\,theoretical} = 2$ with different methods at $X_{mon} = 0.58$. Figure (a) presents also the simulation of the normalized mean phase function and estimated D_f in dot lines.

Results obtained with Butterwoth method have larger bias and consistency compared to those in Table 2.7 (Ag_DLA_Df2.0_N74_1). This is because $g(n)$ equation was

built based on n obtained for other aggregates. Therefore, this bias and consistency are actually showing the reliability of $g(n)$ on these test cases. Herein, estimated D_f with simulations is closer to theoretical D_f than with measurements, presenting a consistency of 14.39% and 28.37%, respectively. Note that measurements are test cases, thus larger percentages are normal compared to simulations. It is important to mention that Butterworth method is still the most promising method of all four methods to estimate D_f, because it does not take into account oscillations, neither the enhancement that is presented in simulated phase functions at large q, see Figure 2.43.a. In fact, as can be see in this figure, phase functions are simulated for scattering angles from 0° to 180°, contrary to measurements that are up to 130°, thus more data points are presented for simulations where the enhancement appears. Therefore, Farias and Oh_DLCA method are not reliable methods, even when Farias results present smaller bias and consistency than the Butterworth method, because these two methods take into account the last enhancement of the phase function with their proposed boundaries contrary to Butterworth method that only fits the whole phase function curve without boundaries. Moreover, Oh_DLA method takes into account the oscillations and part of the Guinier Zone as can be seen in Figure 2.43.b. Thus there is an underestimation of D_f which makes this method unreliable. In summary, with our oscillating phase functions, the most reliable method is the Butterworth method.

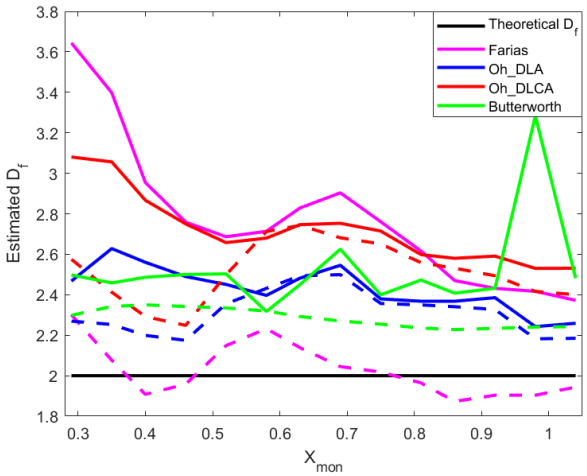

Figure 2.44: Estimated D_f at different X_{mon} from measurements (solid lines) and simulations (dashed lines) of normalized mean phase functions in q-space of aggregates with $D_{f\,theoretical} = 2$.

In conclusion, averaging three aggregates of same fractal dimension did not smooth phase function curves in q-space as we initially suppose. Thus from all four methods the most promising for our oscillating phase functions is the Butterworth method as for the previous section. Future works need more test cases to validate $g(n)$ function and to verify that the Butterworth method is the best adapted method. Additionally, averaging phase functions of more than 3 aggregates of same D_f is necessary to see if

oscillations disappear.

		Simulation			Measurement		
Ag_DLA	Method	$< D_f >$	Bias	Consistency %	$< D_f >$	Bias	Consistency %
Df2.0_N74_1 Df2.0_N74_2 Df2.0_N74_3	Farias	2.03	0.03	6.59	2.78	0.78	42.90
	Oh_DLA	2.32	0.32	16.64	2.43	0.43	22.14
	Oh_DLCA	2.52	0.52	26.77	2.72	0.72	37.15
	Butterworth	2.28	0.28	14.39	2.52	0.52	28.37

Table 2.8: Estimation of $< D_f >$ with its corresponding bias and consistency based on mean phase functions in q-space of aggregates with $D_{f\,theoretical} = 2$.

2.5.2.3 Phase functions of aggregates with average orientation including a size distribution effect

After averaging aggregate phase functions at different orientations and X_{mon}, a power law distribution effect $X_{mon}^{-3.5}$ was applied, similar to Section 2.4.3. Farias, Oh_DLA and Oh_DLCA methods were applied in the same proposed boundaries. For Butterworth method, another relation between n and $D_{f\,theoretical}$ was found ($G(n)$) because relations shown in Equation 2.8 were not adapted due to the size distribution effect. This means relations $g(n)$ are only applicable for aggregates with average orientation, while $G(n)$ relations are for aggregates with average orientations including this specific size distribution effect.

$$G(n) = 1.8634n - 2.6754. \tag{2.12}$$

Figure 2.45 presents an example of phase functions in q-space of aggregate Ag_DLA_-Df2.0_N74_1, applying the size distribution effect. As size distribution in this study is applied for different λ and thus X_{mon}, abscissa in Figure 2.45 is represented for $X_{mon} = 0.29$ which has the largest weight of the distribution. Including size distribution slightly smoothed phase functions of all aggregates. However, the last oscillations at large q did not disappear for measured phase functions, and in the case of simulations, there is still an enhancement as can be seen in Figure 2.45.a (dotted line). This latter produced an incorrect estimation of D_f for Farias, Oh_DLA and Oh_DLCA methods as for previous sections.

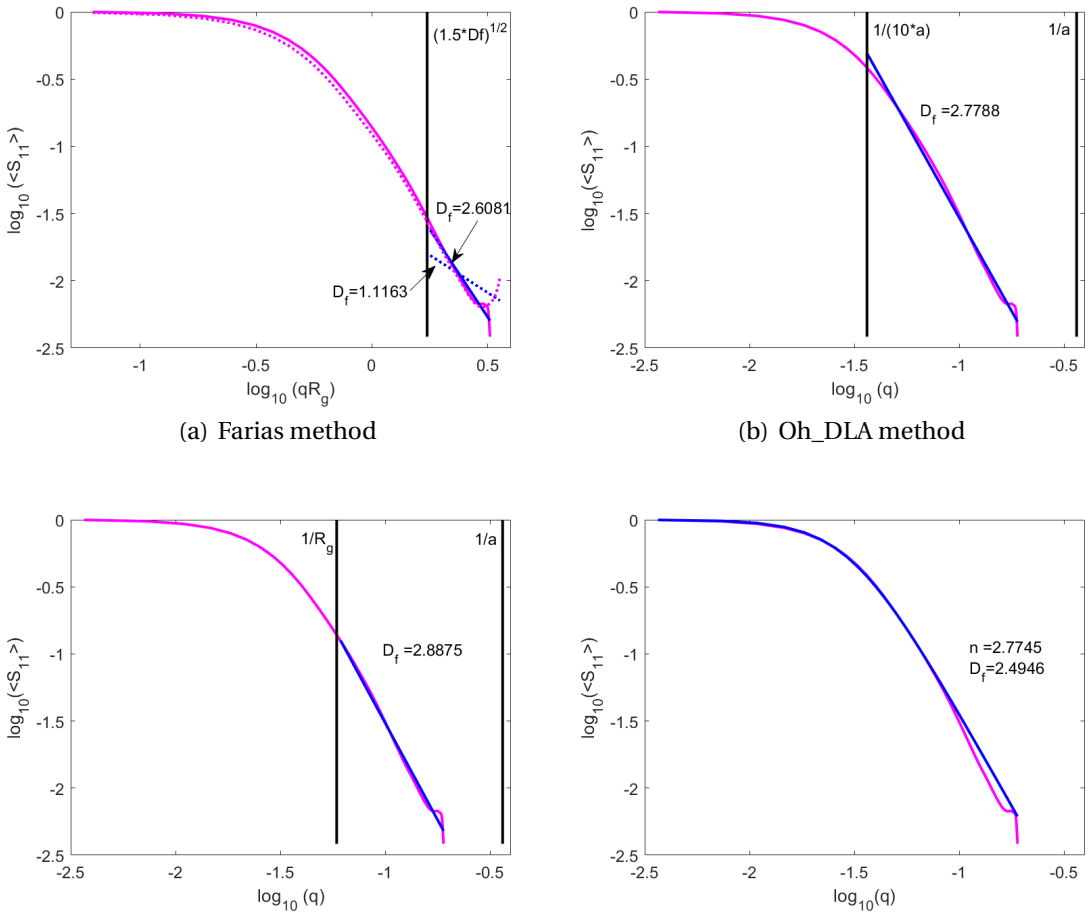

(a) Farias method

(b) Oh_DLA method

(c) Oh_DLCA method

(d) Butterworth method

Figure 2.45: Estimated D_f from measurements of normalized phase function of Ag_-DLA_Df2.0_N74_1 with average orientation and size distribution effect. Figure (a) presents also the simulation of the normalized phase function and estimated D_f in dotted lines.

Table 2.9 contains the mean fractal dimensions, bias and consistency of all five aggregates with different D_f including the size distribution effect. For several aggregates, Butterworth results had the lowest bias compared to other methods, specially for measurements. In some cases, this bias was lower for the other methods, yet estimations of D_f with Farias, Oh_DLA and Oh_DLCA of simulated phase functions were affected by the enhancement of the curve at large q, as mentioned in previous sections (and presented in all aggregates as shown in Figure 2.45.a dotted line). For measurements, these three estimations method were affected by the last oscillation. Butterworth results had consistencies no larger than 24.73%, proving again the stability of the method for all aggregates. Figure 2.46 shows estimated D_f versus theoretical D_f for all methods. As can be seen estimated D_f with Butterworth method is the

only one that has similar behaviors and levels between simulations (dashed lines) and measurements (solid lines). Note that phase function measurements are test cases and even by being test cases, D_f estimations are consistent with simulations.

		Simulation			Measurement		
Ag_DLA	Method	$< D_f >$	Bias	Consistency %	$< D_f >$	Bias	Consistency %
Df2.8_N74	Farias	0.72	2.08	74.28	3.16	0.36	12.94
	Oh_DLA	2.63	0.17	6.19	2.87	0.07	2.66
	Oh_DLCA	2.54	0.26	9.29	3.59	0.79	28.07
	Butterworth	2.49	0.31	11.20	2.64	0.16	5.78
Df2.5_N74	Farias	2.47	0.03	1.35	3.95	1.45	58.11
	Oh_DLA	2.74	0.24	9.77	3.21	0.71	28.24
	Oh_DLCA	2.35	0.15	5.95	3.57	1.07	42.62
	Butterworth	2.66	0.16	6.25	2.75	0.25	9.90
Df2.0_N74_1	Farias	1.12	0.88	44.18	2.61	0.61	30.41
	Oh_DLA	2.24	0.24	11.79	2.78	0.78	38.94
	Oh_DLCA	2.06	0.06	2.90	2.89	0.89	44.37
	Butterworth	2.16	0.16	8.19	2.49	0.49	24.73
Df1.7_N74	Farias	1.66	0.04	2.46	2.43	0.73	43.05
	Oh_DLA	1.83	0.13	7.55	2.26	0.56	33.11
	Oh_DLCA	1.81	0.11	6.50	2.32	0.62	36.21
	Butterworth	1.76	0.06	3.55	1.96	0.26	15.21
Df1.5_N74	Farias	1.85	0.35	23.65	2.26	0.76	50.85
	Oh_DLA	1.93	0.43	28.52	2.28	0.78	52.25
	Oh_DLCA	1.95	0.45	29.69	2.28	0.78	52.29
	Butterworth	1.43	0.07	4.44	1.50	0.00	0.11

Table 2.9: Estimation of $< D_f >$ with its corresponding bias and consistency based on phase functions in q-space of aggregates with average orientation and size distribution effect of $X_{mon}^{-3.5}$.

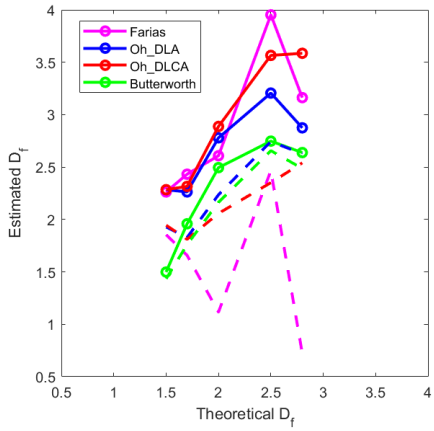

Figure 2.46: Estimated D_f compared to theoretical D_f with different methods. Measurements (solid lines with circles) and simulations (dashed lines).

2.5.2.4 Conclusions

In conclusion, from all three studies (Sections 2.5.2.1 2.5.2.2 and 2.5.2.3) Farias, Oh_-DLA and Oh_DLCA methods presented boundaries that are not adapted to the phase functions of our aggregates because all of them considered the last oscillations for measurements and enhancement for simulations, thus an incorrect estimation of D_f. These oscillations were thought to be caused by a poor averaging, yet the second and third study proved that even by averaging more, these oscillations did not disappear. As mentioned before, these boundaries were based on approximate numerical methods of scattered intensities where coupling between monomers were neglected. Thus, having perfect asymptotic behaviors of scattered intensities is an approximation and this is not our case.

Additionally, Mroczka_FSE method could measure exactly the linear zone. Yet, input parameters for the algorithm, i.e., size of the window and step (to move the window), were a problem because in many cases, the criteria was not satisfied. Yet, in the cases where the criteria was satisfied the slope of the linear zone was overestimated compared to $D_{f\,theoretical}$. This latter led to the supposition that our aggregates are not enough fractals to estimate D_f. In fact, a real fractal object has an infinite extension. In [169], it is mentioned that to determine a slope equal to D_f, R_g/a must be larger than 100 (which is the case for aggregates with small monomer radius and large number of monomers). In our case, this ratio was never 100 but between 3.6 (for the most compact aggregate) to 11.7 (for the most fluffy aggregate). Moreover, in [165] it is said that the number of monomers needs to be of the order of 10^3 to have self-similar aggregates. These two papers indicated that in order to determine D_f, fractality needs to increase by increasing the number of monomers. Our fractal-like aggregates have 74 monomers, and based on previous papers, it is not enough to have a good estimation of D_f. Future works should increase the number of monomers in order to see if the slope corresponds to D_f.

Even if our aggregates do not have enough monomers, using the Butterworth method proved that it is possible to estimate D_f based on phase functions of aggregates with 74 monomers. This method synthetically damps oscillations providing a linear zone. This zone has an associated n (exponent of Butterworth equation) and thanks to $g(n)$ and $G(n)$ functions, it is possible to estimate D_f. In order to validate this promising method, future works should test these two relations on other aggregates phase functions.

Finally, we showed that each fractal dimension has a different phase function behavior, thus a unique scattering signature. Future works should recombine phase functions of different fractal dimensions in order to create populations of aggregates of different D_f and see if the signature is still unique for the different created populations. This opens the possibility to search for signs of fractal particles in phase functions measured in disks and potentially estimate the D_f.

2.6 Conclusions

In this chapter, scattering measurements and simulations of analog aggregates of dust in protoplanetary disks were presented. The control of geometry, refractive index and orientation of these aggregates provided unique scattering measurements thanks to our microwave scattering experiment in CCRM giving clues to interpret their morphology based on five scattering parameters: phase function, DLP, sphericity or $\frac{<S_{22}>}{<S_{11}>}$, $\frac{<S_{34}>}{<S_{11}>}$ and $\frac{<S_{44}>}{<S_{11}>}$.

All five scattering parameters gave complementary (or validated) information of the compactness or porosity of aggregates. A first study of scattering parameters of aggregates with average orientation was made at different wavelengths or monomer size parameters. The change of X_{mon} demonstrated that the scattering parameters of fluffy aggregates ($D_f \leq 2$) presented Rayleigh-like behaviors while compact aggregates had pseudo-sphere behaviors. Scattering parameters $\frac{<S_{34}>}{<S_{11}>}$ and $\frac{<S_{44}>}{<S_{11}>}$ validated the scattering behaviors that were already seen with the phase function and DLP, while $\frac{<S_{22}>}{<S_{11}>}$ gave extra information identifying between fluffy aggregates, intermediate aggregates and compact aggregates based on their levels.

Then, a second study of scattering parameters of aggregates with average orientation and size distribution effect was presented. Different indices of power law distributions were tested in order to see how scattering parameters were affected. Knowing that for protoplanetary dust the index is supposed to be $n_s = 3.5$, two other indices around this value were chosen $n_s = 2$ and $n_s = 5$. From all five scattering parameters, DLP and $\frac{<S_{22}>}{<S_{11}>}$ are the two most promising scattering parameters to study in protoplanetary scattered observations because they are not affected by the number of monomers that aggregates can contain. Instead, they are completely related to sphericity and coupling, thus to morphology.

Differences between one index to another were shown, specially for phase function and DLP. Phase functions with $n_s = 2$ had narrower forward scattering peaks and important backscattering enhancements while DLP with $n_s = 5$ presented maximum levels around 0.5 and 0.9 with negative polarization branches between 0 to -0.1. These characteristics of the phase function with $n_s = 2$ and the DLP with $n_s = 5$ are the closest compared to the the ones observed with laboratory scattering measurements and numerical scattering simulations of analog aggregates of protoplanetary disks. It is suggested for future works, to fabricate aggregates in the geometrical scattering range $X_{agg} = 100$ to narrow even more the forward scattering peak and produce a greater backscattering of the phase function, as well as to increase the real part of the refractive index around $m = 3 + 0.01i$ in order to obtain phase functions closer to the phase function observed for the debris disk HR4796A.

Finally, the estimation of the fractal dimension based on phase functions represented in q-space was done for our seven aggregates. Different methods that were already presented in other works were applied in order to determine the slope and thus D_f. Moreover, a novel method, based on the Butterworth filter function, was proposed. The most promising method to estimate D_f on our aggregates phase functions

was the one proposed in this thesis, the Butterworth method. Yet, more test cases are necessary to validate functions $g(n)$ and $G(n)$. Additionally, it is recommended to fabricate aggregates in the future with greater number of monomers to increase fractality and verify if the slope of the phase function in q-space smooths and thus find D_f. A final prospect is to recombine phase functions of different fractal dimensions and verify if with the scattering signature (phase function) is still possible to estimate an average D_f. This opens the possibility to search for signs of fractal particles with phase functions measured from disks.

3 Irregular compact grains

Sommaire

3.1 Introduction . . . 173
3.2 Analogs of grains . . . 176
3.2.1 Virtual generation . . . 177
3.2.2 3D printing by stereolithography . . . 178
3.2.3 Grain size analogy . . . 179
3.3 Scattering properties of grains . . . 179
3.3.1 Setup parameters . . . 180
3.3.1.1 Number of necessary measurements . . . 180
3.3.1.2 Co and cross terms . . . 181
3.3.1.3 Forward and backward measurements . . . 183
3.3.2 Grains with average orientation . . . 183
3.3.2.1 Phase function . . . 183
3.3.2.2 Degree of linear polarization . . . 186
3.3.2.3 Conclusions . . . 189
3.3.2.4 Other scattering parameters . . . 189
3.3.2.5 Conclusions . . . 195
3.3.2.6 Comparison of scattering parameters of grains and aggregates . . . 195
3.3.3 Grains with average orientation and size distribution effect . . . 201
3.3.3.1 Probability distribution . . . 201
3.3.3.2 Phase function . . . 202
3.3.3.3 Degree of linear polarization . . . 204
3.3.3.4 Other scattering parameters . . . 206
3.3.3.5 Conclusions . . . 210
3.3.3.6 Comparison of scattering parameters of grains and aggregates . . . 210
3.3.4 Direct comparison of scattering parameters found in literature . . . 214
3.3.4.1 Laboratory measurements . . . 215
3.3.4.2 Numerical simulations . . . 216
3.3.4.3 Observations . . . 218
3.3.4.4 Conclusions . . . 219
3.4 Analogs of chondrules and CAI . . . 219
3.4.1 Virtual generation . . . 219

3.4.2 3D printing by fused filament fabrication . . . 220
3.4.3 Chondrules and CAI size analogy . . . 222
3.5 Scattering properties of chondrules and CAI . . . 223
3.5.1 Setup parameters . . . 223
3.5.1.1 Number of necessary measurements . . . 224
3.5.1.2 Forward and backward measurements . . . 224
3.5.2 Chondrules and CAI with average orientation . . . 224
3.5.2.1 Phase function . . . 224
3.5.2.2 Degree of linear polarization . . . 227
3.5.2.3 Other scattering parameters . . . 229
3.5.2.4 Conclusions . . . 233
3.5.2.5 Comparison of scattering parameters of chondrules, CAI, grains and aggregates . . . 233
3.5.3 Chondrules and CAI with average orientation and size distribution effect . . . 243
3.5.3.1 Probability distribution . . . 243
3.5.3.2 Phase function . . . 244
3.5.3.3 Degree of linear polarization . . . 246
3.5.3.4 Other scattering parameters . . . 248
3.5.3.5 Conclusions . . . 250
3.5.3.6 Comparison of scattering parameters of chondrules, CAI, grains and aggregates . . . 251
3.5.4 Direct comparison of scattering parameters found in literature . 261
3.5.4.1 Laboratory measurements . . . 261
3.5.4.2 Observations . . . 263
3.5.4.3 Conclusions . . . 264
3.6 Conclusions . . . 264

3.1 Introduction

Evidence that dust particles are not perfect spheres in the interstellar medium, comets, asteroids [170], and scattering simulations of perfect spheres that do not fit with observations of scattered light coming from protoplanetary dust [7], have been increasing in the last years. In order to have a better understanding of the scattering behavior of these irregular dust particles, studies have been done through observations, numerical models and laboratory measurements. Numerical and experimental methods were developed because the Lorentz-Mie solution of spheres was not appropriate to solve the scattering of irregular particles. Hence, a series of experiments and calculus were adapted to study the scattering of such non-spherical structures [16] with: microwave scattering technique, numerical simulations and light scattering technique.

The understanding of the scattering properties of these irregular particles or non-spherical particles has been carried out since the eighties with the model and mi-

crowave scattering measurements of Mukai [171]. This microwave scattering technique uses the microwave analogy which is based on the scale invariance rule (SIR). This rule states that analog particles can have the same scattering properties as the real particles if the analog electromagnetic system has geometrical dimensions that are scaled in proportion to the incident wavelength, while keeping the same refractive index [12]. To respect this proportion, the use of the size parameter (X) needs to be addressed, defined as the ratio between the particle size (R radius of the smallest sphere enclosing the particle) to the incident wavelength (λ), $X = 2\pi R/\lambda$. Based on this technique, in [13] the phase function and degree of linear polarization (DLP) of several non-spherical particles were calculated based on microwave scattering measurements and compared to the phase function and DLP of Mie spheres. Unfortunately, the comparison of these two scattering parameters did not exactly match with the scattering of Mie spheres. For this reason is of outmost importance to perform microwave scattering measurements on non-spherical objects. Furthermore, in [13] was highlighted the advantages of using this technique: control of orientation, size, shape, structure and refractive index of measured analogs.

In [16], are summarized the main scattering behaviors of non-spherical particles that have been seen in literature in terms of the Mueller matrix elements. The main conclusion is that the circular backscattering depolarization, that is related to the element S_{44} of the Mueller matrix, is the most reliable indicator of non-sphericity. However, depending on size parameter and refractive index of these particles, scattering parameters and thus properties prominently change (see Table 3.1 for more details on the size parameter and refractive index of some scattering studies of rough particles). Several studies have been focused on simulated scattering behaviors of virtual irregular particles created in different ways. For example, in [172, 173], studies in geometric optics range of irregular ice particles were performed with two types of simulations, improved geometric-optics method (IGOM) and pseudo-spectral time domain method (PSTD). These virtual ice particles were generated by taking a regular solid hexagon and then altering its faces.

Furthermore, in [174, 175] the creation of Gaussian random particles was done based on the covariance function. The scattering of these particles was numerically studied with Discrete Dipole Approximation method (DDA). Moreover, in [156] other type of virtual irregular particles was proposed, in which DDA simulations were again used to study the scattering behavior of rough particles. These previous studies presented scattering simulations based on discretized irregular particles, affecting the size of their meshes, constraining their morphologies and therefore their scattering properties. Additionally, when using only numerical simulations, open questions are raised, as for example, how fine the meshing of these irregular particles should be when details of their roughness are becoming very fine? For this reason, numerical simulations need to work together with laboratory scattering measurements. For example, in [176], scattering simulations with T-matrix method using Chebyshev particles (based on Chebyshev polynomials) were performed and compared with measurements. However, these comparisons were not made with the same shape of

the Chebyshev virtual particles but with hematite aerosol samples.

Another way of obtaining scattering properties of irregular particles is with light scattering measurements. For example, in [98], scattering properties of irregular cosmic dust analogs were studied with laboratory measurements and ray-optics model simulations. Yet, size parameters of particles were in the geometrical scattering regime (or geometric optics) which is not the regime in which we are interest on for studying protoplanetary dust. However, behaviors of the phase function and DLP are similar to what has been observed in Debris disks. First, forward-scattering peaks of phase function become narrower while increasing X but also while increasing inclusions of highly absorbing materials in weakly absorbing hosts. This augmentation of the refractive index with hematite inclusions also produced an enhancement in backscattering of the phase function. Second, augmentation of maximum DLP levels which is due to the increase of inclusions and X. On the other hand, adding surface roughness narrows the forward-scattering peak but flattens backscattering of the phase function and decreases the DLP. In [9], measurements of phase function and DLP of cosmic dust analog in the geometric optics range were performed and compared to the observed scattering parameters of Comet 67P/Churyumov Gerasimenko. The scattering parameters of this comet matched with a porous irregular dust analog (cotton ball).

Reference	Refractive index ($m = n \pm ik$)	Size parameter ($X = 2\pi R/\lambda$)
Escobar cerezo et al. [98]	$m = 3 + 0.01i$ inside a weakly absorbing host $m = 1.5 + 10^{-5}i$	$X = 100$
Kahnert et al. [176]	$m = 3.0 + 0.1i$	$X = 0.2$ to 14
Liu et al. [172]	$m = 1.31$	$X = 100$ and $X = 1000$
Mishchenko et al. [16]	-	-
Muinonen et al. [174]	$m = 1.313$ $m = 1.6 + 0.0005i$	$X = 1$ to 7
Nousiainen & Muinonen [175]	$m = 1.2 + 0.0i$ $m = 1.4 + 0.2i$	$X = 1, 2, 3$ and 9
Zerull [13]	$m = 1.57 - 0.006i$ $m = 1.5 - 0.005i$ $m = 1.54$ $m = 1.45 - 0.05i$ $m = 1.55 - 0.01i$	$X = 5.3$ to 14 $X = 1.9$ to 17.8 $X = 150$ $X = 27$ $X = 190$
Zhang et al. [173]	$m = 1.31$	$X = 20$ to 50
Zubko et al. [156]	$m = 1.313 + 0i$ $m = 1.5 + 0.1i$ $m = 1.6 + 0.0005i$ $m = 1.855 + 0.45i$	$X = 1$ to 50 $X = 1$ to 32 $X = 1$ to 26 $X = 1$ to 32

Table 3.1: Refractive index and size parameter in some previous scattering studies of rough particles.

Even if these previous studies present the scattering behaviors in which we are interested in, the size parameter is not in the size range of our interest. In order to be in the Mie scattering regime, microwave scattering measurements are an option, providing the wanted regime thanks to its used wavelengths and size of analog that

can be measured. The present chapter studies the scattering properties of irregular solid particles, named hereafter grains, intended to be analogs of protoplanetary dust, using the microwave analogy and controlling the shape (roughness) and refractive index with additive manufacturing processes, which is innovative and complementary compared to previous works. The advantage of using the microwave analogy and the additive manufacturing is to measure the scattering parameters of such grains in controlled conditions. As shown before, previous works have studied scattering properties of irregular particles for multiple applications with analogs of: cometary dust, atmospheric particles, interplanetary dust and cosmic dust, but to our knowledge there are no studies using the microwave analogy of irregular particles being analogs of protoplanetary dust.

Herein, I first present six grains with size parameters between $X = 1.07$ to $X = 7.73$ and refractive index of $m = 1.7 + 0.003i$, which were measured in CCRM and numerically simulated with Finite Element Method (FEM), at wavelengths ranging from $\lambda = 16.7$ mm to $\lambda = 100$ mm. Their virtual generation is described as well as their fabrication which was made by a collaboration with CTTM. Different scattering parameters are studied: the phase function, DLP, and other elements of the Mueller matrix (S_{22}, S_{34} and S_{44}), in order to understand how the roughness affects these scattering parameters and thus the scattering properties of these grains.

Then, scattering measurements of natural rough objects are performed with four analogs of chondrules and of one Calcium-Aluminum-rich Inclusion (CAI), which are elements of rocky meteorites/chondrites that participate in the planetary formation, having size parameters between $X = 1.08$ to $X = 18.67$ and similar refractive indices. I described their virtual generation and fabrication which was made with the collaboration of Lab-STICC laboratory and Laboratoire IUSTI. The idea of this second group of particles is to see if similar particles, as the ones that participate in the Solar System formation, are also present in protoplanetary disks. I also study the scattering parameters of these particles. This time the scattering parameters are only based on scattering measurements due to the remaining uncertainty on how to discretize them to be able to simulate them. Finally, I present the conclusions and prospects for future works.

3.2 Analogs of grains

Dust particles in protoplanetary disks undergo different growth processes, producing different outcomes, e.g., sticking, bouncing, fragmentation, abrasion, erosion, cratering and mass transfer (see Section 1.2.3.2). These outcomes affect the morphology of dust, producing irregular grains. To go further in the understanding of this dust evolution, indirect information on their structure can be obtained with scattered light observations of protoplanetary disks. However, scattering behaviors of these irregular particles must be first understood. Herein, scattering parameters of six different grains, varying their roughness, are retrieved to understand their scattering properties. In

order to produce these analogs, two steps are necessary: their virtual generation and their 3D printing, described in the following sections.

3.2.1 Virtual generation

A first family of grains was generated following several steps. First, the surface of a sphere of initial radius r = 16.25mm, was meshed with similar triangles. For all grains the number of triangles was 320, except for the last object (named Gr_n2_r13.2) which was 80 as a first attempt to have a closer geometry to an astronomical pebble (see following section, Figure 3.2.f). Then, the distance from the center of the sphere to the vertex of each triangle was perturbed with a random perturbation r_{rand} (between $+l_s$ and $-l_s$), creating a rough radius r_{rough} (see Figure 3.1 where R_{max} is the final radius of the bounding sphere of each grain after perturbations):

$$r_{rough} = r + r_{rand}(\pm l_s), \tag{3.1}$$

$l_s = \lambda / n$ being the fraction of λ at λ = 30 mm, where the denominator n takes values between 2 to 10. For the two roughest grains n = 2, then this value increases with steps of 2, from n = 4 to n = 10 (this last value corresponds to the smoothest grain, close to a perfect sphere).

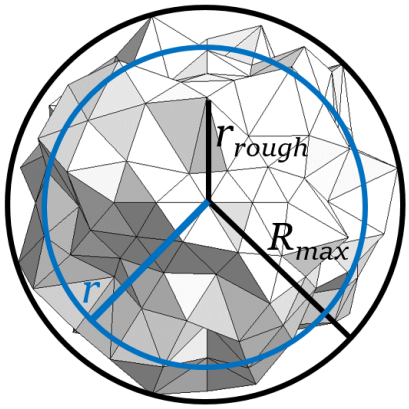

Figure 3.1: Example of a grain virtual generation, where r is the initial radius of the sphere to mesh, r_{rough} are the perturbed distances from the center of the sphere r to each triangle vertex and R_{max} is the radius of the bounding sphere named maximum radius.

To calculate the roughness and sphericity of our grains based on their meshed files, we chose a software named SHAPE [177] that characterizes the grain morphology. The roughness is defined as:

$$Roughness = R_{std,norm} = \frac{R_{std}}{R_{mean}}, \tag{3.2}$$

where R_{std} is the standard deviation from the centroid of the grain to each vertex and R_{mean} is the mean of all vertex radius.

The sphericity is defined as [177, 178]:

$$Sphericity = \frac{6V}{\left(\frac{6V}{\pi}\right)^{1/3} S}, \tag{3.3}$$

where V is the volume of the grain and S is the surface area.

3.2.2 3D printing by stereolithography

The grains were 3D printed with stereolithography (SLA), using acrylic resin of a refractive index of $1.7+0.03i$, which is close to the refractive index of the astronomical silicate [14]. This same printing method and material were described and used in the previous chapter for the aggregates.

Table 3.2 presents the properties of each grain, starting with their technical name that is a string composed of: Gr being the abbreviation of grain, then n being the denominator of l_s (see Equation 3.1) followed by its value, and then the letter r (roughness) followed by the percentage of roughness of the grain. Other columns in this table are the maximal radius, percentage of roughness and percentage of sphericity. Then the size parameter, $X = 2\pi R_{max}/\lambda$, is presented at the minimum and maximum wavelengths (λ) and finally, the material packing density (which is the ratio of the grain volume to the total volume of the bounding sphere). Among these presented grains, three of them were already presented in another collaborative study [126] but with different names: GravelLike corresponding to Gr_n2_r13.2, Rough sphere 223 to Gr_n2_r13.3 and Rough sphere 228 to Gr_n10_r2.6. Figure 3.2 shows the pictures of the printed grains with their corresponding technical name.

Grain technical name	Radius of the bounding sphere (mm)-R_{max}	Roughness %	Sphericity %
Gr_n10_r2.6	17.00	2.6	98.2
Gr_n8_r3.4	17.20	3.4	97.0
Gr_n6_r4.7	17.60	4.7	95.1
Gr_n4_r6.7	18.40	6.7	90.7
Gr_n2_r13.3	20.00	13.3	75.6
Gr_n2_r13.2	20.50	13.2	89.9

Grain technical name	Size parameter of the grain λ = 16.7 mm to λ = 100 mm			Material packing density-ρ
Gr_n10_r2.6	6.41	to	1.07	0.85
Gr_n8_r3.4	6.48	to	1.08	0.82
Gr_n6_r4.7	6.66	to	1.11	0.76
Gr_n4_r6.7	6.94	to	1.16	0.67
Gr_n2_r13.3	7.55	to	1.26	0.51
Gr_n2_r13.2	7.73	to	1.29	0.42

Table 3.2: Analog grain properties.

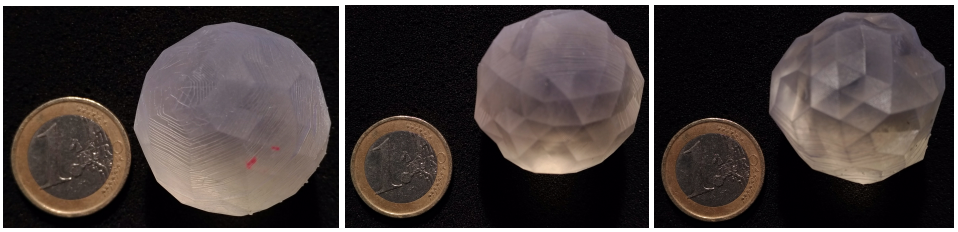

(a) Gr_n10_r2.6 (b) Gr_n8_r3.4 (c) Gr_n6_r4.7

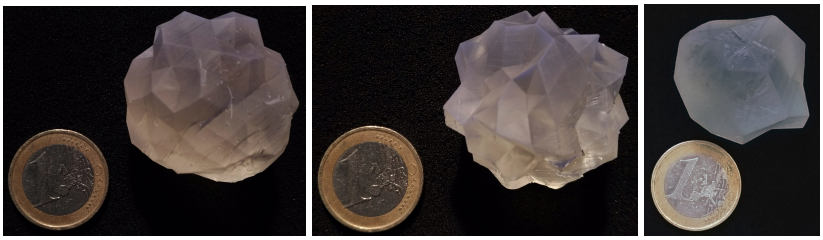

(d) Gr_n4_r6.7 (e) Gr_n2_r13.3 (f) Gr_n2_r13.2

Figure 3.2: 3D printed grains with their corresponding technical name.

3.2.3 Grain size analogy

The mean radius of the bounding spheres of our six grains is 18.45mm with mean size parameter ranging from $X_{mean} = 1.16$ to $X_{mean} = 6.94$ (calculated based on Table 3.2). Supposing these same size parameters, the corresponding mean radius of protoplanetary dust would have different values depending on the wavelength range, as shown in Table 3.3.

Range name	Wavelength	Radius of protoplanetary grain
Optical (nm)	400 to 700	74 to 773
NIR(µm)	1.00 to 2.50	0.185 to 2.76
Millimeter(mm)	0.30 to 2.60	0.055 to 2.87

Table 3.3: Grain radius corresponding to different wavelength ranges (units are noted in the first column).

3.3 Scattering properties of grains

Scattering measurements of the six grains were performed in our anechoic chamber (explained in Section 1.5.2) with wavelengths ranging from 100 mm to 16.7mm (corresponding to frequencies of 3 GHz to 18 GHz), using the forward experimental setup, thus scattering angles from −130° to 130° (see Section 1.5.2). Numerical simulations were performed with FEM (see Section 1.6), using the same geometric files of the 3D grains as the ones used for 3D printing. Both procedures, measurements

and numerical simulations were similarly performed to our aggregates presented in Section 2.4. This means performing scattering measurements and numerical simulations of random orientation of non-interacting grains, which is represented by the Mueller matrix in Equation 1.35. Note that differences between these Mueller matrix elements including or not the cross-polarized elements are negligible (as shown in Figure 3.4 and explained in Section 3.3.1.2). There is just one exception for S_{22} where the inclusion of the cross-polarized elements is essential to then be able to normalize by S_{11}. If this inclusion is not made, then $S_{22} = S_{11}$. Thus, based on our measurements, the Mueller matrix elements that could be obtained are S_{11}, S_{12}, S_{44} and S_{34}. Notice that in terms of numerical simulations, all these elements were obtained, as well as S_{22} (see Equation 2.3).

Based on these five Mueller matrix elements, five scattering parameters were calculated based on measurements and numerical simulations, i.e., phase function (S_{11}), degree of linear polarization (DLP, $-S_{12}/S_{11}$), normalized S_{34} and S_{44}, and only for numerical simulations for normalized S_{22}.

3.3.1 Setup parameters

In this section I describe: i) the number of necessary measurements and simulations for each grain, ii) the effect of including or not the cross-polarized elements on the different scattering parameters and iv) the zone where measurements could be performed.

3.3.1.1 Number of necessary measurements

A calculus of the number of necessary orientations per grain to retrieve mean phase functions and DLP to converge, at a given percentage of error, was performed based on [126] (see an example in Figure 3.3 for the calculus of the phase function, named brightness, and DLP, named polarization, of grain Gr_n2_r13.3 at $\lambda = 25\,\text{mm}$). This same analysis was made for each grain at different wavelengths and percentage of errors, and then the maximum number of measurements at all wavelengths was taken at a given percentage of error. We needed between 20 ± 10 orientations for the least rough grain (Gr_n10_r2.6) to 70 ± 10 orientations for Gr_n2_r13.2, obtaining an accuracy of 1% for the measured phase function. And for DLP, we needed between 13 ± 10 to 44 ± 10 orientations with an accuracy of 1%. Thus, for these two scattering parameters, 72 orientations were necessary for Gr_n2_r13.3, Gr_n2_r13.2 and Gr_n4_-r6.7 and 36 orientations for the rest of the grains. In terms of simulation, the number of necessary orientations to obtain the same accuracy decreased, 36 orientations were needed to obtain an accuracy of 1% for the phase function and DLP, for all grains. The same number of orientations, obtained for measurements and numerical simulations of phase function and DLP, were used to retrieve the other scattering parameters. Note that the exact position of the grain is not precisely known in the experiments, producing slight differences between measured and simulated scattering parameters.

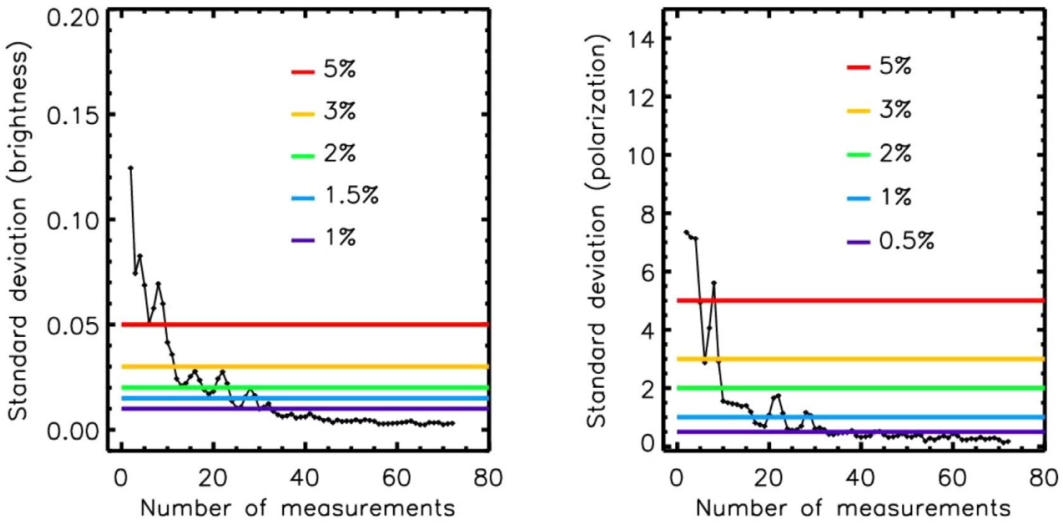

Figure 3.3: Example of necessary number of measurements for grain Gr_n2_r13.3 at $\lambda = 25\,\text{mm}$, $X = 5.03$ [taken from 126].

Note that we average the phase functions of the same grain with the necessary number of orientations, obtaining $< S_{11} >$, and for the other scattering parameters that are represented with the normalization of $< S_{11} >$, the average was made before the normalization, obtaining: $DLP = \frac{<S_{12}>}{<S_{11}>}$, $\frac{<S_{22}>}{<S_{11}>}$, $\frac{<S_{34}>}{<S_{11}>}$ and $\frac{<S_{44}>}{<S_{11}>}$. This average was decided to be calculated in this way because protoplanetary dust is supposed to be randomly oriented when doing the observations of the different Mueller matrix elements, thus, Mueller matrix elements that are already averaged in terms of orientation.

3.3.1.2 Co and cross terms

FEM numerical simulations were used to verify the effect of cross-polarization on the scattering parameters of interest. Figure 3.4 presents these scattering parameters with (dashed-dotted lines) and without (dashed lines) cross-polarization for grain Gr_n2_r13.3. The differences between including and not the cross-polarization, increases as the size of the scatterer increases (X). Nevertheless, these differences are negligible for all grains, thus our scattering parameters will be only defined in terms of co-polarized elements except for $\frac{<S_{22}>}{<S_{11}>}$. This last parameter needs to be defined including the cross-polarization because when only co-polarized elements are included $< S_{22} >=< S_{11} >$ and by normalizing with $< S_{11} >$, $< S_{22} >$ becomes 1. Therefore, all scattering parameters will be represented with only co-polarized elements, except for $\frac{<S_{22}>}{<S_{11}>}$, where cross-polarization needs to be included (this is possible only with simulations).

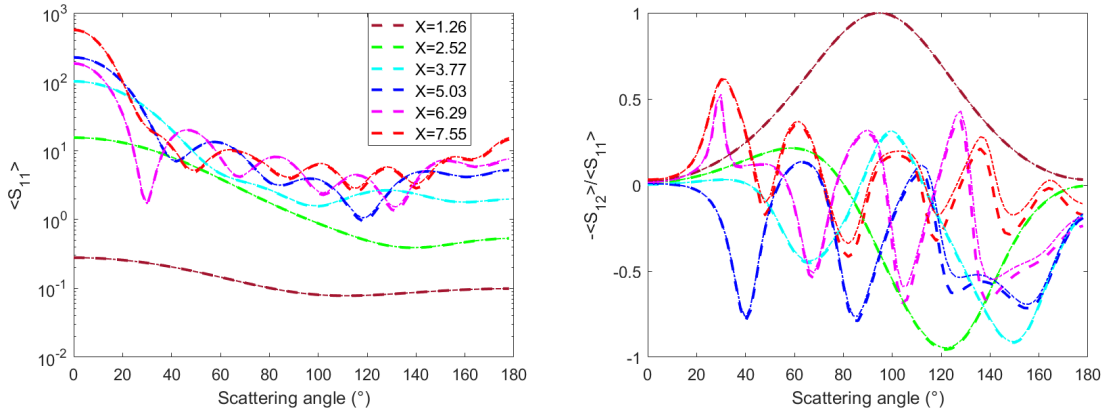

(a) Phase function (b) DLP

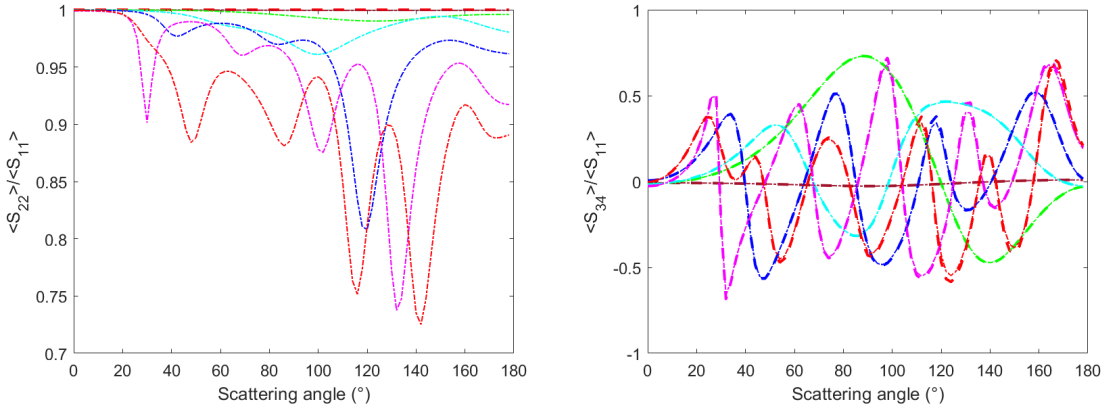

(c) Normalized S_{22} (d) Normalized S_{34}

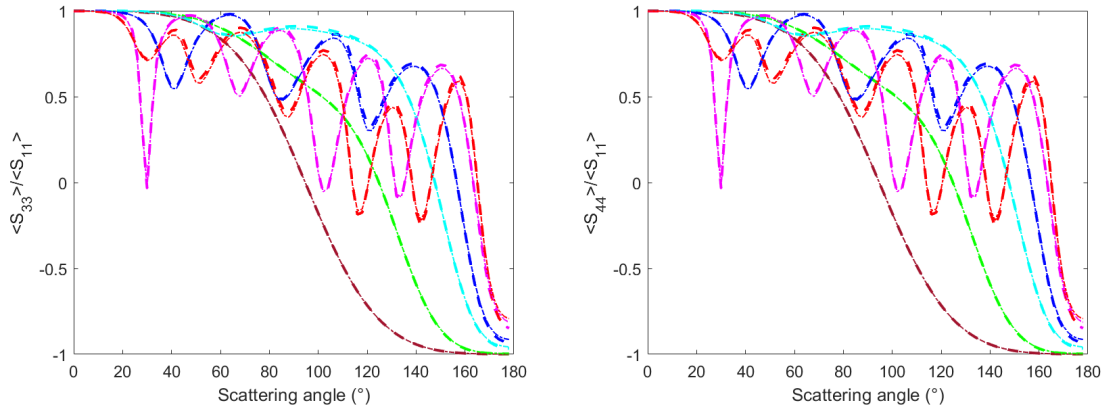

(e) Normalized S_{33} (f) Normalized S_{44}

Figure 3.4: FEM numerical simulations of Gr_n2_r13.3, considering co-polarized Jones matrix elements (dashed lines) and co-polarized plus cross-polarized elements (dashed-dotted lines), from $X = 1.26$ to $X = 7.55$.

Additionally, in Figure 3.4, $\frac{<S_{33}>}{<S_{11}>}$ and $\frac{<S_{44}>}{<S_{11}>}$ illustrate almost identical scattering behaviors, proving once again that cross-polarized elements are negligible. As previously explained cross-polarization is not included for our grains scattering parameters (except for $\frac{<S_{22}>}{<S_{11}>}$). Thus, $\frac{<S_{33}>}{<S_{11}>} = \frac{<S_{44}>}{<S_{11}>}$ (based on Equation 2.3), which is named from hereon only by $\frac{<S_{44}>}{<S_{11}>}$.

3.3.1.3 Forward and backward measurements

After knowing the effect of including or not the cross-polarized Jones matrix elements to calculate the scattering parameters of grains, and knowing that measurements were only performed with both antennas in the two same linear states of polarization (co-polarized elements), then based on measurements, four parameters are obtained: the phase function, DLP, $\frac{<S_{44}>}{<S_{11}>}$ and $\frac{<S_{34}>}{<S_{11}>}$. Furthermore, measurements can be performed in the forward zone and backward zone. Yet, as previously explained with aggregates, we decided to perform these measurements only in the forward zone because the backward zone presents a lower accuracy and the time per measured grain is multiplied by 2, thus we decided to measure more analogs in only the forward zone. Hence, scattering parameters are represented until scattering angles of 130°.

After verifying and deciding all the setup parameters, the Mueller matrix elements of our grains were studied and compared between each other. Two types of scattering results are presented in the following sections: first, scattering parameters of grains with average orientation (Section 3.3.2) and second scattering parameters of grains with average orientation applying a size distribution effect (Section 3.3.3).

3.3.2 Grains with average orientation

3.3.2.1 Phase function

The average phase functions of all six grains are illustrated in Figure 3.5 at six different wavelengths 100 mm, 50 mm, 33 mm, 25 mm, 20 mm, and 16.7mm (out of a total of sixteen wavelengths), expressed in terms of the corresponding size parameter that is between $X = 1.07$ to $X = 7.73$. Phase function measurements and numerical simulations are very similar with little discrepancies that can be seen at larger X. In order to quantify these differences, we used the same comparison criterion as for aggregates (see Equation 2.4). The $RMSD_{IQR}$ is presented in Figure 3.6 for the phase function of all grains in different colors and in gray for the comparison between an exact Mie calculus of a solid sphere with a radius of 16.25mm (initial radius of the sphere that was used to generate all grains) and a refractive index of $1.7 + i0.03$, and the simulation of the same sphere with FEM. This gray line gives a reference of the minimal values that may be obtained with such FEM computations. Thus, when $RMSD_{IQR}$ values of the phase function of grains are around this gray line, there is a good agreement between measurements and simulations. For the phase function, the deviation is smaller than the gray line reference, up to $X_{mean} = 4.25$, showing a good agreement.

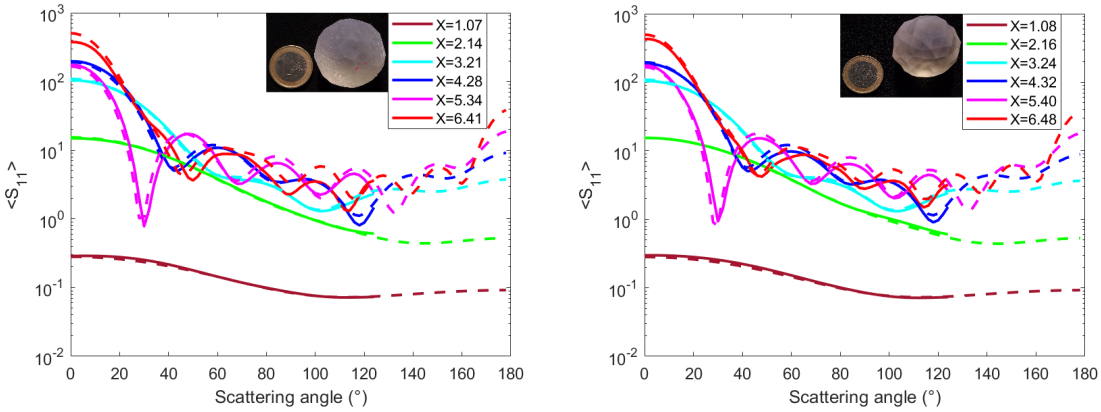

(a) Gr_n10_r2.6

(b) Gr_n8_r3.4

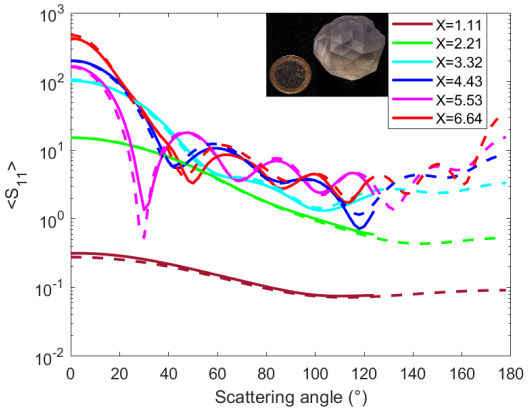

(c) Gr_n6_r4.7

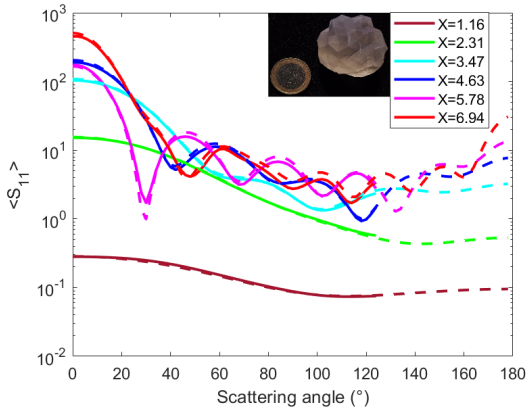

(d) Gr_n4_r6.7

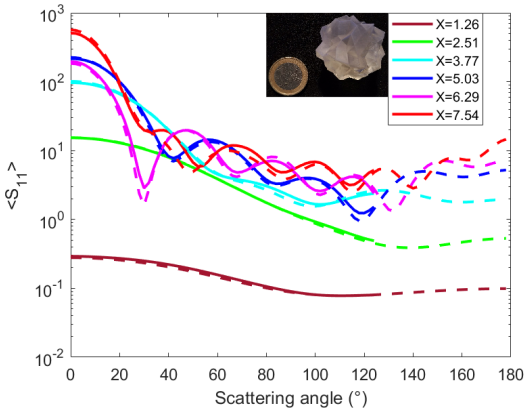

(e) Gr_n2_r13.3

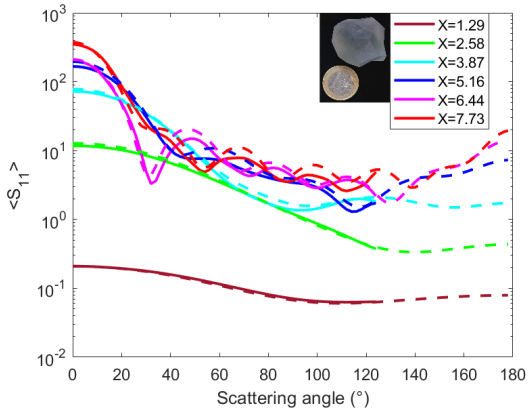

(f) Gr_n2_r13.2

Figure 3.5: Phase function of grains, measurements (solid lines) and numerical simulations (dashed lines).

Then, deviations increase for all grains, up to $RMSD_{IQR} = 0.2$. We think this is due to the increment of grain sizes, thus roughness compared to the wavelength, requiring a finer mesh size for smaller wavelengths for the simulations and creating these little deviations with measurements. Future simulations with finer mesh are needed to verify this. In general, simulations and measurements of the phase function have similar behaviors.

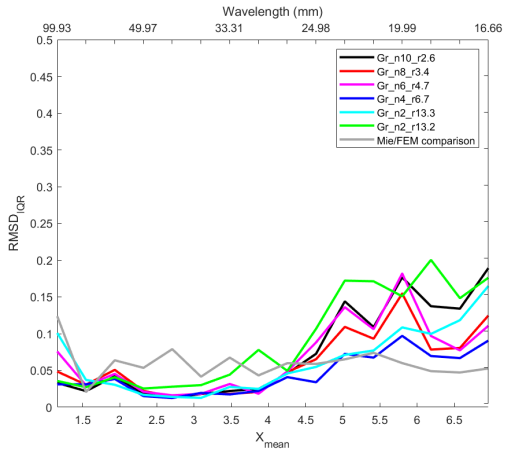

Figure 3.6: Normalized root mean square deviations on the log of the phase function plotted for all grains, taking their FEM numerical simulation as reference. The gray line is a comparison of the Mie simulation versus FEM numerical simulation with a sphere of radius 16.25mm.

Phase functions of all grains have similar curve shapes and levels, as can be seen in Figure 3.5. The differences between phase functions of the grains are visible at large X. This latter is due to the fact that at large X, grains and their roughness are larger compared to the wavelength, meaning that the wave has a larger distance to cover inside the grain, thus more time to change its nature and shape. This is also shown in Figure 3.7 at $\lambda = 16.7$mm, where the simulated phase functions of all grains are superposed. At this wavelength, there are the biggest differences between the phase function of all grains, and yet, they have almost the same behavior in terms of levels and shapes. Levels of the phase function at each wavelength are very similar because sizes between grains do not change much (see radius of the bounding sphere in Table 3.2 for each grain). Indeed, grains were generated with the same initial sphere. Furthermore, shapes of phase function curves resemble, proving that the type of roughness that we used does not affect this scattering parameter.

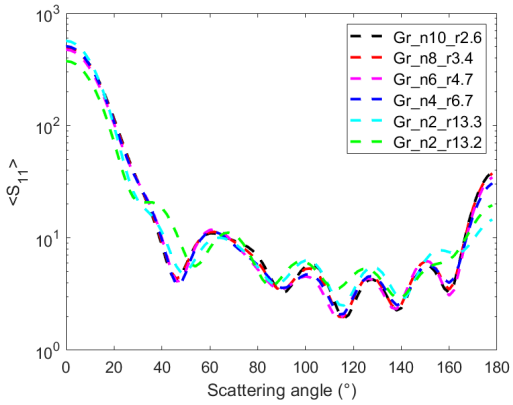

Figure 3.7: FEM numerical simulations of phase function of grains at $\lambda = 16.7$mm with a size parameter of $X_{mean} = 6.94$.

Another characteristic that can be analyzed based on the phase function (Figure 3.5) is the Half Width at Half Maximum (HWHM) of the forward scattering peak shown in Table 3.4. Values of the width obtained with measured and simulated phase functions, for each grain, have differences no larger than 6°, proving again the resemblance between measurements and simulations. As can be seen at each X_{mean}, the values of HWHM of grains are almost identical between each other, except at $X_{mean} = 6.94$ ($\lambda = 16.7$mm) as was already shown and explained with Figure 3.7. In summary, the phase functions of grains with average orientation do not provide much information of their roughness differences. The levels, HWHM and curve shapes of the phase functions of the different grains resemble when comparing them at each wavelength or X_{mean}.

X_{mean} / Gr	n10_r2.6	n8_r3.4	n6_r4.7	n4_r6.7	n2_r13.3	n2_r13.2
1.16	60 (60)	62 (60)	60 (60)	62 (60)	62 (60)	60 (58)
2.32	66 (68)	66 (68)	66 (68)	66 (68)	70 (70)	76 (74)
3.48	46 (44)	46 (44)	46 (44)	46 (44)	46 (44)	48 (48)
4.64	36 (34)	34 (34)	36 (34)	34 (34)	34 (34)	36 (36)
5.80	22 (24)	22 (24)	24 (24)	22 (24)	24 (24)	24 (22)
6.94	36 (30)	30 (30)	32 (30)	30 (30)	24 (26)	28 (24)

Table 3.4: HWHM of phase function in degrees at different X_{mean} of grains. Measured values (numerical values).

3.3.2.2 Degree of linear polarization

In the case of DLP presented in Figure 3.8 for all grains, differences between measurements and simulations are visually more important compared to the phase function. This could be due to their representation, one is logarithmic and the other linear, however this difference was verified with the criterion tool (which is latter explained and showed in Figure 3.10).

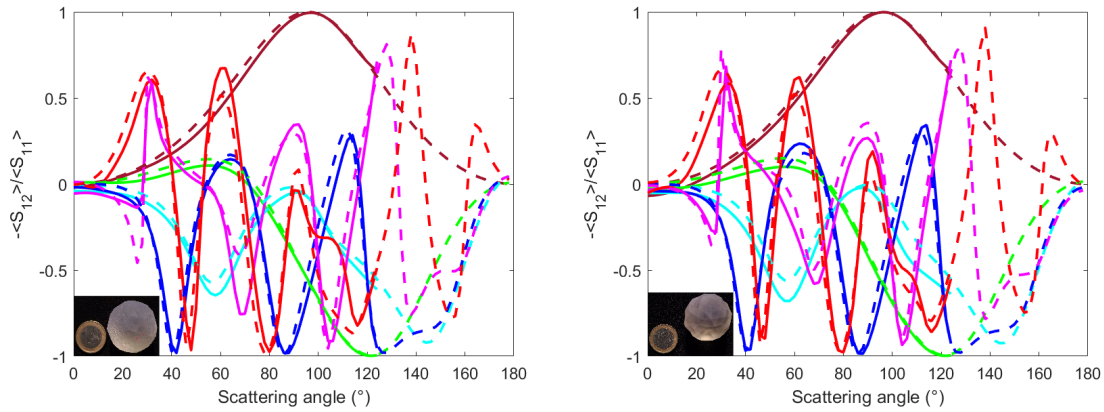

(a) Gr_n10_r2.6

(b) Gr_n8_r3.4

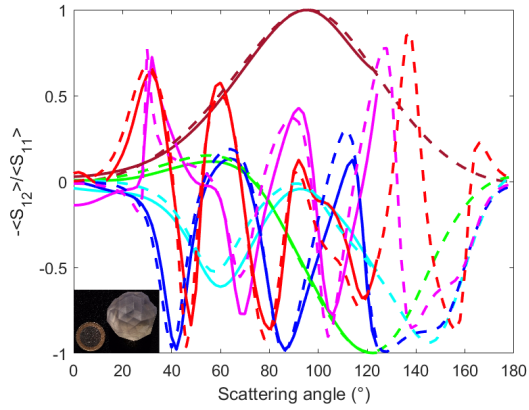

(c) Gr_n6_r4.7

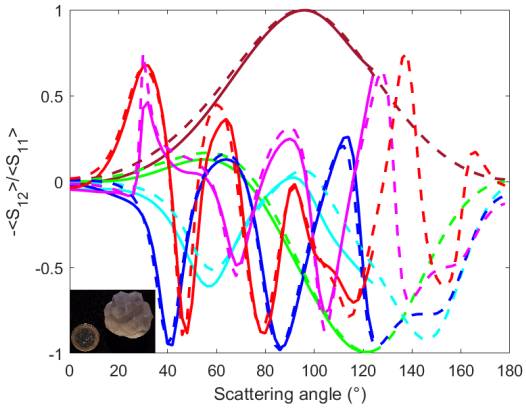

(d) Gr_n4_r6.7

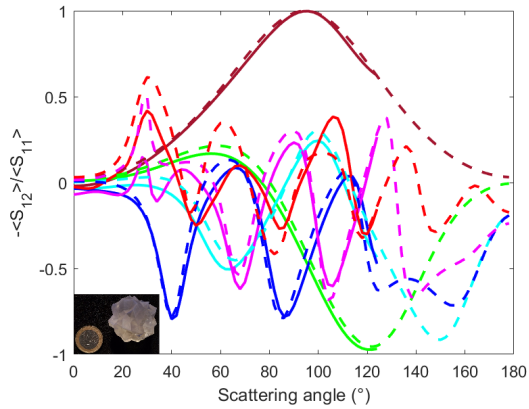

(e) Gr_n2_r13.3

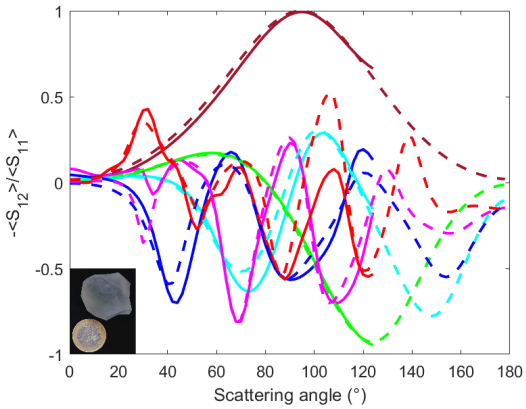

(f) Gr_n2_r13.2

Figure 3.8: DLP of grains, measurements (solid lines) and numerical simulations (dashed lines), see legends of Figure 3.5

Note that the DLP of all grains have the same Rayleigh behavior for the smallest X (brown lines), and that differences between grains DLP are visible at the three largest X, showed with the oscillation amplitude (see Figure 3.9 for an example of this behavior). These amplitudes are smaller for the roughest grains and as roughness decreases (becoming almost spherical grains), the oscillation amplitude becomes larger, showing a pseudo-sphere behavior. This scattering parameter, DLP, has more differences between grains than the phase function between grains. Thus DLP is a more adequate parameter if we want to identify scattering differences for the type of roughness, or sphericity, that our grains have. Indeed, there is a correlation between the grains roughness and sphericity, in the grains that we considered. The roughest grains are the least spherical while the smoothest grains are the most spherical (see Table 3.2).

The scattering angles corresponding to maximum levels of DLP at different X were not analyzed for the grains as was the case for aggregates (shown in Table 2.4) because there are many oscillations presenting maximum levels all allong the scattering angles (as shown in Figure 3.9). Thus this characteristic is not interesting to be analyzed because there is not a distinguishable order of maximum DLP levels or corresponding scattering angles depending on the roughness of grains.

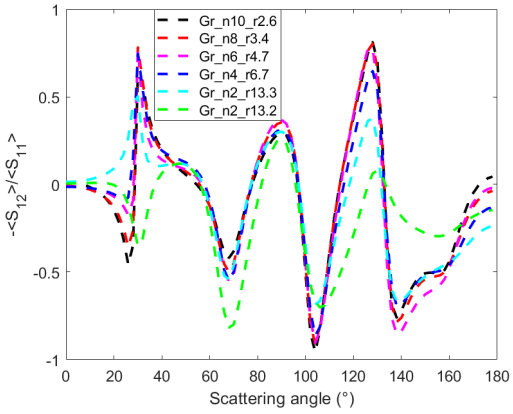

Figure 3.9: FEM numerical simulations of DLP of grains at $\lambda = 20\,\text{mm}$ with a size parameter of $X_{mean} = 5.80$.

Differences between measurements and FEM simulations of DLP were quantified with our comparison criterion tool, $RMSD_{IQR}$. The results of this comparison can be found in Figure 3.10. Deviations are larger for smaller wavelengths ($\lambda = 20$ to 16.7mm) and larger wavelengths (around $\lambda = 60\,\text{mm}$), compared to the phase function $RMSD_{IQR}$, arriving to values around $RMSD_{IQR} = 0.6$. Indeed, DLP is more sensitive than the phase function as it is a division between two average Mueller matrix elements. Thus this larger sensitivity could has caused larger deviations that may be caused by: first, the number of meshes for FEM simulations could be insufficient for DLP, and second, the grain size was too large compared to the wavelength so the

hypothesis of having a incident plane wave with simulations was not 100% valid for DLP.

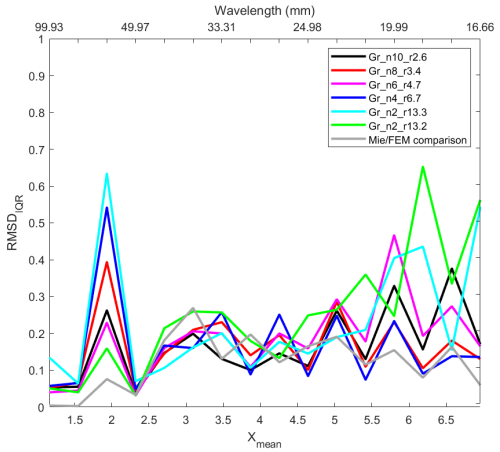

Figure 3.10: Normalized root mean square deviations on the log of the DLP plotted for all grains, taking their FEM numerical simulation as reference. The gray line is a comparison of the Mie simulation versus FEM numerical simulation with a sphere of radius 16.25mm.

3.3.2.3 Conclusions

Measurements and simulations of the phase function and DLP are consistent, presenting lower $RMSD_{IQR}$ in the case of phase functions. Moreover, phase functions of grains have very similar curve shapes and levels between each other, proving that this scattering parameter is not affected by the type of roughness that our grains present. In the case of grains DLP, their differences are seen with the amplitude of oscillations, indeed rough grains have small amplitudes of oscillations and as roughness decreases (or sphericity increases), amplitudes increase. Therefore, this characteristic of our grains DLP can be used for identifying which of our grains is rougher than the other.

3.3.2.4 Other scattering parameters

Polarimetric images of protoplanetary disks contain information of the phase function and degree of linear polarization of dust. These two scattering parameters are the only parameters that can be observed with telescopes. Yet, as previously explained in Section 2.4.2.4, there will be developments in the telescope instruments to obtain other scattering parameters. Therefore, the aim of this section is to study other three scattering parameters: $\frac{<S_{22}>}{<S_{11}>}$, $\frac{<S_{44}>}{<S_{11}>}$ and $\frac{<S_{34}>}{<S_{11}>}$, to validate or understand other scattering behaviors already seen or not seen with the phase function and DLP of grains. In this way, the different analysis presented hereon will help to understand and interpret observations of future scattered light images of protoplanetary disks.

Parameter $\frac{<S_{22}>}{<S_{11}>}$ is presented in Figure 3.11 for all grains. Notice that this parameter is represented only with numerical simulations, as previously explained in Section 3.3.1.2. Remember that this parameter is sensitive to asphericity (or non-sphericity) as was noted for our aggregates and mentioned in [179] for studies of rough spheres in which $\frac{<S_{22}>}{<S_{11}>}$ curves are farther from 1 when asphericity is bigger. It can be seen in Figure 3.11 that as the size parameter increases for $\frac{<S_{22}>}{<S_{11}>}$, this effect is more visible because the grain size is larger compared to the wavelength, as well as its roughness. Thus, the two largest asphericities obtained are for grain Gr_n2_r13.3 at $X = 7.54$ for a scattering angle of $\theta = 142°$ with a minimum value of 0.72, and for grain Gr_n2_r13.2 at $X = 7.73$ at the same scattering angle with a minimum value of 0.7. For other grains, as roughness decreases and sphericity increases, the amplitudes of $\frac{<S_{22}>}{<S_{11}>}$ curves decrease and converge toward 1. Thus, the minimum value for the smoothest grain, Gr_n10_r2.6, is around 0.97. See Figure 3.12 where $\frac{<S_{22}>}{<S_{11}>}$ of all grains is presented at $\lambda = 16.7$mm ($X_{mean} = 6.94$), showing the smallest values $\frac{<S_{22}>}{<S_{11}>}$. This figure presents $\frac{<S_{22}>}{<S_{11}>}$ curves that are organized from the two most spherical grains, Gr_n10_r2.6 (sphericity of 98.2%) and Gr_n8_r3.4 (sphericity of 97.0%), to the two least spherical grains, Gr_n2_r13.3 (sphericity of 75.6%) and Gr_n2_r13.2 (sphericity of 89.9%). Therefore the curves organization are in accordance with the calculated percentage of sphericity presented in Table 3.2. On the contrary, when $\lambda = 100$mm ($X_{mean} = 1.16$), grains become Rayleigh scatterers and $\frac{<S_{22}>}{<S_{11}>}$ tends to 1. In summary, when $X_{mean} > 1.16$ this scattering parameter is able to show that its levels are correlated with the sphericity of our grains, presenting $\frac{<S_{22}>}{<S_{11}>}$ curves that are organized from the smoothest (close to 1) to the roughest grain (smaller than 1).

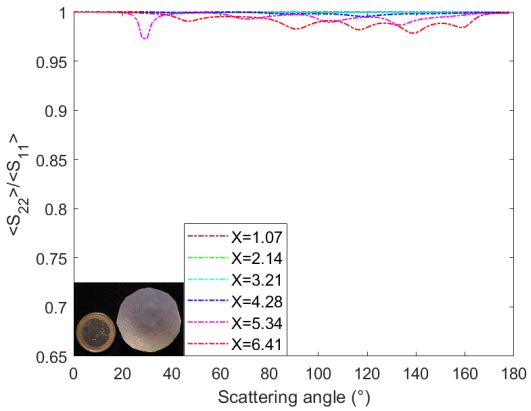

(a) Gr_n10_r2.6

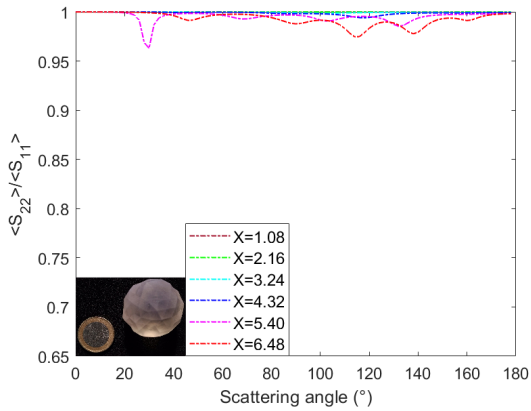

(b) Gr_n8_r3.4

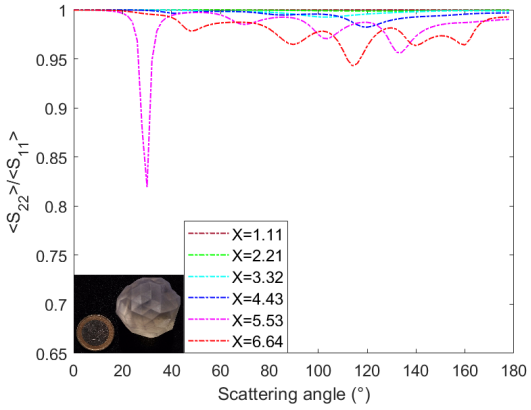

(c) Gr_n6_r4.7

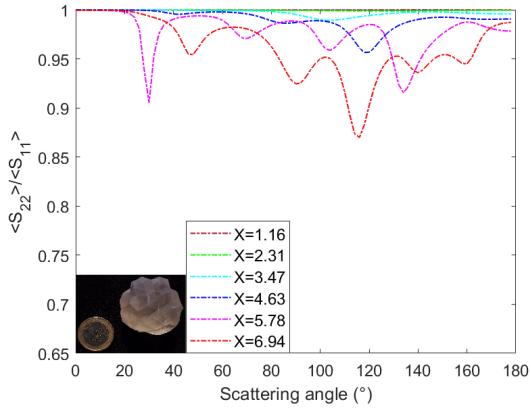

(d) Gr_n4_r6.7

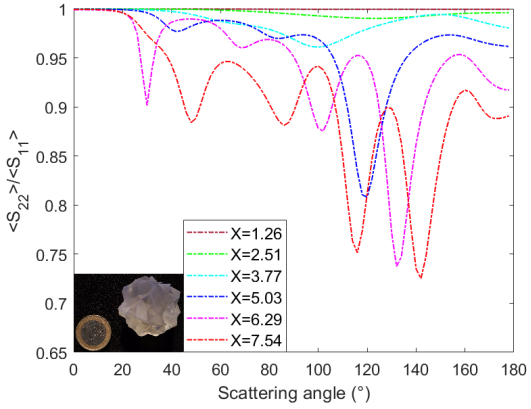

(e) Gr_n2_r13.3

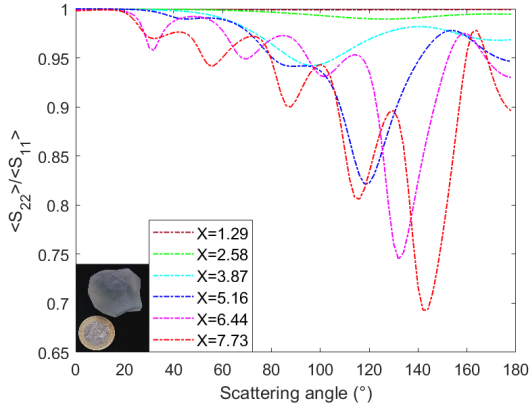

(f) Gr_n2_r13.2

Figure 3.11: FEM numerical simulations of $< S_{22} > / < S_{11} >$ including co and cross-polarized Jones matrix elements of grains.

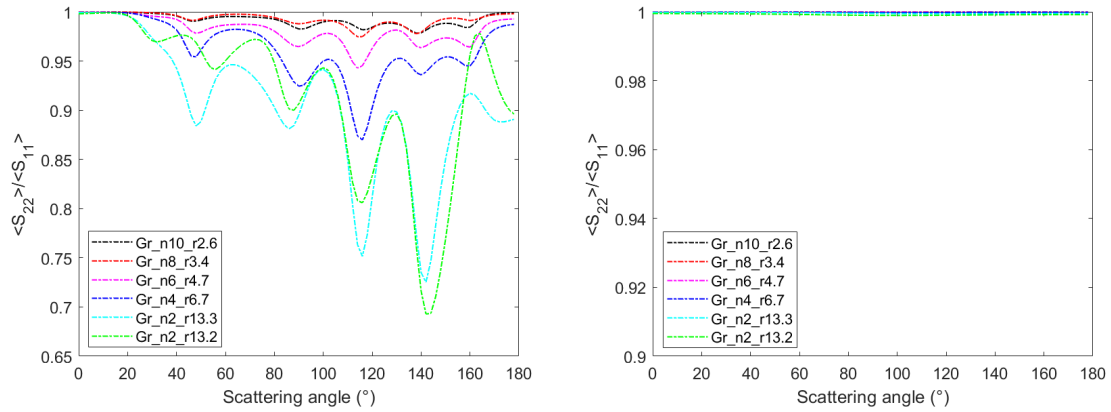

(a) $X_{mean} = 6.94$ (b) $X_{mean} = 1.16$

Figure 3.12: FEM numerical simulations of $< S_{22} > / < S_{11} >$ of grains at $\lambda = 16.7$mm with a size parameter of $X_{mean} = 6.94$ and $\lambda = 100$ mm with a size parameter of $X_{mean} = 1.16$.

Another parameter is $\frac{<S_{44}>}{<S_{11}>}$ which is equal to $\frac{<S_{33}>}{<S_{11}>}$, as shown in Figure 3.4, with and without cross-polarization. This equality highlights one of the Mie identities, $S_{33} = S_{44}$, which is not only the case for spheres but also for rough spheres as written in [179], and radially homogeneous and in-homogeneous spheres as noted in [180]. Our grains have also this Mueller matrix identity. Figure 3.13 presents $\frac{<S_{44}>}{<S_{11}>}$ (which is proportional to the degree of circular depolarization [79]) of all grains, where measurements and simulations have similar behaviors. At the smallest X (brown lines), $\frac{<S_{44}>}{<S_{11}>}$ curves have soft falls which is characteristic of Rayleigh scatterers, but for larger size parameters the falls are composed of oscillations (Mie-like behaviors). This general behavior of soft falls for small X and oscillating falls for larger X is presented for all grains and was already seen with DLP, thus $\frac{<S_{44}>}{<S_{11}>}$ validates this scattering information.

Parameter $\frac{<S_{34}>}{<S_{11}>}$ is shown in Figure 3.14 for all grains. At the smallest X, $\frac{<S_{34}>}{<S_{11}>}$ is almost constant, having values around zero all along the scattering angles for all grains (Rayleigh behavior). For larger X, oscillations appear, reaching up to ± 0.7 for the roughest grain, Gr_n2_r13.3. For other grains, the amplitude increases as roughness decreases (Mie-like behavior) or sphericity increases, reaching amplitudes of ± 1 for Gr_n10_r2.6. These two behaviors were already seen with DLP, hence this parameter does not add any extra scattering information on our grains.

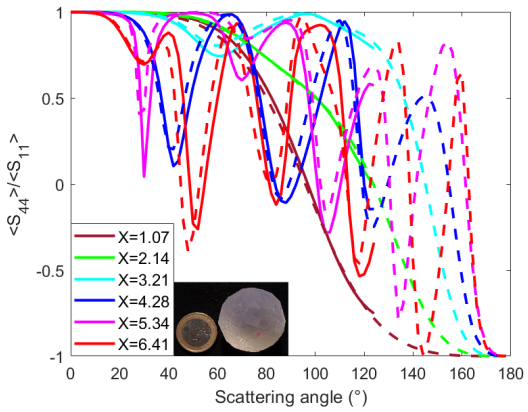

(a) Gr_n10_r2.6

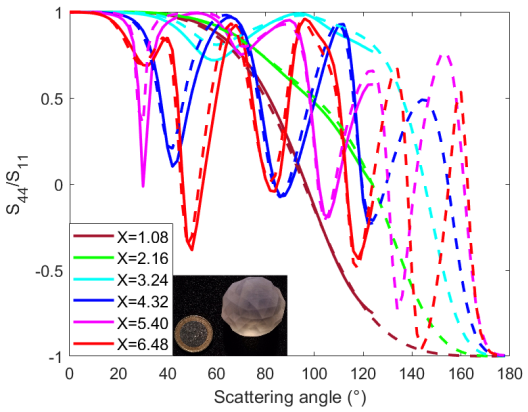

(b) Gr_n8_r3.4

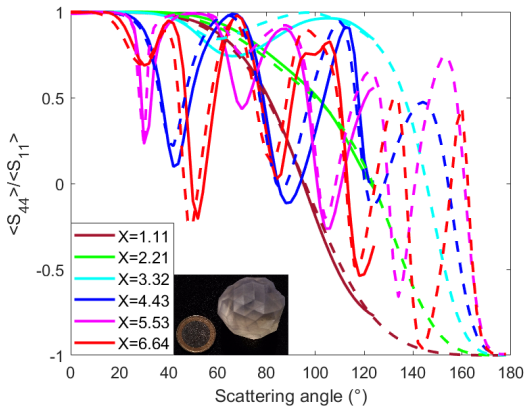

(c) Gr_n6_r4.7

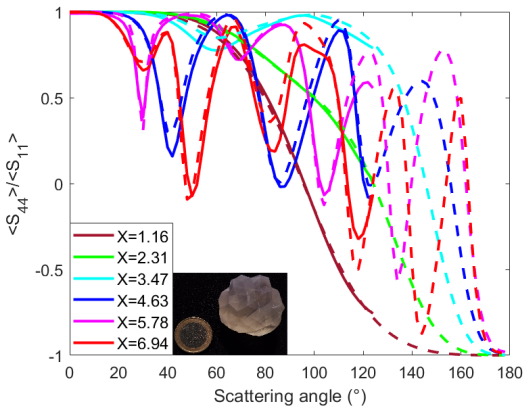

(d) Gr_n4_r6.7

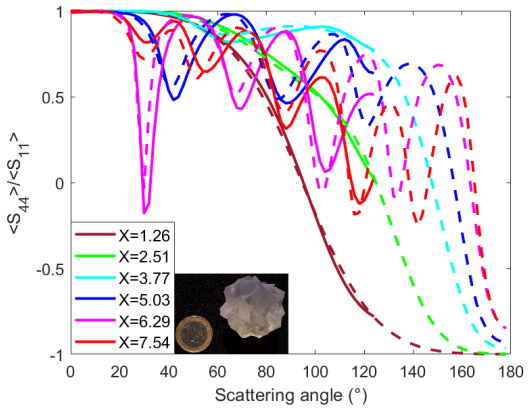

(e) Gr_n2_r13.3

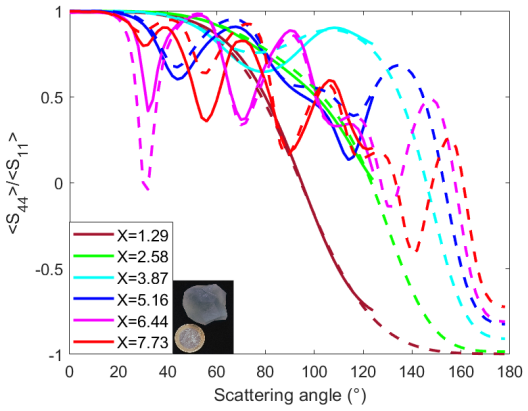

(f) Gr_n2_r13.2

Figure 3.13: $< S_{44} > / < S_{11} >$ of grains, measurements (solid lines) and numerical simulations (dashed lines).

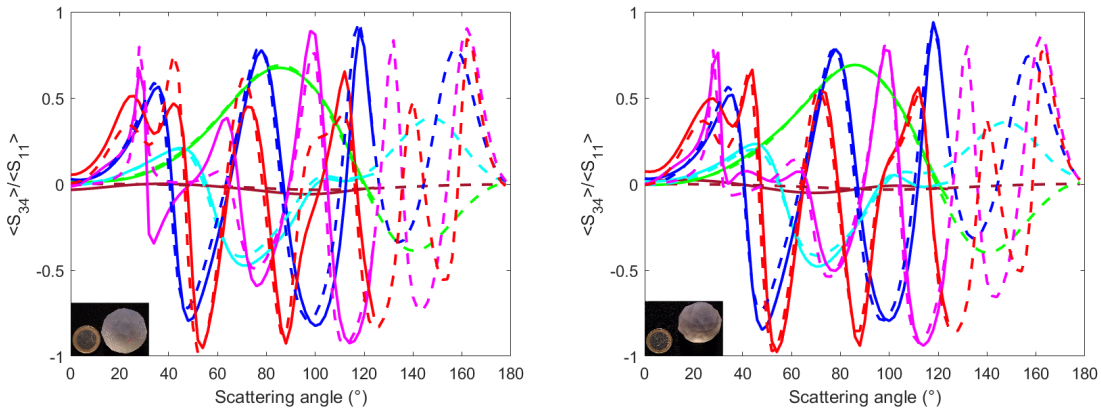

(a) Gr_n10_r2.6

(b) Gr_n8_r3.4

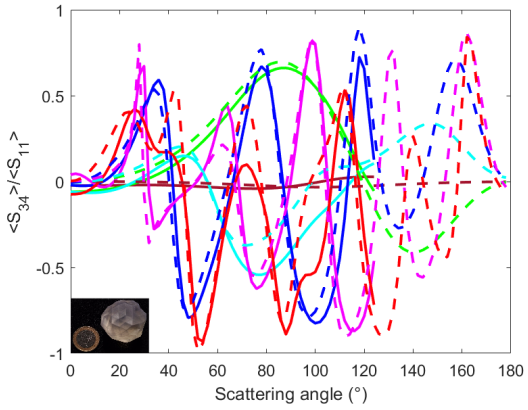

(c) Gr_n6_r4.7

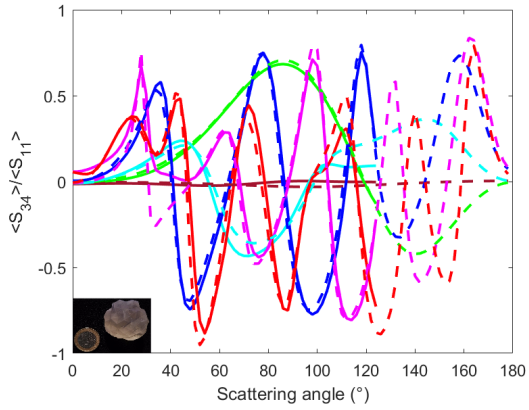

(d) Gr_n4_r6.7

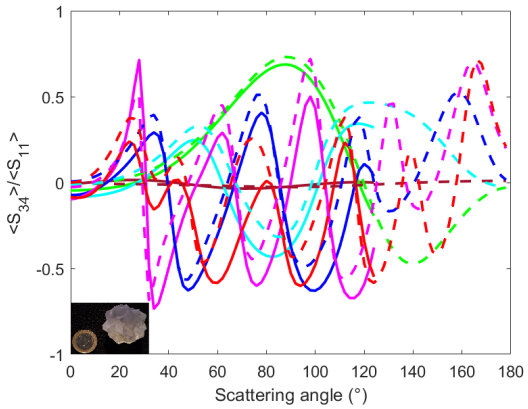

(e) Gr_n2_r13.3

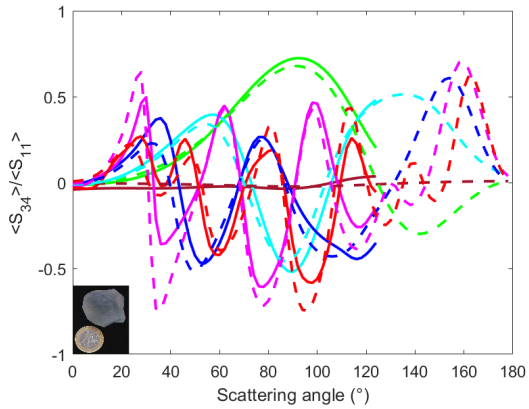

(f) Gr_n2_r13.2

Figure 3.14: $< S_{34} > / < S_{11} >$ of grains, measurements (solid lines) and numerical simulations (dashed lines). See legends of Figure 3.13.

3.3.2.5 Conclusions

In conclusion, measurements and numerical simulations of all these three scattering parameters are consistent between them. Furthermore, $\frac{<S_{22}>}{<S_{11}>}$ is the only one that add an extra scattering information on our grains compared to the phase function and DLP. With this parameter, we are able to identify which grain is more spherical than the others with levels of $\frac{<S_{22}>}{<S_{11}>}$ and presenting curves of grains organized from the most spherical grain (around 1) to the least spherical grain (around 0.7). Moreover, scattering parameters, $\frac{<S_{44}>}{<S_{11}>}$ and $\frac{<S_{34}>}{<S_{11}>}$, validate the same behaviors already seen with the phase function and DLP: at the smallest X of each grain ($X_{mean} = 1.16$), all these four scattering parameters have Rayleigh-like behaviors, and for larger X, these parameters have Mie-like behaviors.

3.3.2.6 Comparison of scattering parameters of grains and aggregates

In this section, I will compare the scattering properties of grains and aggregates based on their scattering parameters, in order to see if there are differences or similarities between these two morphologies. This will give some clues to analyze the scattering observations of protoplanetary disks and ideas about which morphology could be present in those disks. Note that our analogs are measured at the same wavelengths, but as their sizes (or bounding spheres) are different, their size parameters (X) have not the same values at the same wavelengths. Thus, I tried to find the closest X between aggregates and grains to be able to compare their scattering parameters, eliminating the variation of X and therefore possible effects that this change could cause on their scattering parameters.

When comparing the phase functions of our grains and aggregates at similar size parameters (see Figure 3.15), three main differences are noticed: i) the number of phase function bumps of grains are greater at the two largest X, ii) the forward scattering peaks of grains decrease faster arriving to minimum values for smaller scattering angles and iii) backscattering levels of the grains phase functions have higher levels at the largest X. If the comparison is made with a fluffier aggregate, Ag_DLA_Df2.0_N74_1, these three differences are even more visible. Figure 3.15.d shows that the phase function of grain Gr_n2_r13.3 resembles more to the phase function of aggregate Ag_DLA_Df2.8_N74 than aggregate Ag_DLA_Df2.0_N74_1, which was expected because these two first morphologies have the similarity of being more compact, yet they still can be identified with their phase functions. This proves that phase functions of grains and aggregates have different behaviors, thus even if aggregates can be considered as rough particles, their porosities affect this scattering parameter.

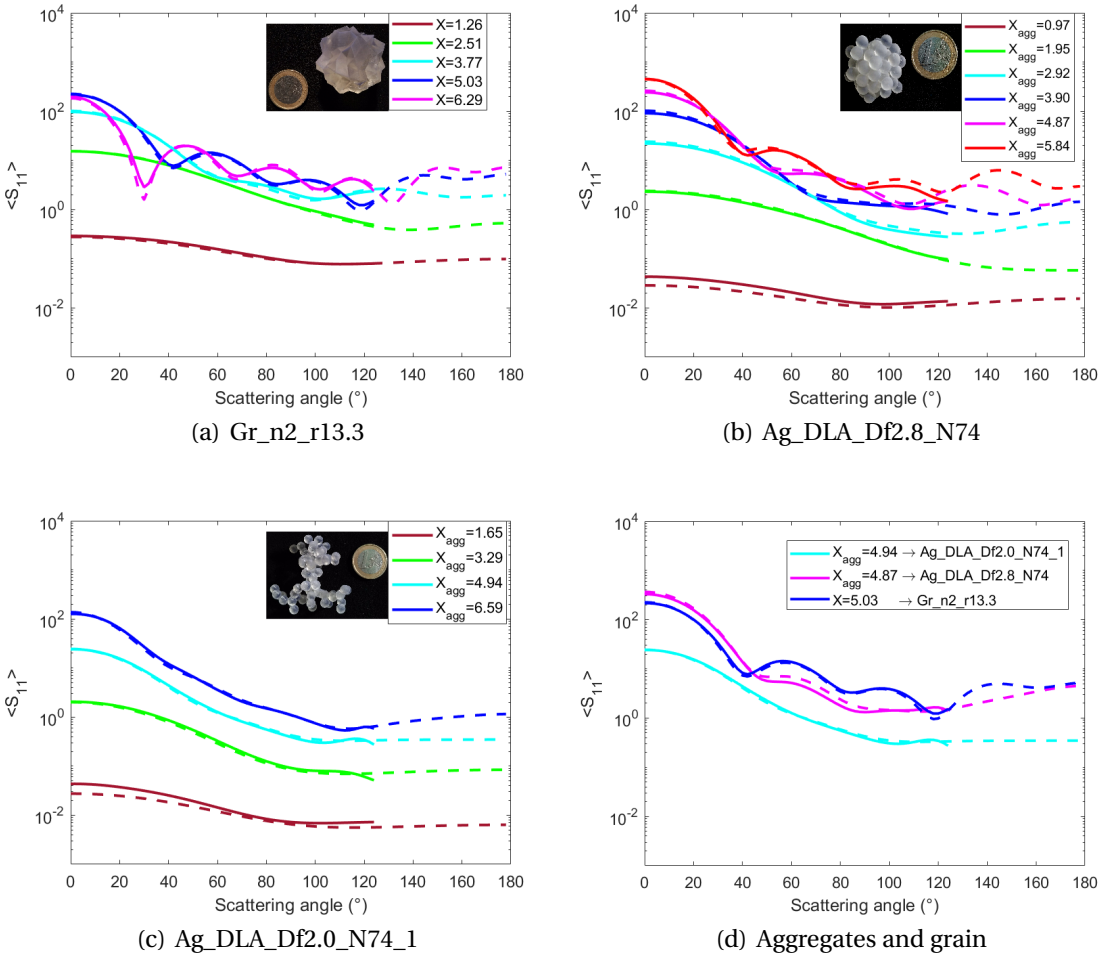

(a) Gr_n2_r13.3

(b) Ag_DLA_Df2.8_N74

(c) Ag_DLA_Df2.0_N74_1

(d) Aggregates and grain

Figure 3.15: Phase function of grains and aggregates, measurements (solid lines) and numerical simulations (dashed lines). Note that colors are given at six wavelengths but depending on the size of the object this creates different size parameters, see Figure (d) to have comparable size parameters.

By comparing the DLP (see Figure 3.16) at similar size parameters, both DLP have a Rayleigh behavior at the largest wavelength (brown lines). When increasing X, DLP of grains have a similar behavior as DLP of the most compact aggregate, Ag_DLA_-Df2.8_N74. There is just a slight difference between grains and compact aggregates: i) DLP curves of the grain have more oscillations than DLP curves of the aggregate, and ii) DLP minimum values are closer to -1. Thus, this can be a characteristic when comparing DLP of compact grains and compact aggregates. On the other hand, when the comparison is between DLP of grains with DLP of a fluffier aggregate, Ag_-DLA_Df2.0_N74_1, even when increasing X, DLP of fluffy aggregates has a Rayleigh behavior, thus the difference between fluffy aggregates and grains is more visible. This can be seen in Figure 3.16.d that superposes DLP curves of one grain and two

aggregates with different fractal dimensions at their closest X.

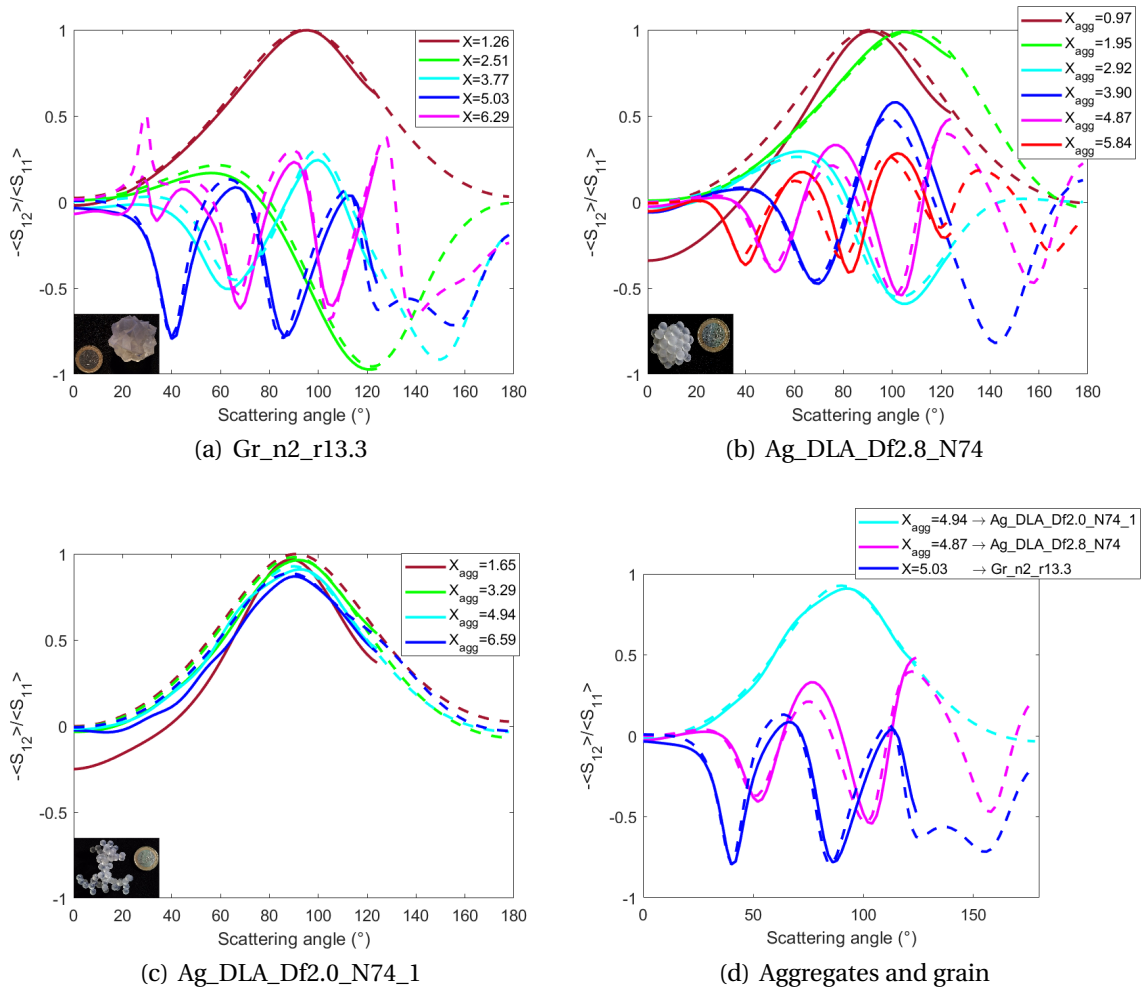

(a) Gr_n2_r13.3

(b) Ag_DLA_Df2.8_N74

(c) Ag_DLA_Df2.0_N74_1

(d) Aggregates and grain

Figure 3.16: DLP of grains and aggregates, measurements (solid lines) and numerical simulations (dashed lines).

In the case of parameter $\frac{<S_{22}>}{<S_{11}>}$, it is only possible to differentiate three groups shown in Figure 2.21 (the most fluffy aggregates, intermediate aggregates and the most compact aggregate which means more spherical), while $\frac{<S_{22}>}{<S_{11}>}$ of all grains are organized with a clear separation from the roughest to the smoothest grain which means more spherical (see Figure 3.12). Therefore, this parameter is even more sensitive to differentiate between our grains than our aggregates. Moreover, when comparing $\frac{<S_{22}>}{<S_{11}>}$ of grain Gr_n2_r13.3 to aggregates Ag_DLA_Df2.8_N74 and Ag_-DLA_Df2.0_N74_1 (Figure 3.17), two behaviors are observed: i) $\frac{<S_{22}>}{<S_{11}>}$ levels of grain are smaller compared to $\frac{<S_{22}>}{<S_{11}>}$ levels of both aggregates, proving a more important depolarization and therefore a larger asphericity for the grain, and ii) $\frac{<S_{22}>}{<S_{11}>}$ curves of

this grain have more oscillations than for both aggregates. Figure 3.17.d shows $\frac{<S_{22}>}{<S_{11}>}$ of the grain with these two aggregates at a similar size parameter, where there is a clear evidence that the grain along with its roughness depolarizes more than both aggregates. Thus, the roughness of our grains affects more this parameter than the morphology of aggregates, showing a larger visible difference between grains and aggregates than previous comparisons with phase functions and DLP.

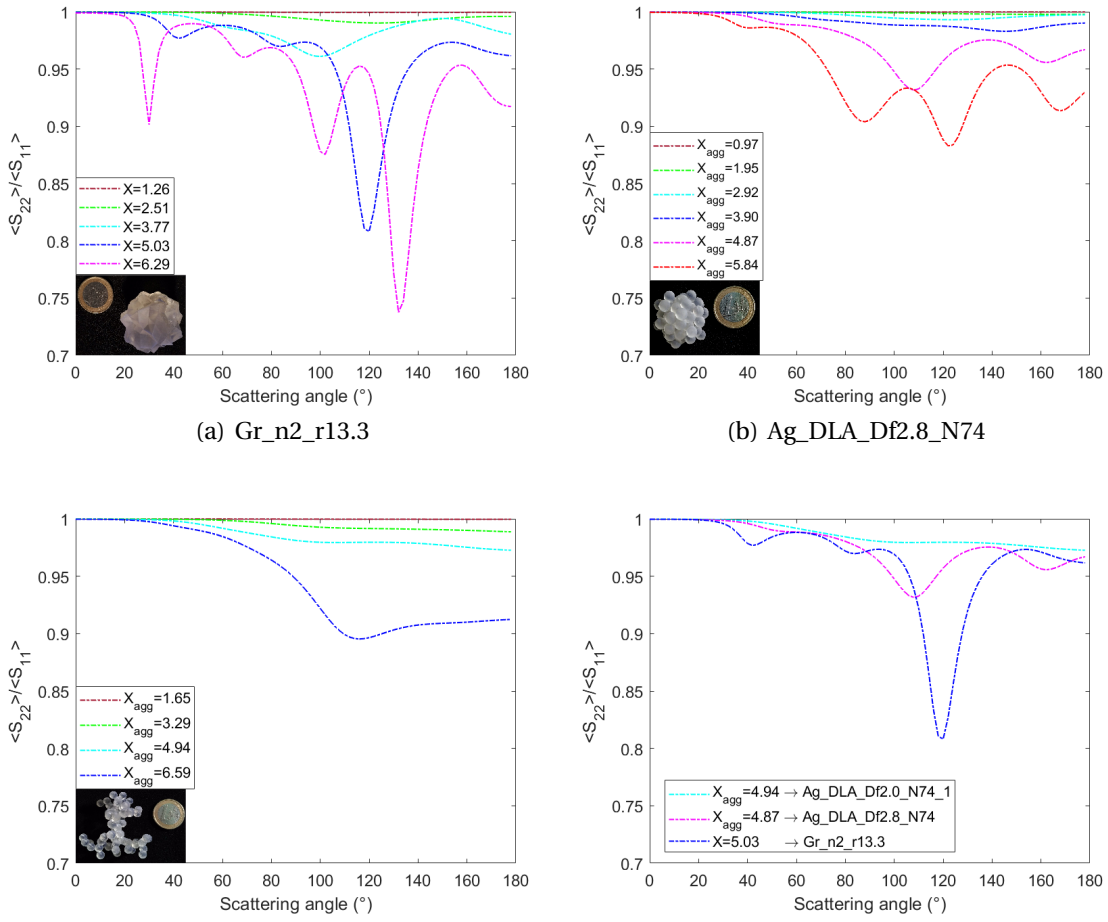

(a) Gr_n2_r13.3

(b) Ag_DLA_Df2.8_N74

(c) Ag_DLA_Df2.0_N74_1

(d) Aggregates and grain

Figure 3.17: $< S_{22} > / < S_{11} >$ of grains and aggregates including co and cross-polarized Jones Matrix elements.

When comparing $\frac{<S_{44}>}{<S_{11}>}$ of aggregates with that of grains, there are several differences (see Figure 3.18): i) aggregates presented much less oscillating curves with smaller amplitudes of oscillations than grains (the most compact aggregate being the one with the highest number of oscillations while other aggregates present smooth curves similar to Rayleigh scatterers). ii) $\frac{<S_{44}>}{<S_{11}>}$ of all grains oscillates from 20° to 180°, while for aggregates it starts at 60°. Therefore, these differences in $\frac{<S_{44}>}{<S_{11}>}$ behaviors demonstrates

that there are scattering differences between the morphologies of aggregates and compact grains. These differences were already seen with phase functions, DLP and $\frac{<S_{22}>}{<S_{11}>}$ of both morphologies.

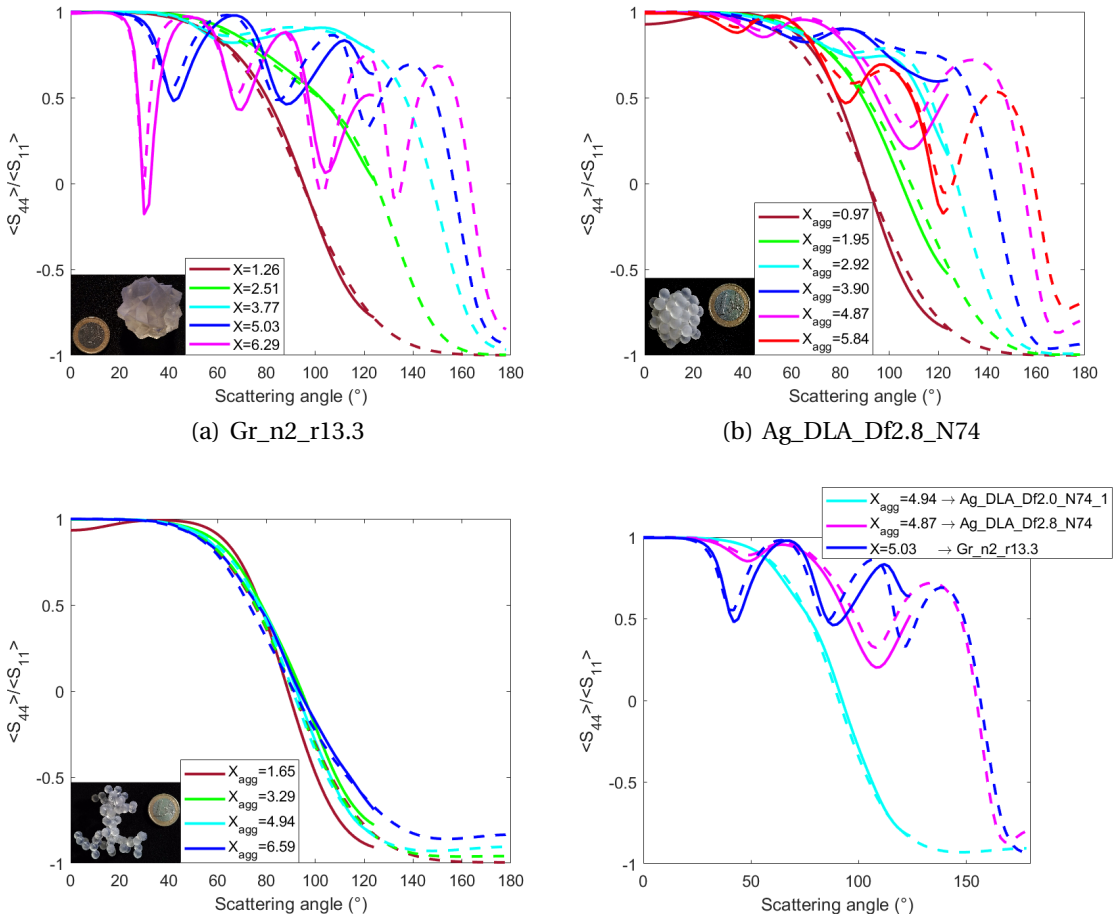

(a) Gr_n2_r13.3

(b) Ag_DLA_Df2.8_N74

(c) Ag_DLA_Df2.0_N74_1

(d) Aggregates and grain

Figure 3.18: $< S_{44} > / < S_{11} >$ of grains and aggregates, measurements (solid lines) and numerical simulations (dashed lines).

Finally, $\frac{<S_{34}>}{<S_{11}>}$ of grains are compared with that of our aggregates (see Figure 3.19). In general $\frac{<S_{34}>}{<S_{11}>}$ curves of our aggregates do not oscillate especially when $D_f \leq 2$. On the other hand, the most compact aggregate (Ag_DLA_Df2.8_N74) is the one that presents the highest number of oscillations from all aggregates, and still it has less oscillations than grains. Thus, when comparing $\frac{<S_{34}>}{<S_{11}>}$ of this aggregate with that of our grains, differences can be seen in the number of oscillations per wavelength and the amplitude of oscillations, both characteristics being larger for grains than for aggregates (similar to the oscillating behaviors already observed when comparing all other scattering parameters of grains and aggregates). Thus, this parameter verifies

the behaviors that were already highlighted with other scattering parameters.

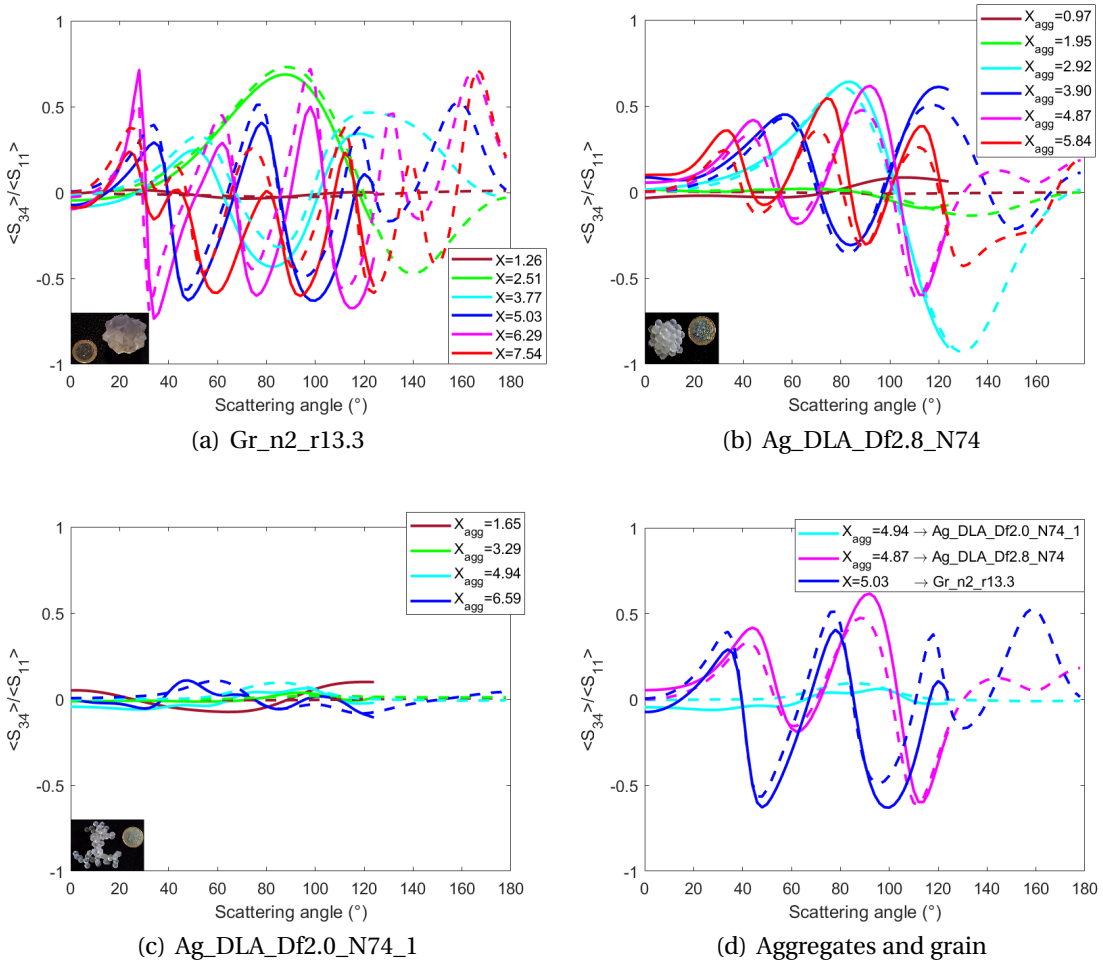

(a) Gr_n2_r13.3

(b) Ag_DLA_Df2.8_N74

(c) Ag_DLA_Df2.0_N74_1

(d) Aggregates and grain

Figure 3.19: $< S_{34} > / < S_{11} >$ of grains and aggregates, measurements (solid lines) and numerical simulations (dashed lines).

In conclusion, comparisons of all five scattering parameters between grains and aggregates showed two main differences: first, the number of oscillations per wavelength is greater for grain scattering parameters and second, the amplitude of oscillations are larger for grain scattering parameters. Between grains and fluffy aggregates with $D_f \leq 2$, aggregates present visible differences because in the case of grains, they behave like Mie scatterers, while aggregates (with $D_f \leq 2$), like Rayleigh scatterers (shown for all five scattering parameters). However, when comparing grains with the most compact aggregate (Ag_DLA_Df2.8_N74), their phase function and DLP resemble more than when comparing with fluffy aggregates, and only greater differences can be observed with $\frac{<S_{22}>}{<S_{11}>}$ (minimum levels) and $\frac{<S_{44}>}{<S_{11}>}$ (number of oscillations and scattering angles corresponding to these oscillations).

Notice that in order to have a complete analysis of the scattering behaviors of grains and to differentiate them from aggregates, the phase function or DLP can be used to differentiate between grains and fluffy aggregates, while $\frac{<S_{22}>}{<S_{11}>}$ or $\frac{<S_{44}>}{<S_{11}>}$ can be used to differentiate between grains and compact aggregates. Therefore, there is a necessity to continue the instrumental developments of telescopes to measure more than the phase function and DLP.

All these five scattering parameters are studied in the following section, including a size distribution effect to have more realistic scattering behaviors. Indeed, protoplanetary disks have populations of dust of different sizes, all being observed at the same time, thus the necessity to apply a size distribution to our scattering parameters.

3.3.3 Grains with average orientation and size distribution effect

3.3.3.1 Probability distribution

As mentioned in Section 1.2.3, protoplanetary dust sizes of our interest are between 0.1µm to 10µm considering NIR and optical data and following a power law distribution of index −3.5. Remember that millimeter sized dust can be present in protoplanetary disks but they are bad emitters at these range wavelengths, as previously indicated in Section 2.4.3.1.

Thus, if we consider dust with these micrometer sizes and we choose optical wavelengths, based on Table 1.2, size parameters would be from $X_{min} = 0.90$ to $X_{max} = 157.08$. As can be seen, X_{min} is very close to our grains minimal size parameter of $X_{mean} = 1.16$ (calculated with the mean radius of the bounding sphere of all grains of 18.45mm). On the contrary, the maximal size parameter of our grains is $X_{mean} = 6.94$, thus not even in the orders of the maximum protoplanetary dust size parameter. Even so, the probability of finding our grain maximum size parameter is of 0.0021. This latter means that larger size parameters can be neglected because they are less likely to be present. In this way, the size distribution that follows protoplanetary dust can be artificially applied to our grains by using a size distribution X^{-n_s}, where $n_s = 3.5$, from $X_{mean} = 1.16$ to $X_{mean} = 6.94$. This size distribution on X is named in this thesis as a size distribution effect with index n_s (explained in Section 2.4.3, expressed in Equation 2.5) and it is shown in Figure 3.20 for our grains. Notice that two more indices were added in this study, $n_s = 2$ and $n_s = 5$, in order to analyze the effect of n_s on the scattering parameters, as it was also made for the scattering parameters of aggregates.

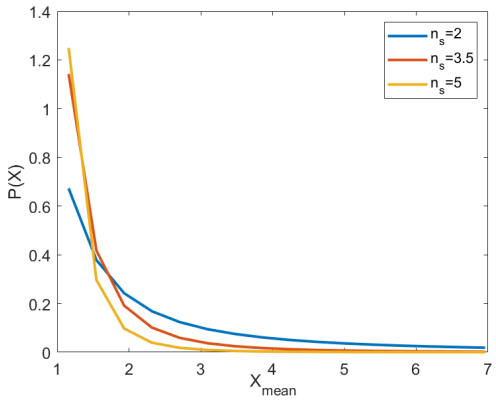

Figure 3.20: Probability distribution with three different indices (see legend) in terms of X_{mean}, from 1.16 to 6.94.

3.3.3.2 Phase function

The size distribution effect was applied to the different scattering parameters of our grains at the three chosen n_s. The phase functions of all six grains are shown in Figure 3.21 with similar measurements and simulations. Phase function curves of different grains are alike at the forward scattering angles, having smooth curves and similar width values (HWHM) at each n_s, as shown in Table 3.5. Their similarities of HWHM values for each n_s is due to the fact that the radius of the bounding spheres of all grains is very close, thus the size of their scattering spots are almost the same. Differences between their phase functions are visible at backscattering angles, where levels at 180° of normalized phase functions are larger for the smoothest grains and decrease as roughness of grains increases (or sphericity decreases), shown at all three n_s (note that this normalization is made at 0° as shown in Figure 3.22). Hence, Gr_n10_r2.6 which is the smoothest grain, has the largest phase function levels at backscattering angles for all n_s (see Table 3.6).

At $n_s = 3.5$, the HWHM of the forward scattering peaks are around 52° for measurement and 50° for simulations. The HWHM is narrower for a size distribution of $n_s = 2$ and wider for $n_s = 5$. This effect was expected since power law distributions with larger coefficients give more weight to small X, thus smaller grains. Moreover, phase function enhancements at backscattering angles have the largest levels at $n_s = 2$. This is caused by the fact that larger X have more weight in this distribution (shown for each grain at different X in Figure 3.5) and as X increases backscattering enhancement increases too.

In summary, at the same n_s, grains with different roughness can be differentiated with their backscattering levels. Comparisons between phase functions of different n_s can be differentiated with their HWHM and their backscattering levels.

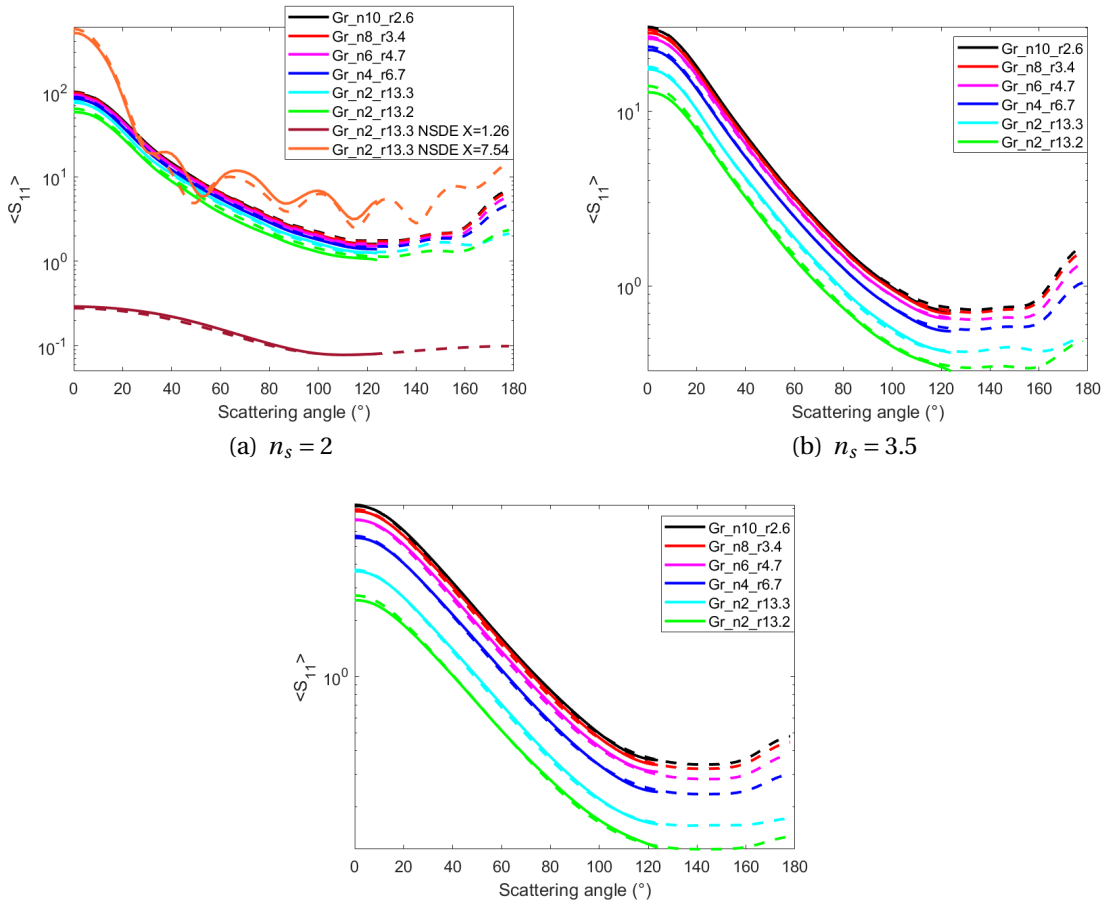

(a) $n_s = 2$ (b) $n_s = 3.5$

(c) $n_s = 5$

Figure 3.21: Phase function of grains with average orientation and with power law distributions of different n_s, measurements (solid lines) and numerical simulations (dashed lines). Figure (a) also presents the phase function of the roughest grain at $X = 1.26$ (in brown) and at $X = 7.54$ (in orange) with No Size Distribution Effect (NSDE).

n_s / Gr	n10_r2.6	n8_r3.4	n6_r4.7	n4_r6.7	n2_r13.3	n2_r13.2
2	44 (42)	44 (42)	44 (42)	42 (42)	44 (42)	46 (42)
3.5	52 (50)	52 (50)	52 (50)	50 (50)	52 (50)	52 (50)
5	58 (58)	58 (58)	58 (58)	58 (58)	58 (56)	58 (58)

Table 3.5: HWHM of phase function of grains with average orientation and with power law distributions of different n_s. Measured values (numerical values), both in degrees.

Another analysis that can be made is comparing the phase functions with a size distribution effect, with the phase functions without this effect (presented in subsec-

tion 3.3.2.1). This comparison is possible thanks to the control of orientation and multiple wavelengths with our scattering experiment in CCRM. Figure 3.21.a presents the phase function of the roughest grain at $X = 7.54$ ($\lambda = 16.7$mm) and at $X = 1.26$ ($\lambda = 100$ mm) named Gr_n2_r13.3 NSDE. Note that the phase functions of other grains with NSDE at the same wavelengths have a very similar curve shape, thus these NSDE curves (shown in Figure 3.21.a) are in representation of other grains. When comparing phase functions with size distribution effect and without it, the bumps of the phase functions (brown lines) have completely disappeared. This latter is due to the average made for each grain at different X (or wavelengths).

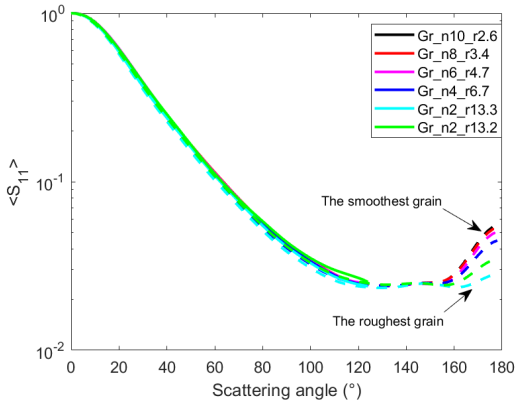

Figure 3.22: Normalized phase function of grains with average orientation and with power law distributions of $n_s = 3.5$, measurements (solid lines) and numerical simulations (dashed lines).

n_s / Gr	n10_r2.6	n8_r3.4	n6_r4.7	n4_r6.7	n2_r13.3	n2_r13.2
2	0.051	0.049	0.045	0.036	0.011	0.019
3.5	0.031	0.030	0.026	0.021	0.005	0.011
5	0.017	0.016	0.014	0.011	0.004	0.007

Table 3.6: Backscattering levels of phase functions of grains with average orientation and with power law distributions of different n_s. Calculated with the difference of the maximum numerical value at 180° and the minimum numerical value of the phase function curve.

3.3.3.3 Degree of linear polarization

The degree of linear polarization including the size distribution effect of our grains is shown in Figure 3.23. Two phenomena are identified at the three power law indices. First, maximum levels of DLP drastically change depending on n_s. At $n_s = 3.5$ maximum values of DLP are around orders of 0.10 with scattering angles of 85°, while at $n_s = 2$ maximum values decrease with scattering angles of 20°, and at $n_s = 5$ maximum

values are the largest of all three n_s with scattering angles of 98° (see Table 3.7 for maximum DLP values for each grain). This behavior seen at $n_s = 5$ is caused by the contribution of DLP levels of small grains due to distribution, having Rayleigh-like behaviors and therefore presenting maximum values. On the contrary, at $n_s = 2$, the largest contribution comes from Mie-like behaviors, where the average of oscillating DLP curves produce maximum values around 0° with an important negative polarization branch. The second observed phenomenon is the negative polarization branch between scattering angles of 150° and 160°. This branch has the largest negative values at $n_s = 2$, and when increasing n_s negative branch values tend to 0.

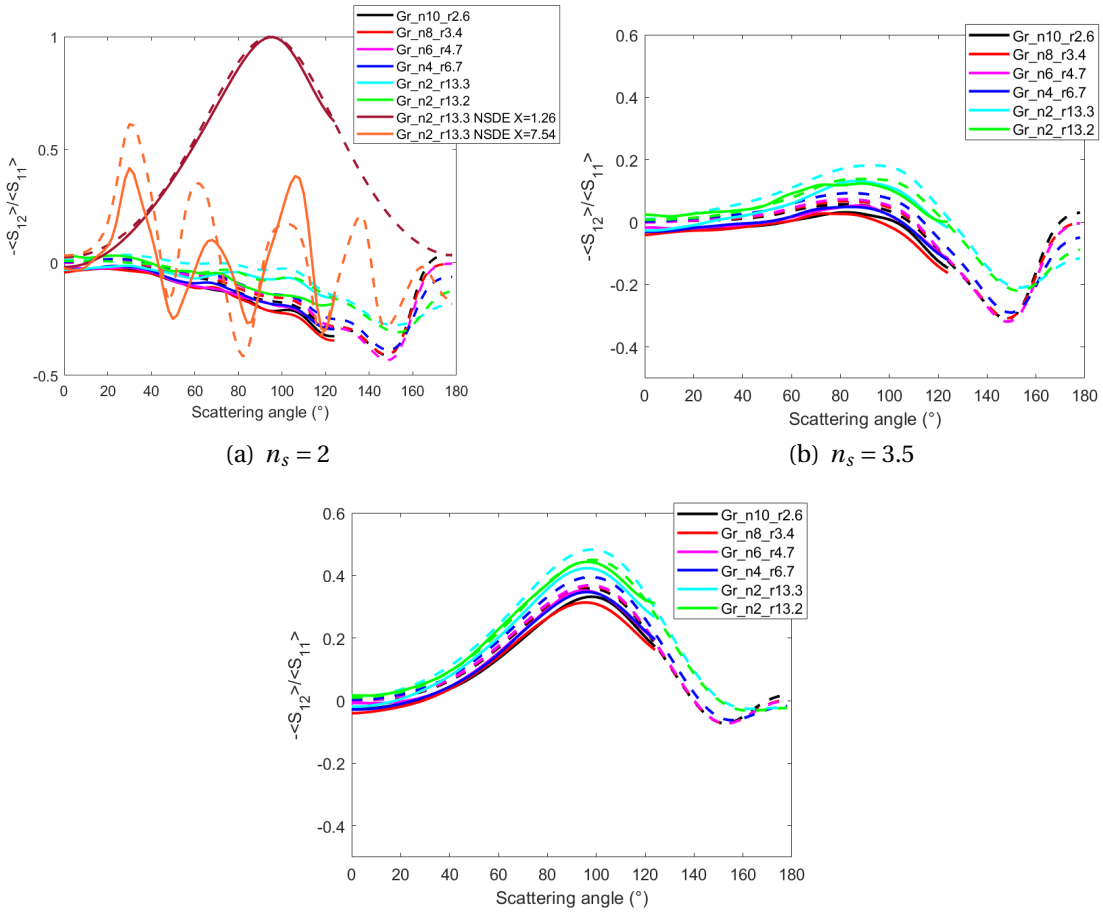

(a) $n_s = 2$

(b) $n_s = 3.5$

(c) $n_s = 5$

Figure 3.23: DLP of grains with average orientation and with power law distributions of different n_s, measurements (solid lines) and numerical simulations (dashed lines). Figure (a) also presents DLP of the roughest grain at $X = 1.26$ (in brown) and at $X = 7.54$ (in orange) with No Size Distribution Effect (NSDE).

At all three n_s, two groups of grains can be differentiated. On one hand, the group

of the roughest grains or the least spherical (Gr_n2_r13.3 and Gr_n2_r13.2) that have the smallest negative polarization branches and the largest maximum DLP levels. On the other hand, the group of the smoothest grains or the most spherical (Gr_n10_r2.6, Gr_n8_r3.4, Gr_n6_r4.7 and Gr_n4_r6.7) that have the largest negative polarization branches and smallest maximum DLP levels. Hence, based on this scattering parameter, roughness of grains (or sphericity) is revealed with two elements: levels of maximum DLP and negative polarization branch. Additionally, the effect of changing n_s also affects these two elements.

n_s / Gr	n10_r2.6	n8_r3.4	n6_r4.7	n4_r6.7	n2_r13.3	n2_r13.2
2	-0.03 (0.01)	-0.03 (0.01)	-0.02 (0.01)	-0.02 (0.02)	-0.01 (0.03)	0.03 (0.01)
3.5	0.03 (0.06)	0.03 (0.07)	0.05 (0.07)	0.05 (0.09)	0.13 (0.18)	0.12 (0.14)
5	0.33 (0.36)	0.31 (0.37)	0.35 (0.37)	0.35 (0.40)	0.42 (0.48)	0.44 (0.45)

Table 3.7: Levels of maximum DLP of grains with average orientation and with power law distributions of different n_s. Measured values (numerical values).

DLP with size distribution effect and without this effect are represented and compared in Figure 3.23.a. Curves with no size distribution effect (NSDE) represent DLP of grain Gr_n2_r13.3 at the smallest and largest wavelength, leading to $X = 7.54$ (orange line) and $X = 1.26$ (brown line). The behaviors of these two curves are representative of the other grains DLP with NSDE. As can be seen, oscillations of Gr_n2_r13.3 NSDE at $X = 7.54$ have disappeared by applying the size distribution effect because the weight is given mostly to small particles (Gr_n2_r13.3 NSDE at $X = 1.26$). Hence, DLP with $n_s = 2$ have closer values to Gr_n2_r13.3 NSDE at $X = 7.54$, while DLP with $n_s = 5$ have similar behaviors to Gr_n2_r13.3 NSDE at $X = 1.26$. These behaviors are caused by the type of weight given at each n_s. For example, in the case of $n_s = 2$, the weight is given to larger grains compared to $n_s = 5$. The same effect was seen for the phase functions with the three different power law indices.

3.3.3.4 Other scattering parameters

Parameter $\frac{<S_{22}>}{<S_{11}>}$ is presented in Figure 3.24 based on numerical simulations, for all three n_s. As mentioned by [179] and shown in Section 3.3.2.4, this parameter is related to the sphericity of grains (see the percentage of sphericity in Table 3.2). This is the case for all three size distribution indices and all grains except for Gr_n2_r13.2, which has the smallest $\frac{<S_{22}>}{<S_{11}>}$ value contrary to its calculated sphericity that does not have the smallest percentage of all grains. This might be caused by its morphology that is different from the rest of the grains because it was meshed with 80 triangles instead of 320, producing a different shape, more elongated one, and depolarizing more than the other grains. Actually, if a grain is more elongated this should affect its percentage of sphericity. However, the way we calculated sphericity does not take into account changes in terms of elongation, thus Gr_n2_r13.2 presents a larger percentage of sphericity contrary to what $\frac{<S_{22}>}{<S_{11}>}$ illustrates. For this reason, we propose to analyze

$\frac{<S_{22}>}{<S_{11}>}$ with another characteristic that is the grain material packing density (shown in Table 3.2). Indeed, if a grain is more elongated (which affects its sphericity), its packing density is smaller. As can be seen, for the three n_s, grains with the largest material packing density ρ, present the maximum $\frac{<S_{22}>}{<S_{11}>}$ values around 1, and as ρ decreases, $\frac{<S_{22}>}{<S_{11}>}$ values decrease too. Thus, Gr _n10_r2.6 with $\rho = 0.85$ has $\frac{<S_{22}>}{<S_{11}>}$ values around 1, while Gr_n2_r13.2 with $\rho = 0.42$ has the smallest $\frac{<S_{22}>}{<S_{11}>}$ values. In other words, this scattering parameter shows a consistent organization of its curves related to the calculated material packing density for all our grains and sphericity for most of our grains, which is a complementary information on the grain morphologies compared to the phase function and DLP.

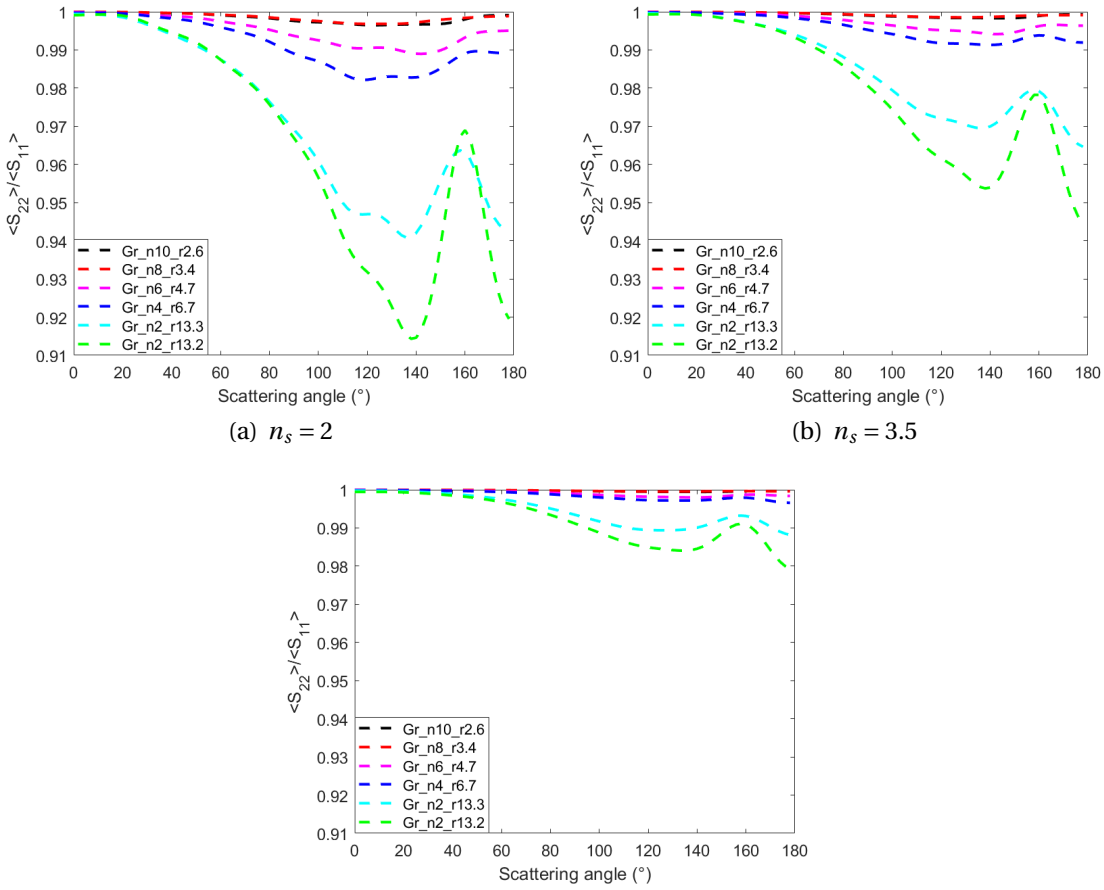

(a) $n_s = 2$ (b) $n_s = 3.5$

(c) $n_s = 5$

Figure 3.24: $< S_{22} > / < S_{11} >$ of grains with average orientation and with power law distributions of different n_s based on numerical simulations (dashed lines).

Notice that when comparing this parameter with and without size distribution effect, oscillations and levels of $\frac{<S_{22}>}{<S_{11}>}$ have decreased due to the average produced by

the size distribution, as was also noticed for the phase function and DLP.

Parameter $\frac{<S_{44}>}{<S_{11}>}$ for grains is presented in Figure 3.25. With $n_s = 5$, smooth curves of different grains are almost superposed, presenting a Rayleigh behavior (expected because more weight is given to small grains, $X_{mean} = 1.16$). With $n_s = 3.5$, curves have very similar behaviors between them but this time presenting a characteristic bump at 148° and slight enhancements at 180° for the two roughest grains. This bump comes from the Mie oscillations at different λ that were averaged with the size distribution effect. Finally, with $n_s = 2$, $\frac{<S_{44}>}{<S_{11}>}$ curves present the most important differences between grains, observed with the bump at 148° and backscattering enhancements, and yet there are not enough differences to identify between one grain to another. Therefore, this scattering parameter is not sensitive to the level of roughness that our grains have.

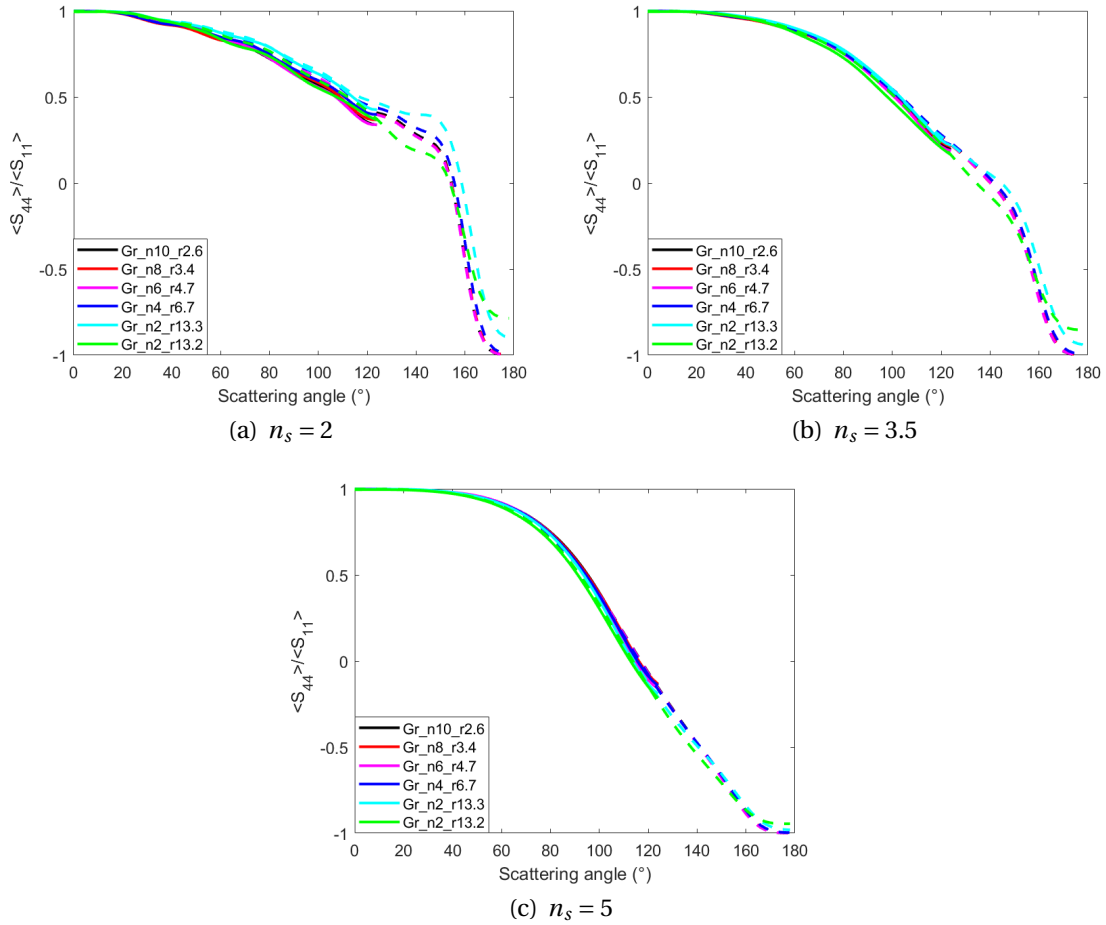

(a) $n_s = 2$ (b) $n_s = 3.5$

(c) $n_s = 5$

Figure 3.25: $< S_{44} > / < S_{11} >$ of grains with average orientation and with power law distributions of different n_s, measurements (solid lines) and numerical simulations (dashed lines).

$\frac{<S_{34}>}{<S_{11}>}$ shown in Figure 3.26, presents two behaviors for our grains at all three n_s: first, a positive large oscillation at forward scattering angles around $\frac{<S_{34}>}{<S_{11}>}$ values of 0.15, and second, a peak at 160° with different levels depending on n_s. The first behavior is the effect of averaging different oscillations and creating an envelope. The second behavior is caused by a characteristic peak that was presented at small wavelengths or large size parameters for all our grains (see Figure 3.14 at the three largest X) and when applying the size distribution effect, it is not eliminated. We suggest that this characteristic peak is a resonance for our grains with large size parameter, thus it is amplified mostly for $n_s = 2$. Apart from this resonance that can be a characteristic that differentiate grains, this scattering parameter does not add another significant scattering information compared to the phase function, DLP and $\frac{<S_{22}>}{<S_{11}>}$.

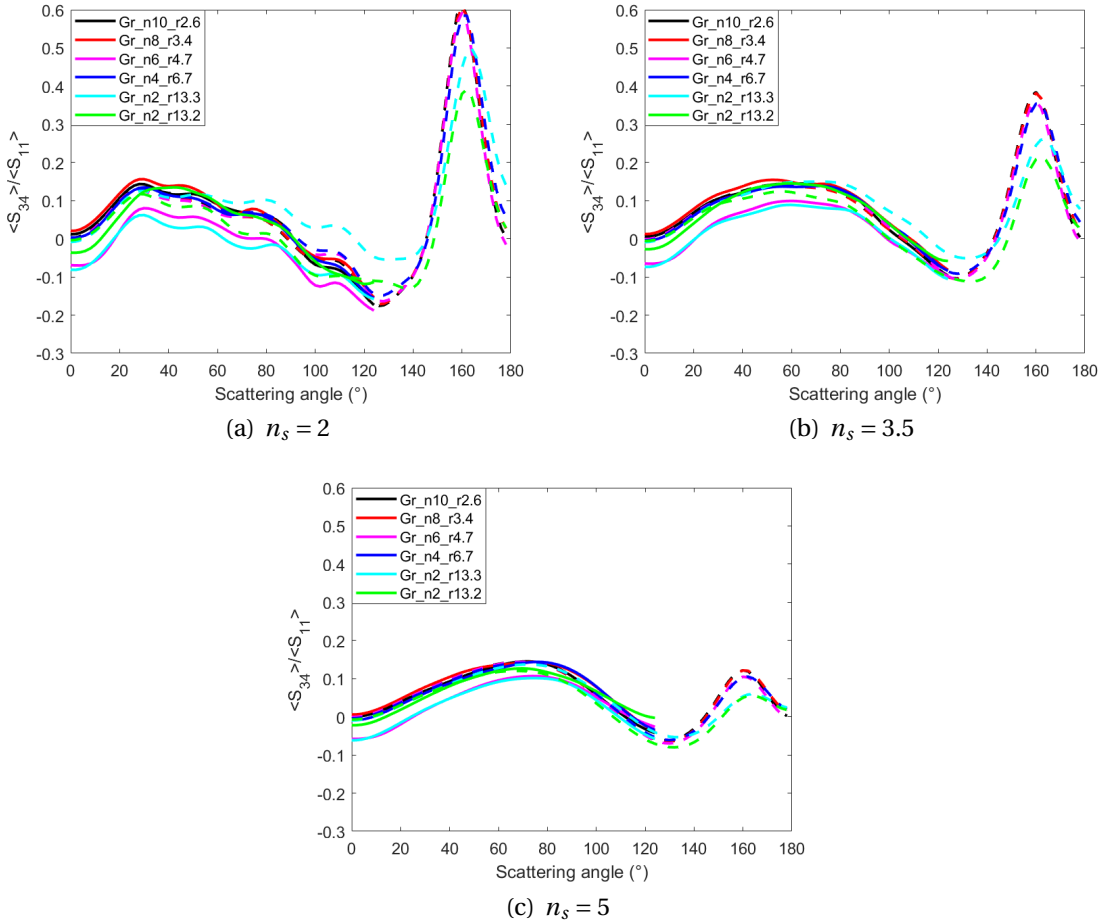

(a) $n_s = 2$ (b) $n_s = 3.5$

(c) $n_s = 5$

Figure 3.26: $< S_{34} > / < S_{11} >$ of grains with average orientation and with power law distributions of different n_s, measurements (solid lines) and numerical simulations (dashed lines).

3.3.3.5 Conclusions

In conclusion, from these three scattering parameters $\frac{<S_{22}>}{<S_{11}>}$, $\frac{<S_{44}>}{<S_{11}>}$ and $\frac{<S_{34}>}{<S_{11}>}$, levels of $\frac{<S_{22}>}{<S_{11}>}$ are related to the material packing density (that gives notions on how elongated are our grains) of all our grains and to our calculated sphericity for most of our grains. This is a specific information that cannot be obtained with other scattering parameters. $\frac{<S_{22}>}{<S_{11}>}$ together with the phase function (backscattering levels) and DLP (levels of maximum DLP and negative polarization branch) can give complementary scattering information and differentiate grains of different roughness at a same n_s. Finally, thanks to our multiple wavelength measurements and numerical simulations, we were able to compare between scattering parameters including or not a size distribution effect. This allowed us to identify when a characteristic of a scattering parameter was caused by the morphology or by the change of index in the size distribution, which is a particular advantage of our scattering experiment in CCRM.

3.3.3.6 Comparison of scattering parameters of grains and aggregates

The scattering parameters with size distribution effect of grains were compared with the ones of aggregates at $n_s = 3.5$ (power law index used for protoplanetary dust). Hence, the aim of this section is to see if these two morphologies present different scattering properties that can be identified with their scattering parameters. In this way, this analysis will help to give some clues to analyze the scattering observations of protoplanetary disks and thus have some ideas on which morphology could be present in those disks.

When comparing the phase function of our aggregates and our grains, in both cases phase functions are smooth curves. Furthermore, the HWHM values depend on the radius of their bounding sphere. Thus, if an aggregate and a grain have the same radius they present similar HWHM values (see for example HWHM values of Ag_Df_2.5_N74 and Gr_n4_r6.7 at each n_s). Hence this characteristic cannot be a parameter to differentiate these two morphologies. On the contrary, enhancements of the backscattering are more important for grains than aggregates, as shown in Figure 3.27 for numerical simulations. For $n_s = 3.5$, backscattering enhancements start at 160° for grains and at 120° for aggregates. Moreover, aggregates phase functions have larger variation of amplitudes (from 10^0 to $10^{-2.5}$) than grains phase functions (from 10^0 to $10^{-1.8}$), which can be seen with measurements and numerical simulations. Thus, the backscattering enhancements and the variation of amplitude of the phase function can be used as parameters to differentiate these two morphologies.

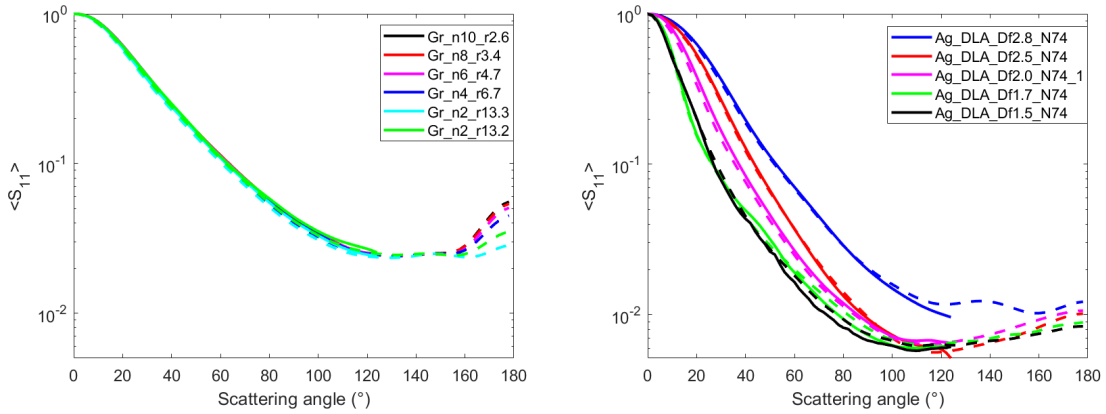

(a) Grains (b) Aggregates

Figure 3.27: Normalized phase function of grains and aggregates with average orientation and with power law distributions of $n_s = 3.5$, measurements (solid lines) and numerical simulations (dashed lines).

Comparisons between DLP of grains and aggregates are shown in Figure 3.28. Grains DLP curves have evidently smaller maximum levels (from 0 to 0.2) at smaller scattering angles (around 80° to 90°), while aggregates DLP curves present larger maximum levels (from 0.3 to 0.9) at larger scattering angles (around 90° to 100°). Indeed, as previously mentioned for aggregates, maximum levels of DLP and consequently depolarization, are affected by the morphology of the whole object and coupling between monomers. Therefore, in the case of grains, the depolarization is caused by their whole compact structure (roughness, sphericity and packing density) while for aggregates, as they are porous structures composed of multiple monomers, depolarization is affected by their porosity and coupling of monomers. These two characteristics affect less the depolarization than having completely compact structures. Thus, levels of maximum DLP and their corresponding scattering angles can be a way to differentiate these two morphologies. Furthermore, negative polarization branches of both morphologies are different. Grains DLP curves have a larger negative branch (with values of -0.3 at 150° for the four smoothest grains and -0.2 at 154° for the two roughest grains) than that of aggregates (with values of orders of -0.01 at 178° for all aggregates except for Ag_DLA_Df2.8_N74 of -0.2 at 154°). In sum, DLP curves show how morphology affects this scattering parameter demonstrated with levels of maximum DLP and negative backscattering branch. The differentiation between grains and aggregates was also possible with their phase functions. Thus, in the future either the phase function or the DLP can be helpful for this purpose.

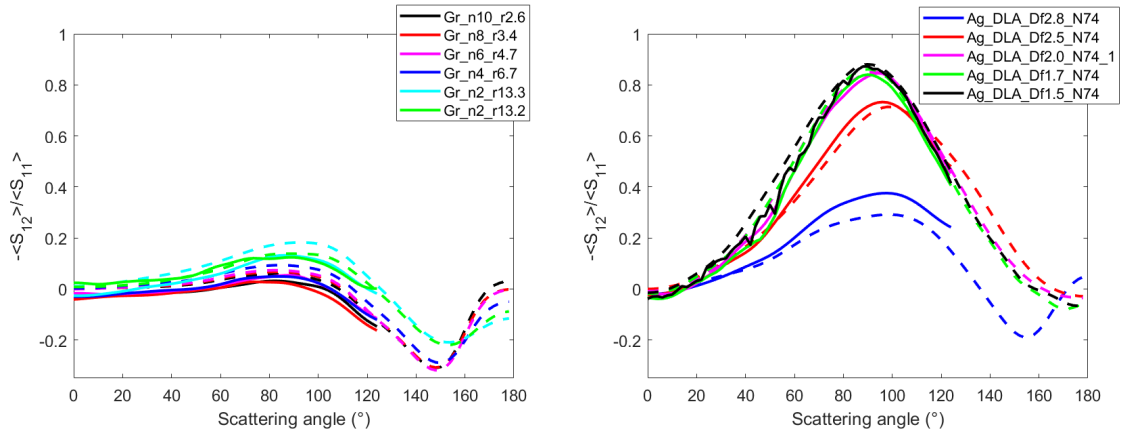

(a) Grains (b) Aggregates

Figure 3.28: DLP of grains and aggregates with average orientation and with power law distributions of $n_s = 3.5$, measurements (solid lines) and numerical simulations (dashed lines).

When comparing $\frac{<S_{22}>}{<S_{11}>}$ of grains with that of aggregates (see Figure 3.29), this scattering parameter is more sensitive to grains than aggregates. Indeed, grains present an organization level of $\frac{<S_{22}>}{<S_{11}>}$ from the two smoothest grains (or the most spherical with values around 1) to the two roughest grains (or the least spherical). This latter was not the case for aggregates where only two groups can be differentiated: the most compact aggregate and the rest of aggregates with $\frac{<S_{22}>}{<S_{11}>}$ superposed curves. Notice that the most compact aggregate (Ag_Df2.8_N74) has similar $\frac{<S_{22}>}{<S_{11}>}$ levels to that of grains, which means that for future observations differentiating grains from aggregates with $D_f > 2.5$ will be difficult because they both have the same behavior. In brief, this scattering parameter shows an organization of levels related to the sphericity of grains, which is a complementary information compared to previous scattering parameters. $\frac{<S_{22}>}{<S_{11}>}$ together with the backscattering enhancements of the phase function and levels of the maximum DLP and negative branch, will help to differentiate between grains and aggregates.

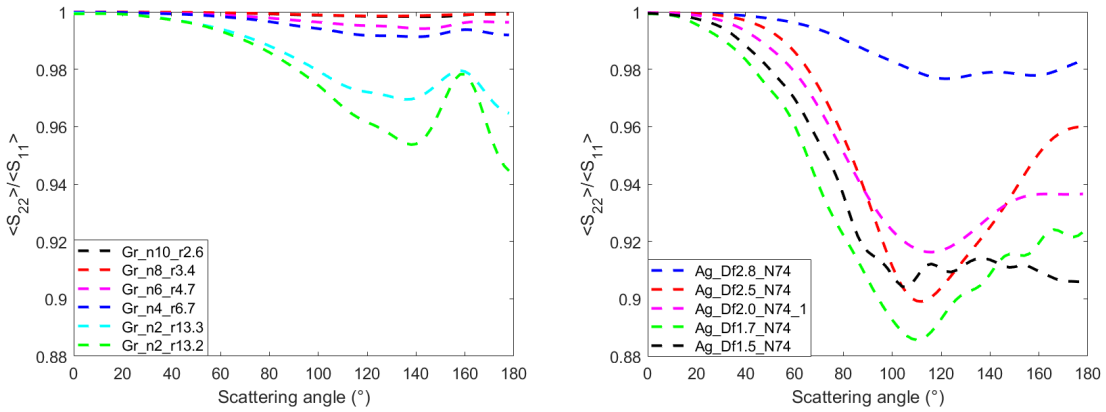

(a) Grains (b) Aggregates

Figure 3.29: $< S_{22} > / < S_{11} >$ of grains and aggregates with average orientation and with power law distributions of $n_s = 3.5$, measurements (solid lines) and numerical simulations (dashed lines).

$\frac{<S_{44}>}{<S_{11}>}$ of aggregates presents more differences between them than between that of grains (see Figure 3.30). This scattering parameter is more sensitive to the porosity of our aggregates, presenting different curves, than for our grains where all curves are superimposed. Notice that all grain curves resemble to the curve of the most compact aggregate, Ag_DLA_Df2.8_N74. Therefore, this parameter is not adapted to differentiate between grains and compact aggregates with $D_f > 2.5$, suggesting that future observations might not be able.

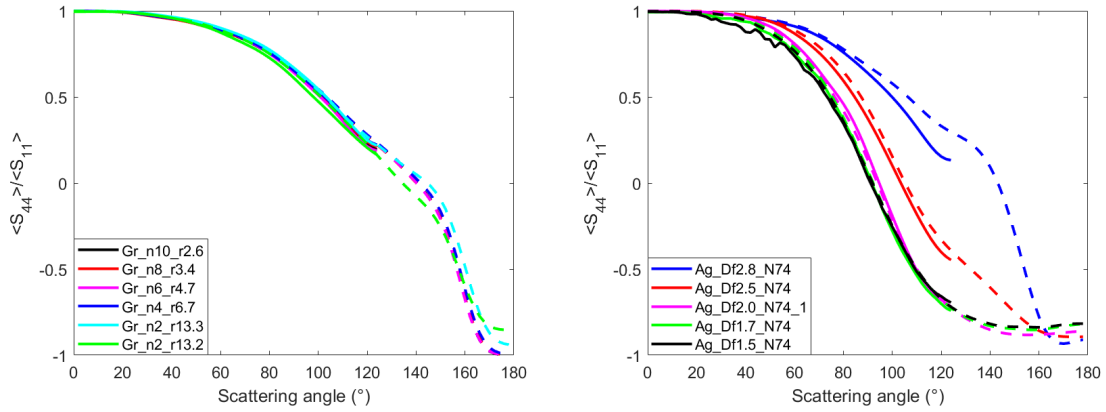

(a) Grains (b) Aggregates

Figure 3.30: $< S_{44} > / < S_{11} >$ of grains and aggregates with average orientation and with power law distributions of $n_s = 3.5$, measurements (solid lines) and numerical simulations (dashed lines).

Finally, $\frac{<S_{34}>}{<S_{11}>}$ of grains and aggregates is shown in Figure 3.31 and compared. Compact aggregates and all grains present a large oscillation at forward scattering angles around $\frac{<S_{34}>}{<S_{11}>}$ values of 0.15 to 0.20. Then, there is a clear difference between these two groups: all grains present a characteristic positive peak at 160°, named before as a resonance, while compact grains have negative oscillations. Moreover, when comparing $\frac{<S_{34}>}{<S_{11}>}$ of fluffy aggregates with grains, $\frac{<S_{34}>}{<S_{11}>}$ of aggregates have values around 0 all along the scattering angles. Therefore the main difference between $\frac{<S_{34}>}{<S_{11}>}$ of grains and aggregates is the resonance that is present for all grains in backward scattering angles and absent for all aggregates.

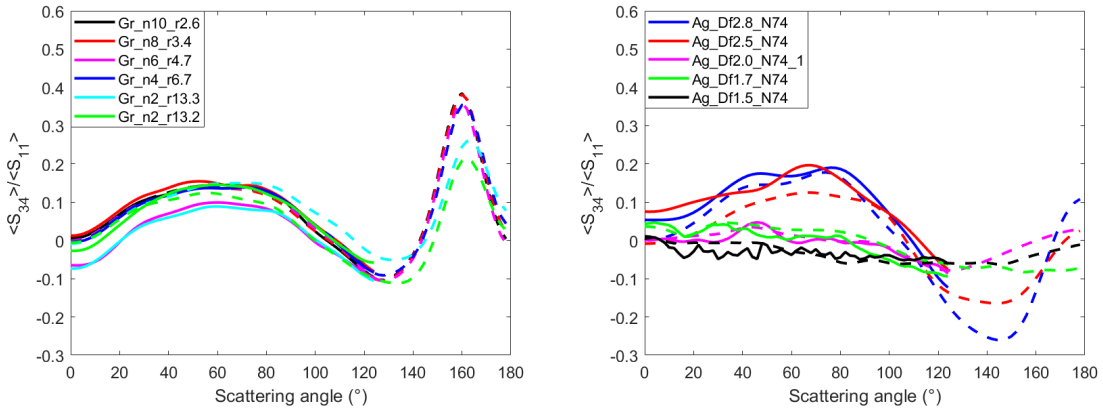

(a) Grains (b) Aggregates

Figure 3.31: $< S_{34} > / < S_{11} >$ of grains and aggregates with average orientation and with power law distributions of $n_s = 3.5$, measurements (solid lines) and numerical simulations (dashed lines).

In conclusion, $\frac{<S_{34}>}{<S_{11}>}$ presented a resonant peak at 160° for all grains which is a property that aggregates did not present. Therefore, this characteristic together with the variations of amplitude of the phase function, levels of backscattering enhancements of the phase function, levels of maximum DLP, levels of negative polarization branch and levels of depolarization of $\frac{<S_{22}>}{<S_{11}>}$ (related to the sphericity and packing density), are all together important characteristics that give information about the morphology, making possible the distinction between aggregates and grains.

3.3.4 Direct comparison of scattering parameters found in literature

After obtaining the scattering parameters of our grains and applying a size distribution effect at different indices, these parameters were compared with the same scattering parameters of other grains found in literature. These comparisons were made as a first step to validate our parameters with that of other laboratory measurements,

numerical simulations and optically thin circumstellar disks. Moreover, the idea of comparing is to see which scattering parameter and index have the closest behaviors to the ones presented in other works with similar morphologies. Note that a direct comparison with scattering parameters of protoplanetary disks (optically thick) is not possible because we need to produce the scattered image of the synthetic disk based on the Mueller matrix elements (using a radiative transfer code) and then compare this synthetic image with the observed scattered images of protoplanetary disks. This latter aspect is not within the objectives of this PhD study but for future works.

3.3.4.1 Laboratory measurements

In [107] phase functions of three dust grains made of enstatite ($m = 1.58 + 0.00002i$ and $X = 3.8 \times 10^4$), quartz ($m = 1.54 + 0i$ and $X = 4.6 \times 10^4$) and volcanic material from Mount Etna ($m = 1.59 + 0.01i$ and $X = 4.1 \times 10^4$) were measured with light scattering technique and compared to the observed phase function of the Fomalhaut disk from 30° to 170° (Debris disk with the same size distribution as protoplanetary disks, $n_s = 3.5$), presenting similar behaviors between each other. These phase functions are compared with the ones obtained for our grains (as shown in Figure 3.32, with $n_s = 3.5$) in order to see if our grain phase functions reproduce the same behaviors as the phase function of the disk Fomalhaut. As seen in this figure, the behavior of the phase functions of our grains is very different compared to the ones presented in [107]. Our phase functions decrease from 30° to 120°, then flat behaviors are present up to 160° and finally an enhancement in backscattering angles. On the contrary, the phase functions in [107] have a continuous increase from 30° to 170°. The main cause for this great difference is the size parameter that is 10^4 orders of difference being in the geometrical scattering range, while our grains are in the Mie scattering range. Note that the refractive indices of this paper [107] are similar to the astronomical silicate $1.67 + 0.03i$ at their used wavelength 527 nm, thus close to our grains that are analog of astronomical silicates. Therefore, the only difference is the range of the size parameter, producing different behaviors on the compared phase functions. The same comparison was made with the phase functions of our grains obtained at $n_s = 2$ and $n_s = 5$, but in neither case our phase functions were similar to the ones presented in [107] because of the great difference of the size parameter. Therefore, if the Fomalhaut disk phase function want to be reproduced in a future with our analogs, size parameters of our grains need to increase.

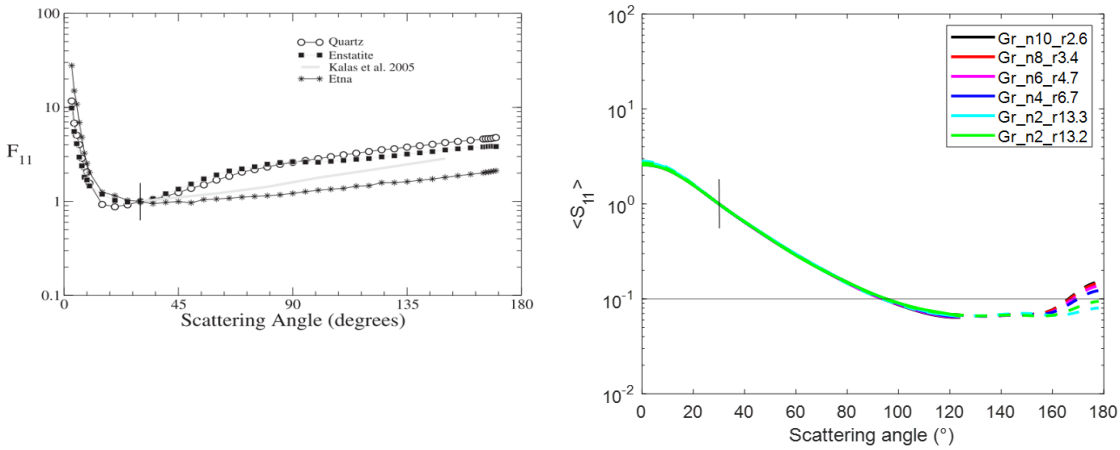

(a) Phase functions taken from [107]

(b) Our phase function

Figure 3.32: Laboratory scattering measurements comparison of the phase function normalized at 30° (vertical black line). (a) Phase function of three grains (Quartz, enstatite and Etna) and Fomalhaut disk (in legend as Kalas et al. 2005) [see Figure 7 in 107], (b) phase functions of our grains with power law distribution effect of $n_s = 3.5$ for measurements (solid lines) and numerical simulations (dashed lines).

3.3.4.2 Numerical simulations

In [156] DDA simulations were studied for irregularly shaped particles at different refractive indices, the one of our interest being $m = 1.6+0.0005i$ (close to astronomical silicate) with a size parameter of $X = 1-26$. In this study, particles have a power-law size distribution with indices of 1.5, 2.5 and 3.5. The phase function and DLP of these irregularly shaped particles are compared to the ones that we observed with our grains at the same power-law index of $n_s = 3.5$. The phase function comparison is presented in Figure 3.33, where the particle with the highest material packing density in [156] $\rho = 0.336$ is compared to our grain Gr_n2_r13.3, that has the closest packing density of all our grains, $\rho = 0.51$. Behaviors of these two phase functions are not identical because there are differences in ρ, which means a difference in their bounding spheres. This leads to differences in levels and widths of the phase functions at forward scattering angles. On the contrary, for side and backscattering angles, behaviors and levels are similar for these two phase functions.

DLP comparison is presented in Figure 3.34. DLP maximum levels are different: our grain presents levels around 20% while the one in [156] have a maximum of 30%. This difference is normal because global structures of both particles are different (not having the same roughness and sphericity), thus maximum levels are affected by this global structure. Furthermore, in [156] negative polarization branches are not smaller than −0.1, which is not the case for our grains. I think that our negative polarization branch values are due to the sphericity of our grains having Mie-like behaviors, which,

with the average of size distribution, produces this important negative branch. This is not the case in [156] where particles are much less spherical.

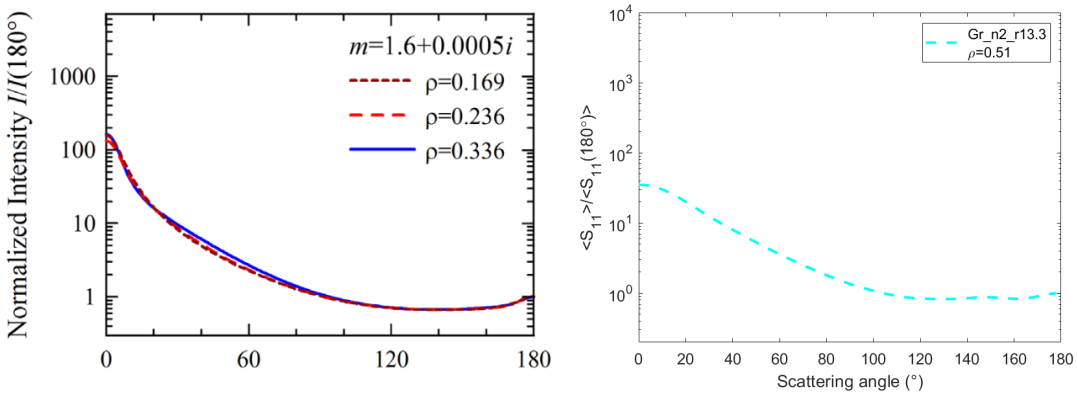

(a) Phase functions taken from [156] (b) Our phase function

Figure 3.33: Numerical scattering comparison of the phase function normalized at 180°. (a) Phase function of grain with $\rho = 0.336$ [see Figure 5 in 156], (b) phase functions of our grain with power law distribution effect of $n_s = 3.5$ for numerical simulations (dashed line).

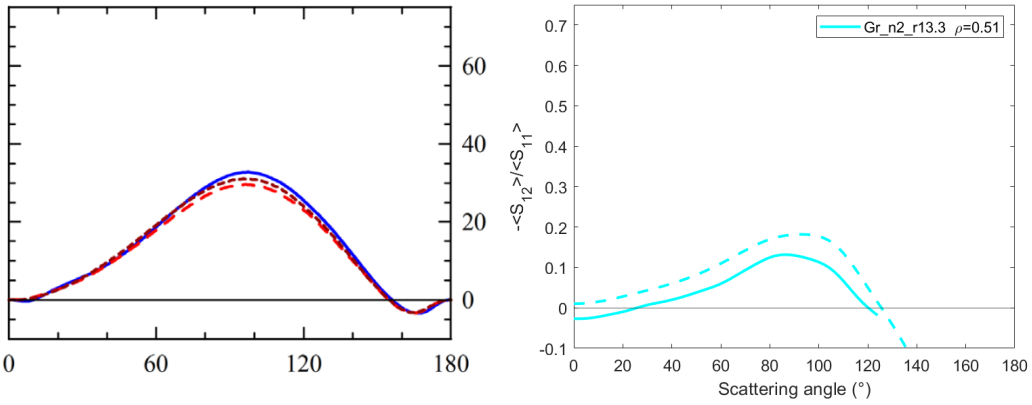

(a) DLP taken from [156] (b) Our DLP

Figure 3.34: Numerical scattering comparison of DLP. (a) DLP of grain with $\rho = 0.336$ [see Figure 5 in 156], (b) DLP of our grain with power law distribution effect of $n_s = 3.5$ for measurements (solid line) and numerical simulations (dashed line).

Furthermore, in [156], two smaller n_s were used, 2.5 and 1.5. Even if they are not exactly the same indices as I used in the study of our grains, it can be seen in [156] that the maximum DLP levels decrease as n_s decreases, while the negative polarization

branches increase. Additionally, visual changes in the width of the forward scattering peak of the phase function decrease as n_s decreases. I also observed these same behaviors with our grains DLP and phase functions. Thus, there is an important influence when changing the index of the size distribution on these two scattering parameters as shown with our grains and as can be seen in figures presented in [156]. In brief, morphologies of our grains and the ones presented in [156] are not identical but similar scattering behaviors were observed and when they were not similar, the reasons behind it were discussed. Hence, this comparison helps as a validation of our grain scattering parameters with scattering parameters of other rough structures studied in literature.

3.3.4.3 Observations

Observations of disk HR4796A in [78] present the phase function of the scattered light from dust. This phase function has a very prominent forward scattering peak and an increase of the phase function from 40° up to backscattering angles. Compared to the phase functions of our grains, none of them present the behavior of this disk as was also seen for our aggregates phase functions in Section 2.4.4.3. Figure 3.35 presents a comparison between the phase function observed for the disk and the phase function of our grains at $n_s = 2$ because this corresponds to the case where the phase functions of our grains have the narrowest forward scattering peaks and the most important backscattering enhancements. Even when comparing with the narrowest phase functions, the behaviors between phase functions of our grains do not approach the one of the disk. As previously mentioned for aggregates and also with the comparison of the Fomalhaut disk in Section 3.3.4.1, size parameters of our future analogs must be in the geometrical scattering range and the refractive index should increase, in order to have these phase function behaviors of these debris disks.

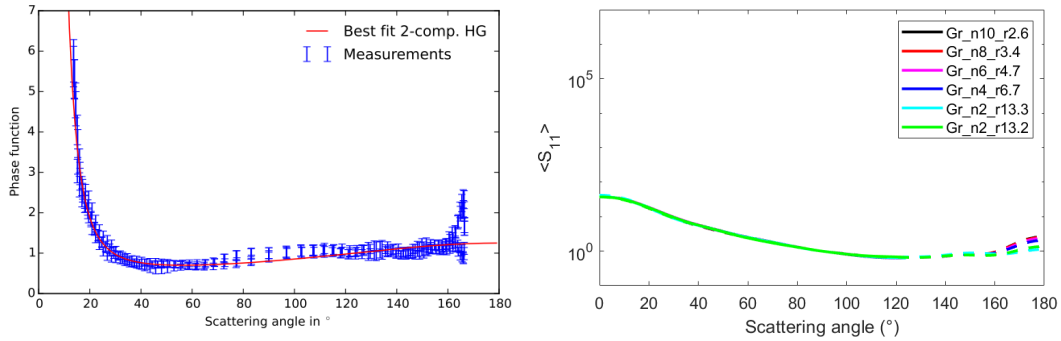

(a) Phase function taken from [78]

(b) Our phase function

Figure 3.35: Observational scattering comparison of phase function normalized at 90°. (a) Phase function of disk HR4796A [see Figure 17 in 78], (b) phase function of our grains with power law distribution effect of $n_s = 2$ for measurements (solid lines) and numerical simulations (dashed lines).

3.3.4.4 Conclusions

In conclusion, based on previous comparisons, the behaviors of phase functions and DLP obtained for our grains are consistent with the size parameter and refractive index that were used to fabricate them. The behaviors observed when changing n_s of the phase function and DLP were also consistent as was shown in [156]. Therefore, we validate these two scattering parameters with literature. However, one concern is how to obtain the phase function of observed circumstellar disks (in this case we compare with debris disk). Based on this concern, I suggest to increment the size parameter of future analogs and explore other refractive indices like for example inclusions of amorphous carbon, which is an abundant species that can be found in these disks (see its refractive index in the bibliographical study in Section 1.7.2).

3.4 Analogs of chondrules and CAI

All previous sections presented in this Chapter 3 were focused on the study of scattering parameters of grains with synthetic roughness (first family of grains). Now let us study the second family of grains which consists of grains with natural roughness, scanned from a meteorite.

Chondrites are rocky meteorites that were formed during the formation of the Solar System and that could possibly contain pristine information on its origin. They are composed of: chondrules (igneous rocks that were formed at high temperatures, mostly made of olivine and pyroxene), refractory inclusions (Calcium-Aluminium rich Inclusions-CAI or Amoeboid Olivine Aggregates-AOA), Metallic Fe-Ni grains and a matrix (mixture of silicates, oxides, metallic Fe-Ni, sulfides and organic material). The study of chondrites and its elements can provide information on the grain growth in circumstellar disks, accretion process and planetary material [181]. Therefore, understanding its scattering properties can give us access to this information. In this way, the objective of this section is to take these pristine elements, specifically, chondrules and CAI, that participated in the Solar System formation and study their scattering properties based on their scattering parameters. The morphology of the chondrules and CAI, were obtained with a X-ray computed tomography of a meteorite, then scaled and finally 3D printed. This second family of grains is the closest approach to a real natural morphology ever studied during this PhD. To our knowledge, this is the first time that 3D printed analogs of chondrules and CAI are studied using the microwave scattering technique.

3.4.1 Virtual generation

The morphology of chondrules and CAI were obtained using a X-ray computed tomography (XCT) on one chondrite with the collaboration of Yves Marrocchi from Le Centre de Recherches Pétrographiques et Géochimiques. XCT is a noninvasive and nondestructive technique that provides information about the internal structure of

a chondrite in a full 3D data set. Each image, taken with the XCT and reconstructed with the radon transform, is named slice. Each slice contains pixels with different gray levels related to the density of the material. Thus, the darkest pixels are the materials with the lowest densities and the brightest ones are the materials with the highest densities. Based on these levels, the different components of a chondrite are identified, in our case of interest chondrules and CAI. After obtaining different slices, the voxels are built (pixels in 3D) and painted with this gray level information. Then, by interpolation, the chondrules and CAI are modeled in a 3D volume. Finally, to separate the elements of interest, e.g. chondrules and CAI, from its environment, a Blob3D software is used [182] (see Figure 3.36 where the chondrite is in gray levels and the elements of interest in color). This way, 3D files of the three chondrules and CAI were obtained.

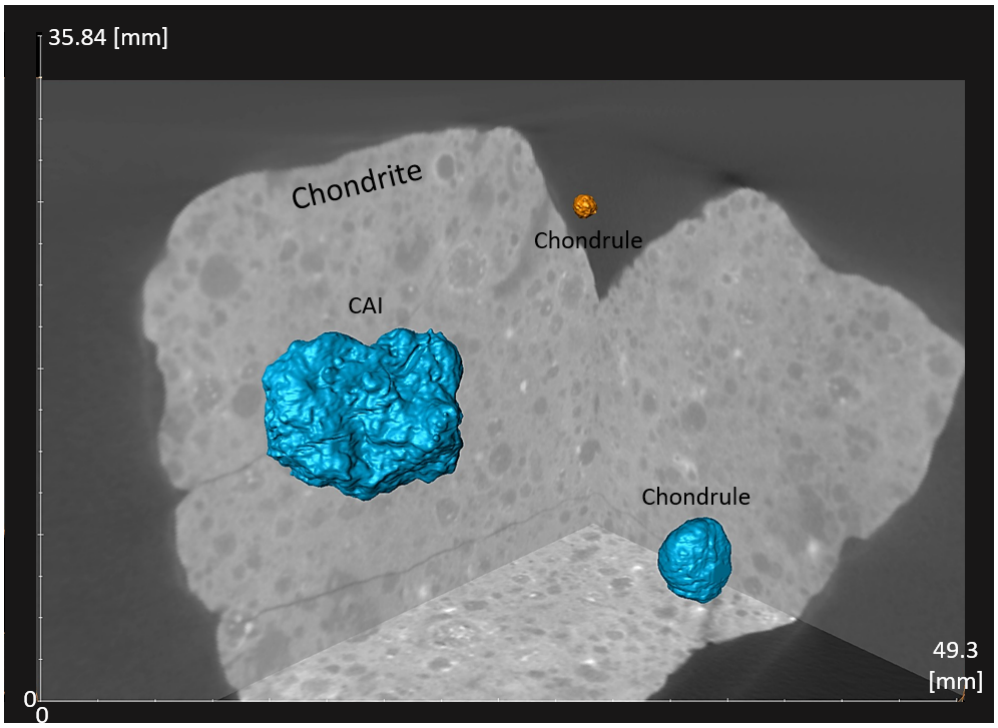

Figure 3.36: X-ray computed tomography of chondrules and CAI inside its chondrite.

3.4.2 3D printing by fused filament fabrication

To print chondrules and CAI, another additive manufacturing technique compared to aggregates and grains (SLA) was used, the Fused Filament Fabrication (FFF). The fabrication of this objects was made with the collaboration of the Lab-STICC laboratory (Azar Maalouf) and Laboratoire IUSTI (Jean-Marie Felio). The FFF printer of Lab-STICC has a resolution of 0.8mm by layer and maximum dimensions that can be printed are 600 mm x 325 mm x 500 mm. The FFF printer of Laboratoire IUSTI has

a better resolution, ranging from 0.006mm to 0.275mm, and maximum printable dimensions are smaller 260 mm x 200 mm x 300 mm. In both cases, compared with SLA (used for aggregates and grain), larger objects can be printed but with lower resolution. The main advantage of this technique is the variety of thermoplastics that can be printed, therefore a larger range of refractive indices (permittivities).

The principle of FFF is to heat a thermoplastic wire inside an extrusion nozzle, then deposit layer by layer (with movements in 2D that are controlled by the computer) the molten material onto a substrate being solidified just after the extrusion and welded to the previous layer. Thus, each layer is filled with a continuous molten filament and then the nozzle is moved vertically to deposit another layer. At the end, the deposition of several layers produces a 3D object [183].

Our chondrules and CAI were printed using the 3D files from XCT. Note that the real sizes of the chondrules and CAI are of the orders of millimeters but in order to do the analogy and have coherent size parameters with our wavelengths, these objects were scaled up. Three types of materials were used to print them: acrylonitrile butadiene styrene (ABS), orange polylactide (PLA), gray polylactide (PLA) and preperm acrylonitrile butadiene styrene (ABS450), having refractive indices of $m = 1.58 + 0.01i$, $m = 1.66 + 0.01i$, $m = 1.55 + 0.01i$ and $m = 2.11 + 0.004i$, respectively. PLA and ABS have very close refractive indices to that of Draine and Lee astronomical silicate from $\lambda = 0.2$ to 3 μm [14], representing silica-rich chondrules (Type I). In the case of ABS450, its refractive index is higher than that of the astronomical silicate, thus it can be considered as a FeO-rich silicate chondrule (Type 2) [184]. It is important to note that all the particles were 3D printed with plain material, except for the CAI analog where the shell was printed and then the interior was filled with sand (refractive index around $m = 1.7$ with a negligible imaginary part). This type of fabrication is another technique that we wanted to explore to produce analogs with more filling material possibilities than just the materials that can be 3D printed. Notice that in this study, our CAI has the refractive index of silica, however this is a first approach to understand its morphology. Actually, CAIs have smaller/larger refractive indices. In fact, they are composed of calcium aluminum oxide minerals as grossite (with a real refractive index of $n = 1.63$), hibonite ($n = 1.8$) and corundum ($n = 1.76$) [185, 186]. Therefore, it is suggested to use closer refractive indices for future CAI analogs.

Table 3.8 presents the properties of each analog starting with their technical name that is a string composed of the type of chondrite constituent: C (Chondrule) or CAI (Calcium-Aluminum Inclusion), then if the analog is a chondrule they are enumerated from 0 to 2 (representing three different morphologies of chondrules), followed by the print material, the color of the printed material and the letter r (for roughness) followed by its percentage. Other columns contain: the maximal radius of the sphere in which the analog can be contained known as the radius of the bounding sphere, the roughness (see Equation 3.2), the sphericity (see Equation 3.3), the size parameter at the smallest and the largest wavelengths and finally, the material packing density. Figure 3.37 shows the pictures of the printed particles with their corresponding technical name. Note that C0_ABS450_white_r5.04 and C0_PLA_orange_r5.04 are the same

chondrule but with different sizes and materials.

Chondrules and CAI technical name	Radius of the bounding sphere (mm)-R_{max}	Roughness %	Sphericity %
C0_ABS450_white_r5.04	16.39	5.04	88.83
C0_PLA_orange_r5.04	18.42	5.04	88.83
C1_PLA_gray_r12.34	24.36	12.34	83.20
C2_PLA_gray_r13.26	22.00	13.26	82.25
CAI_ABS_blue_r24.05	57.09	24.05	66.11

Chondrules and CAI technical name	Size parameter λ = 16.7 mm to λ = 100 mm			Material packing density-ρ
C0_ABS450_white_r5.04	6.18	to	1.03	0.99
C0_PLA_orange_r5.04	6.95	to	1.16	0.99
C1_PLA_gray_r12.34	9.19	to	1.53	0.34
C2_PLA_gray_r13.26	8.30	to	1.38	0.37
CAI_ABS_blue_r24.05	21.53	to	3.59	0.19

Table 3.8: Analog chondrule and CAI properties.

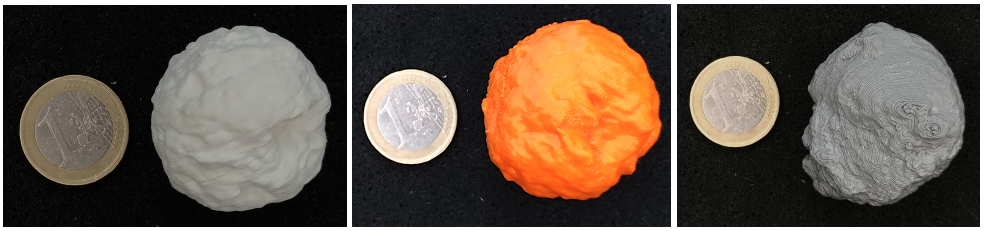

(a) C0_ABS450_white_r5.04 (b) C0_PLA_orange_r5.04 (c) C1_PLA_gray_r12.34

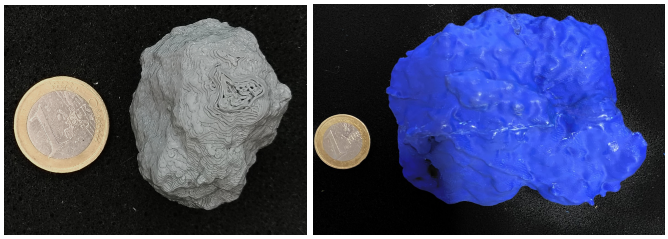

(d) C2_PLA_gray_r13.26 (e) CAI_ABS_blue_r24.05

Figure 3.37: 3D printed chondrules and CAI with their corresponding technical name.

3.4.3 Chondrules and CAI size analogy

The mean radius of the bounding sphere of all four chondrules is 20.29mm with mean size parameter ranging from X_{mean} = 1.28 to X_{mean} = 7.65 (calculated based on Table 3.8). Additionally, for the CAI, the radius of the bounding sphere is 57.09mm leading to X = 3.59 to X = 21.53. Thus, supposing these same size parameters, the

corresponding radius of protoplanetary dust would have different values depending on the wavelength range, as shown in Table 3.9.

Range name	Wavelength	Radius of chondrules	Radius of CAI
Optical (nm)	400 to 700	81 to 850	228 to 2393
NIR (µm)	1.00 to 2.50	0.20 to 3.04	0.57 to 8.55
Millimeter(mm)	0.30 to 2.60	0.06 to 3.16	0.17 to 8.89

Table 3.9: Chondrule and CAI radius corresponding to different wavelength ranges (units are noted in the first column).

3.5 Scattering properties of chondrules and CAI

Scattering properties of our four chondrules and one CAI were studied based on scattering measurements performed at the anechoic chamber at the same 16 wavelengths as those of aggregates and grains, from 100 mm to 16.7mm. This time, FEM numerical simulations were not made because these analogs present a natural roughness for which a suitable meshing would lead to an enormous number of cells that we can not smooth without any impact on their scattering parameters. Thus, open questions are raised, as for example, how small the size of the FEM mesh need to be without having any impact on their scattering parameters? Hence, this meshing limitation in the numerical simulations shows the importance of using our measurements on these natural rough particles. Notice that our measurements were already cross-validated with FEM simulations for aggregates and grains. In this way, this section only presents the scattering measurements of chondrules and CAI, showing a first step for future experimental works to overcome the limits of numerical simulations due to roughness (fine mesh problems) or very large objects (computational memory limits).

Remember that measurements, during my PhD, were made with two states of polarization for the antennas, both vertically polarized and both horizontally polarized. Thus, four Mueller matrix elements were retrieved, S_{11}, S_{12}, S_{34} and S_{44} (see Equation 2.3). Based on these Mueller matrix elements four scattering parameters of chondrules and CAI were studied: the phase function ($< S_{11} >$), the DLP ($-\frac{<S_{12}>}{<S_{11}>}$) and the normalized elements $\frac{<S_{34}>}{<S_{11}>}$ and $\frac{<S_{44}>}{<S_{11}>}$.

3.5.1 Setup parameters

In this section I verify and decide i) the number of necessary measurements and ii) the zone where measurements could be performed.

3.5.1.1 Number of necessary measurements

The number of necessary measurements and orientations to retrieve mean scattering parameters, phase functions and DLP of our chondrules and CAI, was based on [126]. To have a phase function accuracy of 1%, 35 ± 10 measurements were needed for C0_ABS450_white_r5.04 and C0_PLA_orange_r5.04, 70 ± 10 measurements for C1_PLA_gray_r12.34 and 100 ± 10 measurements for C2_PLA_gray_r13.26 and CAI_ABS_blue_r24.05. To have a DLP accuracy of 1%, 32 ± 10 measurements were needed for C0_ABS450_white_r5.04 and C0_PLA_orange_r5.04, 50 ± 10 measurements for C1_PLA_gray_r12.34 and C2_PLA_gray_r13.26, and 60 ± 10 measurements for CAI_ABS_blue_r24.05. Knowing that the support where the analog is placed was rotated to give 36 orientations (see Section 2.4.1.1 for more details), and that we chose the highest number of necessary measurements between these two scattering parameters (phase function and DLP), thus we performed 36 orientations for C0_ABS450_white_r5.04 and C0_PLA_orange_r5.04, 72 orientations for C1_PLA_gray_r12.34 and 108 orientations for C2_PLA_gray_r13.26 and CAI_ABS_blue_r24.05. The same number of measurements was used to calculate the other scattering parameters, $\frac{<S_{34}>}{<S_{11}>}$ and $\frac{<S_{44}>}{<S_{11}>}$.

3.5.1.2 Forward and backward measurements

Measurements can be performed in the forward and backward zones. Yet, as for aggregates and grains, we decided to only measure in the forward zone (from 0° to 130°). Actually, in the backward zone, the experiments are not as precise as in the forward zone and it would have largely increased the time of measurements per analog.

After verification and definition of the setup parameters, the scattering parameters of chondrules and CAI were analyzed in two different ways: first, the scattering parameters with average orientation (Section 3.5.2) and second, the scattering parameters with average orientation including a size distribution effect (Section 3.5.3).

3.5.2 Chondrules and CAI with average orientation

3.5.2.1 Phase function

The average phase functions of our chondrules and CAI are presented in Figure 3.38, at the same six wavelengths that we chose to represent the scattering parameters of our aggregates and grains in previous sections (100 mm, 50 mm, 33 mm, 25 mm, 20 mm and 16.7mm corresponding to different size parameters). Levels of these phase functions are different because size parameters between these chondrules and CAI are not the same, as well as their refractive indices. Indeed, these two elements affect the scattering cross sections and therefore the levels of the intensity of the scattered light. For example, if we compare C1_PLA_gray_r12.34 and C2_PLA_gray_r13.26, that have the same refractive index but not the same size parameter, the levels of the phase

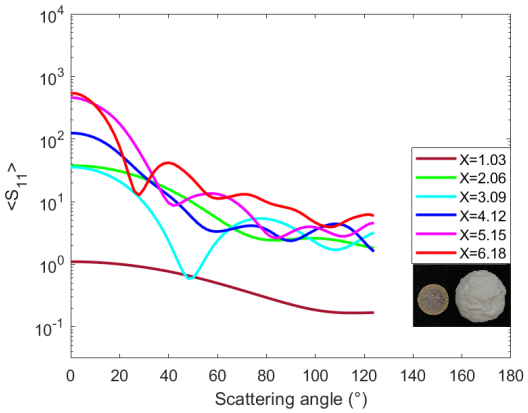

(a) C0_ABS450_white_r5.04

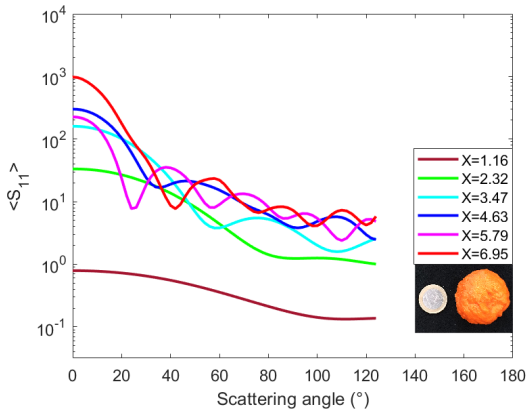

(b) C0_PLA_orange_r5.04

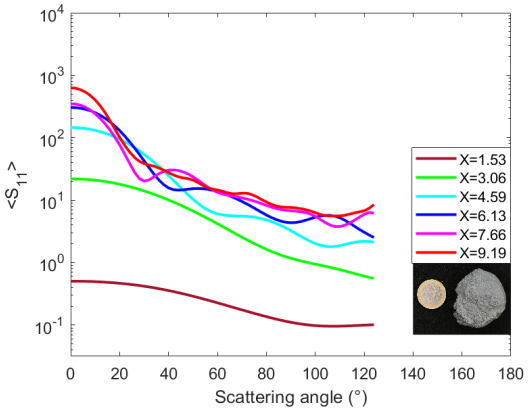

(c) C1_PLA_gray_r12.34

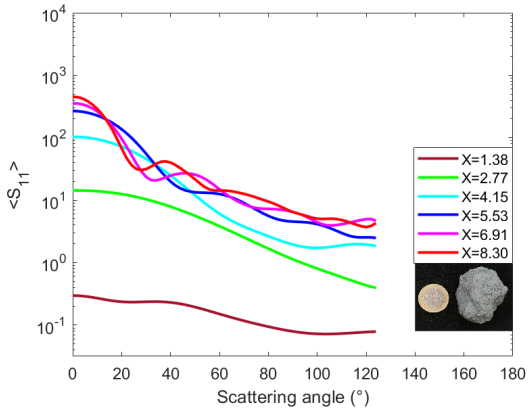

(d) C2_PLA_gray_r13.26

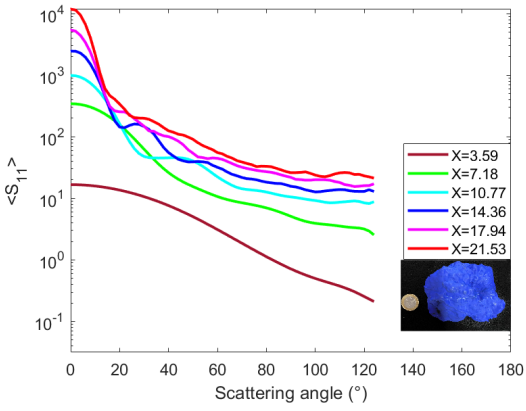

(e) CAI_ABS_blue_r24.05

Figure 3.38: Phase function of chondrules and CAI, measurements (solid lines) with their corresponding size parameter.

function are higher for C1_PLA_gray_r12.34 because it has larger X. If the comparison is made between C1_PLA_gray_r12.34 and C0_PLA_orange_r5.04, the real part of the refractive index is higher for C0_PLA_orange_r5.04 and thus its phase function levels increase. The particle with the highest phase function levels and the narrowest forward scattering peak is CAI_ABS_blue_r24.05. These two characteristics of the CAI are caused by its large size parameters, compared to chondrules. The width of these forward scattering peaks can be seen in Table 3.10 with values of HWHM for all particles. In this table, HWHM values are similar for chondrules compared to HWHM values of CAI, which was expected due to the large difference of the bounding spheres between chondrules and CAI.

Chondrules X_{mean}	CAI X	C0_ABS450_ white_r5.04	C0_PLA_ orange_r5.04	C1_PLA_ gray_r12.34	C2_PLA_ gray_r13.26	CAI_ABS_ blue_r24.05
1.28	3.59	60	64	62	62	72
2.55	7.18	50	54	64	72	44
3.83	10.77	32	44	44	48	24
5.10	14.36	36	30	32	38	18
6.38	17.94	32	20	24	26	16
7.65	21.53	22	28	24	20	16

Table 3.10: HWHM of phase function in degrees at different X_{mean} of chondrules and X of CAI.

Another characteristic that can be observed is the presence of secondary lobes at small wavelengths, called bumps, for the two most spherical chondrules, C0_-ABS450_white_r5.04 and C0_PLA_orange_r5.04. As already explained and shown, for the phase functions of grains and compact aggregates, these bumps are characteristic of spherical particles and they decrease when sphericity decreases and roughness increases, as can be seen for example for C0_PLA_orange_r5.04, C2_PLA_gray_r13.26 and CAI_ABS_blue_r24.05. Figure 3.39 presents a comparison of the normalized phase functions between all chondrules and CAI at the smallest wavelength (16.7mm), thus the highest size parameter, where this behavior of bumps is showed.

In summary, levels of phase function and HWHM are related to size parameters and refractive indices of chondrules and CAI. In terms of their morphology, the difference can be observed with their bumps. Indeed, chondrules tends to be more spherical (see sphericity in Table 3.8 around orders of 85%) thus more bumps, while CAI is less spherical (around 66%) which means less bumps. Therefore, based on the phase function bumps, we can obtain some insights about their sphericity.

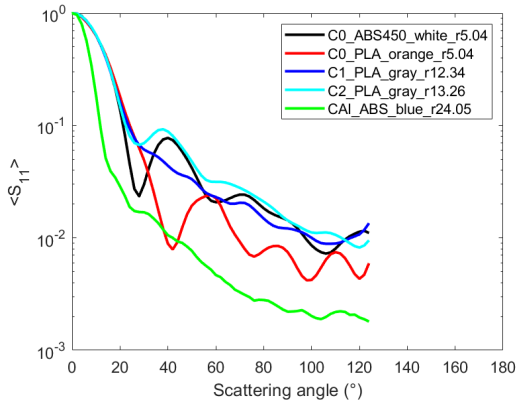

Figure 3.39: Normalized phase functions of chondrules and CAI at $\lambda = 16.7$mm, corresponding to $X_{mean} = 7.65$ for chondrules and $X = 21.54$ for CAI.

3.5.2.2 Degree of linear polarization

The degree of linear polarization of all four chondrules and CAI were calculated and shown in Figure 3.40 at the same six chosen wavelengths. At the smallest size parameter of all chondrules ($X_{mean} = 1.28$), DLP presents Rayleigh behaviors with maximum values around 1. For the CAI, the DLP curve is also a bell but with a smaller maximum value of 0.29. This is because of its large size parameters and its particular structure, depolarizing more than chondrules. The maximum levels of DLP at larger X were not analyzed because DLP for all particles have very oscillating behaviors, all along the scattering angles (Mie-like behaviors) similar to DLP of grains, so there is no sense in analyzing the maximum DLP and relate it with their roughness.

Notice that the amplitude of DLP curves decreases as the size parameter and roughness of chondrules and CAI increase, thus levels of local maximum DLP of CAI are the smallest, having values around 0. Note that this DLP behavior of the CAI has never been seen for the different morphologies that have been studied herein (aggregates and the first family of grains). Figure 3.41 presents DLP of chondrules and CAI at the largest X. As already seen for DLP of grains, amplitudes of DLP oscillations are more important for the smoothest particles (C0_ABS450_white_r5.04 and C0_PLA_-orange_r5.04) than DLP amplitudes for the roughest particle (CAI_ABS_blue_r24.05). Indeed, rougher particles are less spherical, depolarizing more. In summary, DLP amplitudes can gives us some signs of chondrules and CAI roughness, differentiating them. Note that as for the first family of grains, as roughness increases, sphericity decreases. Indeed, these two characteristics are related as shown in Table 3.8. Thus, these DLP amplitudes can be analyzed either by the particles roughness or sphericity.

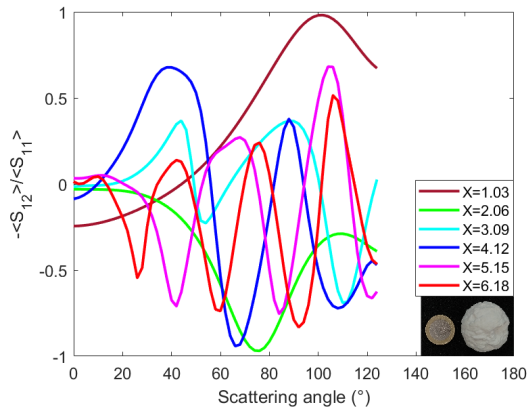

(a) C0_ABS450_white_r5.04

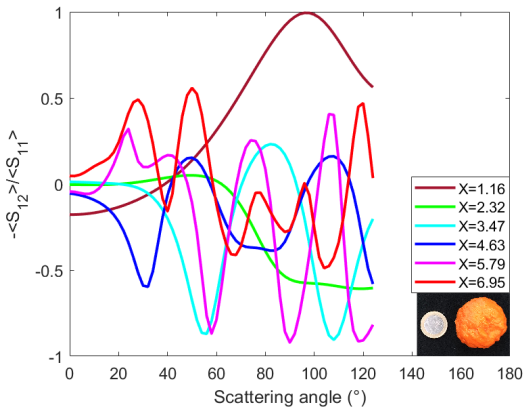

(b) C0_PLA_orange_r5.04

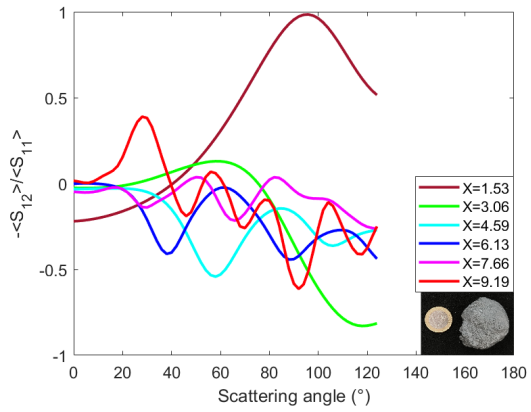

(c) C1_PLA_gray_r12.34

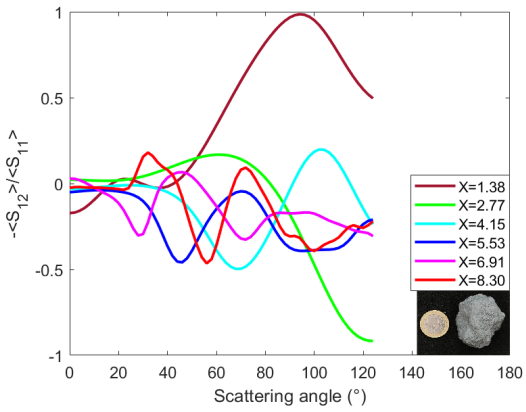

(d) C2_PLA_gray_r13.26

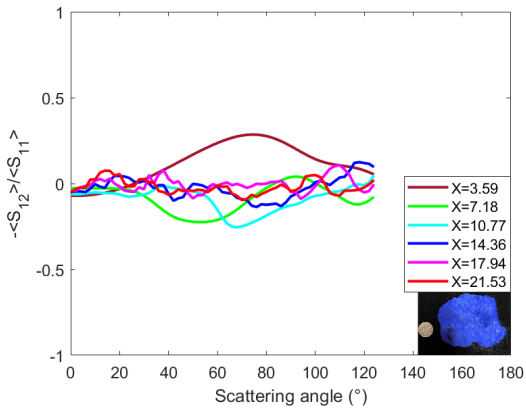

(e) CAI_ABS_blue_r24.05

Figure 3.40: DLP of chondrules and CAI, measurements (solid lines) with their corresponding size parameter.

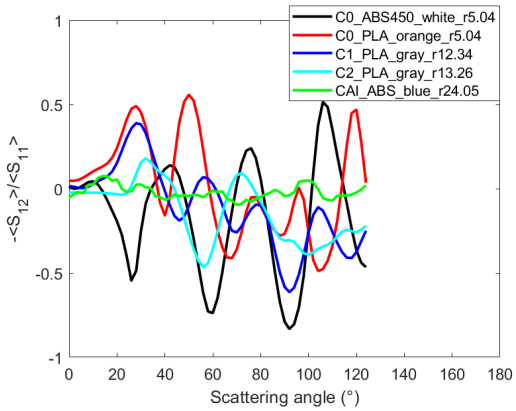

Figure 3.41: DLP of chondrules and CAI at $\lambda = 16.7$mm, corresponding to $X_{mean} = 7.65$ for chondrules and $X = 21.53$ for CAI.

3.5.2.3 Other scattering parameters

This section presents the analysis of two other scattering parameters, $\frac{<S_{44}>}{<S_{11}>}$ and $\frac{<S_{34}>}{<S_{11}>}$, in order to see if complementary information, compared to the phase function and the DLP, can be obtained. Remember that these two scattering parameters cannot yet be retrieved with nowadays telescopes but there is an interest in understanding them for future applications.

Parameter $\frac{<S_{44}>}{<S_{11}>}$ is shown in Figure 3.42, for chondrules and CAI. At the smallest X (brown lines), chondrules present smooth $\frac{<S_{44}>}{<S_{11}>}$ curves, typical of Rayleigh behaviors. Furthermore, when X increases, $\frac{<S_{44}>}{<S_{11}>}$ of chondrules oscillates from 20° to 130°. For CAI, $\frac{<S_{44}>}{<S_{11}>}$ curves do not act as Rayleigh curves neither as Mie ones. In fact CAI curves act very similar at the different wavelengths, decreasing slowly from 1 at 0° to 0.5 at 130°.

Note that as roughness increases from 5.04% to 24.05% (or sphericity decreases), amplitudes of $\frac{<S_{44}>}{<S_{11}>}$ oscillations increasingly damp. This can be seen in Figure 3.42, where $\frac{<S_{44}>}{<S_{11}>}$ of all particles are represented at their highest X ($\lambda = 16.7$mm). It is important to highlight that C0_ABS450_white_r5.04 has the same roughness as C0_PLA_orange_-r5.04 but with a higher refractive index that may produce larger amplitudes of $\frac{<S_{44}>}{<S_{11}>}$ (see differences with Figure 3.42.a and 3.42.b). In brief, the amplitude of oscillations presented from 20° to 130° is a characteristic of $\frac{<S_{44}>}{<S_{11}>}$ to differentiate between chondrules and CAI of different roughness.

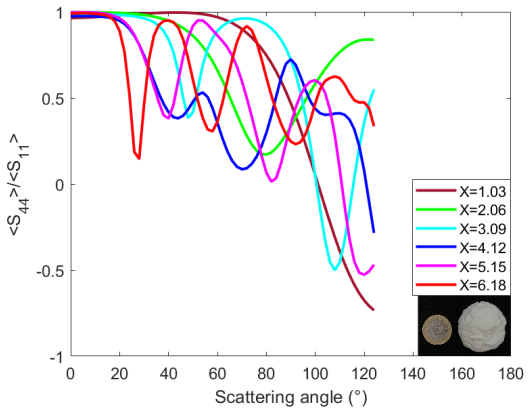

(a) C0_ABS450_white_r5.04

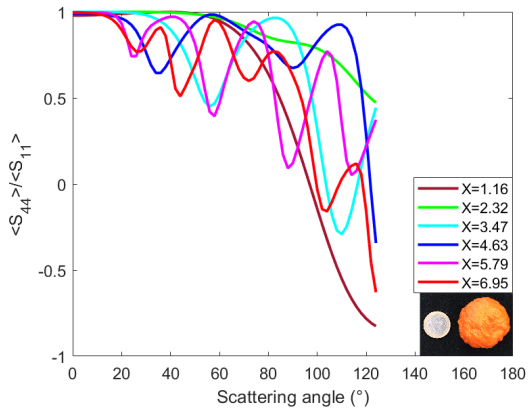

(b) C0_PLA_orange_r5.04

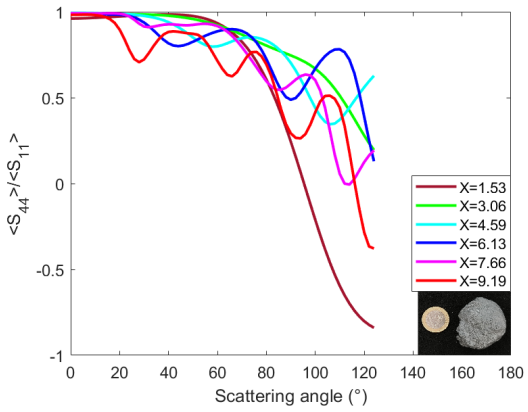

(c) C1_PLA_gray_r12.34

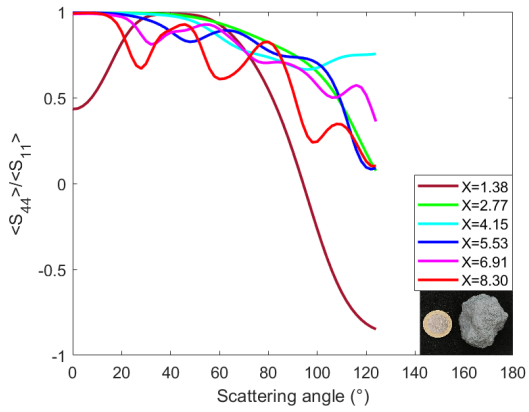

(d) C2_PLA_gray_r13.26

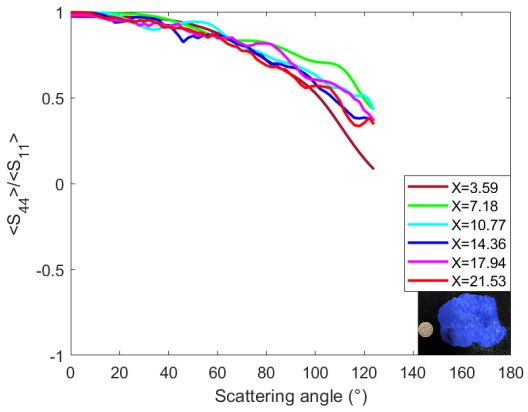

(e) CAI_ABS_blue_r24.05

Figure 3.42: $< S_{44} > / < S_{11} >$ of chondrules and CAI, measurements (solid lines) with their corresponding size parameter.

Finally, notice that for C2_PLA_gray_r13.26, $\frac{<S_{44}>}{<S_{11}>}$ curve at $X = 1.38$ presents anomalies from 0° to 30°. Normally values should be 1 as for others X and chondrules. This was a problem of calibration caused at large wavelengths that is more visible for this scattering parameter, than for the phase function and DLP. Future works need to find a better calibration for this chondrule at large wavelengths.

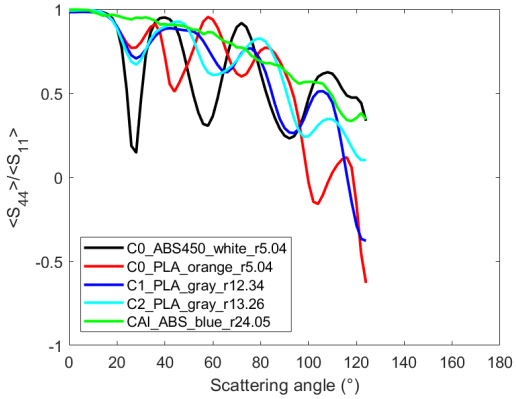

Figure 3.43: $< S_{44} > / < S_{11} >$ of chondrules and CAI at $\lambda = 16.7$mm, corresponding to $X_{mean} = 7.65$ for chondrules and $X = 21.53$ for CAI.

Parameter $\frac{<S_{34}>}{<S_{11}>}$ is shown in Figure 3.44. Differences between $\frac{<S_{34}>}{<S_{11}>}$ from one chondrule to another are again related to the amplitude of oscillation and roughness (or sphericity), as observed with the phase function, DLP and $\frac{<S_{44}>}{<S_{11}>}$. Moreover, at $X \approx 1$ all chondrules present curves around 0 all along the scattering angles (evidence of a Rayleigh behavior for this scattering parameter) and as X increases, oscillations increase too. Both behaviors were also seen with previous scattering parameters. Thus, $\frac{<S_{34}>}{<S_{11}>}$ does not add any extra information compared to phase function, DLP and $\frac{<S_{44}>}{<S_{11}>}$.

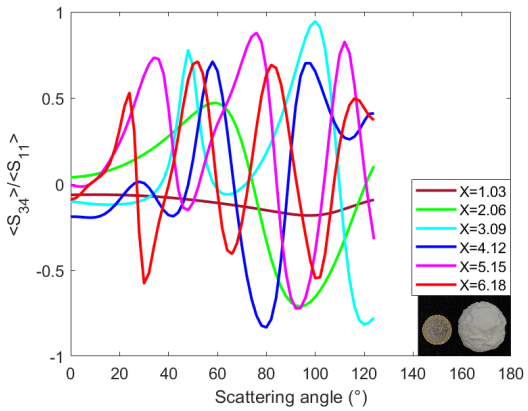

(a) C0_ABS450_white_r5.04

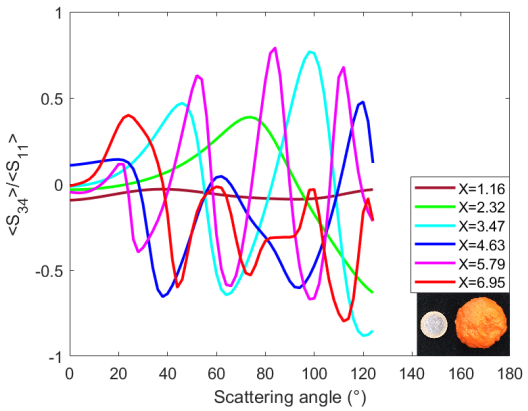

(b) C0_PLA_orange_r5.04

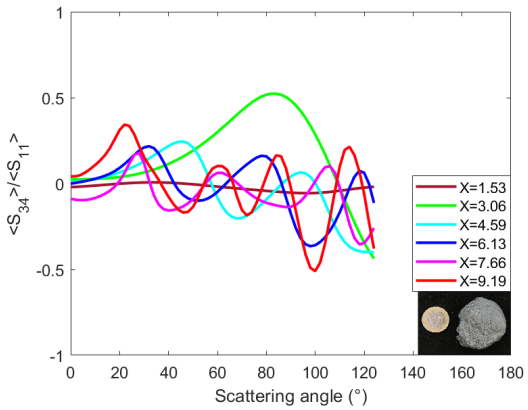

(c) C1_PLA_gray_r12.34

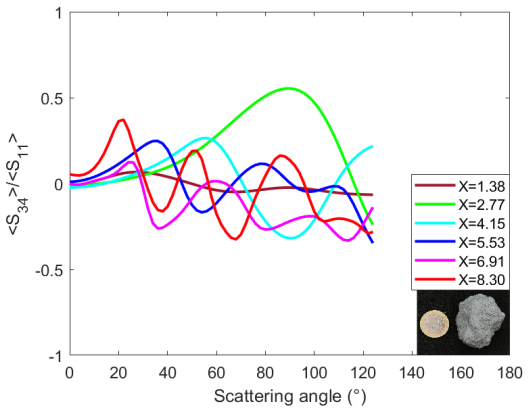

(d) C2_PLA_gray_r13.26

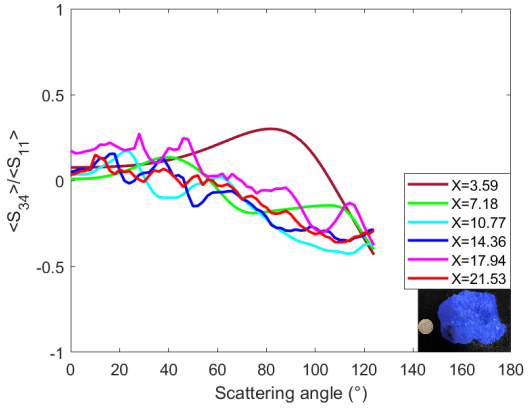

(e) CAI_ABS_blue_r24.05

Figure 3.44: $< S_{34} > / < S_{11} >$ of chondrules and CAI, measurements (solid lines) with their corresponding size parameter.

3.5.2.4 Conclusions

In conclusion, scattering measurements of analogs of four chondrules and one CAI were performed, calculating their scattering parameters. Differences among chondrules and CAI can be identified with changes in amplitudes of: phase functions, DLP, $\frac{<S_{44}>}{<S_{11}>}$ and $\frac{<S_{34}>}{<S_{11}>}$. All these four parameters present the same relation between their amplitudes of oscillations and roughness of analogs (or sphericity), which is, as roughness increases (or sphericity decreases) amplitudes decrease. In the case of chondrules, at $X_{mean} = 1.28$, all four scattering parameters have Rayleigh-like behaviors, while at larger X, oscillations or leftover oscillations of Mie behaviors are present. In the case of our CAI, at the smallest size parameter, $X = 3.59$, curves of the different scattering parameters do not present Rayleigh-like behaviors neither Mie-like behaviors but a transition between both. Then for larger X, each CAI scattering parameter has very similar curves behaviors. For the phase function, CAI curves have narrow forward scattering peaks and damped bumps. For DLP, CAI have little oscillating curves around 0 values. For $\frac{<S_{44}>}{<S_{11}>}$, CAI have curves decreasing from 1 to 0.5 and for $\frac{<S_{34}>}{<S_{11}>}$, levels are between 0 to negative values. All these behaviors were never seen with our other studied morphologies (first family of grains and aggregates). Therefore, differences with all four scattering parameters can be used to identify chondrules from CAI. Future works need to verify if these same scattering behaviors of our CAI can be also observed with other CAIs.

In order to identify chondrules from each other, DLP is a good parameter because amplitudes of DLP are related to their depolarization and therefore to chondrule roughness (or sphericity). In fact, smaller levels of DLP are present for rougher chondrules. This differentiation between chondrules could also be made with the phase function by analyzing the amplitudes of bumps or with $\frac{<S_{44}>}{<S_{11}>}$ or $\frac{<S_{34}>}{<S_{11}>}$, also with the amplitude of oscillation. However, astronomical observations cannot yet obtain these two last scattering parameters. In the case of the phase function, we think it is more difficult to differentiate chondrules by comparing the amplitude of secondary lobes or bumps because these bumps might disappear with the size distribution average, as was the case for aggregates and first family of grains. In brief, DLP is the best scattering property to differentiate between different chondrules and CAI.

Future works should be focused on measuring chondrules and CAI in the backward zone of our scattering experiment in CCRM. Therefore, the analysis of phase function backscattering enhancements and DLP negative polarization branches are missing to complete the scattering study of these particles.

3.5.2.5 Comparison of scattering parameters of chondrules, CAI, grains and aggregates

In this section, I will compare the scattering properties of the three studied morphologies, aggregates and two families of grains, based on their scattering parameters. The idea is to identify which scattering characteristic makes them different, with the pur-

pose to understand which morphologies are present in protoplanetary disks. In order to do this comparison I tried to find the closest X between the three morphologies to eliminate any effect in terms of their sizes and consequently in their scattering parameters. Notice that in Section 3.3.2.6, the comparison between the first family of grains and aggregates was already done. Thus, the final conclusions herein, take also into account the comparisons presented in this previous section.

Phase functions of chondrules and CAI are compared to the ones of grains. Note that the nature of roughness is different for both types of morphologies. For grains, roughness was produced artificially with random distances from the vertex of triangles and the center of grains. For chondrules and CAI, roughness was taken from a XCT of a chondrite which is a natural roughness. Figure 3.45 presents a comparison between grain Gr_n4_r6.7 and chondrule C0_PLA_orange_r5.04, having same size parameters, similar roughness and similar refractive index. Both present similar phase function shapes and same number of bumps at the same wavelengths (represented with the same colors). This is due to their similar sphericity, in the case of C0_PLA_orange_-r5.04 being of 88.83% and for Gr_n4_r6.7 of 90.7%. Slight differences are noticed in terms of their levels due to the small difference in their refractive indices.

On the contrary, if we compare C2_PLA_gray_r13.26 and Gr_n2_r13.3, even if both particles have similar size parameters, roughness and refractive index, they have different phase functions (see Figure 3.46). The chondrule phase functions have damped bumps (sphericity of 82.25%), while for the grain these bumps are well defined (sphericity of 75.6%) which is characteristic of spherical particles. Yet, the grain sphericity is smaller than for the chondrule. Thus, I think that the difference of the amplitude of the phase function bumps is related with their type of morphology. Natural roughness of chondrules produces damped bumps while synthetic peaky roughness of grains produces larger oscillation of amplitude. This difference is noticed in this second comparison (between the grain and chondrules of roughness of 13%) because the percentage of roughness is larger than for the first comparison (previous paragraph, grain and chondrule roughness around 5 to 7%). Therefore, as roughness increases, differences between phase function behaviors of our grains and chondrules are more important, as showed with their bumps.

In the case of CAI phase function, its behavior does not resemble neither the grains phase functions nor the aggregates phase functions. The width of its forward scattering peaks (the narrowest of all our particles phase functions) and the absence of bumps are due to its large size parameter and morphology, respectively.

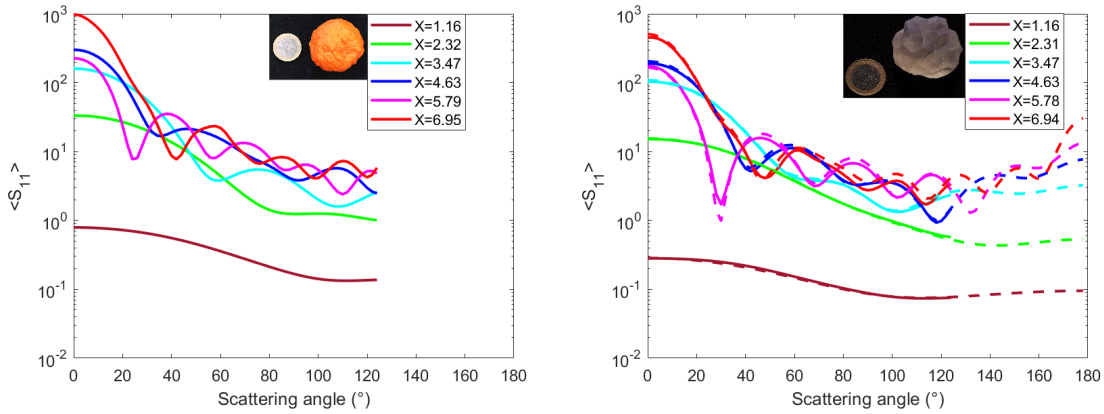

(a) C0_PLA_orange_r5.04 (b) Gr_n4_r6.7

Figure 3.45: Phase function of chondrule C0_PLA_orange_r5.04 and grain Gr_n4_r6.7, measurements (solid lines) and numerical simulations (dashed lines).

If the comparison is made between phase functions of chondrules and aggregates, differences are observed on their bumps. The number of bumps for phase functions of chondrules is greater than for compact aggregates in forward scattering angles, even for chondrule C2_PLA_gray_r13.26 that has damped bumps. In the case of fluffy aggregate, Ag_DLA_Df2.0_N74_1, the difference is even more important because these bumps are absent. The same difference was observed when comparing phase functions of grains with aggregates in Section 3.3.2.6. Thus, both families of grains present similar number of bumps compared to aggregates, and these bumps can also distinguish grains from chondrules at large roughness (around 13.3% where chondrules phase functions have damped oscillations while for grains these bumps have well defined peaks and valleys), proving that these three morphologies presented differentiable phase functions behaviors.

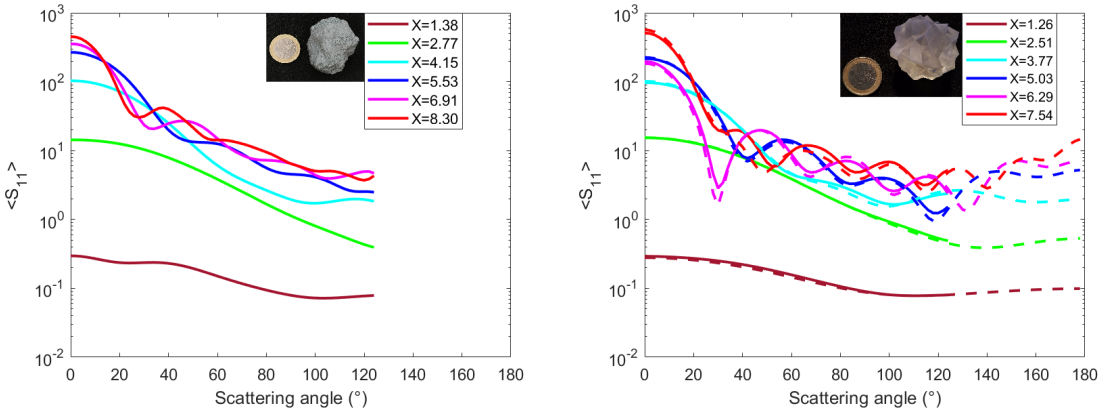

(a) C2_PLA_gray_r13.26 (b) Gr_n2_r13.3

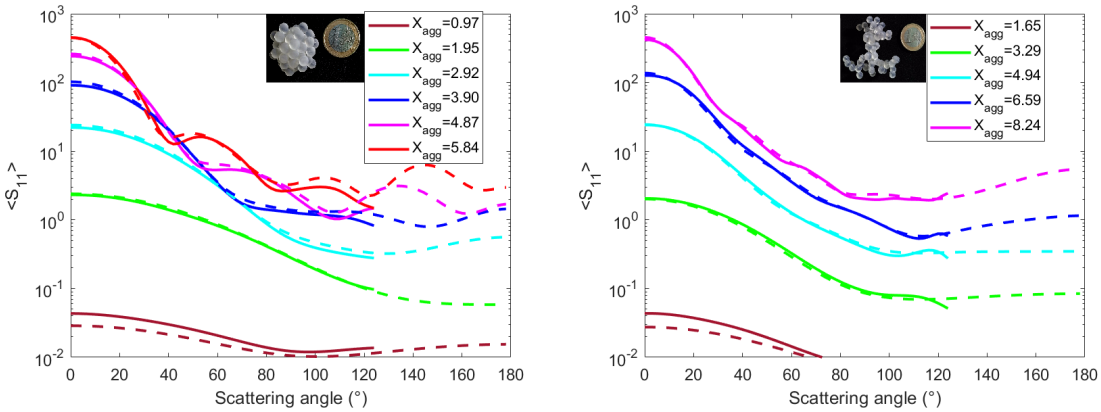

(c) Ag_DLA_Df2.8_N74 (d) Ag_DLA_Df2.0_N74_1

Figure 3.46: Phase function of chondrule, grain and aggregates, measurements (solid lines) and numerical simulations (dashed lines).

When comparing DLP of chondrules with that of other morphologies, similarities are found with grains DLP. Figure 3.47 presents similar DLP behaviors between C0_-PLA_orange_r5.04 and grain Gr_n4_r6.7. On the other hand, Figure 3.48 presents more DLP differences, where amplitudes of DLP oscillations are more damped for the chondrule, C2_PLA_gray_r13.26, compared to that of the grain, Gr_n2_r13.3. In the case of second comparison, roughness has increased for the chondrule and grain (around 13.3%), therefore DLP differences between this two morphologies are more important. These two comparisons were also made to their phase functions, giving same conclusions with the amplitudes of the phase functions bumps and showing larger differences when roughness was around 13.3%. Thus, this scattering parameter does not add any extra information when comparing grains and chondrules.

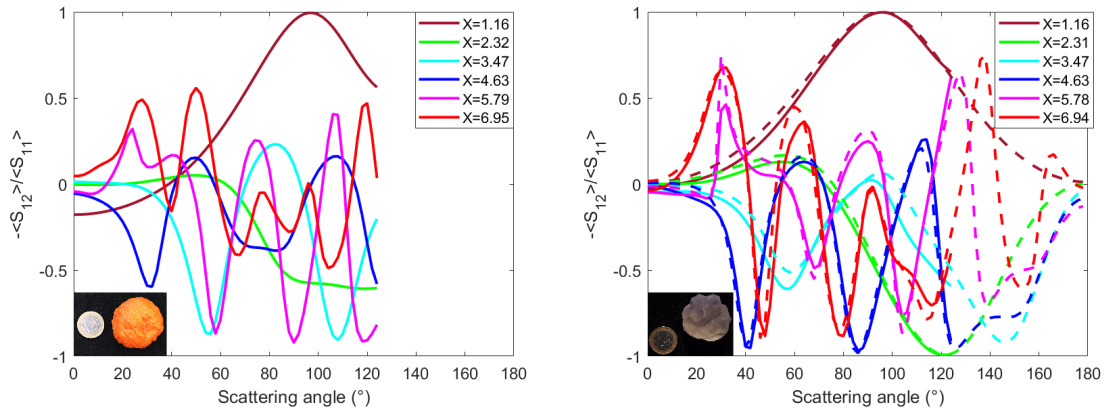

(a) C0_PLA_orange_r5.04 (b) Gr_n4_r6.7

Figure 3.47: DLP of chondrule C0_PLA_orange_r5.04 and grain Gr_n4_r6.7, measurements (solid lines) and numerical simulations (dashed lines).

Comparing chondrules DLP and fluffy aggregates DLP, fluffy aggregate, Ag_DLA_-Df2.0_N74_1, presents bell DLP curves at all X, while chondrule C2_PLA_gray_r13.26 has only this behavior at its smallest size parameter, $X = 1.38$. Differences are visible at larger X. Hence, if we compare at $X = 8.30$ for the chondrule and $X = 8.24$ for the aggregate, DLP of aggregate has a Rayleigh-like behavior (bell) even for this large X (the same behavior is observed for other aggregates with $D_f \leq 2$) while DLP of chondrule has damped oscillating behaviors around values of 0. If the comparison is made between chondrule C2_PLA_gray_r13.26 and the most compact aggregate, the distinction is not very clear. What can be observed is that the damped DLP oscillations of the chondrule are irregular curves (misshaped) which is also the case for chondrule C1_PLA_gray_r12.34 (showed in Figure 3.40). In summary, DLP of fluffy aggregates ($D_f \leq 2$) can easily be differentiated from chondrules and grains, yet DLP of the most compact aggregate does not present much difference with chondrules C1 and C2, contrary to chondrules C0. In the case of CAI DLP, neither the aggregates, grains or chondrules DLP present little oscillations around 0 values as CAI DLP does. The DLP of CAI presents the largest depolarization of all our particles.

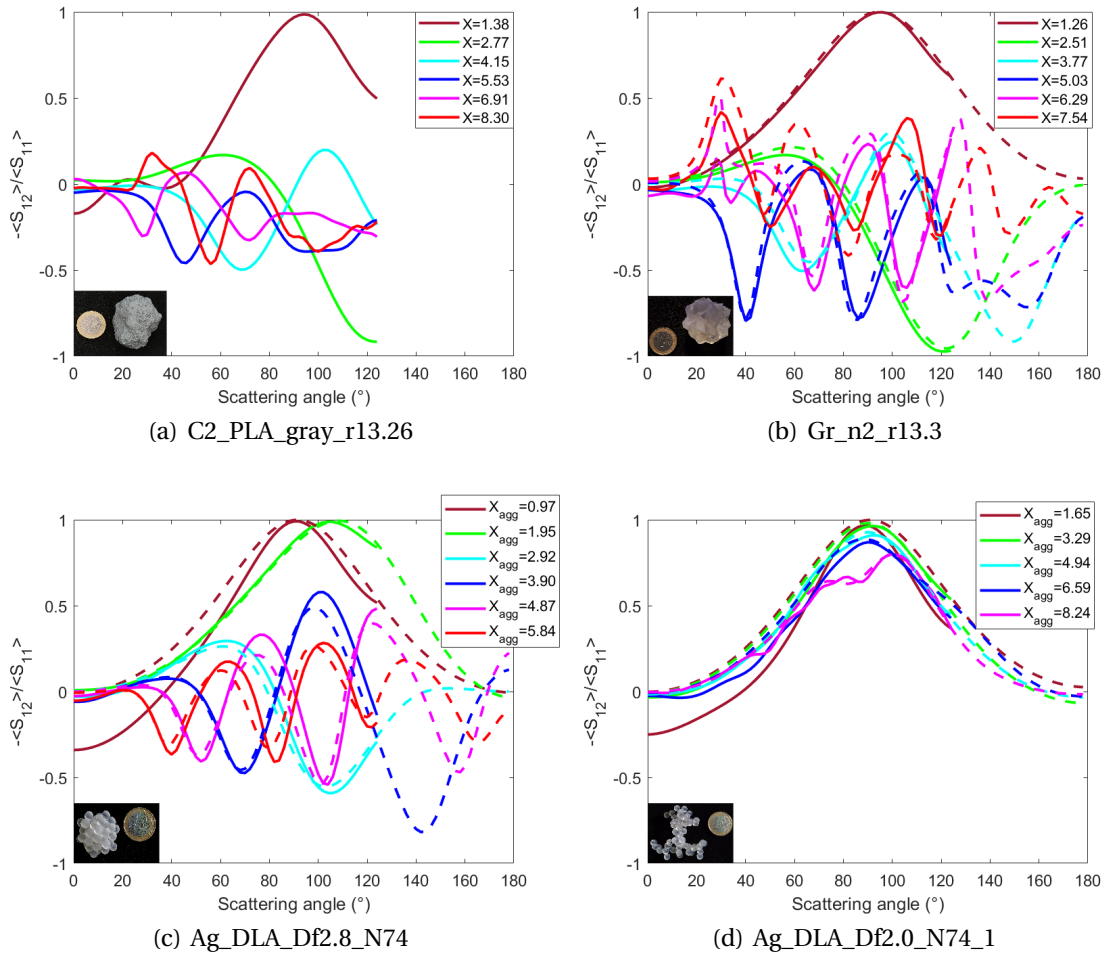

(a) C2_PLA_gray_r13.26 (b) Gr_n2_r13.3

(c) Ag_DLA_Df2.8_N74 (d) Ag_DLA_Df2.0_N74_1

Figure 3.48: DLP of chondrule, grain and aggregates, measurements (solid lines) and numerical simulations (dashed lines).

When comparing $\frac{<S_{44}>}{<S_{11}>}$ of chondrules with that of grains (see Figures 3.49 and 3.50), it can be seen that no matter the percentage of roughness, in both cases oscillations of $\frac{<S_{44}>}{<S_{11}>}$ have larger amplitudes for grains than for chondrules. When the comparison is made with the phase function and DLP, differences are only visible at a roughness of 13.3%, thus this scattering parameter is more sensitive to differentiate between these two types of roughness. Moreover, by analyzing $\frac{<S_{44}>}{<S_{11}>}$ of chondrules with that of aggregates, the difference is observed at forward scattering angles from 0° to 60°. Indeed, $\frac{<S_{44}>}{<S_{11}>}$ of all our chondrules always oscillates (except at X around 1) while our aggregates have curves almost constant around values of 1. Then, after 60°, compact aggregates oscillate up to backscacttering angles, while fluffy aggregates smoothly decrease with Rayleigh behavior. In summary, $\frac{<S_{44}>}{<S_{11}>}$ has characteristic behaviors between the three morphologies and also within the same morphology: i) $\frac{<S_{44}>}{<S_{11}>}$ of rough particles starts oscillating at 20°, while $\frac{<S_{44}>}{<S_{11}>}$ of aggregates starts at 60°, ii) $\frac{<S_{44}>}{<S_{11}>}$

of chondrules has damped oscillations compared to that of grains, and iii) $\frac{<S_{44}>}{<S_{11}>}$ of compact aggregates has oscillations from 60° to backscattering angles while that of fluffy aggregates does not oscillate.

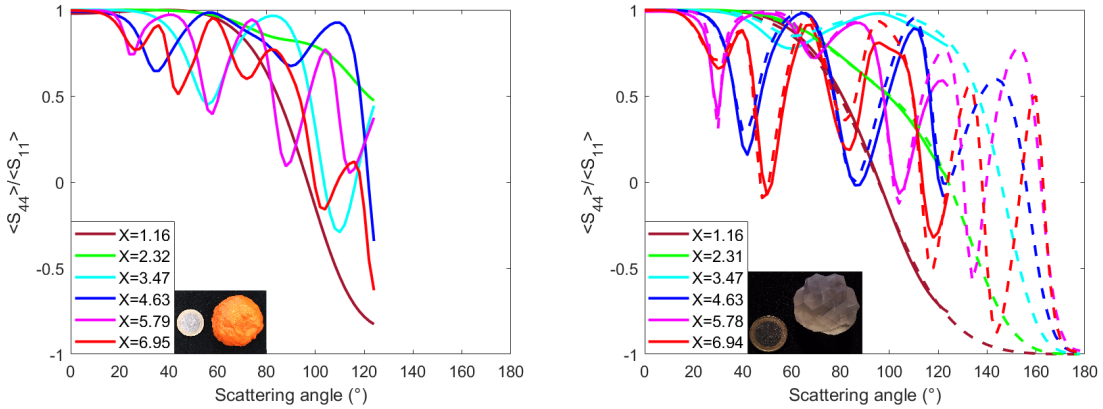

(a) C0_PLA_orange_r5.04 (b) Gr_n4_r6.7

Figure 3.49: $< S_{44} > / < S_{11} >$ of chondrule C0_PLA_orange_r5.04 and grain Gr_-n4_r6.7, measurements (solid lines) and numerical simulations (dashed lines).

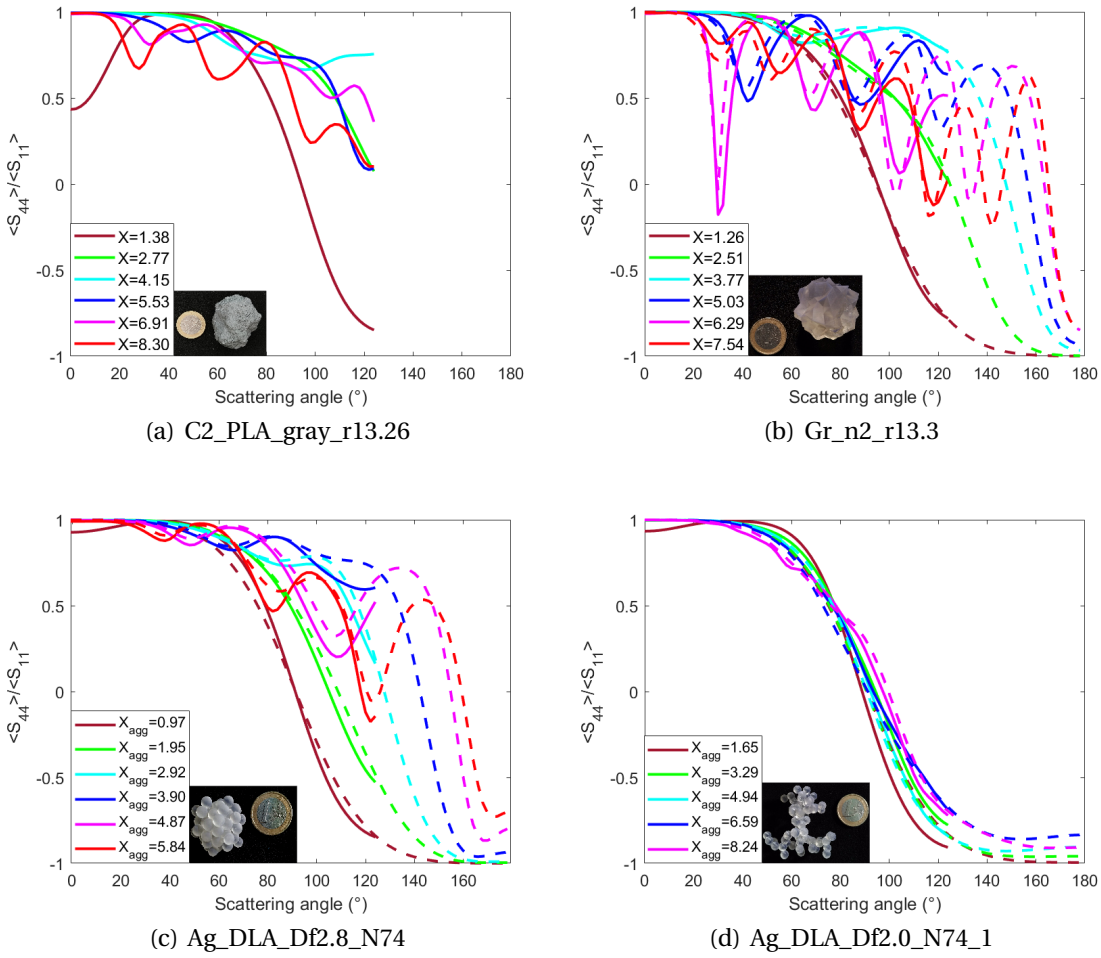

(a) C2_PLA_gray_r13.26

(b) Gr_n2_r13.3

(c) Ag_DLA_Df2.8_N74

(d) Ag_DLA_Df2.0_N74_1

Figure 3.50: $< S_{44} > / < S_{11} >$ of chondrule, grain and aggregates, measurements (solid lines) and numerical simulations (dashed lines).

Finally, in the case of $\frac{<S_{34}>}{<S_{11}>}$, Figure 3.51 presents a comparison between C0_PLA_-orange_r5.04 and Gr_n4_r6.7. Both particles have the same size parameter, thus at $X = 1.16$ they have almost a constant behavior along the scattering angles around 0, and for larger X, both present oscillations at similar $\frac{<S_{34}>}{<S_{11}>}$ values. Therefore, distinguishing both types of roughness, based on $\frac{<S_{34}>}{<S_{11}>}$, is not possible. However, if the chondrule is rougher, the difference of $\frac{<S_{34}>}{<S_{11}>}$ between chondrules and grains is immediately visible (see for example Figure 3.52.a and 3.52.b), as for the phase function and DLP. As previously observed with other scattering parameters, oscillations of this parameter are damped for C2_PLA_gray_r13.26 compared to that of Gr_n2_r13.3 (grains presents large amplitudes of oscillations). The same was observed for chondrule C1 and CAI. In the case of aggregates with $D_f \leq 2$, their $\frac{<S_{34}>}{<S_{11}>}$ curves are different from chondrules and grains, having curves that fluctuate around 0, all along the scattering angles. For the most compact aggregate, $\frac{<S_{34}>}{<S_{11}>}$ has oscillations, smaller than grains but larger than

chondrule C2, thus it is difficult to know with this parameter if the aggregate is a grain but with a larger roughness, or if it is a chondrule with a smaller roughness. In short, this scattering parameter is less sensitive than $\frac{<S_{44}>}{<S_{11}>}$ to identify between the two types of roughness (chondrules and grains), when particles roughness are around 5%, as was the case for the phase function and DLP. Additionally, differences between $\frac{<S_{34}>}{<S_{11}>}$ of the most compact aggregate and chondrules or grains is very slight, which implies possible confusions between the three morphologies.

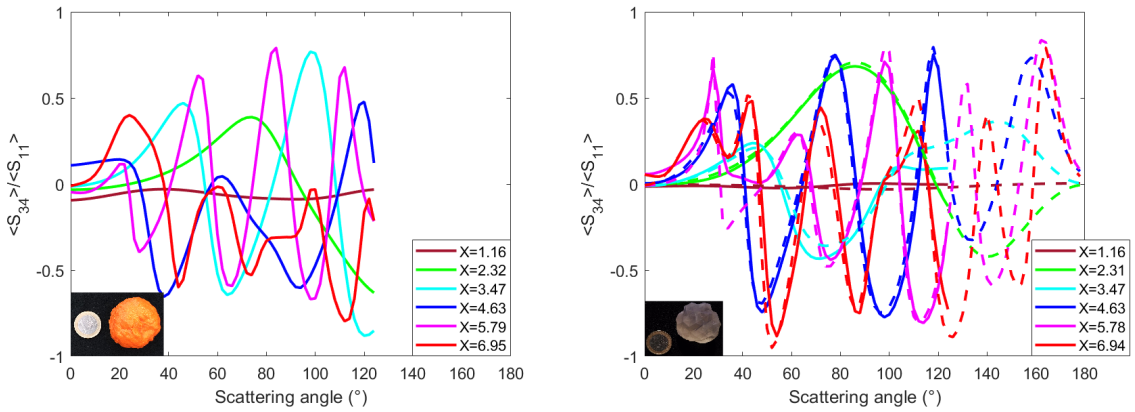

(a) C0_PLA_orange_r5.04 (b) Gr_n4_r6.7

Figure 3.51: $< S_{34} > / < S_{11} >$ of chondrule C0_PLA_orange_r5.04 and grain Gr_-n4_r6.7, measurements (solid lines) and numerical simulations (dashed lines).

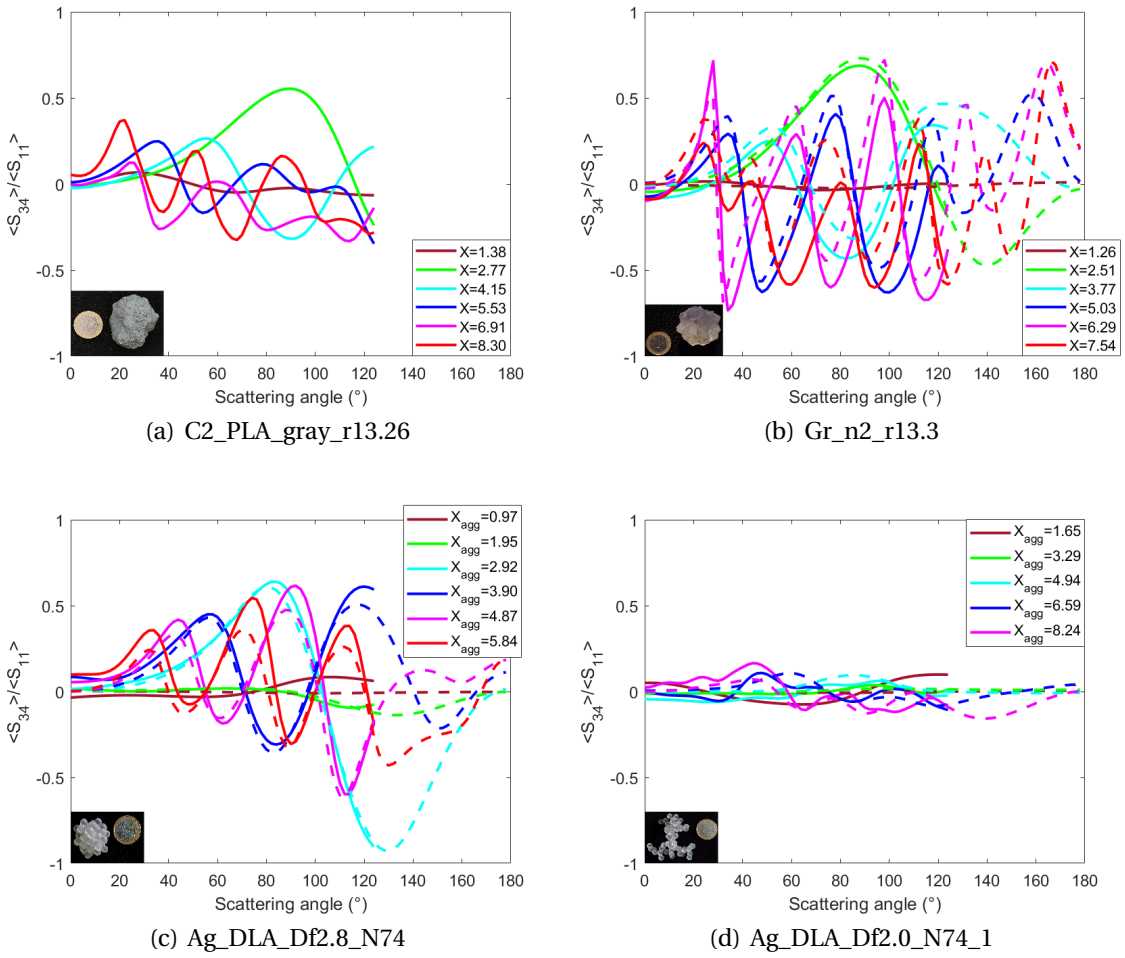

(a) C2_PLA_gray_r13.26

(b) Gr_n2_r13.3

(c) Ag_DLA_Df2.8_N74

(d) Ag_DLA_Df2.0_N74_1

Figure 3.52: $< S_{34} > / < S_{11} >$ of chondrule, grain and aggregates, measurements (solid lines) and numerical simulations (dashed lines).

In conclusion, we found similarities between scattering parameters of grains and chondrules. Yet, among all the scattering parameters, $\frac{<S_{44}>}{<S_{11}>}$ is the most sensitive parameter presenting the greatest difference between these two morphologies that resemble but have different natures of roughness (one synthetic and another one natural). Chondrules have clearly $\frac{<S_{44}>}{<S_{11}>}$ curves with smaller amplitude of oscillations than grains. Additionally, based on this parameter, we were able to identify between characteristic behaviors of the most compact aggregate compared to grains and chondrules and also with fluffy aggregates. Hence, $\frac{<S_{44}>}{<S_{11}>}$ is an excellent parameter to identify between our three types of morphologies.

In order to complete the scattering study of chondrules and CAI, in the following section, a size distribution effect will be applied to the same four scattering parameters and compared again with the other two morphologies, grains and aggregates.

3.5.3 Chondrules and CAI with average orientation and size distribution effect

3.5.3.1 Probability distribution

The size distribution effect applied to the scattering parameters of grains, in Section 3.3.3, is also applied to the scattering parameters of chondrules and CAI, which means, a power law distribution on X with index $n_s = 3.5$, calculated in the optical range, thus protoplanetary dust with size parameters from $X_{min} = 0.90$ to $X_{max} = 157.08$ (see Equation 2.5). Based on the mean radius of the bounding sphere of chondrules (20.29mm), their size parameters are from $X_{mean} = 1.28$ to $X_{mean} = 7.65$, corresponding to a probability of 0.819 and 0.0016, respectively. For the CAI, size parameters are from $X = 3.59$ to $X = 21.54$, corresponding to a probability of 0.022 and 0.00004, respectively. Probability of distribution for chondrules and CAI is shown in Figure 3.53.

Notice that the size distribution of chondrules and CAI is still a highly debated subject. Some authors accept a power law distribution for CAI [187] where the index is still not well defined, while other authors propose a lognormal size distribution for chondrules and CAI [188]. Thus, we decided to use the same size distribution as protoplanetary dust, in order to be able to compare their scattering parameters with the ones of our aggregates and grains. Additionally, two more power law indices were applied ($n_s = 2$ and $n_s = 5$), as for aggregates and grains, to study how the change of index affect their scattering parameters. Note that if the size distribution of chondrules and CAI is proved to be different in a future, our measurements and simulations of their scattering parameters can be used and only the size distribution effect need to be changed on X.

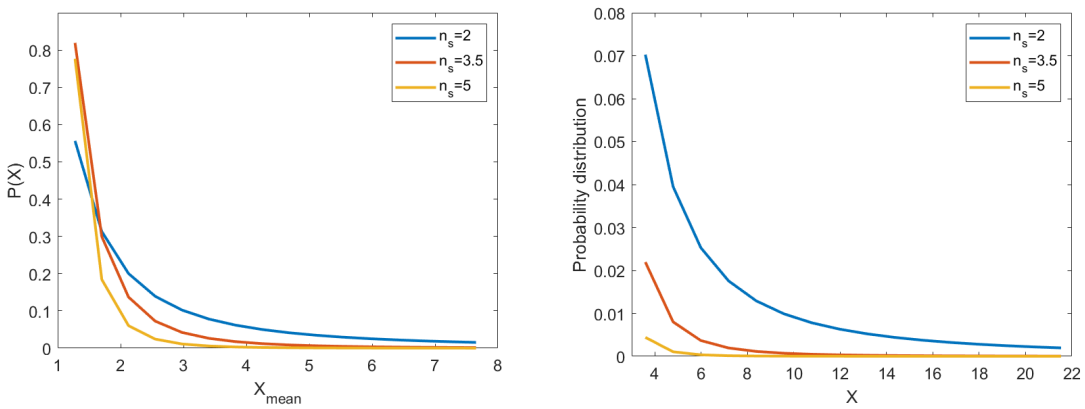

(a) Chondrules (b) CAI

Figure 3.53: Probability distribution with three different indices (see legend) in terms of X_{mean} for chondrules, from 1.28 to 7.65 (Figure a), and in terms of X for CAI, from 3.59 to 21.54 (Figure b).

3.5.3.2 Phase function

After applying the size distribution effect at the three chosen n_s, the scattering properties were analyzed. Phase functions of chondrules and CAI are shown in Figure 3.54. As n_s increases, levels of the forward scattering peak decrease and HWHM values increase.

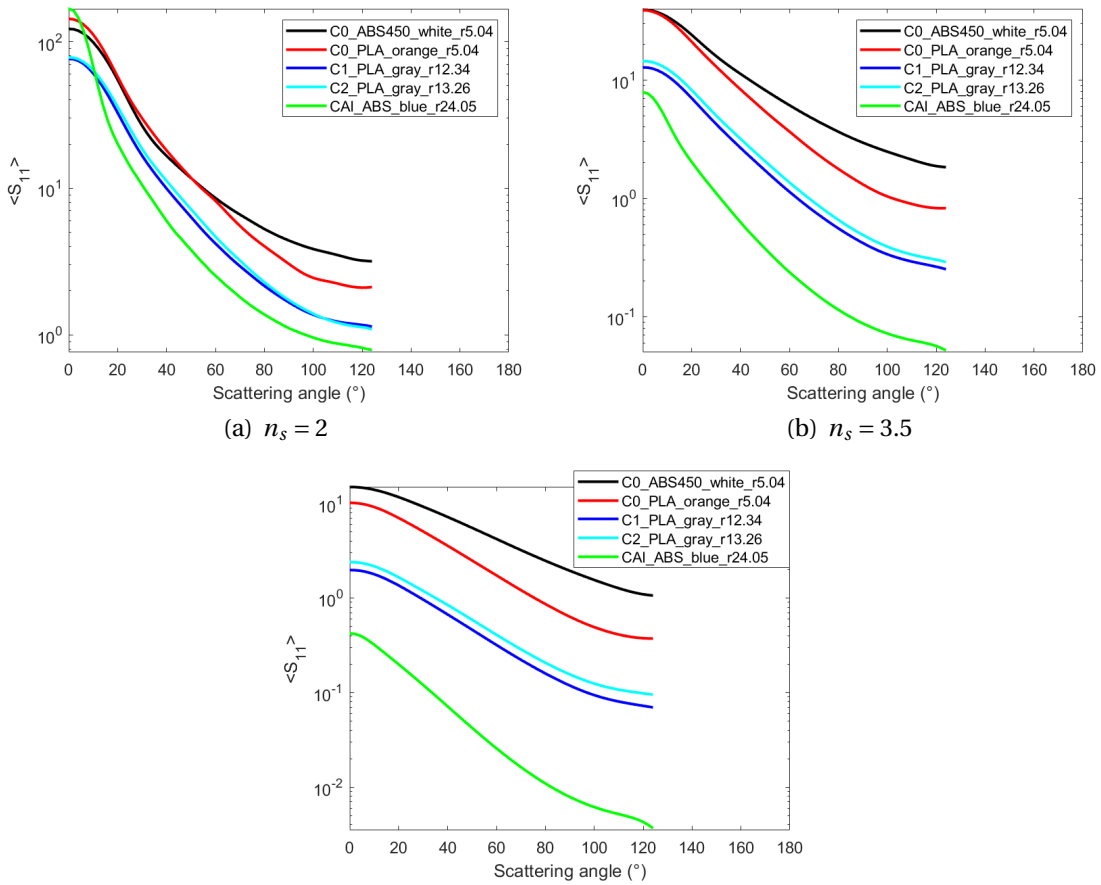

(a) $n_s = 2$ (b) $n_s = 3.5$

(c) $n_s = 5$

Figure 3.54: Phase function of chondrules and CAI with average orientation and with power law distributions of different n_s, measurements (solid lines).

Levels of their phase functions are caused by the radius of the bounding sphere. For example, both chondrules C0 have similar radius (the two smallest radius of these particles) therefore similar X, giving the same weight and producing large phase function levels (small particles have more weight than large particles for the size distribution of chondrules). The same is seen for C1_PLA_gray_r13.24 and C2_PLA_-gray_r13.26, which have the second largest levels. For CAI, even if it has the largest radius and consequently the largest X, its size distribution is inverted compared to chondrules, thus at $n_s = 2$ the CAI has the largest weight compared to other two power

law indices. Therefore, these phase function levels are associated to the radius of their bounding spheres and size distributions, giving specific levels for each particle. In fact, these levels do not give information about their morphology but size.

Moreover, the HWHM of the measured phase function portion (up to 130°) were retrieved (see Table 3.11). Chondrules have similar HWHM values, except for C0_-ABS450_white_r5.04 at $n_s = 2$ and $n_s = 5$. These values need to be remeasured with the whole phase function curve (including backscattering angles) because the software, that estimates HWHM, takes the last point (at 130°) as the minimum phase function value to calculate the height of the curve. But since the real minimum value is not known until having the whole curve, then these values should be revisited. As can be seen, CAI presents the smallest HWHM values at three n_s: this is due to its large size compared to chondrules. This can also be seen in Figure 3.55, where the phase function of chondrules and CAI are normalized, showing the narrowest width for the CAI phase function.

n_s	C0_ABS450_ white_r5.04	C0_PLA_ orange_r5.04	C1_PLA_ gray_r12.34	C2_PLA_ gray_r13.26	CAI_ABS_ blue_r24.05
2	36	40	44	46	32
3.5	50	50	50	52	44
5	62	56	56	56	56

Table 3.11: HWHM of phase function of chondrules and CAI with average orientation and with power law distributions of different n_s. Measured values in degrees.

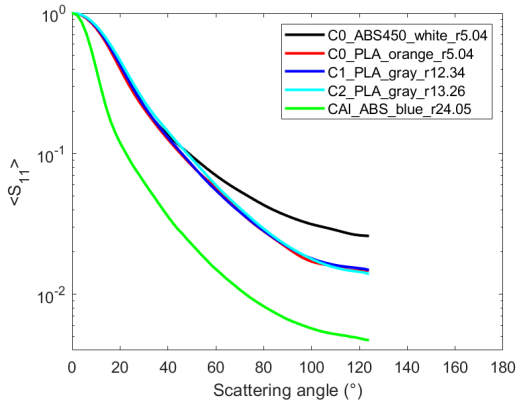

Figure 3.55: Normalized phase function of chondrules and CAI with average orientation and with power law distributions of $n_s = 3.5$, measurements (solid lines).

Contrary to the first family of grains, this second family does not have the values of the phase function at backscattering angles. Thus, we could not associate their backscattering enhancements to their morphology and roughness (or sphericity).

Future works need to measure these particles at backscattering angles in order to complete their scattering analysis. In summary, with incomplete phase function curves, the only possible analyses are in terms of their levels and HWHM values which are related to their size and not to their morphology.

3.5.3.3 Degree of linear polarization

Figure 3.56 shows the degree of linear polarization with the size distribution effect at the three chosen indices. Maximum DLP levels increase as n_s increases, for all chondrules and CAI (see Table 3.12). The scattering angles corresponding to these maximum DLP levels are similar for all chondrules. At $n_s = 2$ these maximum levels are at forward scattering angles, from 0° to 10°. At $n_s = 3.5$, maximum DLP levels are at scattering angles around 90°, and at $n_s = 5$ around 96°. This shift of maximum DLP from small scattering angles to larger scattering angles as n_s increase (only for chondrules), is caused by the important increase of weight given to small size parameters of the size distribution. Small size parameters have DLP with Rayleigh behaviors in which the maximum DLP is found at side scattering angles. In the case of CAI, maximum DLP levels correspond to scattering angles larger than 115° with the three n_s, therefore it is the maximum scattering angle of all the maximum DLP of grains (in this case, for DLP represented up to 130°). However, there is no certainty to know if it is the maximum of the whole DLP curve (if the backscattering values were included). Indeed, backscattering measurements need to be performed in a future to conclude about the scattering angle position of the maximum DLP of CAI.

Furthermore, the maximum DLP levels are different depending on the particle roughness (or sphericity). This difference is visible at $n_s = 3.5$ and $n_s = 5$, where the roughest chondrule, C2_PLA_gray_r13.26, presents the highest maximum DLP levels, followed by C1_PLA_gray_r12.34 and C0_PLA_orange_r5.04. This relation between the maximum DLP levels and roughness (or sphericity) was also seen for the first family of grains. In the case of C0_ABS450_blue_r5.04, it presents the smallest DLP level, even if this chondrule contains the same roughness and morphology as C0_-PLA_orange_r5.04, its refractive index (real part) is greater, depolarizing more. This behavior that the refractive index affects the polarimetric response more than the particle morphology was already seen in [156] for virtual rough particles. Finally, CAI presents a particular DLP behavior. First, its maximum DLP is not at the same scattering angle as that of chondrules. Second, its DLP levels do not follow the behavior that was identified for grains and chondrules related to roughness. The reason is that CAI has the largest size which means a larger depolarization and therefore smaller maximum DLP values compared to those of chondrules.

In brief, DLP levels are affected by: i) the index of the size distribution, ii) the type of roughness (in the case of chondrules C0_PLA_orange_r5.04, C1_PLA_gray_r12.34 and C2_PLA_gray_r13.26), iii) the refractive index (there were visible differences between C0_PLA_orange_r5.04 and C0_ABS450_white_r5.04), and iv) the size parameter (CAI has the largest X presenting large depolarizations). If only morphology wants to

be distinguished based on DLP, the size parameter and refractive index need to be constant among the different studied particles, as was the case for our first studied family of grains. However, this is not the case for protoplanetary dust where particles are of different sizes and mixed materials. Thus, we will explore two more scattering parameters, in the following section, to see if other scattering properties of this type of morphology can be observed.

Notice that future works need to perform measurements in backscattering angles to be able to analyze the negative polarization branch of the DLP. As was previously mentioned for the first family of grains, this branch is related to morphology.

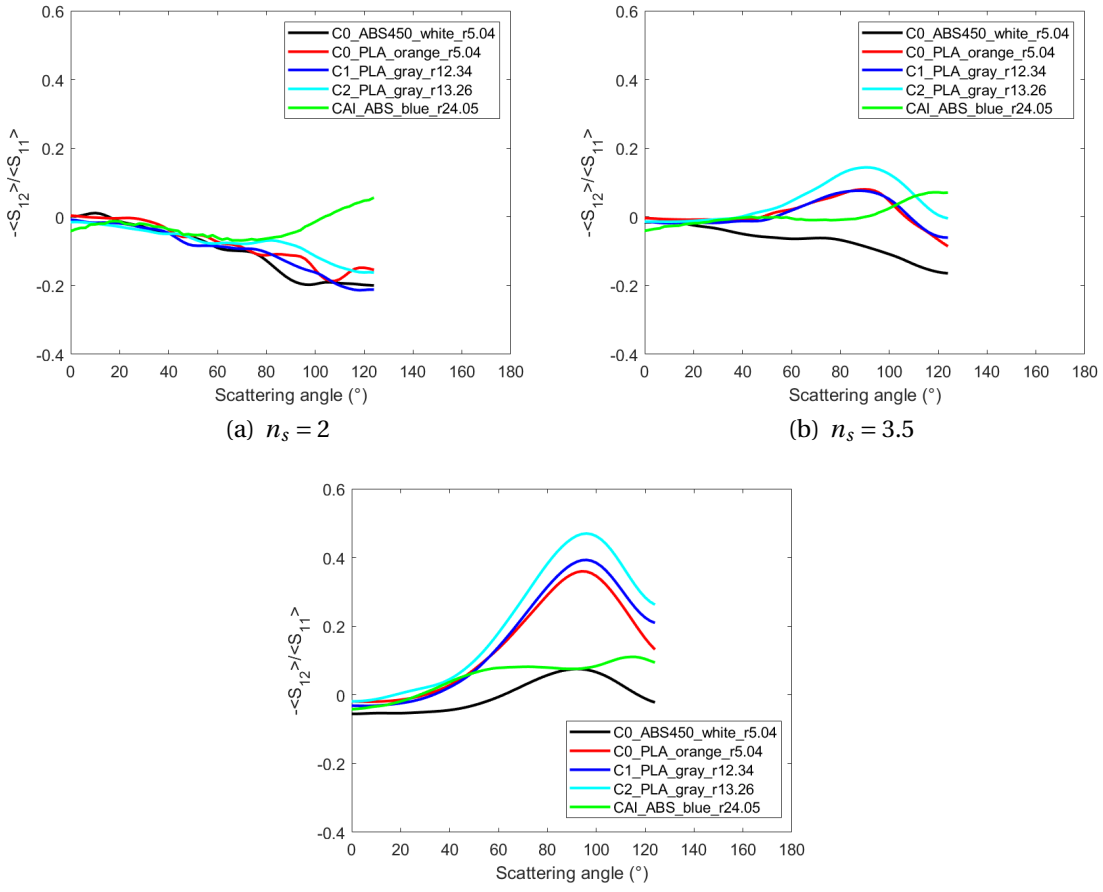

(a) $n_s = 2$

(b) $n_s = 3.5$

(c) $n_s = 5$

Figure 3.56: DLP of chondrules and CAI with average orientation and with power law distributions of different n_s, measurements (solid lines).

n_s	C0_ABS450_ white_r5.04	C0_PLA_ orange_r5.04	C1_PLA_ gray_r12.34	C2_PLA_ gray_r13.26	CAI_ABS_ blue_r24.05
2	0.01	0.00	-0.01	-0.01	0.07
3.5	-0.01	0.08	0.08	0.14	0.08
5	0.08	0.36	0.39	0.47	0.11

Table 3.12: Levels of maximum DLP of chondrules and CAI with average orientation and with power law distributions of different n_s. Measured values.

3.5.3.4 Other scattering parameters

Parameter $\frac{<S_{44}>}{<S_{11}>}$ is presented in Figure 3.57. At $n_s = 2$, curves of $\frac{<S_{44}>}{<S_{11}>}$ are superimposed for all chondrules and CAI, from 0° to 100°, except for chondrule C0_ABS450_white_r5.04. After 100° differences are visible, suggesting possible changes of $\frac{<S_{44}>}{<S_{11}>}$ curves in backscattering angles. At $n_s = 3.5$, this difference is larger, distinguishing three groups from 115° to 130°: the two roughest chondrules have the lowest $\frac{<S_{44}>}{<S_{11}>}$ levels (0.08), then the two smoothest chondrules have larger levels (0.2) and finally, the CAI has the largest level (0.4). The same analysis can be made at $n_s = 5$, where the difference between particles is even finer. Levels are organized from the roughest chondrule (the least spherical chondrule) to the smoothest chondrule (the most spherical chondrule).

For CAI_ABS_blue_r24.05, even if its roughness is the largest of all particles, its $\frac{<S_{44}>}{<S_{11}>}$ levels are not lower than those of C2_PLA_gray_r13.26. Actually, in order to have smaller levels, a smoother curve is needed, closer to a Rayleigh behavior which is not the case for the CAI. The size parameters of CAI_ABS_blue_r24.05 are not close to $X = 1$ (Figure 3.42 showed that Rayleigh-like behaviors of $\frac{<S_{44}>}{<S_{11}>}$ are present at $X = 1$, brown lines), thus this scattering parameter is affected by its large size parameter, not following the same organization of $\frac{<S_{44}>}{<S_{11}>}$ that chondrules present. In summary, the levels of $\frac{<S_{44}>}{<S_{11}>}$ can be a clue to identify the different percentages of roughness (or sphericity) of chondrules. Yet as concluded for the phase function and DLP, backscattering information is required to complete the analysis.

Finally, parameter $\frac{<S_{34}>}{<S_{11}>}$ is shown in Figure 3.58. At all three n_s, these particles present similar behaviors: first, chondrules C0_PLA_orange_r5.04, C1_PLA_gray_r12.34 and C2_PLA_gray_r13.26 have same levels and curve shapes (one global positive oscillation that was also seen for the first family of grains). Second, the chondrule with the largest refractive index, C0_ABS450_white_r5.04, has the largest $\frac{<S_{34}>}{<S_{11}>}$ values all along the scattering angles with a final enhancement around 120°. Third, CAI_ABS_blue_r24.05 presents the lowest $\frac{<S_{34}>}{<S_{11}>}$ values. These behaviors are not correlated with their percentage of roughness, neither their sphericity. Therefore, this scattering parameter does not provide much information about the morphology of this second family of grains. Future measurements in backward zone are needed to verify if the resonant peak, seen for the first family of grains at 160°, is also detectable for this second family of grains.

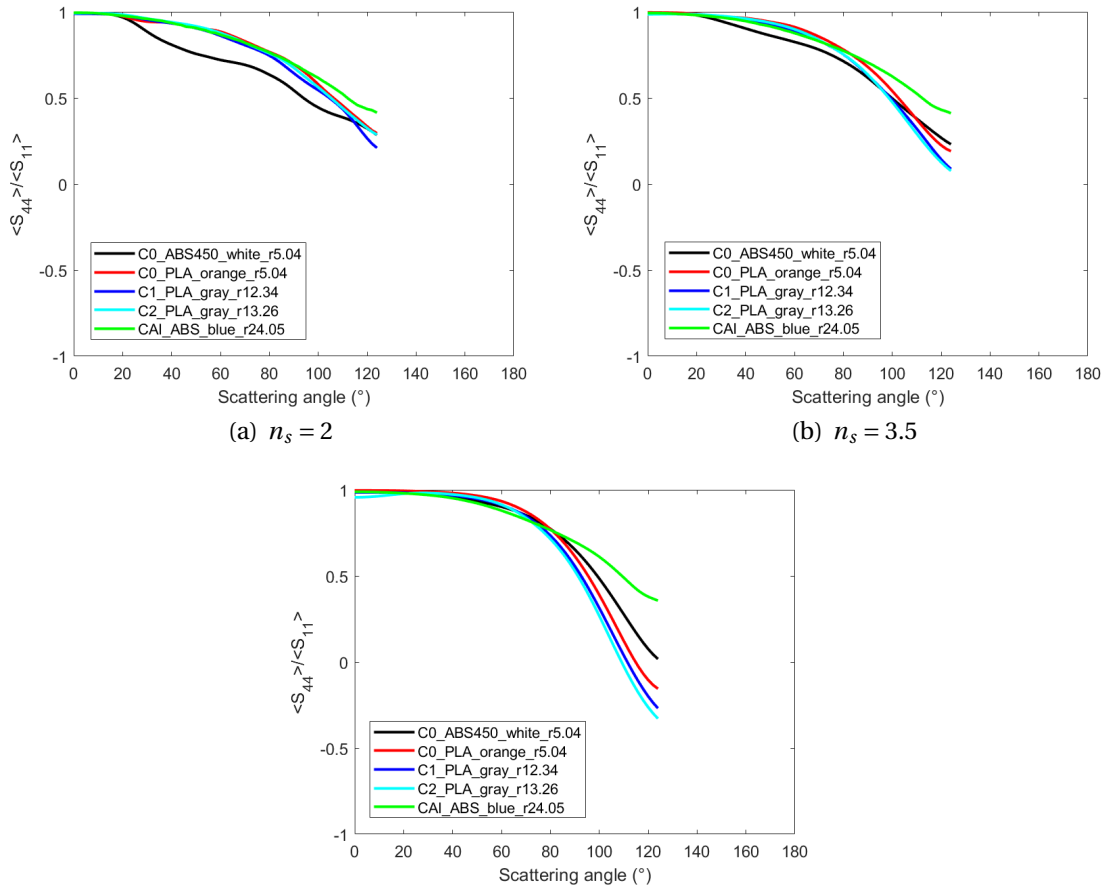

(a) $n_s = 2$ (b) $n_s = 3.5$

(c) $n_s = 5$

Figure 3.57: $< S_{44} > / < S_{11} >$ of chondrules and CAI with average orientation and with power law distributions of different n_s, measurements (solid lines).

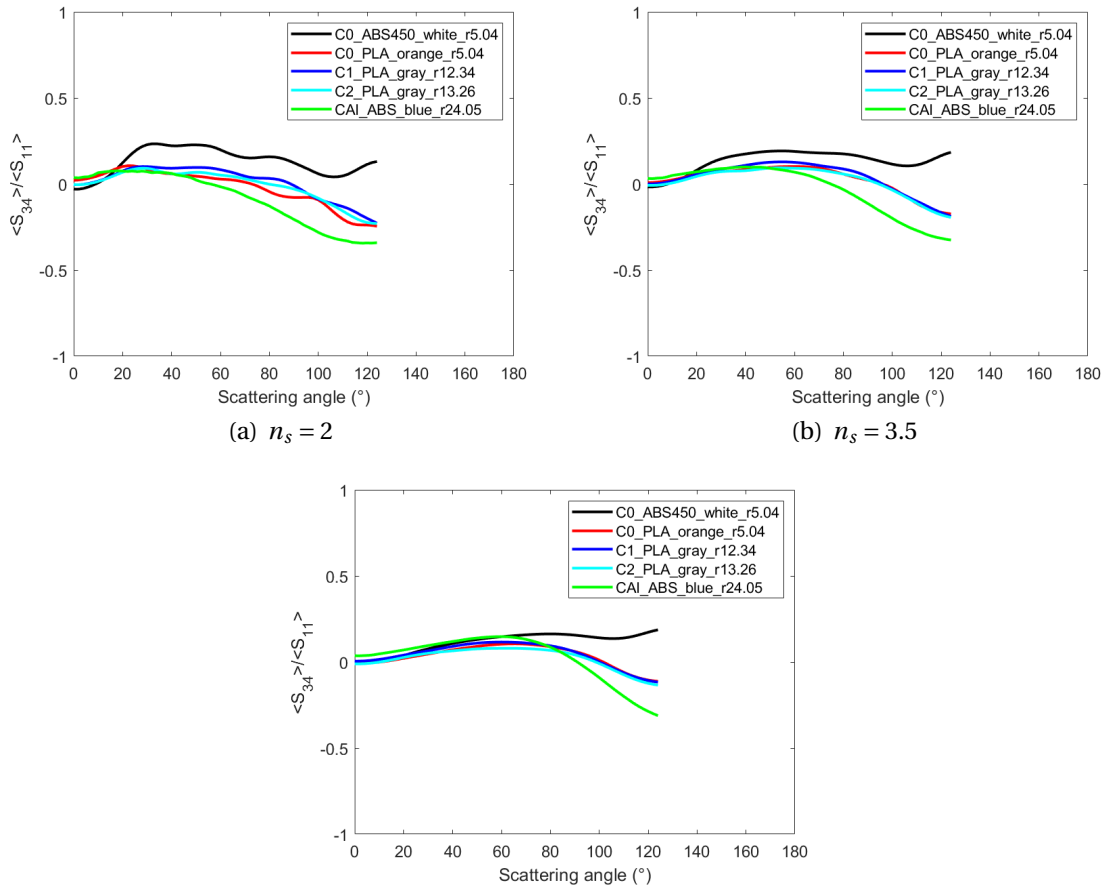

(a) $n_s = 2$ (b) $n_s = 3.5$

(c) $n_s = 5$

Figure 3.58: $< S_{34} > / < S_{11} >$ of chondrules and CAI with average orientation and with power law distributions of different n_s, measurements (solid lines).

3.5.3.5 Conclusions

In conclusion, the scattering parameters retrieved with forward scattering measurements and size distribution effect showed changes when varying n_s, seen with their levels and curve shapes. Among all these four scattering parameters, DLP and $\frac{<S_{44}>}{<S_{11}>}$ are the best ones when finding differences within the morphology of our chondrules (roughness or sphericity). DLP presents an organization of maximum levels (with n_s = 3.5 and n_s = 5), from the roughest chondrule (C2_PLA_gray_r13.26) to the smoothest (C0_PLA_orange_r5.04) and finally the smoothest chondrule with the highest refractive index (C0_ABS450_white_r5.04). In the case of $\frac{<S_{44}>}{<S_{11}>}$ (with $n_s = 3.5$ and $n_s = 5$), levels between 115° to 130° are organized from the smoothest chondrules to the roughest chondrules. For both scattering parameters, the organization is even finer with $n_s = 5$. In the case of CAI, DLP and $\frac{<S_{44}>}{<S_{11}>}$ did not follow neither of these two behaviors, yet a characteristic difference was observed with its DLP. The scattering

angle corresponding to its maximum DLP was larger than 115° while for chondrules it was around 90° to 100°, at $n_s = 3.5$ and $n_s = 5$. Thus, these two parameters can be used to differentiate chondrules and CAI morphologies. As previously mentioned for all four scattering parameters, there is a need to perform measurements in backscattering angles to analyze the phase function enhancements, the negative polarization branch, and the possible peak at 160° for $\frac{<S_{34}>}{<S_{11}>}$ which were important characteristics identified for our first family of grains.

3.5.3.6 Comparison of scattering parameters of chondrules, CAI, grains and aggregates

The aim of this section is to do a final comparison of the scattering properties between the three morphologies that have been studied in this thesis, based on their scattering parameters. In Section 3.5.2.5, I compared their scattering parameters wavelength by wavelength, finding several differences. Still, protoplanetary dust has different sizes presenting a power law size distribution. Thereby, to come closer in doing the analogy, their scattering parameters are compared including a size distribution effect with $n_s = 3.5$, the objective being the differentiation of their morphologies through their scattering parameters. Notice that in Section 3.3.3.6, comparisons between the scattering parameters of the first family of grains and aggregates were performed. Herein, these comparisons are taken into account, doing a final conclusion with all three morphologies.

When comparing the forward phase function of grains and chondrules (see Figure 3.59), HWHM of grains are slightly larger (around 52° for measurements) than HWHM of chondrules (around 50° for measurements). This is caused by the radius of their bounding sphere. Indeed, mean radius of grains is around 18.45mm while mean radius of chondrules is 20.29mm. The main difference between phase function of grains and chondrules (C0, C1 and C2 fabricated with PLA) is their amplitude of oscillation. Grains phase functions have an amplitude with levels arriving at $10^{-1.6}$ while chondrules phase functions have larger amplitudes with levels around $10^{-1.8}$. However, if chondrules present a larger refractive index (as in the case of C0_ABS450_-white_r5.05), their amplitude of oscillations are the same as for our grains (see Figure 3.60). Therefore, distinguishing these two morphologies when the refractive index is not the same, is difficult. Additionally, we do not know if the backscattering phase functions of chondrules behave similarly as those of grains. If this is the case (that need to be verified in a future), then identifying between two types of roughness of compact particles of similar sizes is not possible when we apply a size distribution.

When comparing the phase function of chondrules with that of aggregates (see Figure 3.61), chondrules (C0, C1 and C2 fabricated with PLA) present a similar forward phase function, behavior and levels, to the phase function of the most compact aggregates (Ag_DLA_Df2.8_N74). There is a difference in the amplitude of oscillation between chondrules and aggregates with $D_f \leq 2.5$, as it was the case with the most

compact aggregate and the other aggregates. This means that the phase function of the most compact aggregate can be confused with the phase function of compact rough grains, contrary to that of aggregates with $D_f \leq 2.5$.

In the case of CAI, its phase function clearly has a larger amplitude of oscillation compared to that of grains and chondrules phase functions. Its phase function shapes and levels are similar to those of the two most fluffy aggregates, Ag_DLA_Df1.7_-N74 and Ag_DLA_Df1.5_N74 (see Figure 3.61). This is incredibly surprising because CAI and the two most fluffy aggregates do not have the same bounding radius and the morphology is clearly different. Indeed, CAI is a compact grain (with a material packing density of $\rho = 0.19$), while these two aggregates have the largest porosities of all our aggregates (with $\rho = 0.01$ and 0.03).

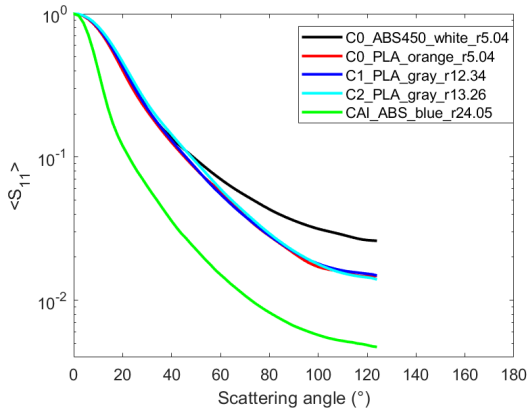

(a) Chondrules and CAI

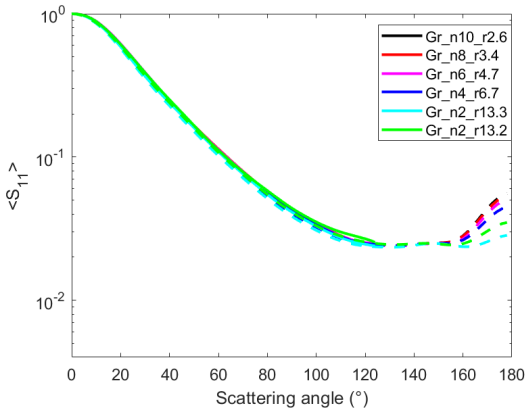

(b) Grains

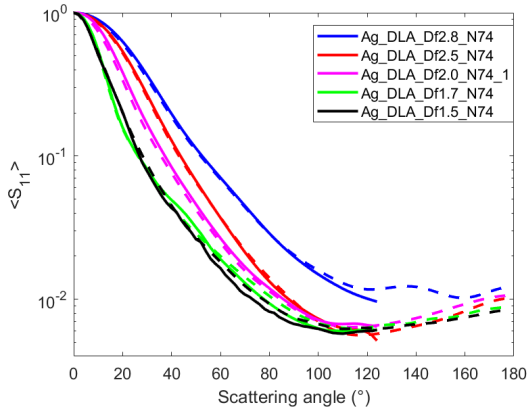

(c) Aggregates

Figure 3.59: Normalized phase function with power law distribution of $n_s = 3.5$, measurements (solid lines) and numerical simulations (dashed lines).

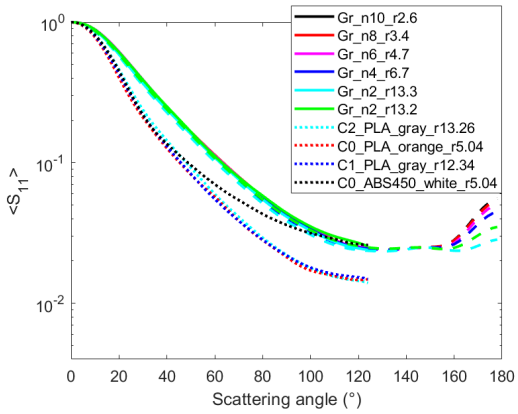

Figure 3.60: Normalized phase function comparison between grains and chondrules with power law distribution of $n_s = 3.5$, measurements of grains (solid lines), numerical simulations of grains (dashed lines) and measurements of chondrules (dotted lines).

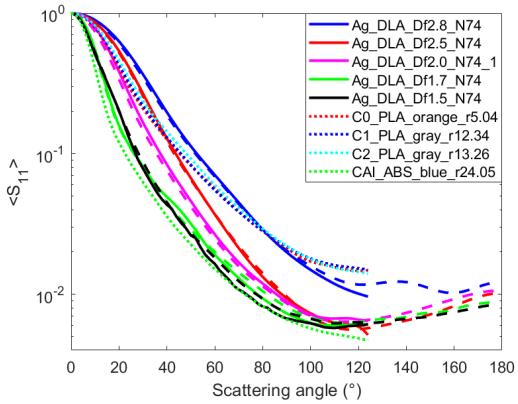

Figure 3.61: Normalized phase function comparison between aggregates, chondrules and CAI with power law distribution of $n_s = 3.5$, measurements of aggregates (solid lines), numerical simulations of aggregates (dashed lines) and measurements of chondrules and CAI (dotted lines).

In summary, based on the phase function, three groups of amplitudes of oscillations are identified: the first group with the smallest amplitudes is grains (or also the chondrule with larger refractive index, C0_ABS450_white_r5.04), the second group with larger amplitudes is chondrules (or also the most compact aggregate Ag_DLA_-Df2.8_N4), and the third group with the largest amplitude of oscillation is aggregates with $D_f \leq 2.5$ (or the CAI). I suggest to revise the backscattering phase function of chondrules and CAI to clarify if these phase functions are similar to that of the most compact aggregate and those of the two most fluffy aggregates, respectively.

Comparison of the degree of linear polarization of all three morphologies is presented in Figure 3.62. DLP maximum levels and forward DLP curves are similar between grains and chondrules (C0, C1 and C2 fabricated with PLA), see Figure 3.63 where DLP of these particles are superposed. In the case of the DLP of chondrule C0_ABS450_white_r5.04, its maximum level and curve shape do not resemble to the DLP of grains and chondrules, indeed its depolarization is larger due to its refractive index. In summary, there are no differences when comparing DLP of grains and that of chondrules (with similar refractive index). Additionally, maximum DLP levels of grains and those of chondrules are no larger than 0.2.

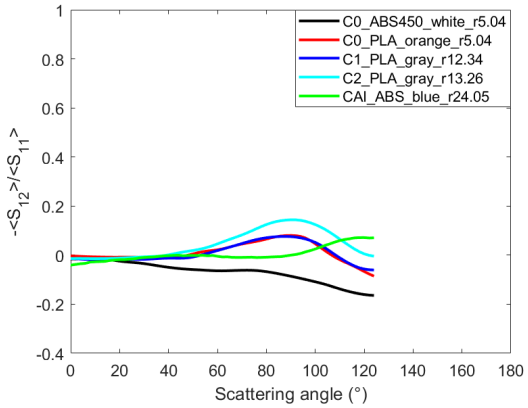

(a) Chondrules and CAI

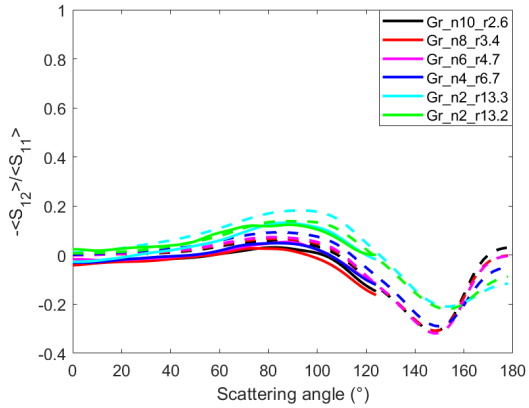

(b) Grains

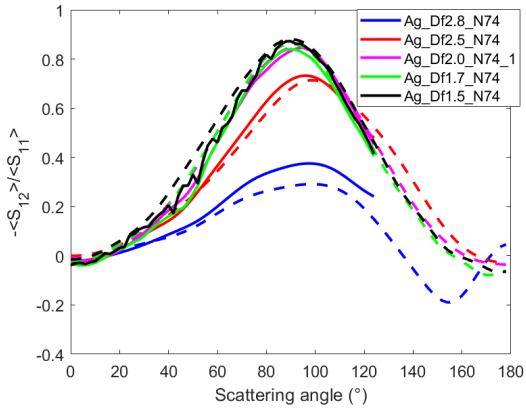

(c) Aggregates

Figure 3.62: DLP with power law distribution of $n_s = 3.5$, measurements (solid lines) and numerical simulations (dashed lines).

On the other hand, when comparing DLP of aggregates with the ones of chondrules and CAI (see Figure 3.64), there is a clear difference between these two types of morphologies. Indeed, aggregates have maximum DLP levels ranging from 0.3 (for the most compact Ag_DLA_Df2.8_N74) to 0.88 (for the most fluffy aggregate Ag_-

DLA_Df1.5_N74), while chondrules and CAI have maximum DLP no larger than 0.2. Additionally, DLP of CAI, presents a maximum DLP corresponding to scattering angles of 130°, while chondrules maximum DLP have scattering angles around 90°, thus the position of maximum DLP can be an element to distinguish between chondrules and CAI.

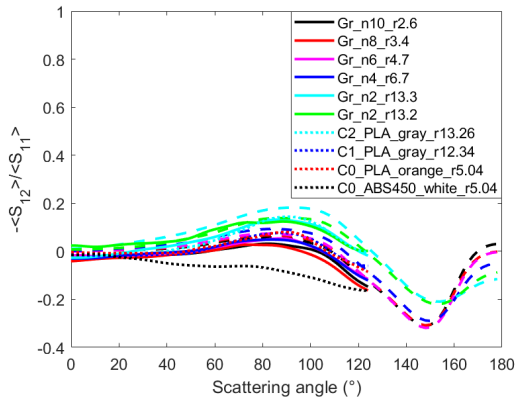

Figure 3.63: DLP comparison between grains and chondrules with power law distribution of $n_s = 3.5$, measurements of grains (solid lines), numerical simulations of grains (dashed lines) and measurements of chondrules (dotted lines).

Therefore, DLP is a good scattering parameter to distinguish between both families of grains, presenting lower maximum DLP levels, and aggregates with larger DLP levels. Moreover, this parameter presents a difference between all grains (grains and chondrules) and CAI with the corresponding scattering angles of maximum DLP. Finally, with DLP it is possible to differentiate between our compact aggregates and fluffier aggregates ($D_f \leq 2$) as already mentioned in Section 2.4.3.3.

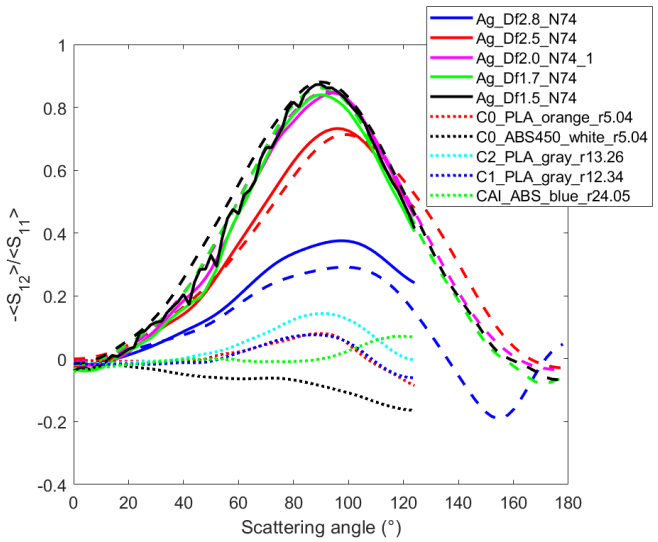

Figure 3.64: DLP comparison between aggregates, chondrules and CAI with power law distribution of $n_s = 3.5$, measurements of aggregates (solid lines), numerical simulations of aggregates (dashed lines) and measurements of chondrules and CAI (dotted lines).

The comparison of parameter $\frac{<S_{44}>}{<S_{11}>}$ for three morphologies is shown in Figure 3.65. $\frac{<S_{44}>}{<S_{11}>}$ of chondrules and CAI resembles to $\frac{<S_{44}>}{<S_{11}>}$ of grains (see Figure 3.66) with only slight differences of the curves of C0_ABS450_white_r5.04 around 50° and CAI_ABS_-blue_r24.05 around 100°. On the other hand, when comparing $\frac{<S_{44}>}{<S_{11}>}$ of aggregates with that of chondrules and CAI (see Figure 3.67), notice that $\frac{<S_{44}>}{<S_{11}>}$ of chondrules and CAI have similar levels and curve shapes to that of the most compact aggregate, contrary to that of aggregates with $D_f \leq 2.5$. In summary, based on this scattering parameter, both families of grains present similar $\frac{<S_{44}>}{<S_{11}>}$ behaviors as well as the most compact aggregate, contrary to that of aggregates with $D_f \leq 2.5$ where their behaviors tend more to Rayleigh-like curves.

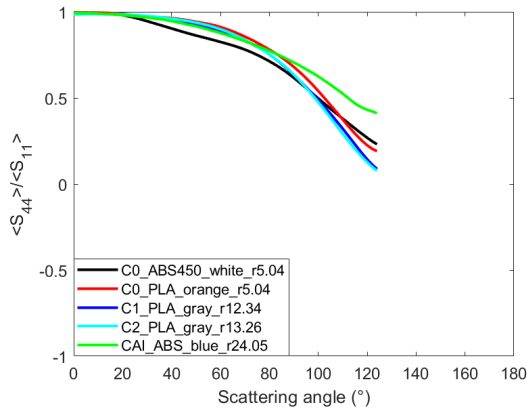

(a) Chondrules and CAI

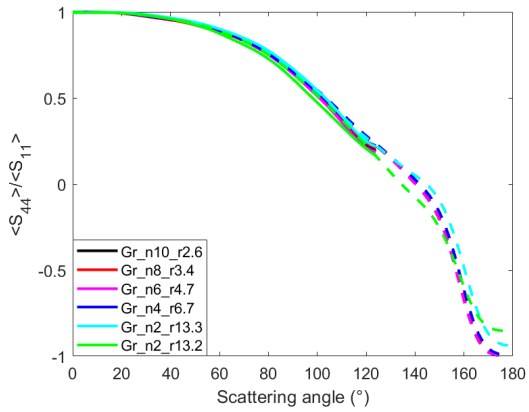

(b) Grains

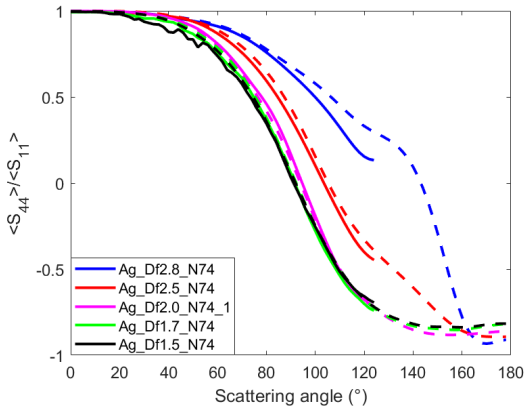

(c) Aggregates

Figure 3.65: $< S_{44} > / < S_{11} >$ with power law distribution of $n_s = 3.5$, measurements (solid lines) and numerical simulations (dashed lines).

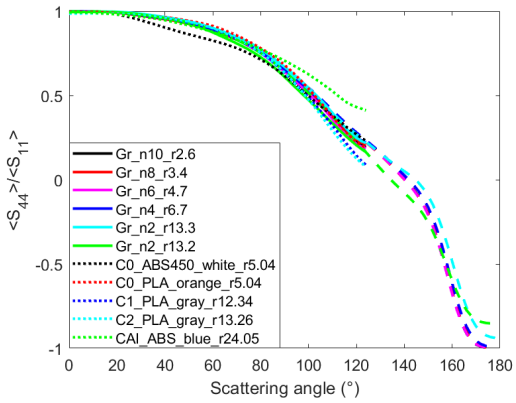

Figure 3.66: $< S_{44} > / < S_{11} >$ comparison between grains, chondrules and CAI with power law distribution of $n_s = 3.5$, measurements of grains (solid lines), numerical simulations of grains (dashed lines) and measurements of chondrules and CAI (dotted lines).

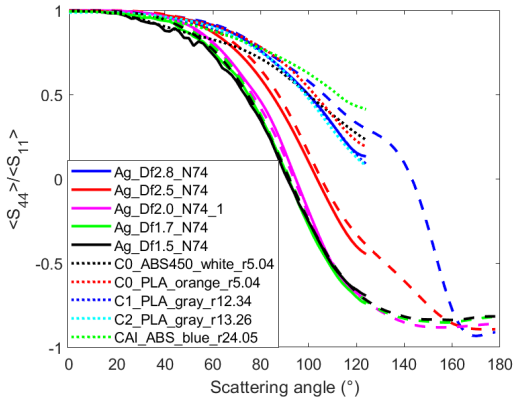

Figure 3.67: $< S_{44} > / < S_{11} >$ comparison between aggregates, chondrules and CAI with power law distribution of $n_s = 3.5$, measurements of aggregates (solid lines), numerical simulations of aggregates (dashed lines) and measurements of chondrules and CAI (dotted lines).

$\frac{<S_{34}>}{<S_{11}>}$ of all three morphologies is presented in Figure 3.68. This scattering parameter presents similar behaviors between chondrules C0, C1 and C2 made with PLA and grains (see Figure 3.69), having a forward positive oscillation from 0° to 120°. This forward positive oscillation is also seen for compact aggregates with $D_f \geq 2.5$ (see Figure 3.70). In the case of C0_ABS450_white_r5.04 and CAI_ABS_blue_r24.05, both present also this oscillation but for the chondrule there is an enhancement that starts at 110° possibly tending to form a peak in the backward zone at smaller scattering angles compared to grains. For the CAI, its oscillation rapidly decreases from 60°, having the lowest $\frac{<S_{34}>}{<S_{11}>}$ values of all particles. In the case of $\frac{<S_{34}>}{<S_{11}>}$ of fluffy aggregates

with $D_f \leq 2.0$, their curves do not present a forward positive oscillation, but a constant behavior with values around 0 all along the scattering angles. In brief, with $\frac{<S_{34}>}{<S_{11}>}$ three groups are identified: first group having forward positive oscillations for all grains, chondrules made of PLA and compact aggregates ($D_f \geq 2.5$); second group having almost linear behaviors around 0 (like Rayleigh scatterers) for fluffy aggregates; and third group having forward oscillations with discrepancies for C0_ABS450_white_r5.04 and CAI_ABS_blue_r24.05.

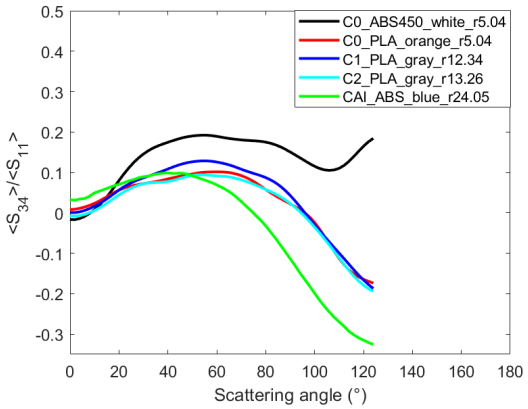

(a) Chondrules and CAI

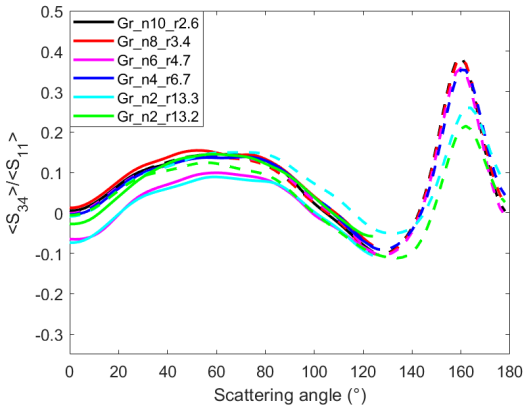

(b) Grains

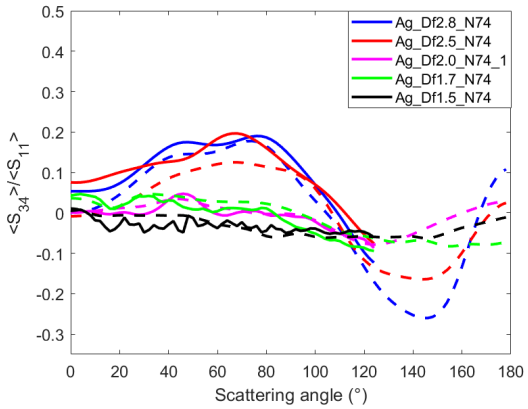

(c) Aggregates

Figure 3.68: $< S_{34} > / < S_{11} >$ with power law distribution of $n_s = 3.5$, measurements (solid lines) and numerical simulations (dashed lines).

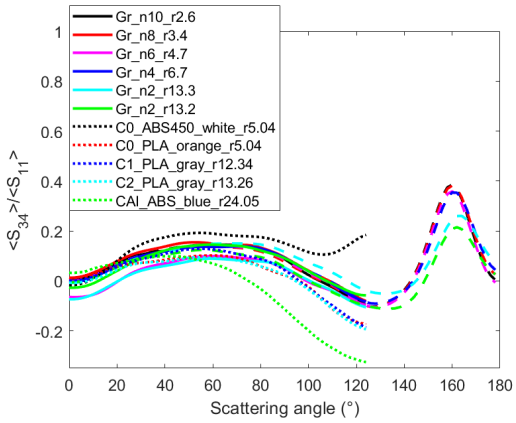

Figure 3.69: $< S_{34} > / < S_{11} >$ comparison between grains, chondrules and CAI with power law distribution of $n_s = 3.5$, measurements of grains (solid lines), numerical simulations of grains (dashed lines) and measurements of chondrules and CAI (dotted lines).

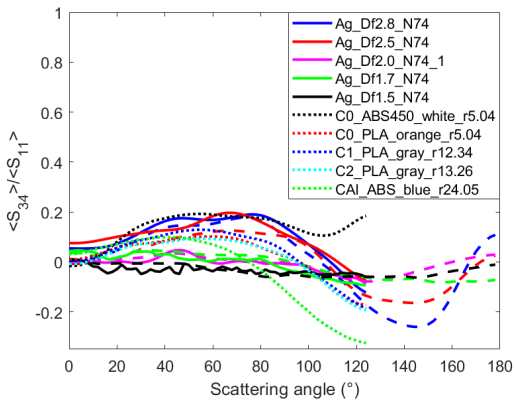

Figure 3.70: $< S_{34} > / < S_{11} >$ comparison between aggregates, chondrules and CAI with power law distribution of $n_s = 3.5$, measurements of aggregates (solid lines), numerical simulations of aggregates (dashed lines) and measurements of chondrules and CAI (dotted lines).

In conclusion, the scattering parameter with which we observe a finer differentiation between our three morphologies is DLP. We can identify morphologies with the levels of maximum DLP where fluffy aggregates ($D_f \leq 2.0$) have the highest maximum DLP levels, then the aggregate with $D_f = 2.5$ have the second highest level, followed by the aggregate with $D_f = 2.8$. Finally, both families of grains present the lowest maximum DLP levels of all three morphologies, where the CAI is identified by its characteristic angle position of maximum DLP around 130° while those of others grains are around 90°.

3.5.4 Direct comparison of scattering parameters found in literature

The aim of this section is to compare scattering properties of our chondrules and CAI with the ones found in literature, based on their scattering parameters. To our knowledge there are no laboratory measurements of scattering parameters of chondrules and CAI but of meteorites (chondrites) or minerals. Thereby, one first comparison with laboratory measurements of dust of chondrites is made with our chondrules and CAI. Then a second comparison with the phase function of the disk HR4796A (which is an optically thin disk where its phase function can be retrieved contrary to protoplanetary disks) is made with the phase functions of our chondrules and CAI, as was also made with the phase functions of our aggregates and first family of grains. The idea is to see if our scattering parameters approach to the ones found in literature to validate our measurements, identify which particles and n_s present closer scattering parameters and/or identify possible causes of their different scattering behaviors.

3.5.4.1 Laboratory measurements

Laboratory measurements of phase functions and DLP of four meteoritic dust samples and two silicate mineral samples were performed with light scattering measurements at $\lambda = 520\,\text{nm}$ [108]. The four meteorites were DaG521, FRO95002, FRO99040 and Allende with estimated refractive indices of $1.65+10^{-3}i$. The two mineral samples were forsterite (Mg-rich olivine) and enstatite with estimated refractive indices of $1.62 + 10^{-5}i$ and $1.58 + 10^{-5}i$, respectively. All six samples had mono-modal and bi-modal size distributions with effective radius no larger than tenths of µm, corresponding to size parameters between $X = 30$ to $X = 105$. In our case, chondrules and CAI have a power law size distribution effect and theirs size parameters are no larger than $X = 21.53$. Taking into account these differences between our particles and the ones in [108], lets us see if they present comparable scattering behaviors.

Phase functions comparison is presented in Figure 3.71. At large phase angles our CAI is the only one presenting the largest phase function levels from 175° to 135°, where its behavior has comparable values to those of chondrites DaG521, FRO95002, FRO99040 and Allende, and to minerals olivine and enstatite (all these samples are superposed). Notice that tholins phase function is not compared because of its low refractive index ($1.35 + 0.023i$). Then all these samples have phase function levels ranging between our chondrules C1_PLA, C2_PLA, C3_PLA and C0_ABS450_white_-r5.04 from 135° to 50°. This means, that our chondrules and CAI have comparable phase function levels and curve shapes to the ones presented in [108] from 175° to 50°.

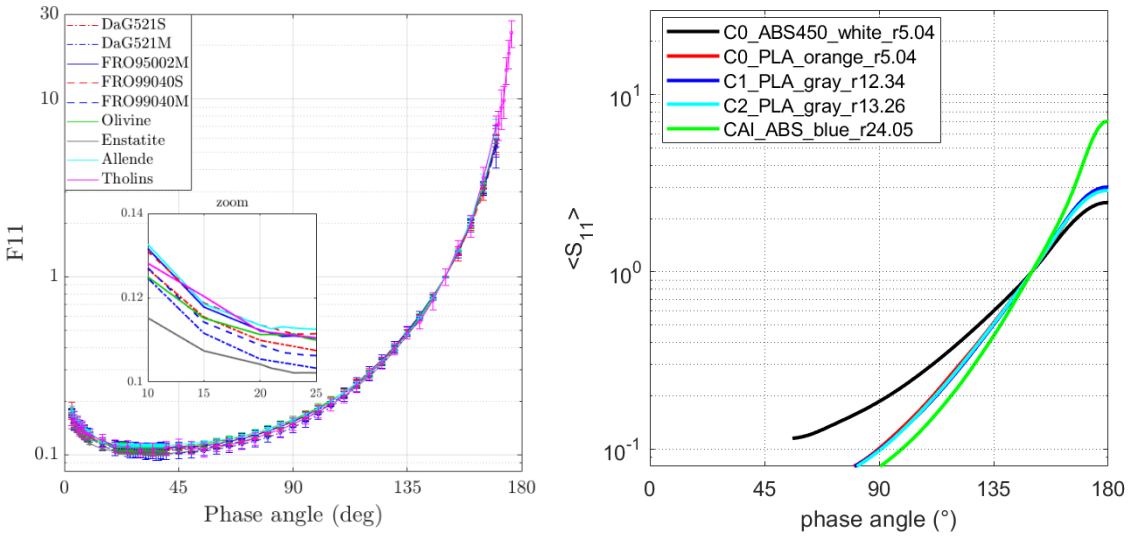

(a) Phase function taken from [108]

(b) Our phase function

Figure 3.71: Laboratory scattering measurement comparison of phase function normalized at a phase angle of 150°. (a) Phase function of chondrite and mineral samples [see Figure 4 in 108], (b) phase function of our chondrules and CAI with power law distribution effect of $n_s = 3.5$ for measurements (solid lines).

DLP comparison is presented in Figure 3.72. The levels of our maximum DLP are at the same orders of the ones presented in [108], except for chondrule C0_ABS450_-white_r5.04 which depolarizes more due to its large refractive index $(2.11 + 0.004i)$. Furthermore, the width of the DLP peak of our chondrules and CAI is narrower than the DLP width of the samples in [108], which could be caused by their different size parameters and size distribution. Indeed, our chondrules and CAI present this DLP shape when the size distribution has an index of $n_s = 5$, which means more weight to smaller particles that act as Rayleigh scatterers (see Figure 3.56.c).

Hence, our chondrules and CAI have comparable phase functions levels and curve shapes, as well as maximum DLP levels, compared to the samples presented in [108]. Scattering differences could be attributed to their different size distributions and size parameters.

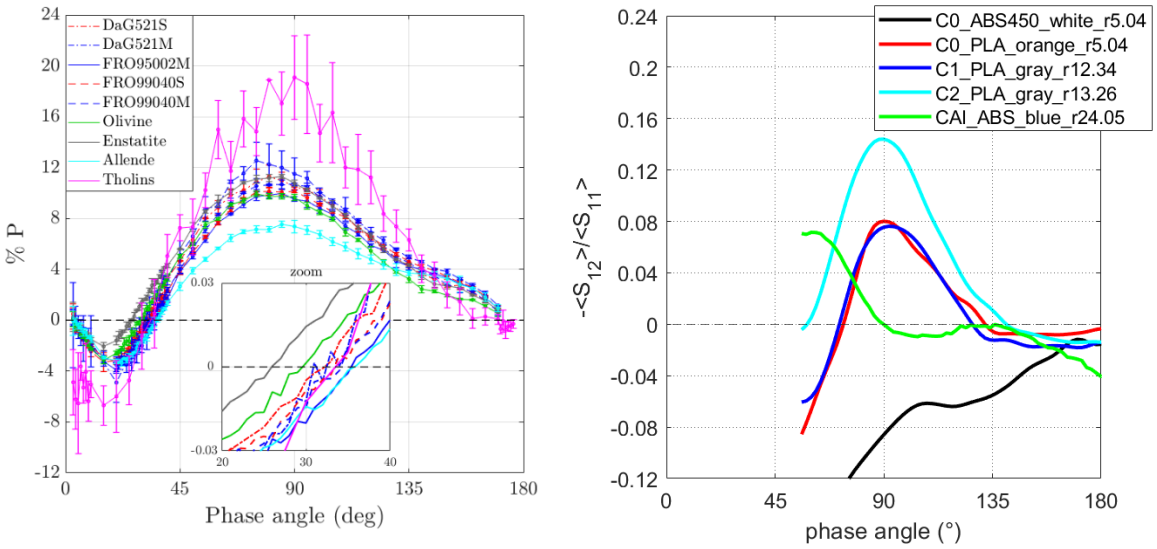

(a) Phase function taken from [108]

(b) Our phase function

Figure 3.72: Laboratory scattering measurement comparison of DLP. (a) DLP of chondrite and mineral samples [see Figure 5 in 108], (b) DLP of our chondrules and CAI with power law distribution effect of $n_s = 3.5$ for measurements (solid lines).

3.5.4.2 Observations

Phase function of disks HR4796A is shown in [78]. The comparison of its phase function with our chondrules and CAI phase function is shown in Figure 3.73. We chose to present the phase function with a size distribution index of $n_s = 2$ because it is when our particles present the narrowest forward scattering peak (as was explained in Section 3.5.3.2), thus the closest to the phase function of disks HR4796A. However, even when choosing the narrowest forward scattering phase function, our particles do not present similar phase functions to that of the disk. This was also the case for phase functions of our aggregates and our grains. In previous comparisons with aggregates and grains, I suggested to increment X. Herein CAI is the particle with the largest X and its forward phase function presents narrower widths with larger levels. This behavior was also seen for the phase function of the most fluffy aggregate in the comparison presented in Section 2.4.4.3. Thereby, future analogs could have the morphology of these two particles (CAI_ABS_blue_r24.05 and Ag_DLA_Df1.5_N74) but with larger X, and verify if they present phase functions closer to that of this disk.

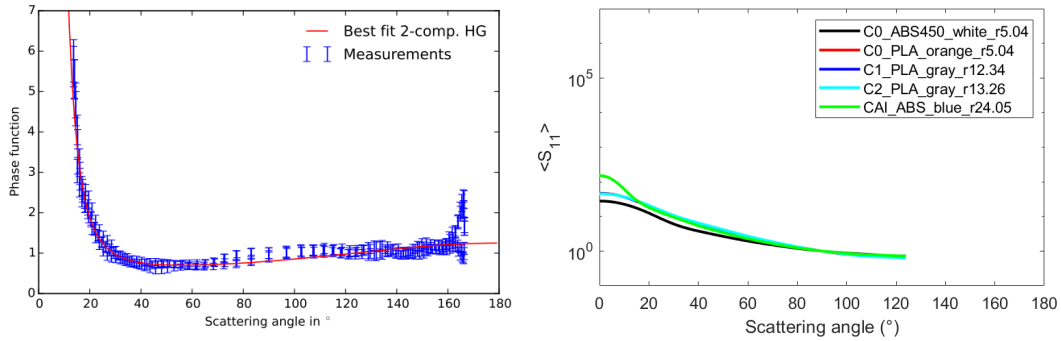

(a) Phase function taken from [78]

(b) Our phase function

Figure 3.73: Observational scattering comparison of phase function normalized at 90°. (a) Phase function of disk HR4796A [see Figure 17 in 78], (b) phase function of our chondrules and CAI with power law distribution effect of $n_s = 2$ for measurements (solid lines).

3.5.4.3 Conclusions

In conclusion, we obtain similar scattering behaviors compared to other laboratory measurements, validating the phase function and DLP retrieved for our chondrules and CAI. It is suggested that the differences found herein are due to their different size parameter and size distribution. Note that our size distribution can be changed in the future using the same scattering data. Thus, if in the future the comparison wants to be more precise, changing the size distribution effect can be an option. Moreover, the comparison with the disk phase function showed that our chondrules presented very low levels with a wider forward scattering peak of the phase function. The only particle presenting a larger phase function level was the CAI, leading to the idea of using this morphology for future measurements but with larger X in order to narrow even more the forward scattering peak and increment its level. The CAI phase function has almost the same behavior as the aggregate Ag_DLA_Df1.5_N74, hence its is also suggested to explore this morphology, increasing X, to obtain phase function behaviors closer to those retrieved for the phase function of this disk.

3.6 Conclusions

In this chapter, scattering properties of two families of grains were studied based on their scattering parameters retrieved with our microwave scattering measurements and numerical simulations. The first family of grains was fabricated with controlled synthetic roughness and then 3D printed with stereolithography. After verifying the setup parameters, five scattering parameters of these grains were retrieved: phase function, DLP, $\frac{<S_{22}>}{<S_{11}>}$, $\frac{<S_{34}>}{<S_{11}>}$ and $\frac{<S_{44}>}{<S_{11}>}$. Two types of studies were performed. First, a study on the scattering parameters averaged over several orientations of grains at

different wavelengths, corresponding to different size parameters of grains. Among all the scattering parameters, DLP proved to be a good indicator of the grains roughness. Indeed as roughness decreased (sphericity increased) the amplitude of DLP oscillations increased. Moreover, $\frac{<S_{22}>}{<S_{11}>}$ provided complementary information on the morphology of our grains, specifically their sphericity which was related with its levels, where values around 1 were the most spherical grains and as these levels decreased their sphericity decreased too.

A second study was focused on using the same grain scattering parameters but including a power law size distribution effect. Three power law indices were used, $n_s = 2$, 3.5 and 5. From all five scattering parameters (with all three n_s), three of them presented characteristic behaviors related to roughness and sphericity, thus morphology of grains. First, phase function presented ordered backscattering enhancements related to grains roughness. Second, maximum DLP and negative polarization branches presented levels that were correlated to the grains roughness. Third, $\frac{<S_{22}>}{<S_{11}>}$ levels were again related to the sphericity and to the material packing density (gave notion of elongated grains). Finally, comparisons of the phase function and DLP with the ones found in literature of similar morphologies validated our two scattering parameters. Our grains presented similar scattering behaviors as the ones of laboratory measurements and numerical simulations, and when scattering parameters did not have similar behaviors, the reasons behind were understood. Phase functions comparisons between our grains and disks HR4796A and Fomalhaut proved that, in order to obtain similar phase functions to these disks, our grains size parameters should be increased as well as the real part of refractive indices (for example with inclusions of amorphous carbon which is a possible material that can be found in protoplanetary disks).

The second family of grains, chondrules and CAI, was fabricated based on X-ray computed tomography on a chondrite, scaled and then 3D printed with fused filament fabrication. These analogs were only measured due to their natural because the size of the virtual mesh to perform the numerical simulations still raises an unsolved question: how small the size of the FEM mesh need to be without having any impact on their scattering parameters? Thereby, scattering parameters were only obtained based on our microwave scattering measurements from 0° to 130°. Four scattering parameters were retrieved: phase function, DLP, $\frac{<S_{34}>}{<S_{11}>}$ and $\frac{<S_{44}>}{<S_{11}>}$. The same two studies as for the first family of grains were performed. First, scattering parameters averaged over several orientations of chondrules and CAI at different wavelengths (or size parameters). Herein, DLP showed to be the best scattering parameter to identify between our different chondrules and CAI, where the amplitudes of oscillations were related to their depolarization and therefore to their roughness (or sphericity). Furthermore, these four scattering parameters were compared to the scattering parameters of aggregates and the first family of grains. It was found that chondrules and grains had very similar scattering parameters (phase function, DLP, $\frac{<S_{34}>}{<S_{11}>}$ and $\frac{<S_{44}>}{<S_{11}>}$), yet $\frac{<S_{44}>}{<S_{11}>}$ was proved to be the most sensitive parameter presenting the greatest differences between chondrules, CAI, grains, fluffy aggregates ($D_f \leq 2.0$) and compact aggregates

($D_f > 2.0$).

In the second study the same four scattering parameters were retrieved with a size distribution. DLP and $\frac{<S_{44}>}{<S_{11}>}$ were sensitive to the roughness (or sphericity) of our chondrules, presenting organized levels related to the percentage of their roughness. Moreover, at $n_s = 3.5$ and $n_s = 5$, the corresponding scattering angles of the maximum DLP of chondrules and CAI were different. Chondrules had scattering angles of maximum DLP around 90° to 100°, while CAI had scattering angles larger than 115°. Furthermore, within this second study, comparisons of the scattering properties of the three morphologies (aggregates, first and second family of grains) were made based on their scattering parameters, using a power law index of $n_s = 3.5$. DLP was the best scattering parameter presenting the largest differences within all three morphologies. Indeed, thanks to DLP we were able to identify fluffy aggregates ($D_f \leq 2.0$) with the highest maximum DLP levels (0.88), followed by the aggregate with $D_f = 2.5$ (0.7), then aggregate with $D_f = 2.8$ (0.3) and finally both families of grains with maximum levels no larger than 0.2. Finally, comparisons of scattering parameters of our chondrules and CAI with scattering parameters found in literature with similar morphologies were made. The comparison with scattering parameters from laboratory measurements showed similar phase function behaviors to those of our chondrules and CAI, and similar maximum DLP levels. Differences in the width of DLP peak were suggested to be caused by their different size parameters and distributions. Thus, we validated our scattering parameters and understood their differences with the ones presented in literature. In the case of the phase function comparison with the disk HR4796A, I suggested to continue with two potential morphologies, Ag_DLA_Df1.5_N74 and CAI_ABS_blue_r24.05, that had the largest levels and the narrowest forward peaks of all our particles. If the size parameter of these two particles is incremented, then higher phase function levels and narrower peaks can be retrieved, obtaining phase functions closer to that of the disk.

Based on this second family of grains, I recommended to performed scattering measurements in the backscattering in order to complete the different scattering parameters and analysis. This could help to answer questions such as: are the scattering parameters of this second family of grains similar to those of the first family of grains in the backscattering? Can we generalize the behavior of the scattering parameters of both families of grains? Finally, future works need to change the 3D printing material for our CAI to have a closer refractive index to real CAI [185, 186]. It is suggested to use materials as preperm (PPE320), having a real refractive index of $n = 1.79$.

General conclusions and perspectives

This PhD thesis consisted in studying the scattering properties of protoplanetary dust analogs using laboratory measurements, i.e. microwave scattering measurements, and numerical simulations, i.e. finite element methods. The studied scattering parameters were the phase function, the degree of linear polarization (DLP) and other Mueller matrix elements. These scattering parameters were studied in the Mie scattering range. The scattering measurements were performed in the anechoic chamber of CCRM using 3D printed analogs with three different morphologies, e.g. fractal aggregates, and two families of compact rough grains. Therefore, the aim of this thesis was to explore the scattering properties of possible morphologies of dust that could be found in protoplanetary disks in order to give insights to understand the scattered light observations of these disks.

Our dust analogs were geometrically controlled thanks to two different additive manufacturing processes, i.e. stereolithography and fused filament fabrication. Moreover, their refractive indices were selected to have similar values as the astronomical silicate (Draine and Lee silicate [14]). Their sizes were chosen to have a similar size proportion as protoplanetary dust compared to the used wavelengths to do observations (specifically optical and NIR wavelengths). In this way, the control of the size proportion and the refractive index reproduced similar scattering behaviors as real dust with our laboratory measurements, thanks to the scale invariance rule of the Maxwell equations. Additionally, our scattering experiment allowed a complete control of the orientation of the measured analogs in the scattering plane. Hence, the control of geometry, refractive index and orientation of all our analogs provided unique scattering measurements, giving clues to interpret their morphologies based on their scattering parameters in the Mie scattering range.

1. The first morphology, fractal aggregates, was studied with seven different aggregates, having fractal dimensions ranging from $D_f = 1.5$ to $D_f = 2.8$. The size parameters of these aggregates were between $X_{agg} = 1$ to $X_{agg} = 20$ and monomers between $X_{mon} = 0.17$ to $X_{mon} = 1.04$. Five scattering parameters were retrieved for this first morphology: the phase function, DLP, $\frac{<S_{22}>}{<S_{11}>}$, $\frac{<S_{34}>}{<S_{11}>}$ and $\frac{<S_{44}>}{<S_{11}>}$. Three studies were performed based on these scattering parameters.
    - The first study consisted in obtaining and analyzing scattering parameters that were averaged over several orientations of the aggregates at different wavelengths, thus at different size parameters. The change on this

size parameter X_{mon}, proved that the scattering parameters of fluffy aggregates ($D_f \leq 2.0$) behaved as Rayleigh-like scatterers while compact aggregates ($D_f > 2.0$) behaved as pseudo-spheres, this was seen with the phase function and DLP, and validated with $\frac{<S_{34}>}{<S_{11}>}$ and $\frac{<S_{44}>}{<S_{11}>}$. On the contrary, $\frac{<S_{22}>}{<S_{11}>}$ gave a finer distinction between the different fractal dimensions at $X_{mon} = 0.35$, allowing to identify fluffy aggregates ($D_f \leq 1.7$) from intermediate aggregates ($D_f \leq 2.5$) and from compact aggregates ($D_f = 2.8$).

- The second study was focused on retrieving the same scattering parameters of these aggregates including a power-law size distribution. Herein, three indices of the power-law were used, $n_s = 3.5$ used for protoplanetary dust, and two others around this value to study the effect on the scattering parameters, $n_s = 2$ and $n_s = 5$. Among all five scattering parameters, it was shown that DLP and $\frac{<S_{22}>}{<S_{11}>}$ are the two most promising parameters to study aggregates with protoplanetary light scattered observations. In fact, these parameters are not affected by the number of monomers that aggregates can contain, instead, they are completely related to sphericity and coupling between monomers, thus to the morphology of the aggregate.
- The third study consisted in determining the fractal dimension based on the aggregates phase function represented in q-space. Different methods found in literature were applied on our phase functions to find the slope and thereby D_f. Furthermore, a novel method to determine D_f was proposed, based on the Butterworth filter function. The most promising method to find D_f with our aggregates phase function was the Butterworth method where two functions to relate the measured slope and D_f were retrieved, $g(n)$ and $G(n)$. Future works need to validate these two functions applying them to larger number of data cases. This latter with the purpose of confirming the effectiveness of the proposed Butterworth filter modeling approach. Additionally, increasing the number of monomers is also suggested for future aggregates in order to increase their fractality. This increase will possibly reduce the phase function oscillations, allowing an easier determination of the slope and therefore of D_f.

2. The second morphology, grains with controlled synthetic roughness, was studied with six grains having different percentages of roughness from 2.6% to 13.3%. The size parameters of these grains were between $X = 1.07$ to $X = 7.73$. The same two first studies, as for aggregates, were performed, retrieving the same five scattering parameters.

    - For the first study (at different size parameters), the DLP was proved to be a good indicator of the grains roughness (or sphericity), thus morphology, based on its amplitude of oscillation. In addition, $\frac{<S_{22}>}{<S_{11}>}$ gave extra information on the grains morphology, by its levels that were organized and related to the sphericity of grains.

- For the second study (including a size distribution), three scattering parameters showed characteristic behaviors related to the roughness and the sphericity of grains: i) the backscattering enhancement of phase function, ii) the maximum DLP levels and negative polarization branch and iii) levels of $\frac{<S_{22}>}{<S_{11}>}$.

3. The third morphology, also consisted on grains but with natural roughness extracted from a X-ray tomography of a chondrite, obtaining three chondrule structures and one CAI structure. The percentage of roughness of this second family of grains ranged from 5.04% to 24.05% and the size parameter from $X = 1.03$ to $X = 21.53$. Four scattering parameters were retrieved in the forward scattering zone of our experimental setup: phase function, DLP, $\frac{<S_{34}>}{<S_{11}>}$ and $\frac{<S_{44}>}{<S_{11}>}$.
   - Based on the first study (scattering parameters retrieved at different X), DLP proved to be the best parameter to differentiate within chondrules and CAI, where its amplitude of oscillations were related to depolarization and roughness (or sphericity).
   - In the second study (including a size distribution), DLP and $\frac{<S_{44}>}{<S_{11}>}$ showed organized levels related to the percentage of chondrules roughness. Additionally, the differentiation between chondrules and CAI structures was possible thanks to the corresponding scattering angles of their maximum DLP. Indeed, chondrules had scattering angles around 90° to 100° while CAI had scattering angles larger than 115° (for $n_s = 3.5$ and $n_s = 5$). Notice that future works of scattering measurements at backscattering angles of chondrules and CAI are necessary, in order to complete their scattering analysis, and study: their phase function backscattering enhancement, negative polarization branch and possible peak of $\frac{<S_{34}>}{<S_{11}>}$ at 160° (as the first family of grains presented). This backscattering study will also help to verify if the scattering parameter behaviors of chondrules can be generalized with the first family of grains (irregular grains with controlled roughness). Indeed, after applying the size distribution, these two morphologies presented similar forward DLP and $\frac{<S_{44}>}{<S_{11}>}$, and only slight differences were identified for the phase function and $\frac{<S_{34}>}{<S_{11}>}$. One last prospect is to measure other CAIs to see if the observed scattering properties were unique for our CAI or if other CAIs present the same particular scattering behavior. Additionally, future works need to change the material for our CAI to have a closer refractive index to real CAI [186]. It is suggested to use materials as preperm (PPE320) to 3D print future CAI analogs having a real refractive index of 1.79.

After retrieving the scattering parameters of all three morphologies, their scattering parameters were compared with the aim to identify which scattering parameter presented the finest differentiation between these morphologies. When the comparison was made with their scattering parameters at different X, chondrules and the first family of grains presented similar scattering properties. Yet, based on $\frac{<S_{44}>}{<S_{11}>}$, we found

characteristic behaviors for each morphology: i) $\frac{<S_{44}>}{<S_{11}>}$ of rough particles (both grain families) started oscillating at 20°, while that of aggregates started at 60°, ii) $\frac{<S_{44}>}{<S_{11}>}$ of chondrules had damped oscillations compared to that of the first family of grains, and iii) $\frac{<S_{44}>}{<S_{11}>}$ of compact aggregates had oscillations from 60° to backscattering angles, while that of fluffy aggregates did not oscillate. When the comparison was performed with scattering parameters including the size distribution of index $n_s = 3.5$, another parameter showed the largest differences, DLP. Maximum DLP levels proved to distinguish between fluffy aggregates having the highest maximum DLP levels, followed by the maximum DLP levels of the two most compact aggregates and lastly by both families of grains with the lowest maximum DLP levels (without any distinction between both grain families). Based on this study, future works should be more focused on DLP because it could give insights on which morphology is predominant in protoplanetary disks thanks to its capacity to differentiate between aggregates and grains, compared to the other scattering parameters.

Finally, the scattering parameters of all three morphologies were compared to the scattering parameters of similar morphologies found in literature. Based on scattering parameters retrieved with laboratory measurements and numerical simulations, certain scattering parameters of our analogs were validated, in most of the cases the phase function and DLP. Indeed, other scattering parameters are harder to find in literature with similar morphologies and refractive indices as the ones used in this thesis. Therefore, the validation of certain scattering parameters was possible and when differences were found, the reasons behind were discussed. Lastly, the phase functions of all three morphologies were compared to the phase function of disk HR4796A. None of our three morphologies had the narrowness of the forward scattering peak and backscattering enhancement of the phase function that this debris disk presented. In order to obtain these two characteristics of the phase function, it is suggested in the future to increase the size parameter of our analogs (around $X = 100$) and to increase the refractive indices which can be done with inclusions of amorphous carbon (this material is highly likely to be found in circumstellar disks). These two properties can be achieved by using fused filament fabrication. This 3D printing technique has more possibilities in terms of printable materials and larger dimensions of printable objects, compared to stereolithography. Moreover, to obtain even larger size parameters, our microwave scattering experiment can be used at wavelengths up to 7.5mm (40GHz), thus it is suggested to perform future measurements with smaller λ to increase X. Additionally, our most fluffy aggregate ($D_f = 1.5$) and CAI presented the narrowest peak and the highest phase function levels, which are characteristics found in the phase functions of disks HR4796A and Fomalhaut. Thus, these two morphologies are suggested to be studied including the increment on X and on the refractive index, as previously mentioned, in order to increase even more their phase function levels and narrow their forward scattering peak.

To achieve the final goal of the project in which this PhD thesis worked in, the scat-

tering parameters or Mueller matrix elements retrieved herein will be used as inputs of a 3D radiative transfer code. This with the objective to generate synthetic light scattered images of protoplanetary disks based on our analogs scattering parameters. After the obtention of such synthetic images, they will be compared with observations of protoplanetary disks, giving insights on which of the three morphologies generates the closest synthetic images to observations.

Our papers

J-B. Renard, J-M. Geffrin, V. Tobon Valencia, et al. “Number of independent measurements required to obtain reliable mean scattering properties of irregular particles having a small size parameter, using microwave analogy measurements”. In: *Journal of Quantitative Spectroscopy and Radiative Transfer* 272 (2021). ISSN: 00224073. DOI: 10.1016/j.jqsrt.2021.107718. URL: https://doi.org/10.1016/j.jqsrt.2021.107718

Journal of Quantitative Spectroscopy & Radiative Transfer 272 (2021) 107718

Contents lists available at ScienceDirect

Journal of Quantitative Spectroscopy & Radiative Transfer

journal homepage: www.elsevier.com/locate/jqsrt

Number of independent measurements required to obtain reliable mean scattering properties of irregular particles having a small size parameter, using microwave analogy measurements

Jean-Baptiste Renard[a,*], Jean-Michel Geffrin[b], Vanesa Tobon Valencia[b], Hervé Tortel[b], François Ménard[c], Pascal Rannou[d], Julien Milli[c], Gwenaël Berthet[a]

[a] LPC2E, CNRS - Université d'Orléans - CNES, Orléans, France
[b] Aix Marseille Université, CNRS, Centrale Marseille, Institut Fresnel, Marseille, France
[c] Université Grenoble Alpes, CNRS, IPAG, Grenoble, France
[d] GSMA - Université de Reims, Reims, France

ARTICLE INFO

Article history:
Received 18 February 2021
Revised 26 April 2021
Accepted 26 April 2021
Available online 26 May 2021

ABSTRACT

Laboratory measurements of light scattered by a cloud of randomly oriented levitating particles are often used to interpret remote sensing measurements of dust in space and in Earth's atmosphere. It is necessary to know how many particles or how many different orientations of the same particles must be considered to retrieve the mean scattering function of brightness and polarization. New laboratory measurements were conducted using the microwave analogy method between frequencies of 3 to 18 GHz, where an "analog" particle with a small size parameter in a range of 0.5-12 will have a size of several cm. Twelve such "analog" particles from compact shapes to aggregates with small fractal dimensions were fabricated by additive manufacturing (3D printing) and were studied. The number of necessary measurements to reach the mean scattering properties of a particle with an accuracy of about 5% is obtained for less than 20 different orientations. To reach a 1.5% (1-σ) error in brightness and a 0.5% (1-σ) error in polarization, the number of necessary measurements is in a range of 20 to 70, depending on the shape, fluffiness, deviation from a perfect sphere, and surface irregularities of the particle. These results show that several tens of randomly oriented particles of the same size are sufficient to retrieve the mean light scattering properties. Also, several tens of orientations of the same particles provide mean scattering properties, compared to modelling calculations using the Finite Element Method, for an aggregate composed of identical monomers.

1. Introduction

Laboratory measurements of light scattered by a cloud of irregular particles are necessary to interpret the brightness and polarization remote sensing measurements of comets, interplanetary dust cloud, and circumstellar material orbiting stars, e.g., protoplanetary and debris disks. Such comparisons are conducted to retrieve bulk physical properties of particles such as composition, size distribution, albedo, and porosity [1–6]. The analyses often assume that the observed particles are randomly oriented inside the cloud, as well as during the reference laboratory measurements. On the opposite, the possible orientation of grains, like in a gas flow or in case of strong magnetic field [7], can modify the scattering properties of an ensemble of particles. Such changes have been shown by [8] during laboratory measurements where the particles were carried and aligned by an airflow, and thus are not considered in this work.

Several databases of laboratory measurements provide optical properties (phase or scattering functions in intensity and in polarization) of levitating particles having the same size and composition, obtained by different techniques at ground or during microgravity conditions [9–14]. Such experiments, for particles having small to large size parameters ($\pi D/\lambda$, where D is the diameter and λ is the wavelength), assume that indeed they are randomly oriented and that enough particles are considered during the measurements, from tens to hundreds or thousands, to retrieve the mean optical properties. As an example, 54 different orientations of the same millimetre-sized particle have been considered by [5] to retrieve the mean scattering properties. Nevertheless, the authors have not quantified in detail how many particles with dif-

* Corresponding author.
E-mail address: jbrenard@cnrs-orleans.fr (J.-B. Renard).

https://doi.org/10.1016/j.jqsrt.2021.107718
0022-4073/

V. Tobon Valencia, J-M. Geffrin, F. Ménard, et al. “Scattering properties of protoplanetary dust analogs with microwave analogy : Aggregates of fractal dimensions from 1.5 to 2.8”. In: *Astronomy and Astrophysics* (accepted) (2022). DOI: 10.1051/0004-6361/202142656

Astronomy & Astrophysics manuscript no. output
August 26, 2022

Scattering properties of protoplanetary dust analogs with microwave analogy: Aggregates of fractal dimensions from 1.5 to 2.8

Vanesa Tobon Valencia[1], Jean-Michel Geffrin[1], François Ménard[2], Julien Milli[2], Jean-Baptiste Renard[3], Hervé Tortel[1], Christelle Eyraud[1], Amélie Litman[1], Pascal Rannou[4], Azar Maalouf[5], and Vincent Laur[5]

[1] Aix Marseille Univ, CNRS, Centrale Marseille, Institut Fresnel, Marseille, France
[2] Univ. Grenoble Alpes, CNRS, IPAG, 38000 Grenoble, France
[3] LPC2E, Université d'Orléans, CNRS, Orléans, France
[4] GSMA, Université de Reims, CNRS, Reims, France
[5] Lab-STICC, Université de Brest, CNRS, Brest, France

Received 12 November 2021/ Accepted 14 June 2022

ABSTRACT

Context. The growth of dust grains in protoplanetary disks is not understood in detail. Several studies have proposed the presence of aggregates and irregular grains to overcome the physical barriers in grain growth models. In order to understand the scattering properties of these aggregates, laboratory measurements of light scattering and microwave scattering have been developed over the last 50 years.
Aims. We aim to measure the scattering properties of different protoplanetary analog aggregates with fractal dimensions of 1.5, 1.7, 2.0, 2.5, and 2.8.
Methods. We used the microwave scattering technique (microwave analogy) for the measurements. The analog particles were virtually generated and fabricated by 3D printing with a controlled size (scaling factor), geometry, and refractive index. The seven analogs were measured at wavelengths ranging from 16.7 mm to 100 mm, leading to aggregate size parameters ranging from $X_{agg} = 1$ to $X_{agg} = 20$. The results were compared to finite element method calculations of the same analogs for cross-validation.
Results. The phase function and the degree of linear polarization were deduced from the scattered field measurements of the different aggregates. These scattering properties are compared and discussed as a function of the fractal dimension.
Conclusions. The scattering properties of aggregates with different fractal dimensions are different. Three different realizations of aggregates with the same fractal dimension but different monomer configurations yield the same phase functions. We verified that the maximum degree of linear polarization is higher for porous aggregates than for compact aggregates. Furthermore, the maximum polarization occurs at larger scattering angles for high fractal dimensions, while the half width at half maximum of the phase functions present larger values for small fractal dimensions.

Key words. Protoplanetary dust–scattering – microwave analogy – fractal dimension – aggregates – phase function – degree of linear polarization

1. Introduction

The processes by which dust grains from the interstellar medium evolve during the collapse of a molecular cloud and grow in a protoplanetary disk to form pebbles, boulders, and finally planetesimals or planets, are still subject to many open questions (see Testi et al. 2014, for a review). Several theoretical scenarios are proposed to overcome the physical barriers to grain growth, and many are tested in laboratory experiments (see Blum 2018, for a review). Fractal aggregates and irregular solid grains have been proposed as the outcome of the dust growth process and their presence was confirmed by the observations of cometary dust in the Solar System (e.g., Fulle & Blum 2017; Güttler et al. 2019, based on recent results from the Rosetta and previous missions). However, observational evidence for complex particles in protoplanetary disks is still missing, despite tremendous progress in high-angular resolution instruments in the (sub)millimeter, near-infrared, and optical wavelengths. Indeed, sensitive panchromatic observations of disks at high-angular resolution are now routinely produced by facilities such as ALMA, SPHERE, and GPI, but most interpretations do not consider aggregates and still rely on compact spherical particles. As a first step to providing more realistic tools to interpret protoplanetary disk observations and study grain growth in those disks, this paper presents a study of the scattering properties of small fractal dust aggregates made of 74 monomers.

Apart from their refractive index, aggregates are characterized by their porosity and their fractal dimension D_f as these two parameters are closely related Bertini et al. (2009). The fractal dimension D_f ranges from one for a very fluffy or porous particle, to three for a compact sphere. The size parameter $X_{agg} = 2\pi R_m/\lambda$ is another important descriptive parameter, where R_m is the radius of the sphere enclosing the aggregate and λ is the incident wavelength. These aggregate characteristics will directly influence their optical properties such as their scattering cross-sections, phase function, asymmetry parameter, degree of polarization, and albedo.

Laboratory experiments to characterize the scattering properties of aggregates have been carried out since the 1970s to

Bibliography

[1] J. B. Pollack, O. Hubickyj, P. Bodenheimer, et al. “Formation of the giant planets by concurrent accretion of solids and gas”. In: *Icarus* 124 (1996), pp. 62–85. ISSN: 00191035. DOI: 10.1006/icar.1996.0190 (cit. on pp. 25, 28, 45).

[2] W. K. M. Rice and P. J. Armitage. “On the formation timescale and core masses of gas giant planets”. In: *The astrophysical Journal* 598 (2003), pp. 55–58 (cit. on pp. 25, 28, 45).

[3] A. C. Boley, M. A. Morris, and E. B. Ford. “Overcoming the meter barrier and the formation of systems with tightly packed inner planets (STIPs)”. In: *Astrophysical Journal Letters* 792.2 (2014), pp. 1–4. ISSN: 20418213. DOI: 10.1088/2041-8205/792/2/L27 (cit. on pp. 25, 28, 52).

[4] M. Ollivier, T. Encrenaz, F. Roques, et al. *Planetary Systems: Detection, Formation and Habitability of Extrasolar Planets (Astronomy And Astrophysics Library)*. Berlin: Springer Berlin Heidelberg, 2009. ISBN: 978-3-540-75747-4. DOI: 10.1007/978-3-540-75748-1 (cit. on pp. 25, 28, 42).

[5] S. Arakawa and T. Nakamoto. “Rocky Planetesimal Formation Via Fluffy Aggregates of Nanograins”. In: *The Astrophysical Journal Letters* 832.2 (2016), pp. 1–5. ISSN: 20418213. DOI: 10.3847/2041-8205/832/2/l19. arXiv: 1611.03859. URL: http://dx.doi.org/10.3847/2041-8205/832/2/L19 (cit. on p. 25).

[6] M. Min, J. W. Hovenier, and A. De Koter. “Modeling optical properties of cosmic dust grains using a distribution of hollow spheres”. In: 920 (2005), pp. 909–920 (cit. on pp. 25, 28, 153).

[7] F. Kirchschlager and G. H. M. Bertrang. “Self-scattering of non-spherical dust grains”. In: *Astronomy Astrophysics* 638 (2020), pp. 1–11. ISSN: 0004-6361. DOI: 10.1051/0004-6361/202037943. arXiv: 2004.13742 (cit. on pp. 25, 28, 173).

[8] O. Muñoz, F. Moreno, D. Guirado, et al. “Experimental determination of scattering matrices of dust particles at visible wavelengths: The IAA light scattering apparatus”. In: *Journal of Quantitative Spectroscopy and Radiative Transfer* 111.1 (2010), pp. 187–196. ISSN: 00224073. DOI: 10.1016/j.jqsrt.2009.06.011 (cit. on pp. 25, 29, 78, 103).

[9] O. Muñoz, F. Moreno, J. C. Gómez-Martín, et al. “Experimental Phase Function and Degree of Linear Polarization Curves of Millimeter-sized Cosmic Dust Analogs”. In: *The Astrophysical Journal Supplement Series* 247 (2020), p. 19. ISSN: 1538-4365. DOI: 10.3847/1538-4365/ab6851 (cit. on pp. 26, 81, 103, 175).

[10] G. Maconi, P. Helander, M. Gritsevich, et al. "4π Scatterometer: A new technique for understanding the general and complete scattering properties of particulate media". In: *Journal of Quantitative Spectroscopy and Radiative Transfer* 246 (2020). ISSN: 00224073. DOI: 10.1016/j.jqsrt.2020.106910 (cit. on pp. 26, 29, 78, 103).

[11] J-B. Renard, J-C. Worms, T. Lemaire, et al. "Light scattering by dust particles in microgravity: Polarization and brightness imaging with the new version of the PROGRA2 instrument". In: *Applied Optics* 41.4 (2002), pp. 609–618. ISSN: 15394522. DOI: 10.1364/AO.41.000609 (cit. on pp. 26, 29, 81, 82, 103).

[12] M. I. Mishchenko. "Scale invariance rule in electromagnetic scattering". In: *Journal of Quantitative Spectroscopy and Radiative Transfer* 101 (2006), pp. 411–415. ISSN: 00224073. DOI: 10.1016/j.jqsrt.2006.02.047 (cit. on pp. 26, 29, 72, 103, 174).

[13] R. H. Zerull. "Laboratory Investigations and Optical Properties of Grains". In: *International Astronomical Union Colloquium* 85 (1985), pp. 197–206. ISSN: 0252-9211. DOI: 10.1017/s0252921100084633 (cit. on pp. 26, 59, 74, 174, 175).

[14] B. T. Draine and H. M. Lee. "Optical properties of interstellar graphite and silicate grains". In: *The Astrophysical Journal* 285 (1984), pp. 89–108. DOI: https://doi.org/10.1086/165385 (cit. on pp. 30, 31, 95, 109, 178, 221, 267).

[15] I. Voznyuk, H. Tortel, and A. Litman. "3-D Electromagnetic Scattering Computation in Free-Space With the FETI-FDP2 Method". In: *IEEE Transactions on Antennas and Propagation* 63.6 (2015), pp. 2604–2613. DOI: 10.1109/TAP.2015.2417977 (cit. on pp. 31, 90).

[16] M. I. Mishchenko, J. W. Hovenier, and L. D. Travis, eds. *Light Scattering by Nonspherical Particles*. California: Academic Press, 2000, p. 690. ISBN: 0124986609 (cit. on pp. 31, 103, 110, 173–175).

[17] M. Wozniak, F. R. A. Onofri, S. Barbosa, et al. "Comparison of methods to derive morphological parameters of multi-fractal samples of particle aggregates from TEM images". In: *Journal of Aerosol Science* 47 (2012), pp. 12–26. ISSN: 18791964. DOI: 10.1016/j.jaerosci.2011.12.008. URL: http://dx.doi.org/10.1016/j.jaerosci.2011.12.008 (cit. on pp. 31, 105, 106).

[18] C. F. McKee and E. C. Ostriker. "Theory of star formation". In: *Annual Review of Astronomy and Astrophysics* 45 (2007), pp. 565–687. ISSN: 00664146. DOI: 10.1146/annurev.astro.45.051806.110602. arXiv: 0707.3514 (cit. on p. 42).

[19] F.H. Shu, F.C. Adams, and S. Lizano. "Star formation in molecular clouds observations and theory". In: *Annual Review of Astronomy and Astrophysics* 25 (1987), pp. 23–81 (cit. on p. 42).

[20] T. Nakano. “Star Formation in Magnetic Clouds”. In: *the Astrophysical Journal* 494 (1998), pp. 587–604 (cit. on p. 42).

[21] J. P. Williams and P. C. Myers. “Evidence for Pressure-driven Flows and Turbulent Dissipation in the Serpens NW Cluster”. In: *The Astrophysical Journal* 537.2 (2000), pp. 891–903. ISSN: 0004-637X. DOI: 10.1086/309084 (cit. on p. 42).

[22] P. Hennebelle, A. Belloche, A. Whitworth, et al. “Protostellar collapse induced by compression”. In: *Monthly Notices of the Royal Astronomical Society* 340.3 (2003), pp. 870–882. ISSN: 0004640X. DOI: 10.1023/B:ASTR.0000045037.91704.0d (cit. on p. 42).

[23] C. F. Lee. “Molecular jets from low-mass young protostellar objects”. In: *Astronomy and Astrophysics Review* 28.1 (2020), pp. 1–38. ISSN: 09354956. DOI: 10.1007/s00159-020-0123-7. arXiv: 2002.05823 (cit. on p. 42).

[24] S. Terebey, F. H. Shu, and P. Cassen. “The collapse of the cores of slowly rotating isothermal clouds”. In: *The Astrophysical Journal* 286 (1984), pp. 529–551. DOI: 10.1086/162628 (cit. on p. 42).

[25] A. J. Maury, Ph André, L. Testi, et al. “Characterizing young protostellar disks with the CALYPSO IRAM-PdBI survey: Large Class 0 disks are rare”. In: *Astronomy and Astrophysics* 621.A76 (2019), pp. 1–44. ISSN: 14320746. DOI: 10.1051/0004-6361/201833537. arXiv: 1810.11221 (cit. on p. 42).

[26] E. Fiorellino, L. Tychoniec, C. F. Manara, et al. “The relation between the Mass Accretion Rate and the Disk Mass in Class I Protostars”. In: *The astrophy* 937.1 (2022), pp. 1–9. DOI: 10.3847/2041-8213/ac8fee. arXiv: arXiv:2209.04343v1 (cit. on p. 42).

[27] S. W. Stahler and F. M. Walter. “Pre-main-sequence evolution and the birth population”. In: *Protostars and Planets III*. Ed. by E. H. Levy and J. I. Lunine. 1993, pp. 405–428 (cit. on p. 43).

[28] S. W. Stahler. “The birthline for low-mass stars”. In: *The astrophysical journal* 274 (1983), pp. 822–829. DOI: 10.1086/161495. URL: https://medium.com/@arifwicaksanaa/pengertian-use-case-a7e576e1b6bf (cit. on p. 43).

[29] A. M. Hughes, G. Duchene, and B. C. Matthews. “Debris Disks : Structure , Composition , and Variability”. In: *Annual Review of Astronomy and Astrophysics* 56.1 (2018), pp. 541–591. DOI: 10.1146/annurev-astro-081817-052035. arXiv: arXiv:1802.04313v1 (cit. on p. 43).

[30] C. J. Lada. “Star formation: from OB associations to protostars”. In: *Symposium - International Astronomical Union* 115 (1987). Ed. by M. Peimbert and J. Jugaku, pp. 1–18. DOI: 10.1017/S0074180900094766 (cit. on p. 43).

[31] P. André, D. Ward-Thompson, and M. Barsony. “Submillimeter continuum observations of $\rho ophiuchi A: The candidate protostar VLA 1623 and prestellar clumps$”. In: *The Astrophysical Journal* 406 (1993), pp. 122–141 (cit. on p. 43).

[32] P. C. Myers and E. F. Ladd. "Bolometric temperature of young stellar objects". In: *The Astrophysical Journal* 413 (1993), pp. 48–50. DOI: 10.1086/186956 (cit. on p. 43).

[33] C. Bertout. "T Tauri stars: wild as dust". In: *Annual Review of Astronomy and Astrophysics* 27 (1989), pp. 351–395 (cit. on p. 44).

[34] G. H. Herbig. "The spectra of Be- and Ae-type stars associated with nebulousity". In: *The Astrophysical Journal Supplement Series* 4 (1960), pp. 337–368 (cit. on p. 44).

[35] Ph. André. "The initial conditions for protostellar collapse: Observational constraints". In: *EAS Publication Series*. Ed. by J. Bouvier and J.-P. Zahn. Vol. 3. 2002, pp. 1–38. DOI: 10.1051/eas (cit. on p. 44).

[36] S. M. Andrews. "Observations of Protoplanetary Disk Structures". In: *Annual Review of Astronomy and Astrophysics* 58.1 (2020), pp. 483–528. DOI: 10.1146/annurev-astro-031220-010302 (cit. on pp. 45, 46, 54).

[37] M. Ansdell, J. P. Williams, L. Trapman, et al. "ALMA Survey of Lupus Protoplanetary Disks. II. Gas Disk Radii". In: *The Astrophysical Journal* 859.1 (2018), p. 21. ISSN: 15384357. DOI: 10.3847/1538-4357/aab890. arXiv: 1803.05923 (cit. on p. 45).

[38] A. Philippe and M. Thierry. "From T Tauri stars to protostars: circumstellar material and young stellar objects in the rho Ophiuchi Cloud". In: *The Astrophysical Journal* 420 (1994), pp. 837–862. DOI: 10.1086/173608 (cit. on p. 46).

[39] Sean M. Andrews and Jonathan P. Williams. "Circumstellar Dust Disks in Taurus-Auriga: The Submillimeter Perspective". In: *The Astrophysical Journal* 631.2 (2005), pp. 1134–1160. ISSN: 0004-637X. DOI: 10.1086/432712. arXiv: 0506187 [astro-ph] (cit. on p. 46).

[40] A. R. Anderson, J. P. Williams, Nienke van der Marel, et al. "Protostellar and Protoplanetary Disk Masses in the Serpens Region". In: *The Astrophysical Journal* 938.1 (2022), p. 55. ISSN: 15384357. DOI: 10.3847/1538-4357/ac8ff0. arXiv: 2204.08731. URL: http://arxiv.org/abs/2204.08731 (cit. on p. 46).

[41] M. Benisty, C. Dominik, K. Follette, et al. "Optical and Near-infrared View of Planet-forming Disks and Protoplanets". In: *Protostars and Planets VII*. Ed. by S. Inutsuka, Y. Aikawa, T. Muto, et al. 2022. arXiv: 2203.09991. URL: http://arxiv.org/abs/2203.09991 (cit. on pp. 46, 47, 56, 57).

[42] P. J. Armitage. *Lecture notes on the formation and early evolution of planetary systems*. 2007. DOI: 10.48550/ARXIV.ASTRO-PH/0701485. URL: http://arxiv.org/abs/astro-ph/0701485 (cit. on pp. 46, 48).

[43] J. E. Pringle. "Accretion discs in astrophysics". In: *Annual Review of Astronomy and Astrophysics* 19 (1981), pp. 137–162. DOI: 10.1146/annurev.aa.19.090181.001033 (cit. on p. 47).

[44] D. Lynden-Bell and J. E. Pringle. "The evolution of viscous discs and the origin of the nebular variables". In: *Monthly Notices of the Royal Astronomical Society* 168 (1974), pp. 603–637. URL: 10.1093/mnras/168.3.603 (cit. on p. 47).

[45] A. M. Hughes, D. J. Wilner, C. Qi, et al. "Gas and Dust Emission at the Outer Edge of Protoplanetary Disks". In: *The Astrophysical Journal* 678.2 (2008), pp. 1119–1126. ISSN: 0004-637X. DOI: 10.1086/586730. arXiv: 0801.4763 (cit. on p. 47).

[46] L. Hartmann, N. Calvet, E. Gullbring, et al. "Accretion and the evolution of T Tauri disks". In: *The Astrophysical Journal* 495.1 (1998), pp. 385–400. DOI: 10.1086/305277 (cit. on p. 47).

[47] Diana Powell, Ruth Murray-Clay, and Hilke E. Schlichting. "Using Ice and Dust Lines to Constrain the Surface Densities of Protoplanetary Disks". In: *The Astrophysical Journal* 840.2 (2017), p. 93. ISSN: 15384357. DOI: 10.3847/1538-4357/aa6d7c. arXiv: 1704.04693. URL: http://dx.doi.org/10.3847/1538-4357/aa6d7c (cit. on p. 47).

[48] S. J. Kenyon and L. Hartmann. "Spectral energy distribution of T Tauri stars: Disk flaring and limits on accretion". In: *The Astrophysical Journal* 323 (1987), pp. 714–733. DOI: 10.1086/165866 (cit. on p. 47).

[49] N. Calvet, A. Patino, G. C. Magris, et al. "Irradiation of accretion disks around young objects. I. Near-infrared CO bands". In: *The Astrophysical Journal* 380 (1991), pp. 617–630. DOI: 10.1086/170618 (cit. on p. 47).

[50] C. Pinte, F. Ménard, G. Duchêne, et al. "Direct mapping of the temperature and velocity gradients in discs: Imaging the vertical CO snow line around im Lupi". In: *Astronomy and Astrophysics* 609 (2018), pp. 1–10. ISSN: 14320746. DOI: 10.1051/0004-6361/201731377. arXiv: 1710.06450 (cit. on p. 48).

[51] Erik Weaver, Andrea Isella, and Yann Boehler. "Empirical Temperature Measurement in Protoplanetary Disks". In: *The Astrophysical Journal* 853.2 (2018), p. 113. ISSN: 15384357. DOI: 10.3847/1538-4357/aaa481. arXiv: 1801.03478. URL: http://dx.doi.org/10.3847/1538-4357/aaa481 (cit. on p. 48).

[52] J. P. Williams and L. A. Cieza. "Protoplanetary disks and their evolution". In: *Annual Review of Astronomy and Astrophysics* 49.1 (2011), pp. 67–117. ISSN: 00664146. DOI: 10.1146/annurev-astro-081710-102548. arXiv: 1103.0556 (cit. on pp. 48, 136).

[53] T. Henning and D. Semenov. "Chemistry in protoplanetary disks". In: *Chemical Reviews* 113.12 (2013), pp. 9016–9042. ISSN: 00092665. DOI: 10.1021/cr400128p (cit. on p. 48).

[54] I. Oliveira, J. Olofsson, K. M. Pontoppidan, et al. "On the evolution of dust mineralogy, from protoplanetary disks to planetary systems". In: *The Astrophysical JournalAstrophysical Journal* 734.1 (2011), p. 51. ISSN: 15384357. DOI: 10.1088/0004-637X/734/1/51 (cit. on p. 48).

[55] L. D. Keller, G. C. Sloan, W. J. Forrest, et al. "PAH Emission from Herbig Ae/Be Stars". In: *The Astrophysical Journal* 684.1 (2008), pp. 411–429. ISSN: 0004-637X. DOI: 10.1086/589818. arXiv: 0809.2389 (cit. on p. 48).

[56] M. K. McClure, C. Espaillat, N. Calvet, et al. "Detections of trans-neptunian ice in protoplanetary disks". In: *The Astrophysical Journal* 799.2 (2015). ISSN: 15384357. DOI: 10.1088/0004-637X/799/2/162. arXiv: 1411.7618 (cit. on p. 48).

[57] J. S. Dohnanyi. "Collisional model of asteroids and their debris". In: *Journal of Geophysical Research* 74.10 (1969), pp. 2531–2554 (cit. on pp. 48, 136).

[58] B. T. Draine. "On the Submillimeter Opacity of Protoplanetary Disks". In: *The Astrophysical Journal* 636.2 (2006), pp. 1114–1120. ISSN: 0004-637X. DOI: 10.1086/498130. arXiv: 0507292 [astro-ph] (cit. on p. 48).

[59] L. Testi, T. Birnstiel, L. Ricci, et al. "Dust Evolution in Protoplanetary Disks". In: *Protostars and Planets VI*. Ed. by H Beuther, R Klessen, C Dullemond, et al. Arizona, 2014. DOI: 10.48550/ARXIV.ASTRO-PH/0602041 (cit. on pp. 48, 53, 102).

[60] F. L. Whipple. "On certain aerodynamic processes for asteroids and comets". In: *From Plasma to Planet*. Ed. by A. Elvius. 1972, pp. 211–232 (cit. on p. 49).

[61] N. Van Der Marel, E. F. Van Dishoeck, S. Bruderer, et al. "A major asymmetric dust trap in a transition disk". In: *Science* 340.6137 (2013), pp. 1199–1202. ISSN: 10959203. DOI: 10.1126/science.1236770 (cit. on p. 49).

[62] Koji Wada, Hidekazu Tanaka, Satoshi Okuzumi, et al. "Growth efficiency of dust aggregates through collisions with high mass ratios". In: *Astronomy and Astrophysics* 559 (2013). ISSN: 00046361. DOI: 10.1051/0004-6361/201322259 (cit. on p. 50).

[63] J. Blum. "Dust Evolution in Protoplanetary Discs and the Formation of Planetesimals: What Have We Learned from Laboratory Experiments?" In: *Space Science Reviews* 214.2 (2018), pp. 1–19. ISSN: 15729672. DOI: 10.1007/s11214-018-0486-5. arXiv: 1802.00221. URL: http://dx.doi.org/10.1007/s11214-018-0486-5 (cit. on pp. 50–52, 102).

[64] S. J. Weidenschilling. "Aerodynamics of solud bodies in the solar nebula". In: *Royal Astronomical Society* 180 (1977), pp. 57–70 (cit. on p. 52).

[65] A. P. Boss. "Giant Planet Formation by Gravitational Instability". In: *Science* 276.5320 (1997), pp. 1836–1839 (cit. on p. 52).

[66] C. F. Gammie. "Nonlinear Outcome of Gravitational Instability in Optically Thick Disks". In: *The astrophysical Journal* 553 (2001), pp. 174–183. ISSN: 0252-9211. DOI: 10.1017/s0252921100043530 (cit. on p. 52).

[67] W. K.M. Rice, P. J. Armitage, M. R. Bate, et al. "The effect of cooling on the global stability of self-gravitating protoplanetary discs". In: *Monthly Notices of the Royal Astronomical Society* 339.4 (2003), pp. 1025–1030. ISSN: 00358711. DOI: 10.1046/j.1365-8711.2003.06253.x. arXiv: 0211088 [astro-ph] (cit. on p. 52).

[68] X. N. Bai and J. M. Stone. "Dynamics of solids in the midplane of protoplanetary disks: Implications for planetesimal formation". In: *Astrophysical Journal* 722.2 (2010), pp. 1437–1459. ISSN: 15384357. DOI: 10.1088/0004-637X/722/2/1437. arXiv: 1005.4982 (cit. on p. 52).

[69] J. Drazkowska and Y. Alibert. "Planetesimal formation starts at the snow line". In: *Astronomy and Astrophysics* 608 (2017), pp. 1–11. ISSN: 14320746. DOI: 10.1051/0004-6361/201731491. arXiv: 1710.00009 (cit. on p. 52).

[70] A. N. Youdin and J. Goodman. "Streaming Instabilities in Protoplanetary Disks". In: *The Astrophysical Journal* 620.1 (2005), pp. 459–469. ISSN: 0004-637X. DOI: 10.1086/426895. arXiv: 0409263 [astro-ph] (cit. on p. 52).

[71] P. Bastien and F. Menard. "On the Interpretation of Polarization Maps of Young Stellar Objects". In: 326 (1988), p. 334. DOI: 10.1086/166095 (cit. on p. 53).

[72] P. Bastien and F. Menard. "Parameters of disks around young stellar objects from polarization observations". In: *The Astrophysical Journal* 364 (1990), pp. 232–241. ISSN: 0004-637X. DOI: 10.1086/169406 (cit. on p. 53).

[73] M. Villenave, F. Ménard, W. R. F. Dent, et al. "Observations of edge-on protoplanetary disks with ALMA. Results from continuum data". In: *Astronomy Astrophysics* 164 (2020), pp. 1–22. DOI: https://doi.org/10.1051/0004-6361/202038087 (cit. on pp. 54, 55).

[74] J. de Boer, M. Langlois, R. G. van Holstein, et al. "Polarimetric imaging mode of VLT/SPHERE/IRDIS". In: *Astronomy Astrophysics* 633.A63 (2020), pp. 1–17. ISSN: 0004-6361. DOI: 10.1051/0004-6361/201834989 (cit. on p. 54).

[75] J. De Boer, C. Ginski, G. Chauvin, et al. "Possible single-armed spiral in the protoplanetary disk around HD 34282". In: *Astronomy and Astrophysics* 649 (2021), pp. 1–10. ISSN: 14320746. DOI: 10.1051/0004-6361/201936787 (cit. on p. 54).

[76] H. Canovas, F. Ménard, J. De Boer, et al. "Nonazimuthal linear polarization in protoplanetary disks". In: *Astronomy and Astrophysics* 582.L7 (2015), pp. 2–5. ISSN: 14320746. DOI: 10.1051/0004-6361/201527267. arXiv: 1509.06745 (cit. on p. 55).

[77] C. Pinte, D. L. Padgett, F. Ménard, et al. "Probing dust grain evolution in IM Lupi's circumstellar disc. Multi-wavelength observations and modelling of the dust disc". In: *Astronomy Astrophysics* 489 (2008), pp. 633–650. DOI: 10.1051/0004-6361:200810121 (cit. on p. 56).

[78] J. Milli, A. Vigan, D. Mouillet, et al. "Near-infrared scattered light properties of the HR 4796 A dust ring". In: *Astronomy and Astrophysics* 599.A108 (2017), pp. 1–24. DOI: 10.1051/0004-6361/201527838 (cit. on pp. 56, 58, 151–153, 218, 263, 264).

[79] C. F. Bohren and D. R. Huffman. *Absorption and scattering of light by small particles*. New York: John Wiley & Sons, Inc, 1983, p. 544. ISBN: 9780471057727 (cit. on pp. 58–61, 65, 68, 71, 121, 130, 132, 155, 192).

[80] J. W. Hovenier, C. V. D. Mee, and H. Domke. *Transfer of polarized light in planetary atmospheres: Basic concepts and practical methods*. Dordrecht: Springer Science+Business Media Dordrecht, 2004. ISBN: 978-1-4020-2856-4. DOI: 10.1007/978-1-4020-2856-4 (cit. on pp. 59, 66, 68, 70).

[81] G. W. Petty. *A first course in atmospheric radiation*. 2nd ed. Vol. 4. 1. Madison: Sundog publishing, 2006, pp. 1–475. ISBN: 978-0-9729033-1-8 (cit. on pp. 59, 60).

[82] E. Collett. *Field Guide to Polarization*. Ed. by John E Greivenkamp. Washington: SPIE, 2005. ISBN: 0819458686. DOI: 10.1117/3.626141 (cit. on pp. 62, 65).

[83] R. G. Van Holstein, J. H. Girard, J. De Boer, et al. "Polarimetric imaging mode of VLT/SPHERE/IRDIS: II. Characterization and correction of instrumental polarization effects". In: *Astronomy and Astrophysics* 633 (2020). ISSN: 14320746. DOI: 10.1051/0004-6361/201834996. arXiv: 1909.13108 (cit. on pp. 64, 130).

[84] B. Gay. "Caractérisation de milieux diffusants chargés en particules par imagerie polarisée. Application aux agrégats fractals." PhD thesis. Institut National des Sciences Appliquées de Lyon, 2010 (cit. on pp. 65, 67).

[85] M. I. Mishchenko. *Electromagnetic scattering by particles and particle groups*. New York: Cambridge University Press, 2014. ISBN: 9781107358249. DOI: 10.1017/CBO9781107358249.003 (cit. on pp. 69, 70, 92, 132).

[86] J. M. Greenberg, N. E. Pedersen, and J. C. Pedersen. "Microwave analog to the scattering of light by nonspherical particles". In: *Journal of Applied Physics* 32.2 (1961), pp. 233–242. ISSN: 00218979. DOI: 10.1063/1.1735984 (cit. on pp. 72, 73).

[87] K. Weiss-Wrana, R. H. Giese, and R. H. Zerull. "Microwave and laser facilities to determine scattering and colour signatures related to the physical properties of dust particles". In: *International Astronomical Union Colloquium* (1985), pp. 219–221 (cit. on pp. 73, 74, 76, 77).

[88] R. H. Zerull, B. Å. S. Gustafson, K. Schulz, et al. "Scattering by aggregates with and without an absorbing mantle: microwave analog experiments". In: *Applied Optics* 32 (1993), p. 4088. ISSN: 0003-6935. DOI: 10.1364/ao.32.004088 (cit. on pp. 74, 103, 117).

[89] R. H. Giese, K. Weiss-Wrana, R. H. Zerull, et al. "Large fluffy particles: a possible explanation of the optical properties of interplanetary dust". In: *Astronomy and astrophysics* 65 (1978), pp. 265–272 (cit. on pp. 74, 103).

[90] R. H. Zerull, R. H. Giese, and K. Weiss. "Scattering functions of nonspherical dielectric and absorbing particles vs Mie theory". In: *Applied Optics* 16 (1977), pp. 777–778 (cit. on p. 74).

[91] M. S. Hanner, R. H. Giese, K. Weiss-Wrana, et al. "On the definition of albedo and application to irregular particles". In: *Astronomy and astrophysics* 104 (1981), pp. 42–46 (cit. on p. 74).

[92] B. Å. S. Gustafson, L. Kolokolova, J. E. Thomas-Osip, et al. "Scattering by complex systems II: Results from microwave measurements". In: *Formation and Evolution of Solids in Space*. Springer, Dordrecht, 1999, pp. 549–563. ISBN: 978-94-011-4806-1. DOI: https://doi.org/10.1007/978-94-011-4806-1_34 (cit. on p. 75).

[93] B. Å. S. Gustafson. "Scattering by ensemble of small particles experiment, theory and applications". In: *Reports of the Lund Observatory* 17 (1980) (cit. on p. 75).

[94] D. W. Schuerman, R. T. Wang, B. Å. S. Gustafson, et al. "Systematic studies of light scattering 1: Particle shape". In: *Applied Optics* 20 (1981), pp. 4039–4050. ISSN: 0003-6935. DOI: 10.1364/ao.21.000369 (cit. on p. 75).

[95] L. Kolokolova and B. Å. S. Gustafson. "Scattering by inhomogenous particles: Microwave analog experiments and comparison to effective medium theories". In: *Journal of Quantitative Spectroscopy and Radiative Transfer* 70 (2001), pp. 611–625. ISSN: 00224073. DOI: 10.1016/S0022-4073(01)00033-4 (cit. on p. 75).

[96] J. E. Thomas-Osip, B. Å. S. Gustafson, L. Kolokolova, et al. "An investigation of Titan's aerosols using microwave analog measurements and radiative transfer modeling". In: *Icarus* 179.2 (2005), pp. 511–522. ISSN: 00191035. DOI: 10.1016/j.icarus.2005.06.017 (cit. on pp. 75, 103).

[97] G. Maconi, A. Penttilä, I. Kassamakov, et al. "Non-destructive controlled single-particle light scattering measurement". In: *Journal of Quantitative Spectroscopy and Radiative Transfer* 204 (2018), pp. 159–164. ISSN: 00224073. DOI: 10.1016/j.jqsrt.2017.09.005 (cit. on pp. 77, 78).

[98] J. Escobar-Cerezo, C. Palmer, O. Muñoz, et al. "Scattering Properties of Large Irregular Cosmic Dust Particles at Visible Wavelengths". In: *The Astrophysical Journal* 838 (2017), pp. 1–17. ISSN: 1538-4357. DOI: 10.3847/1538-4357/aa6303 (cit. on pp. 78, 152, 153, 175).

[99] J. Martikainen, A. Penttilä, M. Gritsevich, et al. "Spectral modeling of meteorites at UV-vis-NIR wavelengths". In: *Journal of Quantitative Spectroscopy and Radiative Transfer* 204 (2018), pp. 144–151. ISSN: 00224073. DOI: 10.1016/j.jqsrt.2017.09.017 (cit. on p. 78).

[100] A. Penttilä, T. Väisänen, J. Markkanen, et al. "Rigorous light-scattering simulations of nanophase iron space-weathering effects on reflectance spectra of olivine grains". In: *Icarus* 345 (2020), p. 113727. ISSN: 10902643. DOI: 10.1016/j.icarus.2020.113727 (cit. on p. 78).

[101] A. J. Hunt and D. R. Huffman. "A new polarization-modulated light scattering instrument". In: *Review of Scientific Instruments* 44 (1973), pp. 1753–1762. ISSN: 00346748. DOI: 10.1063/1.1686049 (cit. on p. 78).

[102] H. Volten, O. Muñoz, E. Rol, et al. "Scattering matrices of mineral aerosol particles at 441.6 nm and 632.8 nm". In: *Journal of geophysical research* 106 (2001), pp. 375–401. DOI: 10.1029/2001JD900068 (cit. on p. 79).

[103] O. Muñoz, F. Moreno, D. Guirado, et al. "The Amsterdam-Granada Light Scattering Database". In: *Journal of Quantitative Spectroscopy and Radiative Transfer* 113 (2012), pp. 565–574. ISSN: 00224073. DOI: 10.1016/j.jqsrt.2012.01.014 (cit. on pp. 79, 80).

[104] O. Muñoz, J. Hovenier, F. Moreno, et al. "Experimental light scattering by small particles in Amsterdam and Granada". In: *EPJ Web of Conferences* 5 (2010). ISSN: 2100014X. DOI: 10.1051/epjconf/20100502005 (cit. on pp. 80, 99).

[105] O. Muñoz, H. Volten, J. W. Hovenier, et al. "Experimental and computational study of light scattering by irregular particles with extreme refractive indices: Hematite and rutile". In: *Astronomy and Astrophysics* 446 (2006), pp. 525–535. ISSN: 00046361. DOI: 10.1051/0004-6361:20053727 (cit. on p. 80).

[106] H. Volten, O. Muñoz, J. W. Hovenier, et al. "Experimental light scattering by fluffy aggregates of magnesiosilica, ferrosilica, and alumina cosmic dust analogs". In: *Astronomy and Astrophysics* 470 (2007), pp. 377–386. ISSN: 00046361. DOI: 10.1051/0004-6361:20066744 (cit. on pp. 80, 123, 147, 148).

[107] O. Muñoz, F. Moreno, F. Vargas-Martín, et al. "Experimental Phase Functions of Millimeter-sized Cosmic Dust Grains". In: *The Astrophysical Journal* 846.1 (2017), p. 85. ISSN: 1538-4357. DOI: 10.3847/1538-4357/aa7ff2 (cit. on pp. 80, 152, 215, 216).

[108] E. Frattin, O. Muñoz, F. Moreno, et al. “Experimental phase function and degree of linear polarization of cometary dust analogues”. In: *Monthly Notices of the Royal Astronomical Society* 484 (2019), pp. 2198–2211. ISSN: 13652966. DOI: 10.1093/mnras/stz129. arXiv: 1901.05975 (cit. on pp. 81, 261–263).

[109] E. Hadamcik, J-B. Renard, A. C. Levasseur-Regourd, et al. “Light scattering by agglomerates: Interconnecting size and absorption effects (PROGRA2 experiment)”. In: *Journal of Quantitative Spectroscopy and Radiative Transfer* 110.14-16 (2009), pp. 1755–1770. ISSN: 00224073. DOI: 10.1016/j.jqsrt.2009.03.005 (cit. on pp. 83, 128).

[110] E. Hadamcik, J-B. Renard, J-C. Worms, et al. “Polarization of light scattered by fluffy particles (PROGRA2 experiment)”. In: *Icarus* 155 (2002), pp. 497–508. ISSN: 00191035. DOI: 10.1006/icar.2001.6732 (cit. on pp. 83, 103).

[111] E. Hadamcik, J-B. Renard, A. C. Levasseur-Regourd, et al. “Laboratory light scattering measurements on "natural" particles with the PROGRA2 experiment: An overview”. In: *Journal of Quantitative Spectroscopy and Radiative Transfer* 79-80 (2003), pp. 679–693. ISSN: 00224073. DOI: 10.1016/S0022-4073(02)00313-8 (cit. on pp. 83, 103).

[112] E. Hadamcik, J-B. Renard, A. C. Levasseur-Regourd, et al. “Light scattering by fluffy particles with the PROGRA2 experiment: Mixtures of materials”. In: *Journal of Quantitative Spectroscopy and Radiative Transfer* 100 (2006), pp. 143–156. ISSN: 00224073. DOI: 10.1016/j.jqsrt.2005.11.032 (cit. on pp. 83, 103).

[113] E. Hadamcik, J-B. Renard, F. J. M. Rietmeijer, et al. “Light scattering by fluffy Mg-Fe-SiO and C mixtures as cometary analogs (PROGRA2 experiment)”. In: *Icarus* 190 (2007), pp. 660–671. ISSN: 00191035. DOI: 10.1016/j.icarus.2007.03.010 (cit. on pp. 83, 103, 128).

[114] E. Hadamcik, J-B. Renard, A. Mahjoub, et al. “Optical properties of analogs of Titan’s aerosols produced by dusty plasma”. In: *Earth, Planets and Space* 65.10 (2013), pp. 1175–1184. ISSN: 18805981. DOI: 10.5047/eps.2013.05.019 (cit. on pp. 83, 128).

[115] H. Saleh. “Application of the microwave analogy to study the scattering properties of trees, atmospheric particles and microorganisms”. PhD thesis. Aix-Marseille Université, 2017 (cit. on pp. 87, 90, 92).

[116] J-M. Geffrin, B. García-Cámara, R. Gómez-Medina, et al. “Magnetic and electric coherence in forward-and back-scattered electromagnetic waves by a single dielectric subwavelength sphere”. In: *Nature Communications* 3 (2012). ISSN: 20411723. DOI: 10.1038/ncomms2167 (cit. on p. 87).

[117] V. Tobon Valencia, J-M. Geffrin, F. Ménard, et al. “Scattering properties of protoplanetary dust analogs with microwave analogy : Aggregates of fractal dimensions from 1.5 to 2.8”. In: *Astronomy and Astrophysics* (accepted) (2022). DOI: 10.1051/0004-6361/202142656 (cit. on pp. 88, 89, 123, 274).

[118] C. Eyraud, J-M. Geffrin, A. Litman, et al. “Drift correction for scattering measurements”. In: *Applied Physics Letters* 89 (2006), pp. 1–3. ISSN: 00036951. DOI: 10.1063/1.2404978 (cit. on p. 89).

[119] O. M. Bucci and G. Franceschetti. “On the spatial bandwidth of scattered fields”. In: *IEE Transactions on antennas and propagation* AP-35.12 (1987), pp. 1445–1455. DOI: 10.1109/TAP.1987.1144024 (cit. on p. 89).

[120] C. Eyraud, L. I. Sorsa, J-M. Geffrin, et al. “Full wavefield simulation versus measurement of microwave scattering by a complex 3D-printed asteroid analogue”. In: *Astronomy and Astrophysics* 643 (2020). ISSN: 14320746. DOI: 10.1051/0004-6361/202038510 (cit. on pp. 90, 91).

[121] O. Merchiers, C. Eyraud, J-M. Geffrin, et al. “Microwave measurements of the full amplitude scattering matrix of a complex aggregate: a database for the assessment of light scattering codes”. In: *Optics Express* 18.3 (2010), p. 2056. ISSN: 1094-4087. DOI: 10.1364/oe.18.002056 (cit. on pp. 90, 91, 104).

[122] D. W. Mackowski and M. I. Mishchenko. “Calculation of the T matrix and the scattering matrix for ensembles of spheres”. In: 13.11 (1996), pp. 2266–2278 (cit. on p. 90).

[123] B. T. Draine and P. J. Flatau. “Discrete-Dipole Approximation For Scattering Calculations”. In: *Journal of the Optical Society of America A* 11.4 (1994), pp. 1491–1499. ISSN: 1084-7529. DOI: 10.1364/josaa.11.001491 (cit. on p. 90).

[124] P. R. Amestoy, I. S. Duff, and J. Y. L’Excellent. “Multifrontal parallel distributed symmetric and unsymmetric solvers”. In: *Computer Methods in Applied Mechanics and Engineering* 184 (2000), pp. 501–520. ISSN: 00457825. DOI: 10.1016/S0045-7825(99)00242-X (cit. on p. 91).

[125] O. Schenk and K. Gärtner. “PARDISO”. In: *Encyclopedia of Parallel Computing*. Ed. by David Padua. Boston, MA: Springer US, 2011, pp. 1458–1464. ISBN: 978-0-387-09766-4. DOI: 10.1007/978-0-387-09766-4_90. URL: https://doi.org/10.1007/978-0-387-09766-4_90 (cit. on p. 91).

[126] J-B. Renard, J-M. Geffrin, V. Tobon Valencia, et al. “Number of independent measurements required to obtain reliable mean scattering properties of irregular particles having a small size parameter, using microwave analogy measurements”. In: *Journal of Quantitative Spectroscopy and Radiative Transfer* 272 (2021). ISSN: 00224073. DOI: 10.1016/j.jqsrt.2021.107718. URL: https://doi.org/10.1016/j.jqsrt.2021.107718 (cit. on pp. 98, 107, 111, 112, 178, 180, 181, 224, 272).

[127] M. Fulle and J. Blum. "Fractal dust constrains the collisional history of comets". In: *MNRS* 469 (2017), S39–S44. ISSN: 13652966. DOI: 10.1093/mnras/stx971 (cit. on p. 102).

[128] C. Güttler, T. Mannel, A. Rotundi, et al. "Astrophysics Special issue Synthesis of the morphological description of cometary dust at comet 67P / Churyumov-Gerasimenko". In: 630.A24 (2019), pp. 1–15. DOI: https://doi.org/10.1051/0004-6361/201834751 (cit. on p. 102).

[129] I. Bertini, P. J. Gutierrez, and W. Sabolo. "The influence of the monomer shape in the first stage of dust growth in the protoplanetary disk". In: *Astronomy and Astrophysics* 504 (2009), pp. 625–633. ISSN: 00046361. DOI: 10.1051/0004-6361/200912248 (cit. on pp. 102, 107).

[130] J-B. Renard, E. Hadamcik, B. Couté, et al. "Wavelength dependence of linear polarization in the visible and near infrared domain for large levitating grains (PROGRA2 instruments)". In: *Journal of Quantitative Spectroscopy and Radiative Transfer* 146 (2014), pp. 424–430. ISSN: 00224073. DOI: 10.1016/j.jqsrt.2014.02.024. URL: http://dx.doi.org/10.1016/j.jqsrt.2014.02.024 (cit. on p. 103).

[131] B. Å. S. Gustafson. "Microwave analog to light scattering measurements: A modern implementation of a proven method to achieve precise control". In: *Journal of Quantitative Spectroscopy and Radiative Transfer* 55.5 (1996), pp. 663–672. ISSN: 00224073. DOI: 10.1016/0022-4073(96)00009-X (cit. on p. 103).

[132] D. E. Brownlee. "Interplanetary dust". In: *Reviews of Geophysics and space physics* 17.7 (1979), pp. 1735–1743 (cit. on p. 103).

[133] M. Fraundorf. *Stratospheric Brownlee particles: diverse lesftovers from collapse.* Tech. rep. Washington: NASA, 1980, pp. 294–296 (cit. on p. 103).

[134] Y. L. Xu and B. Å. S. Gustafson. "Experimental and theoretical results of light scattering by aggregates of spheres". In: *Applied Optics* 36.30 (1997), p. 8026. ISSN: 0003-6935. DOI: 10.1364/ao.36.008026 (cit. on p. 103).

[135] Y. Lin Xu and B. Å. S. Gustafson. "A generalized multiparticle Mie-solution: Further experimental verification". In: *Journal of Quantitative Spectroscopy and Radiative Transfer* 70 (2001), pp. 395–419. ISSN: 00224073. DOI: 10.1016/S0022-4073(01)00019-X (cit. on p. 103).

[136] B. Å. S. Gustafson and L. Kolokolova. "A systematic study of light scattering by aggregate particles using the microwave analog technique: Angular and wavelength dependence of intensity and polarization". In: *Journal of Geophysical Research Atmospheres* 104 (1999), pp. 31, 711–31, 720. ISSN: 01480227. DOI: 10.1029/1999JD900327 (cit. on pp. 103, 123).

[137] M. Min, Ch. Rab, P. Woitke, et al. “Multiwavelength optical properties of compact dust aggregates in protoplanetary disks”. In: *Astronomy and Astrophysics* 13 (2016), pp. 1–10 (cit. on pp. 104, 123, 148–150, 153).

[138] R. Tazaki, H. Tanaka, S. Okuzumi, et al. “Light Scattering By Fractal Dust Aggregates. I. Angular Dependence of Scattering”. In: *The Astrophysical Journal* 823 (2016), pp. 1–16. ISSN: 1538-4357. DOI: 10.3847/0004-637x/823/2/70 (cit. on pp. 104, 123, 130).

[139] R. Tazaki and H. Tanaka. “Light Scattering by Fractal Dust Aggregates. II. Opacity and Asymmetry Parameter”. In: *The Astrophysical Journal* 860.1 (2018), p. 79. ISSN: 1538-4357. DOI: 10.3847/1538-4357/aac32d. arXiv: 1803.03775 (cit. on p. 104).

[140] H. Kimura, L. Kolokolova, A. Li, et al. “Light Scattering and Thermal Emission by Primitive Dust Particles in Planetary Systems”. In: *Light Scattering Reviews* 11 (2016), pp. 363–418. DOI: 10.1007/978-3-662-49538-4_8. arXiv: 1603.03123 (cit. on p. 104).

[141] J. Lasue and A. C. Levasseur-Regourd. “Porous irregular aggregates of submicron sized grains to reproduce cometary dust light scattering observations”. In: *Journal of Quantitative Spectroscopy and Radiative Transfer* 100 (2006), pp. 220–236. ISSN: 00224073. DOI: 10.1016/j.jqsrt.2005.11.040 (cit. on p. 104).

[142] J. Lasue, A. C. Levasseur-Regourd, N. Fray, et al. “Inferring the interplanetary dust properties from remote observations and simulations”. In: *Astronomy Astrophysics* 473 (2007), pp. 641–649. DOI: 10.1051/0004-6361:20077623 (cit. on p. 104).

[143] P. Halder, P. Deb Roy, and H. S. Das. “Dependence of light scattering properties on porosity, size and composition of dust aggregates”. In: *Icarus* 312 (2018), pp. 45–60. ISSN: 10902643. DOI: 10.1016/j.icarus.2018.04.026. arXiv: 1804.08324 (cit. on pp. 104, 124).

[144] C. M. Sorensen, Y. W. Heinson, W. R. Heinson, et al. “Q-space analysis of the light scattering phase function of particles with any shape”. In: *Atmosphere* 8.4 (2017). ISSN: 20734433. DOI: 10.3390/atmos8040068 (cit. on p. 104).

[145] C. M. Sorensen, J. Yon, F. Liu, et al. “Light scattering and absorption by fractal aggregates including soot”. In: *Journal of Quantitative Spectroscopy and Radiative Transfer* 217 (2018), pp. 459–473. ISSN: 0022-4073. DOI: https://doi.org/10.1016/j.jqsrt.2018.05.016 (cit. on pp. 104, 155).

[146] L. Liu and M. I. Mishchenko. “Scattering and radiative properties of morphologically complex carbonaceous aerosols: A systematic modeling study”. In: *Remote Sensing* 10.10 (2018). ISSN: 20724292. DOI: 10.3390/rs10101634 (cit. on pp. 104, 123, 150, 151).

[147] L. Kolokolova, M. S. Hanner, A-C. Levasseur-Regourd, et al. "Physical properties of cometary dust from light scattering and thermal emission". In: *Comets II*. 2004, p. 577. DOI: 10.1016/0273-1177(82)90304-0 (cit. on p. 104).

[148] P. Sabouroux, B. Stout, J-M. Geffrin, et al. "Amplitude and phase of light scattered by micro-scale aggregates of dielectric spheres: Comparison between theory and microwave analogy experiments". In: *Journal of Quantitative Spectroscopy and Radiative Transfer* 103.1 (2007), pp. 156–167. ISSN: 00224073. DOI: 10.1016/j.jqsrt.2006.06.001 (cit. on p. 104).

[149] O. Merchiers, J-M. Geffrin, R. Vaillon, et al. "Microwave analog to light scattering measurements on a fully characterized complex aggregate". In: *Applied Physics Letters* 94.18 (2009), pp. 2–4. ISSN: 00036951. DOI: 10.1063/1.3129196 (cit. on pp. 104, 106).

[150] R. Vaillon and J-M. Geffrin. "Recent advances in microwave analog to light scattering experiments". In: *Journal of Quantitative Spectroscopy and Radiative Transfer* 146 (2014), pp. 100–105. ISSN: 00224073. DOI: 10.1016/j.jqsrt.2014.02.031 (cit. on pp. 104, 108).

[151] B. B. Mandelbrot. *The fractal geometry of nature / Benoit B. Mandelbrot, ...* eng. Updated and augmented. New York: W. H. Freeman and Co., 1983. ISBN: 0-7167-1186-9 (cit. on p. 105).

[152] P. Meakin. "Effects of cluster trajectories on cluster-cluster aggregation: A comparison of linear and Brownian trajectories in two- and three-dimensional simulations". In: *Physical Review E* 29.2 (1984), pp. 997–999. DOI: https://doi.org/10.1103/PhysRevA.29.997 (cit. on p. 106).

[153] M. Woźniak. "Characterization of nanoparticle aggregates with light scattering techniques". PhD thesis. Aix-Marseille Université, 2012 (cit. on p. 107).

[154] C. M. Sorensen and G. C. Roberts. "The prefactor of fractal aggregates". In: *Journal of Colloid and Interface Science* 186 (1997), pp. 447–452. ISSN: 00219797. DOI: 10.1006/jcis.1996.4664 (cit. on p. 107).

[155] T. Mukai, H. Ishimoto, T. Kozasa, et al. "Radiation pressure forces of fluffy porous grains". In: *Astronomy and Astrophysics* 262.1 (1992), pp. 315–320. ISSN: 17549469 (cit. on p. 107).

[156] E. Zubko, Y. Shkuratov, and G. Videen. "Effect of morphology on light scattering by agglomerates". In: *Journal of Quantitative Spectroscopy and Radiative Transfer* 150 (2015), pp. 42–54. DOI: 10.1016/j.jqsrt.2014.06.023. URL: http://dx.doi.org/10.1016/j.jqsrt.2014.06.023 (cit. on pp. 107, 137, 174, 175, 216–219, 246).

[157] M. V. Berry and I. C. Percival. "Optics of Fractal Clusters Such as Smoke". In: *Optica Acta: International Journal of Optics* 33.5 (1986), pp. 577–591. DOI: 10.1080/713821987. eprint: https://doi.org/10.1080/713821987. URL: https://doi.org/10.1080/713821987 (cit. on p. 124).

[158] J. R. Bottiger, E. S. Fry, and R. C. Thompson. "Phase matrix measurements for electromagnetic scattering by sphere aggregates". In: *Light scattering by irregularly shaped particles*. Ed. by D. W. Schuerman. Plenum Pre. New york, 1980, pp. 283–290. ISBN: 978-1-4684-3706-5. DOI: 10.1007/978-1-4684-3704-1 (cit. on p. 130).

[159] K. N. Strelow, D. A. Abbink, R. G. Van Holstein, et al. "Circular polarimetric imaging at planetary system scales by hacking SPHERE-IRDIS. Full-Stokes observations of the asymmetric nebula surrounding VY CMa". In: *Astronomy and Astrophysics* (in prep) (cit. on p. 130).

[160] M. I. Mishchenko. "Electromagnetic scattering by nonspherical particles: A tutorial review". In: *Journal of Quantitative Spectroscopy and Radiative Transfer* 110.11 (2009), pp. 808–832. ISSN: 00224073. DOI: 10.1016/j.jqsrt.2008.12.005 (cit. on p. 130).

[161] Partnership ALMA, E. B. Fomalont, C. Vlahakis, et al. "The 2014 alma long baseline campaign: An overview". In: *Astrophysical Journal Letters* 808.1 (2015), pp. 1–11. ISSN: 20418213. DOI: 10.1088/2041-8205/808/1/L1 (cit. on p. 136).

[162] C. M. Sorensen. "Light Scattering by Fractal Aggregates : A Review". In: *Aerosol Science and Technology* 35.2 (2001), pp. 648–687. DOI: 10.1080/02786820117868 (cit. on pp. 153, 156, 159).

[163] J. B. Maughan. "Q-space analysis of the orientally averaged light scattering by particles of varios shapes". PhD thesis. Kansas State University, 2020 (cit. on p. 155).

[164] T. L. Farias, Ü. Ö. Köylü, and M. G. Carvalho. "Range of validity of the Rayleigh–Debye–Gans theory for optics of fractal aggregates". In: *Applied Optics* 35.33 (1996), pp. 6560–6567. ISSN: 0003-6935. DOI: 10.1364/ao.35.006560 (cit. on p. 155).

[165] R. A. Dobbins and C. M. Megaridis. "Absorption and scattering of light by polydisperse aggregates". In: *Applied Optics* 30.33 (1991), pp. 4747–4754. DOI: https://doi.org/10.1364/AO.30.004747 (cit. on pp. 155, 169).

[166] C. Oh and C. M. Sorensen. "Structure factor of diffusion-limited aggregation clusters: Local structure and non-self-similarity". In: *Physical Review E* 57.1 (1998), pp. 784–790. ISSN: 1063651X. DOI: 10.1103/PhysRevE.57.784 (cit. on p. 156).

[167] J. Mroczka, M. Woźniak, and F. R. A. Onofri. "Algorithms and methods for analysis of the optical structure factor of fractal aggregates". In: *Metrology and Measurement Systems* 19.3 (2012), pp. 459–470. ISSN: 08608229. DOI: 10.2478/v10178-012-0039-2 (cit. on p. 156).

[168] S. Butterworth. "On the Theory of Filter Amplifiers." In: *Experimental Wireless The Wireless Engineer* 7 (1930), pp. 536–541. URL: https://www.changpuak.ch/electronics/downloads/On_the_Theory_of_Filter_Amplifiers.pdf (cit. on p. 156).

[169] J. Teixiera. "On Growth and Form: Fractal and Non-Fractal Patterns in Physics". In: ed. by H. E. Stanley and N. Ostrowsky. Dordrecht: Springer Netherlands, 1986. Chap. Experiment, pp. 145–162. ISBN: 978-94-009-5165-5. DOI: 10.1007/978-94-009-5165-5_9 (cit. on p. 169).

[170] P. H. Hasselmann, S. Fornasier, M. A. Barucci, et al. "Modeling optical roughness and first-order scattering processes from OSIRIS-REx color images of the rough surface of asteroid (101955) Bennu". In: *Icarus* 357 (2021), pp. 1–15. ISSN: 10902643. DOI: 10.1016/j.icarus.2020.114106. arXiv: 2010.04032. URL: https://www.sciencedirect.com/science/article/pii/S0019103520304516 (cit. on p. 173).

[171] S. Mukai, T. Mukai, R. H. Giese, et al. "Scattering of radiation by a large particle with a random rough surface". In: *The moon and the planets* 26.2 (1982), pp. 197–208. DOI: 10.1007/BF00929281 (cit. on p. 174).

[172] C. Liu, R. L. Panetta, and P. Yang. "The effective equivalence of geometric irregularity and surface roughness in determining particle single-scattering properties". In: *Optics Express* 22.19 (2014), pp. 23620–23627. ISSN: 1094-4087. DOI: 10.1364/oe.22.023620 (cit. on pp. 174, 175).

[173] J. Zhang, L. Bi, J. Liu, et al. "Optical scattering simulation of ice particles with surface roughness modeled using the Edwards-Wilkinson equation". In: *Journal of Quantitative Spectroscopy and Radiative Transfer* 178 (2016), pp. 325–335. ISSN: 00224073. DOI: 10.1016/j.jqsrt.2016.02.013 (cit. on pp. 174, 175).

[174] K. Muinonen, E. Zubko, J. Tyynelä, et al. "Light scattering by Gaussian random particles with discrete-dipole approximation". In: *Journal of Quantitative Spectroscopy and Radiative Transfer* 106 (2007), pp. 360–377. ISSN: 00224073. DOI: 10.1016/j.jqsrt.2007.01.049 (cit. on pp. 174, 175).

[175] T. Nousiainen and K. Muinonen. "Surface-roughness effects on single-scattering properties of wavelength-scale particles". In: *Journal of Quantitative Spectroscopy and Radiative Transfer* 106 (2007), pp. 389–397. ISSN: 00224073. DOI: 10.1016/j.jqsrt.2007.01.024 (cit. on pp. 174, 175).

[176] M. Kahnert, T. Nousiainen, and P. Mauno. "On the impact of non-sphericity and small-scale surface roughness on the optical properties of hematite aerosols". In: *Journal of Quantitative Spectroscopy and Radiative Transfer* 112 (2011), pp. 1815–1824. ISSN: 00224073. DOI: 10.1016/j.jqsrt.2011.01.022 (cit. on pp. 174, 175).

[177] V. Angelidakis, S. Nadimi, and S. Utili. "SHape Analyser for Particle Engineering (SHAPE): Seamless characterisation and simplification of particle morphology from imaging data". In: *Computer Physics Communications* 265 (2021), pp. 1–9. ISSN: 00104655. DOI: 10.1016/j.cpc.2021.107983. URL: https://doi.org/10.1016/j.cpc.2021.107983 (cit. on pp. 177, 178).

[178] H. Wadell. "Volume , Shape , and Roundness of Rock Particles". In: *The journal of geology* 40.5 (1932), pp. 443–451 (cit. on p. 178).

[179] C. Li, G. W. Kattawar, and P. Yang. "Effects of surface roughness on light scattering by small particles". In: *Journal of Quantitative Spectroscopy and Radiative Transfer* 89 (2004), pp. 123–131. ISSN: 00224073. DOI: 10.1016/j.jqsrt.2004.05.016 (cit. on pp. 190, 192, 206).

[180] O. Dubovik, A. Sinyuk, T. Lapyonok, et al. "Application of spheroid models to account for aerosol particle nonsphericity in remote sensing of desert dust". In: *Journal of Geophysical Research Atmospheres* 111.11 (2006), pp. 1–34. ISSN: 01480227. DOI: 10.1029/2005JD006619 (cit. on p. 192).

[181] E. R. D. Scott and A. N. Krot. "Chondrites and Their Components". In: *Treatise on Geochemistry*. Ed. by Heinrich D Turekian, Holland K, and Karl. Oxford: Pergamon, 2007, pp. 1–72. ISBN: 978-0-08-043751-4. DOI: 10.1016/B0-08-043751-6/01145-2 (cit. on p. 219).

[182] L. Vacher, J. Villeneuve, M. Verdier-paoletti, et al. "Collisional and alteration history of the CM parent body To cite this version : HAL Id : hal-02357533". In: *Geochimica et Cosmochimica Acta* 239 (2018), pp. 213–234. DOI: 10.1016/j.gca.2018.08.006. (cit. on p. 220).

[183] H. Bikas, P. Stavropoulos, and G. Chryssolouris. "Additive manufacturing methods and modeling approaches: A critical review". In: *International Journal of Advanced Manufacturing Technology* 83.1 (2016), pp. 389–405. ISSN: 14333015. DOI: 10.1007/s00170-015-7576-2 (cit. on p. 221).

[184] R. H. Hewins. "Chondrules". In: *Annual Review of Earth and Planetary Sciences* 25.1 (1997), pp. 61–83. ISSN: 00846597. DOI: 10.1146/annurev.earth.25.1.61 (cit. on p. 221).

[185] R. V. Gaines, H. C. W. Skinner, E. E. Foord, et al. In: *Dana's New Mineralogy*. New York: John Wiley and Sons, 1997 (cit. on pp. 221, 266).

[186] A. M. Hofmeister, B. Wopenka, and A. J. Locock. "Spectroscopy and structure of hibonite, grossite, and CaAl2 O4: Implications for astronomical environments". In: *Geochimica et Cosmochimica Acta* 68.21 (2004), pp. 4485–4503. ISSN: 00167037. DOI: 10.1016/j.gca.2004.03.011 (cit. on pp. 221, 266, 269).

[187] S. Charnoz, J. Aléon, N. Chaumard, et al. “Growth of calcium-aluminum-rich inclusions by coagulation and fragmentation in a turbulent protoplanetary disk: Observations and modelisation”. In: *Icarus* 252 (2015), pp. 440–453. ISSN: 10902643. DOI: 10.1016/j.icarus.2015.01.023 (cit. on p. 243).

[188] J. I. Simon, J. N. Cuzzi, K. A. McCain, et al. “Particle size distributions in chondritic meteorites: Evidence for pre-planetesimal histories”. In: *Earth and Planetary Science Letters* 494 (2018), pp. 69–82. ISSN: 0012821X. DOI: 10.1016/j.epsl.2018.04.021 (cit. on p. 243).